

# **Additive manufacture of an aluminium alloy: processing, microstructure, and mechanical properties**

**Nesma T. Aboulkhair, MSc**

**Thesis submitted to the University of Nottingham for the degree of Doctor  
of Philosophy (PhD)**

**DECEMBER 2015**

## **ABSTRACT**

Additive manufacturing of aluminium alloys using selective laser melting (SLM) is of research interest nowadays because of its potential benefits in industry sectors such as aerospace and automotive. However, in order to demonstrate the credibility of aluminium SLM for industrial needs, a comprehensive understanding of the interrelation between the process parameters, produced microstructure, and mechanical behaviour is still needed. This thesis aims at contributing to developing this comprehensive understanding through studying the various aspects of the process, with investigation of the powder raw material to the near fully dense samples, focussing on the alloy AlSi10Mg.

The primary building blocks in the SLM process are the single tracks. Their formation is affected by the physical properties of the material that control the laser-material interactions. Keyhole mode melting was found to be dominant when processing AlSi10Mg, producing conical-shaped melt pools. Porosity was not evident in single tracks and individual layers. Satellites and balling defects, however, were observed on top of the tracks and layers at higher scan speeds, which contribute to porosity formation with layer progression.

The combination of process parameters controls the amount of porosity formed, with the scan speed controlling the type of pore; metallurgical or keyhole pore. A pre-melt scan strategy significantly reduced porosity and successfully produced 99.8% dense samples. Furthermore, the pre-melt scan strategy was seen to effectively reduce the number of pores developed when using powder that does not fully comply with the process standards. The gas

flow rate within the process chamber controlled laser spatter and condensate removal during processing, which in its turn affected the degree of porosity in the samples.

The SLM process resulted in an AlSi10Mg alloy with a characteristically fine microstructure, with fine equiaxed grains at the melt pool core and coarser elongated grains at the boundary. The material showed a strong texture, owing to directional solidification. Cellular dendritic Al with inter-dendritic Si was observed. The material was subjected to a T6 heat treatment that transformed the microstructure into spheroids of Si in the Al matrix.

This study investigated, for the first time, the local mechanical properties within the SLM material using nanoindentation. This showed a uniform nano-hardness profile that was attributed to the fine microstructure and good dispersion of the alloying elements. Spatial variation within the material was recorded after the T6 heat treatment due to phase transformation. This study is also the first to report on the compressive behaviour of solid SLM material, which is important for developing prediction and simulation models. The heat treatment softened the material and provided it with an increased ductility under indentation, tensile, and compressive types of loading. In addition, the material showed good fatigue performance, which was further improved by heat treatment and machining to obtain a smoother surface roughness.

This investigation has, therefore, developed an understanding of the various aspects of the SLM process yielding near fully dense parts and defined the microstructure-mechanical property interrelation promoting the process for Al alloys in a number of industrial sectors.

## LIST OF PUBLICATIONS, CONFERENCES, AND AWARDS

- *Published Journal Papers:*

-**Nesma T. Aboulkhair**, Nicola M. Everitt, Ian Ashcroft, Chris Tuck, “Reducing porosity in AlSi10Mg parts processed by selective laser melting”, *Additive Manufacturing*, Vol. 1-4, 2014, pp. 77-86. DOI:10.1016/j.addma.2014.08.001

-Stewart Bland **Nesma T. Aboulkhair**, “Reducing Porosity in additive manufacturing”, *Metal Powder Report*, Vol. 70, Issue 2, 2015, pp. 79-81. DOI: 10.1016/j.mprp.2015.01.002.

-Marco Simonelli, Chris Tuck, **Nesma Aboulkhair**, Ian Maskery, Ian Ashcroft, Ricky Wildman, Richard Hague, “A Study on the Laser Spatter and the Oxidation Reactions during Selective Laser Melting of 316L stainless steel, Al-Si10-Mg and Ti-6Al-4V”, *Metallurgical and Materials Transactions A*, Vol. 46, Issue 9, pp. 3842-3851, 2015, DOI: 10.1007/s11661-015-2882-8.

-**Nesma T. Aboulkhair**, Chris Tuck, Ian Ashcroft, Ian Maskery, Nicola M. Everitt, “On the precipitation hardening of selective laser melted AlSi10Mg”, *Metallurgical and Materials Transactions A*, Vol. 46, issue 8, pp. 3337-3341, 2015, DOI: 10.1007/s11661-015-2962-9.

-**Nesma T. Aboulkhair**, Ian Maskery, Chris Tuck, Ian Ashcroft, and Nicola M. Everitt, “On the formation of AlSi10Mg single tracks and layers in Selective Laser Melting: Investigations using Nanoindentation”, *Journal of Materials Processing Technology*, Vol. 230, pp. 88-89, DOI: 10.1016/j.jmatprotec.2015.11.016.

-Nicola M. Everitt, **Nesma T. Aboulkhair**, Ian Maskery, Chris Tuck, Ian Ashcroft, “Nanoindentation shows uniform local mechanical properties across melt pools and layers produced by selective laser melting of AlSi10Mg alloy”, *Advanced Materials Letters* (in press).

- *Journal Papers under Review:*

-**Nesma T. Aboulkhair**, Alex Stephens, Ian Maskery, Chris Tuck, Ian Ashcroft, Nicola M. Everitt, “The microstructure and mechanical properties of selectively laser melted AlSi10Mg: The effect of a conventional T6 heat treatment”.

-**Nesma T. Aboulkhair**, Ian Maskery, Chris Tuck, Ian Ashcroft, Nicola M. Everitt, “Improving the fatigue behaviour of a selectively laser melted Aluminium alloy: Influence of heat treatment and surface quality”.

- *Conferences, workshops, and talks:*

-Materials, Mechanics and Structures PhD poster competition, University of Nottingham, March 14<sup>th</sup> 2014. (*Poster presentation: Selective laser melting SLM of AlSi10Mg*)

-Engineering Research Showcase, University of Nottingham, 7<sup>th</sup>-8<sup>th</sup> May 2014. (*Poster presentation: Selective laser melting SLM of AlSi10Mg*)

-Delivered a talk to the journal “Materials Today” on selective laser melting of aluminium alloys that was published as a podcast on their website (<http://www.materialstoday.com/metals-alloys/podcasts/selective-laser-melting/>), January 2015.

-Materials, Mechanics and Structures PhD poster competition, University of Nottingham, February 27<sup>th</sup> 2015. (*Poster presentation: Single tracks in additive manufacturing*)

-4<sup>th</sup> International Laser Applications Symposium ILAS 2015, Chesford Grange Conference Centre, Kenilworth, United Kingdom, March 17<sup>th</sup> 2015. (*Poster presentation: “Nanohardness and microstructure of selective laser melted AlSi10Mg single tracks”*), **Nesma T. Aboulkhair**, Ian Maskery, Chris Tuck, Ian Ashcroft, Nicola M. Everitt, in Industrial Laser Applications Symposium (ILAS 2015), Cath Rose, Editors, Proceedings of SPIE vol. 9657 (SPIE, Bellingham, WA 2015), 965702, DOI:10.1117/12.2190015.

-Engineering Research Showcase, University of Nottingham, 6<sup>th</sup> May 2015. (*Poster presentation: Single tracks in additive manufacturing*)

-22<sup>nd</sup> World of Photonics Congress: Lasers in Manufacturing Conference LiM 2015, International Congress Center Munich, Germany, June 22<sup>nd</sup> – 26<sup>th</sup> 2015. (*Talk: “The role of powder properties on the process-ability of Aluminium alloys in selective laser melting”*), **Nesma T. Aboulkhair**, Ian Maskery, Ian Ashcroft, Chris Tuck, Nicola M. Everitt, Proceedings of the 22<sup>nd</sup> World of Photonics Congress: Lasers in Manufacturing Conference 2015).

-26<sup>th</sup> International Annual Solid Freedom Fabrication Symposium SFF 2015, Austin, Texas, USA, August 10<sup>th</sup> – 12<sup>th</sup> 2015. (*Talk: “Mechanical properties of selective laser melted AlSi10Mg: nano, micro, and macro properties”*), **Nesma T. Aboulkhair**, Alex Stephens, Ian Maskery, Chris Tuck, Ian Ashcroft, Nicola M. Everitt).

-26<sup>th</sup> International Annual Solid Freedom Fabrication Symposium SFF 2015, Austin, Texas, USA, August 10<sup>th</sup> – 12<sup>th</sup> 2015. (“*Fatigue performance enhancement of selectively laser melted aluminium alloy by heat treatment*” Ian Maskery, **Nesma Aboulkhair**, Chris Tuck, Ian Ashcroft, Ricky Wildman, Nicola M. Everitt, Richard Hague).

- *Awards:*

-Dean of Engineering Scholarship for International Research Excellence, October 2012.

-Runner-up in the Materials, Mechanics and Structures PhD poster competition, University of Nottingham, March 14<sup>th</sup> 2014.

-Best poster in the Materials, Mechanics and Structures PhD poster competition, University of Nottingham, February 27<sup>th</sup> 2015.

-Best student manuscript (titled: Nanohardness and microstructure of selective laser melted AlSi10Mg single tracks) in the 4<sup>th</sup> International Laser Applications Symposium ILAS 2015, Chesford Grange Conference Centre, Kenilworth, United Kingdom, March 17<sup>th</sup> 2015.

-University Postgraduate Endowed Prize, Andrew Hendry Scholarship, May 13<sup>th</sup> 2015.

## **ACKNOWLEDGEMENT**

This thesis might not have seen the light without the help of family, academic supervisors (Dr. Nicola M. Everitt, Prof. Ian Ashcroft, and Dr. Chris Tuck), colleagues, and friends. Therefore, I am obliged to start by expressing my gratitude to all who believed in me and supported me to be where I am today.

There is nothing I could ever say to express how indebted I am to my family, so this was probably the most difficult bit to write in the thesis. Tarik Aboulkhair, my father, the moral and financial support that you've always provided are invaluable. Maha Abdelkhalik, my mother and lifetime companion, you've always supported me spiritually in various ways to boost my confidence when I start questioning my capabilities. Ibrahim, my brother, simply you are my backbone. Love you to the moon and back.

When I first came to the University of Nottingham pursuing a PhD degree, I started working on a project and later on recognised that “we were not made for each other!” After one year of trying to make this relationship work, I decided it is just about time to let go and move on to another project. The understanding and support I received from Nicola, until we found an alternate project, is a lesson to learn. She was proactive in a way that inspired me not to give up on my degree and work on finding an alternative, teaching me how a supervisor can set a model in persistence for their students. Thank you, Nicola.

I am thankful for Chris and Ian for the risk of taking on a student having only two years remaining in the course, in which she had to fit a three years PhD. I learnt a lot from you guys and owe you big time for the knowledge you passed on to me over the past two years. I appreciate your efforts in improving my

“abstract” and “conclusions” writing skills, one day I will get there. Thank you all for not thinking that I am a lunatic who might keep on changing topics every year wasting your time, because I thought that of myself at some point!

I am grateful for Ian Maskery for I learnt a lot from our discussions and specifically for teaching me how to “quote my errors”, which was so close to driving him crazy. Thank you, Ian. Marco Simonelli, you might not know it but I see you as the materials guru, thank you for helping me whenever I needed. Mark Hardy, I am sorry that you are the one who had to suffer from my lousy memory because most of the times I got to use the Renishaw machine I kept asking you to remind me how to do so. Thank you for your patience and all the things you taught me. I promise you to take notes next time. I gratefully acknowledge the help of Dr. Nigel Neate, Mr. Tom Buss, and Mr. Jason Greeves in various sample preparations and testing.

My sincere thanks also go to my friends, Karim Abdel Salam, Mohamed Hegazy, Aya El Mehanny, Hesham Sakr, and Yousra Zakareia, for their continuous support. Eiman El Banhawy, thank you for your help when I first arrived here, helping me settle down and phase out my homesickness. To the gem in the crown, Irene Samy, I cannot thank you enough for being by my side during my ups and downs and for caring for my family in my absence.

Special thanks to the Dean of Engineering Scholarship for International Research Excellence, from the University of Nottingham, for providing the tuition fees for this course.

*Thank you all.*

## CONTENTS

ABSTRACT .....	I
LIST OF PUBLICATIONS, CONFERENCES, AND AWARDS .....	III
ACKNOWLEDGEMENT .....	VII
LIST OF FIGURES .....	XIV
LIST OF TABLES.....	XXVII
CHAPTER (1): Introduction .....	1
1.1. Selective laser melting (SLM).....	3
1.2. Aluminium alloys in industry .....	4
1.3. Aluminium alloys and selective laser melting.....	5
1.4. The significance and novelty of this research.....	7
1.5. Thesis aim, objectives, and methodologies .....	9
1.6. Thesis outline/structure.....	11
CHAPTER (2): Literature Review .....	14
2.1. Aluminium and its alloys.....	14
2.2. Aluminium powder for SLM.....	18
2.2.1. Properties of powder .....	18
2.2.2. Tailoring powders .....	20
2.2.3. Alloy development and <i>in-situ</i> composite production .....	20
2.2.4. Powder recycling .....	21
2.3. The processing environment/media in SLM .....	22
2.4. Single scan tracks using SLM.....	23

2.4.1. The motivation behind studying single tracks .....	23
2.4.2. Single track experiments and parameters.....	26
2.4.3. Thermal behaviour within melt pools .....	30
2.5. Overlap of scan tracks in SLM .....	32
2.5.1. Overlap into single layers .....	32
2.5.2. Overlap into thin walls.....	33
2.6. Material qualification research .....	34
2.6.1. Parameters and experimental approaches .....	34
2.6.2. Parametric investigations to produce near fully dense samples.....	41
2.7. Microstructure of the selectively laser melted material.....	44
2.8. Mechanical performance of selectively laser melted parts.....	48
2.9. Further aspects in selective laser melting .....	54
2.10. Summary.....	56
 CHAPTER (3): Materials & Methods .....	 60
3.1. The formation of single tracks and layers.....	60
3.2. Process parameter investigations to produce near fully dense parts.....	63
3.2.1. Hatch spacing study .....	64
3.2.2. Scan speed study .....	65
3.2.3. Scan strategy study .....	66
3.2.4. Evaluating the quality of the produced samples .....	67
3.3. Investigating further parameters in the SLM process.....	68
3.3.1. Powder quality effect .....	68

3.3.2. Gas flow within the processing chamber .....	69
3.4. Fabricating and characterising AlSi10Mg SLM samples .....	70
3.4.1. Microstructural investigations .....	70
3.4.2. Heat treatment study .....	72
3.4.3. Nanoindentation .....	73
3.4.4. Tensile behaviour .....	77
3.4.5. Compressive behaviour .....	78
3.4.6. Fatigue behaviour .....	79
CHAPTER (4): Single tracks and layers in selective laser melting .....	81
4.1. Fusion lines on a substrate material .....	81
4.2. Overlap of fusion lines .....	88
4.3. Single tracks from AlSi10Mg powder .....	90
4.3.1. Single tracks from 40 µm thick powder layer .....	90
4.3.2. Single tracks from 400 µm thick powder layer .....	94
4.3.3. Distinction between balling and satellites .....	100
4.4. Single layers .....	103
4.4.1. Single layer topography .....	103
4.4.2. Single layer cross-sections .....	107
4.5. Summary .....	112
CHAPTER (5): Selective laser melting parametric studies to produce near fully dense parts .....	116
5.1. Powder characterisation .....	117

5.2. Hatch spacing study .....	119
5.3. Scan speed study.....	123
5.4. Scan strategy study .....	130
5.5. Microstructural investigation of melt pools and pores .....	133
5.6. Comparative chemical composition analysis for powder versus bulk samples .....	137
5.7. Further parameters in selective laser melting .....	140
5.7.1. The role of powder properties on the processability of AlSi10Mg...	140
5.7.2. Gas flow within the processing chamber .....	147
5.8. Summary.....	149
CHAPTER (6): Microstructural characterisation of selectively laser melted AlSi10Mg .....	154
6.1. Microstructure of single tracks .....	154
6.2. Microstructure of single layers .....	159
6.3. Analysis of 3D bulk samples .....	160
6.3.1. Topography .....	160
6.3.2. X-ray diffraction and crystallographic texture.....	162
6.3.3. Microstructure and the effect of heat treatment.....	165
6.4. Summary.....	175
CHAPTER (7): Mechanical characterisation of selectively laser melted AlSi10Mg .....	177
7.1. Nano-scale properties using nanoindentation.....	177

7.1.1. Nano-hardness profiles across a single track .....	180
7.1.2. Nano-hardness profiles across a single layer .....	183
7.1.3. Nano-hardness profiles across multi-layered parts .....	186
7.1.4. Nano-hardness in the vicinity of keyhole pores.....	187
7.1.5. Nano-hardness profiles across multi-layers and the effect of heat treatment .....	189
7.2. Micro-scale properties: micro-hardness .....	192
7.3. Macro-scale properties: tensile behaviour .....	197
7.4. Macro-scale properties: compressive behaviour .....	204
7.5. Macro scale properties: fatigue performance .....	206
7.5.1. Surface quality of the test specimens.....	207
7.5.2. Stress-life (S-N) curves.....	208
7.5.3. Fractography .....	216
7.6. Summary.....	229
CHAPTER (8): Conclusions and recommendations for future work.....	232
8.1. Conclusions .....	232
8.2. Benefits of the study to academia.....	235
8.3. Benefits of the study to the industry .....	236
8.4. Recommendations for future work .....	237
REFERENCES .....	241

## LIST OF FIGURES

Figure 1: Thermal conductivity of various materials [16].....	7
Figure 2: Mapping thesis aim, objectives, and methodologies.....	9
Figure 3: Thesis outline/structure. ....	12
Figure 4: The Al-Si alloy system phase diagram [42].....	16
Figure 5: The effect of power density on the laser-material interaction mechanism (a) surface heating, (b) surface melting, and (c) surface vaporisation/keyholing [16]. ....	24
Figure 6: Laser-material interaction mechanism based on the power density and interaction time [16]. ....	24
Figure 7: Schematic presentation for gaseous bubbles motion within a melt pool during SLM at increasing energy density (a) 15KJ/m, (b) 17.5 KJ/m, (c) 20 KJ/m, and (d) 22.5 KJ/m, as illustrated by Dai and Gu [68]. ....	32
Figure 8: Simplified schematic presentation of an SLM machine. ....	36
Figure 9: Schematic presentation of the SLM process. ....	36
Figure 10: Controlling parameters in SLM process [2].....	38
Figure 11: Geometrical parameters in the SLM process. ....	38
Figure 12: Examples of scan patterns (a) uni-directional, (b) meander, and (c) checkerboard scans.....	39
Figure 13: Altering the scan orientation 90° per layer. ....	39
Figure 14: AlSi10Mg sample processed by SLM (a) polished without removing the trapped powder, and (b) the same sample polished until the removal of the sintered powders.....	41
Figure 15: Microstructure of SLM AlSi10Mg as observed from the plane normal to the build direction [4].....	45

Figure 16: Microstructure of SLM AlSi10Mg as seen on the plane parallel to the build direction at (a) low and (b) high magnifications [4].	46
Figure 17: EBSD orientation maps showing the grains orientation in SLM AlSi10Mg in two perpendicular planes.	46
Figure 18: The pole figure and inverse pole figures showing the change in the crystallographic texture of SLM AlSi10Mg with the scan strategy (a) unidirectional scan strategy, (b) alternating scan strategy with 90° rotation per layer, and (c) checkerboard scan strategy [4].	47
Figure 19: Tensile behaviour of SLM AlSi10Mg samples built in two different orientations and compared to the die cast equivalent [49].	50
Figure 20: Fatigue performance of SLM AlSi10Mg samples in their as-built and heat treated (T6) conditions. The samples were built in various orientations (0°, 45°, and 90°) with respect the build plate [18].	52
Figure 21: Mapping the various experiments conducted in this thesis.	60
Figure 22: Schematic presentation for the fusion lines experiments (a) single and (b) overlapping.	61
Figure 23: Selective laser melting of AlSi10Mg (a) in process, (b) process completed, and (c) test cubes on the platform.	64
Figure 24: Laser spatter shown as darker particles surrounding the cubes being built.	68
Figure 25: Schematic presentation for the top view of the processing chamber in the SLM machine showing gas circulation.	70
Figure 26: Planes of a cubic sample with layers in the XY-plane stacking up in the building direction (Z-axis).	72
Figure 27: T6 heat treatment investigations study plan.	73

Figure 28: Samples for nanoindentation.....	74
Figure 29: Nanotest™ indenter tip-sample setup. ....	76
Figure 30: Tensile test sample. ....	77
Figure 31: Compression test specimen. ....	78
Figure 32: Fatigue test samples. ....	79
Figure 33: Fatigue test specimen. ....	80
Figure 34: Thinning of fusion line with increasing the scan speed. ....	82
Figure 35: Reduction in HAZ thickness with increasing scan speed. ....	83
Figure 36: Irregularities in fusion lines using 750, 1000, 1250, and 1500 mm/s. .....	84
Figure 37: Fusion lines produced using different scan speeds showing evidence of micro-porosity. ....	85
Figure 38: Cross-sectional view of the polished fusion lines at different scan speeds. ....	86
Figure 39: Effect of scan speed on width and depth of penetration of the fusion lines (with error bars showing standard error). ....	87
Figure 40: Overlap of fusion lines with 50 μm hatch spacing using (a) 250, (b) 500, and (c) 750 mm/s. ....	89
Figure 41: Lack of overlap between fusion lines at 750 mm/s and 150 μm hatch spacing. ....	89
Figure 42: Transverse view showing overlap of fusion lines processed using a speed of 500 mm/s and a hatch spacing of 50 μm. ....	90
Figure 43: Single tracks of AlSi10Mg from 40 μm thick layers at (a) 250, (b) 500, and (c) 750 mm/s. ....	91

Figure 44: Cross-sectioned single tracks processed from a 40 $\mu\text{m}$ thick powder layer at (a) 250 mm/s, (b) 500 mm/s, and (c) 750 mm/s. ....	92
Figure 45: Single tracks of selective laser melted AlSi10Mg (250 mm/s and 400 $\mu\text{m}$ layer thickness). ....	95
Figure 46: Single tracks of selective laser melted AlSi10Mg (500 mm/s and 400 $\mu\text{m}$ layer thickness). ....	95
Figure 47: Single tracks of selective laser melted AlSi10Mg (750 mm/s and 400 $\mu\text{m}$ layer thickness). ....	95
Figure 48: Cross-sections of single tracks formed using a layer thickness of 400 $\mu\text{m}$ with a 250 mm/s scan speed. ....	97
Figure 49: Different forms of single tracks processed at 500 mm/s using a 400 $\mu\text{m}$ layer thickness (a) free circular cylinder and (b) segmental cylinder. ....	98
Figure 50: Different forms of single tracks processed at 750 mm/s using a 400 $\mu\text{m}$ layer thickness (a) free circular cylinder and (b) segmental cylinder. ....	98
Figure 51: Topography of a 400 $\mu\text{m}$ thick single layer of selective laser melted AlSi10Mg using 750 mm/s scan speed and 50 $\mu\text{m}$ hatch spacing. ....	101
Figure 52: Cross-sectional view of a polished single layer with balling on the surface with the inset showing the balling region after etching. ....	101
Figure 53: A satellite on top of a single track processed from a 40 $\mu\text{m}$ thick powder layer using 250 mm/s (a) low and (b) high magnification, and (c) showing cross-sectioned as-received powder. ....	102
Figure 54: Topography of a 40 $\mu\text{m}$ thick single layer of selective laser melted AlSi10Mg using 250 mm/s scan speed and 50 $\mu\text{m}$ hatch spacing. ....	103

Figure 55: Topography of a 40 $\mu\text{m}$ thick single layer of selective laser melted AlSi10Mg using 500 mm/s scan speed and 50 $\mu\text{m}$ hatch spacing with arrows pointing to small satellites. ....	104
Figure 56: Topography of a 40 $\mu\text{m}$ thick single layer of selective laser melted AlSi10Mg using 750 mm/s scan speed and 50 $\mu\text{m}$ hatch spacing with arrows pointing to larger satellites and gaps or voids in the layer. ....	104
Figure 57: Topography of a 400 $\mu\text{m}$ thick single layer of selective laser melted AlSi10Mg using 250 mm/s scan speed and 50 $\mu\text{m}$ hatch spacing. ....	106
Figure 58: Topography of a 400 $\mu\text{m}$ thick single layer of selective laser melted AlSi10Mg using 500 mm/s scan speed and 50 $\mu\text{m}$ hatch spacing. ....	106
Figure 59: Topography of a 400 $\mu\text{m}$ thick single layer of selective laser melted AlSi10Mg using 750 mm/s scan speed and 50 $\mu\text{m}$ hatch spacing. ....	107
Figure 60: A single layer of 40 $\mu\text{m}$ thick selective laser melted AlSi10Mg formed using a hatch spacing of 50 $\mu\text{m}$ and a scan speed of (a) 250 mm/s, (b) 500 mm/s, and (c) 750 mm/s. ....	108
Figure 61: A 400 $\mu\text{m}$ thick single layer of selective laser melted AlSi10Mg (250 mm/s scan speed and 50 $\mu\text{m}$ hatch spacing). ....	109
Figure 62: Single layers of selective laser melted AlSi10Mg (a-d: 500 mm/s) and (e-g: 750 mm/s) using 50 $\mu\text{m}$ hatch spacing and 400 $\mu\text{m}$ layer thickness. ....	111
Figure 63: Particle size distribution of AlSi10Mg powder supplied by LPW technology with the inset showing the morphology of the powder. ....	118
Figure 64: Cross-sectioned AlSi10Mg powder supplied by LPW Technology showing evidence of inherent porosity at (a) low and (b) high magnification. ....	118

Figure 65: Cellular-dendritic microstructure in the cross-sectioned AlSi10Mg powder. ....	119
Figure 66: Low magnification images for the surface topography of AlSi10Mg test cubes produced by SLM using different hatch spacing values (a) 50 $\mu\text{m}$ , (b) 100 $\mu\text{m}$ , (c) 150 $\mu\text{m}$ , (d) 200 $\mu\text{m}$ , and (e) 250 $\mu\text{m}$ . ....	120
Figure 67: High magnification images for the surface topography of AlSi10Mg test cubes produced by SLM using different hatch spacing values (a) 50 $\mu\text{m}$ , (b) 100 $\mu\text{m}$ , (c) 150 $\mu\text{m}$ , (d) 200 $\mu\text{m}$ , and (e) 250 $\mu\text{m}$ . ....	121
Figure 68: Effect of changing the hatch spacing on the relative density represented by the pore area fraction on micrographs determined using ImageJ. ....	122
Figure 69: Evolution of pores with scan speed (a) 250, (b) 500, (c) 750, and (d) 1000 mm/s. ....	125
Figure 70: Extensive presence of metallurgical pores only at scan speeds below 250 mm/s (a) 100 mm/s, (b) 150 mm/s, and (c) 200 mm/s. ....	125
Figure 71: The influence of energy density variation on a sample's degree of porosity. ....	128
Figure 72: Balling increases with the increase in scan speed (a) 250, (b) 500, (c) 750, and (d) 1000 mm/s. ....	130
Figure 73: Porosity evolution in samples processed using different combinations of scan speeds and scan strategies. ....	132
Figure 74: Influence of scan strategy on relative density for each of the scan speeds investigated 500 mm/s, 750 mm/s, and 1000 mm/s. ....	133
Figure 75: Microstructure of etched samples (HS 50 $\mu\text{m}$ , SS 500 mm/s, and unidirectional single scan): (a) adjacent melt pools, (b) vicinity of a	

keyhole pore where the pore (not shown) is below the coarse	
microstructure, and (c) keyhole pore enclosing non-molten powders. ...	134
Figure 76: Keyhole pore enclosing non-molten powders.....	135
Figure 77: Microstructure of the melt pools demonstrating (a) cell orientation,	
(b) morphology, and (c) grain size distribution.....	136
Figure 78: Microstructure of an AlSi10Mg sample produced by SLM using the	
pre-melt scan strategy at 500 mm/s.....	137
Figure 79: Morphology of (a) fresh powder and (b) laser spatter. ....	139
Figure 80: Elongated and irregular particle morphology in the LPW powder.	
.....	140
Figure 81: Particles in the TLS powder were mostly spherical with observed	
satellites.....	141
Figure 82: Microstructure of the cross-sectioned powder from batch (a) LPW	
and (b) TLS. ....	142
Figure 83: Particle size distribution for AlSi10Mg powders supplied by LPW	
and TLS.....	144
Figure 84: Relative density of SLM samples processed using different scan	
strategies and powders with error bars representing the standard error..	146
Figure 85: Effect of gas circulation on the relative density of SLM Al parts	
showing inter-build variability.....	148
Figure 86: Summary of the study and findings. ....	150
Figure 87: Microstructure of a single track processed using 250 mm/s revealed	
using Keller's reagent at (a) low and (b) high magnification. ....	155
Figure 88: Microstructure of a single track processed using 500 mm/s revealed	
using Keller's reagent. ....	157

Figure 89: Mapping the chemical composition of Si in (a) a scan track processed from a 40 $\mu\text{m}$ powder layer at 250 mm/s scan speed with Si in (b) presented by the green colour. ....	158
Figure 90: Microstructure of overlapping melt pools in a single layer processed at 250 mm/s revealed by Keller's reagent.....	159
Figure 91: Microstructure of overlapping melt pools in a single layer processed at 500 mm/s revealed by Keller's reagent.....	160
Figure 92: Morphology of the top surface of an AlSi10Mg part produced by SLM as seen by (a) secondary electrons detector SE and (b) backscatter electrons detector BSE (surface perpendicular to the building direction). .....	161
Figure 93: Profile measurement for the surface of an AlSi10Mg SLM part..	162
Figure 94: XRD pattern for AlSi10Mg samples processed by SLM.....	163
Figure 95: The (a) (110), (b) (100), and (c) (111) pole figures with (d) unit cell demonstrating the mapped planes. Note the build direction (BD), the scanning direction (SD), and the transverse direction (TD).....	165
Figure 96: Microstructure of as-built AlSi10Mg sample produced by SLM showing XY, XZ, and YZ planes with lower magnification (top) and higher magnification (bottom).....	166
Figure 97: Microstructure of AlSi10Mg part processed by SLM (a) XY-plane and (b) YZ-plane. ....	168
Figure 98: Coarser grains observed at the melt pool boundary in the (a) XY- plane shown as (b) cellular-dendritic grains in the YZ-plane. ....	168

Figure 99: Microstructure of (a) as-built sample XZ plane, (b) as-built sample XY plane, and (c) EDX composition map for Si in the as built sample XY plane. .... 169

Figure 100: Microstructure of SLM samples (a) XY plane after 1 hr SHT, (b) XZ plane after 1 hr SHT and 12 hrs AA , (c) XZ plane after 4 hrs SHT, (d) XZ plane after 4 hrs SHT and 6 hrs AA, and (e) higher magnification image of XZ plane after 1 hr SHT and 6 hrs AA showing the morphology of Si particles..... 172

Figure 101: Higher magnification SEM image clearly showing inter-dendritic Si around the  $\alpha$ -Al boundaries in the as-built sample. .... 173

Figure 102: Particles analysis showing change in (a) average particle size and (b) particle density with heat treatment duration with error bars representing the standard error. .... 174

Figure 103: An illustrative example for loading and unloading in a nanoindentation test (a) schematic presentation for an indentation [137] and (b) load-depth curve..... 179

Figure 104: Nano-hardness profile of a line positioned at half the maximum height of a scan track spanning across both the laser irradiated material and the as-cast material. .... 180

Figure 105: The nano-hardness profile across the AlSi10Mg scan track (a) including the cast substrate and (b) excluding the cast-substrate. The array of indentations from which the nano-hardness map was retrieved is shown in (c). .... 183

Figure 106: The array of indentations on (a) a series of overlapping melt pools in a single layer alongside (b) the corresponding nano-hardness profile. 184

Figure 107: SEM micrographs showing nano-indentations and corresponding chemical compositions within (a) the laser irradiated material (a) and at (b), (c), and (d) various points within the cast substrate. ....	185
Figure 108: An array of indentations across layers in a part fabricated using a single scan strategy showing (a) the microstructure and (b) the corresponding nano-hardness map. ....	187
Figure 109: An array of indentations across layers in a part fabricated using a pre-melt scan strategy showing (a) the microstructure and (b) the corresponding nano-hardness map. ....	187
Figure 110: (a) Coarsened microstructure in the vicinity of a keyhole pore (towards the top) in a sample processed using a unidirectional scan strategy alongside (b) the corresponding nano-hardness profile. ....	188
Figure 111: (a) Coarsened microstructure in the vicinity of a keyhole pore (towards the bottom) in a sample processed using a pre-melt scan strategy alongside (b) the corresponding nano-hardness profile. ....	188
Figure 112: Nano-hardness map demonstrating the property profile within (a) as-built SLM AlSi10Mg and (b) heat-treated SLM AlSi10Mg, as well as examples of the nano-indentations on the tested surfaces (c) as-built SLM material and (d) heat-treated SLM material. ....	190
Figure 113: Microstructure of the SLM AlSi10Mg (a) as-built and (b) heat treated, and (c) high magnification image for the as-built microstructure revealing the inter-dendritic Si within the $\alpha$ -Al matrix. ....	192
Figure 114: Evolution of micro-hardness with heat treatment procedure with error bars representing the standard error. ....	195

Figure 115: Engineering tensile stress-strain curves comparing the behaviour of SLM AlSi10Mg with and without heat treatment. ....	198
Figure 116: The overall fracture surface of a tensile sample with the origin of failure highlighted along with the direction of crack propagation pointed out by arrows. ....	199
Figure 117: Cross-sectional view of the fracture surface of a tensile sample demonstrating crack propagation along melt pool boundaries. ....	199
Figure 118: Fracture surface of SLM AlSi10Mg (a) as-built and (b) heat-treated T6. ....	201
Figure 119: Cross-sectioned fracture surface of tensile samples: (a) as-built material with (b) the corresponding representative chemical composition mapping and (c) heat-treated material with the corresponding chemical composition mapped in (d). ....	202
Figure 120: The compressive behaviour of SLM AlSi10Mg with and without heat treatment (average of three results per condition). The standard error is highlighted in yellow. The inset shows samples before and after testing. ....	205
Figure 121: Surface morphology of the sides of (a) an as-built fatigue sample and (b) a sample with machined surface (surface parallel to the building direction). ....	208
Figure 122: Effect of machining on the fatigue performance of SLM AlSi10Mg. ....	209
Figure 123: Effect of heat treatment on the fatigue behaviour of SLM AlSi10Mg. ....	212

Figure 124: Effect of heat treatment followed by machining on the fatigue behaviour of SLM AlSi10Mg.....	212
Figure 125: S-N curves superimposed for all the investigated conditions, namely, (1) as-built, (2) heat treated, (3) machined, and (4) heat-treated & machined. ....	214
Figure 126: Fracture surface of an as-built sample tested at a maximum stress of 94 MPa. ....	217
Figure 127: Zones of fatigue fracture in an as-built sample loaded by a maximum stress of 94 MPa (a nominal stress of 52 MPa and an amplitude of 42 MPa).....	218
Figure 128: Zones of fatigue fracture in an as-built sample loaded by a maximum stress of 157 MPa (a nominal stress of 86 MPa and an amplitude of 71 MPa).....	219
Figure 129: Zones of fatigue fracture in an as-built sample loaded by a maximum stress of 220 MPa (a nominal stress of 120 MPa and an amplitude of 99 MPa).....	219
Figure 130: Fatigue fracture surface cross-section. ....	220
Figure 131: Fatigue cracks propagating through the fatigue cracked region. ....	221
Figure 132: Fatigue striations on the fracture surface of an as-built sample..	222
Figure 133: Cleavage fans and lines on the fracture surface of as-built samples tested at high stress levels (120 MPa nominal stress). ....	223
Figure 134: The scan tracks building up the sample using the checkerboard scan strategy clearly seen on the fracture surface of the as-built fatigue sample (pointed out by the arrows). ....	224

Figure 135: Foreign particle on the fracture surface of the as-built fatigue test sample..... 225

Figure 136: Mapping the chemical composition at the foreign particle on the fatigue fracture surface. .... 225

Figure 137: Fracture surface of a fatigue test specimen with machined surface showing failure to originate at a sub-surface defect..... 227

Figure 138: Sub-surface pore that was revealed after machining the sample. 227

Figure 139: High magnification images for the fracture surfaces of as-built (left) and heat-treated (right) fatigue samples. .... 228

## LIST OF TABLES

<b>Table 1: Comparison of properties of SLM candidate materials. ....</b>	<b>7</b>
<b>Table 2: Summary of the experimental plan for the single tracks experiments. ....</b>	<b>62</b>
<b>Table 3: Processing parameters combinations used in the hatch spacing study.....</b>	<b>65</b>
<b>Table 4: Combinations of processing parameters used in the scan speed study.....</b>	<b>65</b>
<b>Table 5: Scanning strategies variable parameters.....</b>	<b>66</b>
<b>Table 6: Processing parameters (set 1) using Renishaw AM250 to produce near fully dense parts. ....</b>	<b>71</b>
<b>Table 7: Processing parameters (set 2) using Renishaw AM250 to produce near fully dense parts .....</b>	<b>75</b>
<b>Table 8: Geometrical dimensions of AlSi10Mg single tracks. ....</b>	<b>93</b>
<b>Table 9: Chemical composition of LPW AlSi10Mg powders in relative weight%.....</b>	<b>118</b>
<b>Table 10: Relative density values (%) at different combinations of hatch spacing and scan speed.....</b>	<b>123</b>
<b>Table 11: Chemical composition of powders and bulk sample in relative weight %.....</b>	<b>138</b>
<b>Table 12: Comparing chemical composition of powders from different suppliers - in weight %. ....</b>	<b>143</b>
<b>Table 13: Comparing the micro-hardness of SLM AlSi10Mg with and without heat treatment.....</b>	<b>197</b>

<b>Table 14: Tensile properties of SLM AlSi10Mg developed in this study compared to results from the literature for SLM and die cast counterparts.....</b>	<b>203</b>
<b>Table 15: The compressive properties of SLM AlSi10Mg before and after heat treatment.....</b>	<b>206</b>
<b>Table 16: The evolution of nano-hardness from a single track to a bulk sample.....</b>	<b>229</b>
<b>Table 17: Summary of the effect of a conventional T6 heat treatment on mechanical performance of SLM AlSi10Mg.....</b>	<b>230</b>

## **CHAPTER (1): Introduction**

Various industrial sectors are now benefiting from the possibility of fabricating geometrically complex structures using additive manufacturing (AM) technologies for their several advantages, such as light-weighting and added functionality. AM also has the potential to fulfil demands for reducing the cost and time from design to manufacturing through saving on raw materials and cutting down a series of production processes and replacing them by a one step process. AM processes are sometimes referred to as Layered Manufacturing in reference to the nature of the process where a part is fabricated layer-by-layer from three-dimensional (3D) data [1]. AM is a commonly used term in the industry but the process is also known as autofab (autofabrication), freedom fabrication, layer-based manufacturing, stereolithography, or 3D printing [2]. These processes can be used for the production of prototypes or tools; however the term AM should only be used for the manufacture of end products. Originally, AM was used with polymeric materials and development of powder-bed based AM technology for metals resulted in Selective Laser Melting (SLM). The metallic-based AM processes also include Direct Metal Laser Sintering (DMLS) and Electron Beam Melting (EBM) [3-7].

Modern layered-manufacturing dates back to the mid-1980s and started to flourish during the late 1980s and early 1990s [8, 9]. 1994, however, is the year that marks the onset of an exponential increase in demand for layered-manufacturing machines [9] and only recently it has been considered part of a new industrial revolution [10]. Selective laser melting is gaining wide

popularity at the industrial and research levels [8, 11] as it fulfils the aim of manufacturers in shortening supply chains and lead times [12] and raising the level of automation in manufacturing along with the rates of production [13] via substituting a series of manufacturing process by one process. AM also promotes the possibility of producing cost-effective customised products [10, 14]. As the credibility of AM increases, its impact is expected to affect global business [9]. Already parts produced using AM are widely used in various fields, such as the medical [15], automotive, and aerospace industries [10]. Although AM has several advantages in terms of saving resources and allowing a high degree of fabrication freedom to manufacture complex and intricate parts, it cannot be generalised that AM would be suitable for businesses regardless of their needs and sizes. Conner *et al.* [14] developed a map for AM processes and their feasibility. By means of this map, business leaders can determine, based on the complexity, customisation, and production volume, whether AM is a suitable alternate to conventional manufacturing.

The metallic AM systems are categorised based on the system used to supply the material to be processed. There are three main types, namely, powder-bed systems, powder-feed systems, and wire-feed systems. Also, the heating source deployed is used to differentiate between the various processes; the most popular are electron beam and laser beam [9]. The technology of interest in the current study is SLM, which is a powder-bed process with a laser beam as the heat source.

The use of lasers in manufacturing is very common nowadays. Lasers gained consideration as machine tools and in the industrial processing of materials during the 1970s. Most importantly, the transition of laser processing from

laboratories to industry happened over the 1990s. The 2000s saw laser systems become cheaper, smaller, and more flexible [16].

### **1.1. Selective laser melting (SLM)**

SLM can fabricate components from loose powder that can not only have a comparable physical shape to conventionally manufactured components but also similar properties [17]. Generally, powder-bed processes offer geometrical flexibility in manufacturing industrial parts [18]. SLM can produce complex and intricate parts that would require a series of manufacturing processes if made by conventional techniques, consuming excess material (i.e. wastage), time and energy [17, 19-22]. In some cases it is even possible to manufacture parts using SLM that cannot be achieved using any conventional manufacturing method [10, 17, 23]. In addition, the process has the potential to save cost and time [17, 19-21] by saving costs on raw materials volume for being resource-efficient and shortening the time from design to manufacture through cutting down lead times in multi-process fabrication. Moreover, SLM promotes the possibility of producing large customized products [10] and it is a promising technique to manufacture functionally graded multi-material parts [20, 24].

The interest in SLM is partly motivated by the aim of finding a cleaner and more resource-efficient manufacturing process. In some cases, SLM can have outstanding ecological indicators since it saves resources as wastage has the potential of approaching zero [25] because the leftover powder from one SLM process is usually sieved and goes back into the system for re-use. The effect of using recycled powder was investigated by Ardila *et al.* [26]. They conducted

their experiments using IN718 powder and reported a material use efficiency of 95%. Using AM rather than conventional manufacturing can also reduce the carbon footprint [23]. Another advantage is design optimization since the technique allows complex parts to be created at little or no extra cost, enabling light-weight structures. Drastic weight reduction can be achieved by several methods, such as topology optimisation [27-29] or replacing a bulk of solid material with latticed structures [30-36]. Besides weight-reduction, lattice structures have wide applications in fields such as thermal insulation, shock absorption, acoustic absorptions, as well as being widely used in biomedical implants [37]. In brief, SLM promotes “design for performance” rather than “design for manufacturing” [25].

## **1.2. Aluminium alloys in industry**

Properties of Al alloys are considered outstanding since they have low density ( $2.7 \text{ gm/cm}^3$ ), high strength [38], adequate hardenability [39], good corrosion resistance [40-42], and excellent weldability [39]. As the demand for technologically complex and ecologically sustainable products increases, opportunities for Al in industry are expected to further flourish. Al is suitable for numerous applications, such as automobiles [43], food and beverage packaging, building construction, electricity transmission, transportation infrastructure, defence, aerospace, and machinery and tools production [40, 42].

Al-Si-Mg alloys are widely used in the automotive industry [44]. They are hardened by  $\text{Mg}_2\text{Si}$  so they are excellent for casting and welding in addition to being heat-treatable, hence they are attractive for the automotive and aircraft

industries [45]. Generally, Al alloys are favoured in the automotive industry for their light-weight since each 10% reduction in weight is equivalent to 5.5% reduction in fuel consumption [41]. Al-Si-Mg alloys such as (12% Si- 2.5% Ni – 1% Cu – 1% Mg) are used in manufacturing diesel engines and (9.5%Si – 3% Cu – 1% Mg) alloys are used in manufacturing pistons for automotive internal combustion engines [45]. The alloy Al7075 is extensively used by aircraft manufacturers [41]. Al alloy 296 is used for aircraft fittings and pumps, whereas 356 is used in engine blocks, transmissions, and wheels [42]. Aluminium is a superior candidate in applications where specific strength and stiffness are design considerations.

### **1.3. Aluminium alloys and selective laser melting**

As much as AM processes are finding their way into commercialisation at a fast rate, not many materials are yet processable by SLM [8, 46]. This is due to the different physical properties of the material. The current research interest in SLM mainly focussed on titanium [47, 48], high speed steels [19], and nickel super alloys [9, 49], although a few other commercial alloys are being used in AM, such as tool steels (H13 and Cermets) and some refractory alloys (MoRe, Ta-W, CoCr, and alumina) [9]. This is because these SLM candidate materials process relatively easily compared to others. Also, the fact that SLM has the potential of producing no wastage [25] is appealing to manufacturers using expensive metals for savings on materials cost [50]. Since the interest of this study is mainly to process Al alloys using SLM; particularly the AlSi10Mg alloy, it is important to highlight the challenges facing Al alloys.

### *The challenges in Al SLM*

Al alloy powders are inherently light (low density) with poor flowability and high reflectivity (owing to the high density of free electrons [16]), along with high thermal conductivity relative to other materials, as can be seen in the chart in **Figure 1**. When compared to other SLM candidate materials, such as titanium and stainless steels, as shown in **Table 1**; the difference in thermal conductivity and flowability indicates that Al alloys are expected to face challenges in the process of SLM. The values for the flowability of metal powders in **Table 1** are experimental values determined at the Additive Manufacturing and 3D printing laboratories in the University of Nottingham [51] using a Hall flowmeter after ASTM standard B213 [52]. The “no flow” term in the table corresponds to the flowability of the AlSi10Mg powder and indicates extremely poor flowability. Since the SLM process involves successive deposition of layers of powder, it is important for the powder used to have good flowability; otherwise the deposited layer will not be uniform, leading to the formation of defects. The high thermal conductivity and reflectivity of Al alloys means that high laser power is required for melting to overcome the poor absorption and rapid heat dissipation [42], although the rapid heat dissipation is more of an issue for solid Al substrate than for the Al powder. Laser absorption by Al is poor because it is bound by outer electrons with less energy levels compared to other elements [16, 41]. Moreover, Al alloys are highly susceptible to oxidation, which promotes porosity [4, 16, 53]. Also, the low viscosity of molten Al is a contributor to porosity [16]. One of the major challenges in producing Al alloys parts using SLM is minimizing

porosity and several studies have investigated the effect of processing parameters on porosity [25, 53, 54].

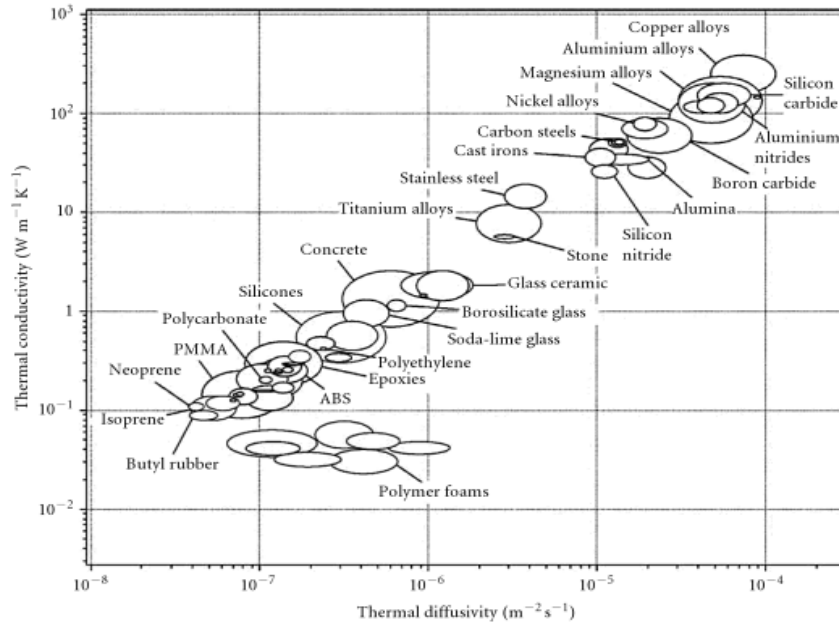


Figure 1: Thermal conductivity of various materials [16].

Table 1: Comparison of properties of SLM candidate materials.

SLM Candidate Material	Flowability (s / 50 gm) <sup>1</sup>	Thermal Conductivity (W/m K)	Reflectivity (%)
Ti64	47	6.7 [55]	53-59 [56]
316L stainless steel	14.6	21.4 [57]	60 [58]
Al6061	77	172 [57]	91[59]
AlSi10Mg	No flow	146 [57]	91 [59]

#### 1.4. The significance and novelty of this research

Although the best candidate materials for SLM are nickel-based alloys and titanium alloys, as claimed by Osakada and Shomi [3], paving the way for SLM to become a substitution to conventional subtractive manufacturing

<sup>1</sup> Experimental values for flowability were determined using Hall flow rate standard test method [52] Standard Test Methods for Flow Rate of Metal Powders Using the Hall Flowmeter Funnel. West Conshohocken: ASTM International; 2013. All powder materials were supplied by LPW Technology, UK.

requires widening the range of usable materials. Owing to its outstanding properties, Al is endorsed for use in a vast number of applications, whether conventional or modern [60]. The possibility of manufacturing parts using SLM from Al alloys will open up further opportunities for the alloy in the industry. This will include not only the parts that are conventionally manufactured but even parts that require machining, where the alloy is difficult to machine, such as the case with AlSi10Mg due to limitations imposed by the presence of the Si hard phase. Understanding the properties of parts produced using SLM from Al alloys, both microstructural and mechanical, is expected to expand the use of these alloys if found to have properties different from conventionally manufactured and more favoured.

The importance of this research lies within the need to develop suitable criteria to be able to successfully manufacture near fully dense AlSi10Mg parts using SLM since studies available so far report parts to suffer from high degrees of porosity. To do so, the challenges facing processing AlSi10Mg have to be resolved. Since the crucial problem arising from all these challenges is the parts' porosity, then the reasons behind the formation of pores in AlSi10Mg parts and their formation mechanisms need to be defined. Based on their definition, the sources of porosity could be traced and rectified to either eliminate or minimize it. A hierarchal study to trace the means of porosity formation and cut them at the source is novel. Furthermore, there is insufficient data on the mechanical behaviour of SLM Al alloys and the effect of heat treatments, which this investigation plans to provide.

## 1.5. Thesis aim, objectives, and methodologies

This research aims to construct a comprehensive understanding of the SLM process considering its various aspects to produce near fully dense samples and the interrelation between the microstructure of the material and its mechanical performance. To achieve this aim, the research is divided into four parts with individual objectives laid out in **Figure 2**.

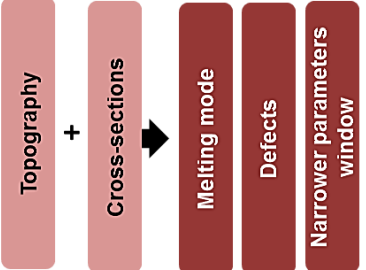
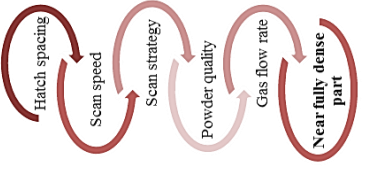
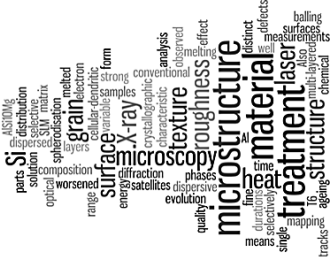
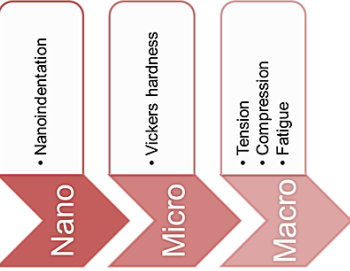
<p><b>Aim:</b> This investigation aims at developing a comprehensive understanding of the SLM process in terms of the role of the process parameters in producing dense parts and the resultant microstructure and mechanical performance to validate its credibility in industry.</p>			
<b>Single tracks &amp; layers</b>	<b>Parametric study</b>	<b>Microstructure</b>	<b>Mechanical properties</b>
<p><b>Objective</b></p> <p>Classify the material's response to laser irradiation in terms of melting &amp; solidification behaviour and types of defects formed plus mitigation means.</p> <p><b>Methodology</b></p> <p>Construct single tracks and layers using a range of scan speeds and powder layer thicknesses.</p> 	<p><b>Objective</b></p> <p>Select best combination of process parameters to produce near fully dense parts.</p> <p><b>Methodology</b></p> <p>Progressive study investigating each parameter separately and feed each output in studying the following parameter</p> 	<p><b>Objective</b></p> <p>Determine the effect of processing on resultant microstructure and its response to heat treatment.</p> <p><b>Methodology</b></p> <p>Characterise the microstructure of near fully dense samples. Determine the microstructural evolution of the SLM material with heat treatment.</p> 	<p><b>Objective</b></p> <p>Evaluate the mechanical performance of the SLM Al material.</p> <p><b>Methodology</b></p> <p>Measure local and global properties of as-built and heat-treated SLM Al near fully dense samples.</p> 
<b>Chapter (4)</b>		<b>Chapter (6)</b>	
<b>Chapter (5)</b>		<b>Chapter (7)</b>	

Figure 2: Mapping thesis aim, objectives, and methodologies.

The thesis objectives are:

1. Determining the melting and solidification behaviour of Al alloys when irradiated with a laser beam during SLM, the formation of single tracks and their stability, and the production of a single layer from overlapping scan tracks.
2. Defining the reasons behind the problem of porosity in Al parts processed by SLM and tackling them to produce dense parts
3. Evaluating the microstructural features of SLM Al tracks, layers, and parts. This incorporates the microstructure of the samples as-built (right out of the machine) and the microstructural response to heat treatment.
4. Assessing the mechanical performance of the SLM Al parts in terms of nano, micro, and macro behaviours.
5. Relating the processing parameters to the microstructure, properties, and performance of the SLM Al parts.

The methodology in this study will be to start from the powders used in SLM covering the various process aspects until producing near fully dense parts and then characterising them. The topography and cross-sections of single tracks and layers formed in SLM using a range of scan speeds and layer thicknesses will be studied to achieve the first objective. A parametric study focussing on the main processing parameters, such as hatch spacing, scan speed, scan strategy, powder quality, and gas flow rate within the processing chamber, will be conducted to select the best combination of processing parameters to produce near fully dense parts, i.e. material qualification (objective 2). It has previously been reported that SLM produces characteristic microstructure [47, 48] that is different from conventionally processed materials for various alloys.

Consequently, it is important to examine this for Al alloys through microstructural characterisation of the near fully dense parts and determining the response of the SLM microstructure to heat treatments (objective 3). Furthermore, the near fully dense samples will be subjected to various types of mechanical loading in order to fulfil objective number 4 and measure the local (nano-hardness) and global (micro-hardness, tension, compression, fatigue) mechanical properties. Lastly, the findings from the abovementioned studies will be tied in together to draw up the big picture and achieve the aim of this investigation by connecting the processing method, produced microstructure, and developed mechanical performance.

The benefits from the outcomes of this study will not be limited to understanding the properties of SLM Al alloys. They will be important for studies concerned with the production of lattice structures to be able to have more solid predictions and understanding of their behaviours. Research concerned with the use of lattice structures [22, 37] to replace solid material and topology optimisation [27, 28, 30, 31] as means for light-weighting is gaining wide attention nowadays and a comprehensive understanding of the SLM process and its outcomes is a great asset for such applications to flourish. Light-weighting using these two approaches in SLM is currently commonplace because they aid in saving materials and resources.

## **1.6. Thesis outline/structure**

In order to build up a comprehensive understanding of the SLM process for Aluminium alloys, this thesis will present the various interrelated aspects of the process in the sequence shown in **Figure 3**.

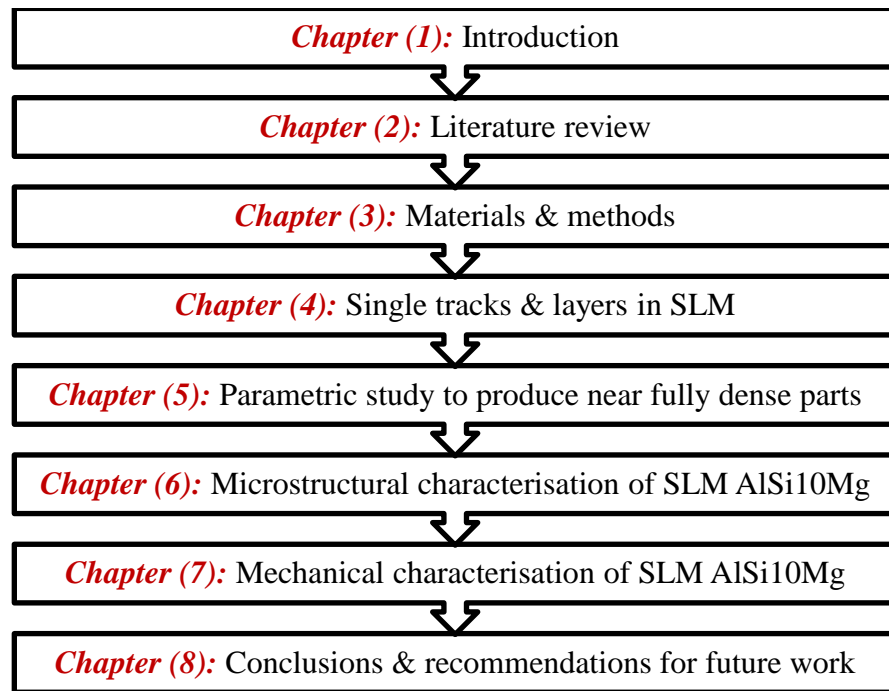


**Figure 3: Thesis outline/structure.**

The first, current, chapter of this thesis is basically an *introduction* to additive manufacturing and the interest in this research field. In addition, the aim and objectives of the study are laid out. This chapter also provides background information and clarifies the context for this research.

The second chapter presents a summary of what has already been done in the area of interest (*literature review*) and where the current study stands and how it fits in. In addition, this chapter sheds the light on the areas that were not fulfilled in the literature but will be resolved in the current study. It also includes some basic definitions and information regarding the SLM process and the material under investigation.

The third chapter describes the *materials and methods* used in conducting the research, i.e. details of the experimental work carried out over the course of this investigation.

Chapters (4) through to (7) present the results achieved over the course of the investigation. The fourth chapter covers the findings achieved from a study on the formation of *single tracks and layers in selective laser melting*. The fifth chapter includes the *parametric study to produce near fully dense AlSi10Mg parts*. Moving on from success in producing near fully dense AlSi10Mg parts using SLM in chapter (5), the sixth chapter focusses on the *microstructural characterisation of selectively laser melted AlSi10Mg*. This chapter also comprises a study on the effect of a conventional T6 heat treatment on the microstructure of the SLM material. The seventh chapter, which is the last chapter covering the results of this thesis, focusses on the *mechanical characterisation of selectively laser melted AlSi10Mg*. A number of mechanical properties are considered in this chapter, such as nano-hardness, micro-hardness, tensile behaviour, compressive properties, and fatigue performance.

The thesis conclusions that highlights the key findings from this study are then summarised in chapter (8) followed by some recommendations for future work. This chapter also puts the research findings in context and highlights their contribution to knowledge in the academic and industrial contexts.

## **CHAPTER (2): Literature Review**

The scope of this chapter is to provide a summary of what was found in the literature regarding research on the various aspects of selective laser melting of aluminium alloys, starting from powder used in SLM to characterising the near fully dense parts. Towards the end of the chapter, the gaps in the literature in the area of selective laser melting of aluminium alloys that this thesis aims at approaching are pointed out.

### **2.1. Aluminium and its alloys**

The metal Aluminium was initially named Alumine as early as 1671. This nomenclature was for the base of alum that was originally used by the Romans and Greeks. The name *Aluminum* was first used in 1807, which was later on changed to *Aluminium*. The International Union of Pure and Applied Chemistry (IUPAC) adopted the name Aluminium in order to conform with the “*ium*” ending of most elements, so Aluminium became the international standard [40]. This spelling was accepted in the United States of America until 1925 when the American Chemical Society decided to revert back to Aluminum [16, 40].

Aluminium is heavily consumed compared to all other non-ferrous metals. The worldwide annual consumption of aluminium is 24 million tons, 18 million tons of which is extracted from ore, i.e. primary Aluminium, and the rest is derived from scrap metal processing, i.e. secondary Aluminium. Aluminium is

known for its very high chemical affinity for oxygen, which is why it cannot be found in nature as a metal but is always found in the form of alumina or other combined oxide form [40]. Aluminium is ranked the second most plentiful metallic element on earth as it represents 8 % of the earth's crust, followed by Iron (5 %), Mg (2 %), Zn, and Sn (0.004 %) [40, 42].

From a chemistry perspective, Al is an element in the third group of the periodic table of elements; its atomic number is 13 and atomic weight is 26.98 based on oxygen [40, 41, 61]. It has no natural isotopes; however artificial isotopes can be produced and are radioactive [40, 61]. From a metallurgical perspective, Al has a face-centred cubic (FCC) crystal structure with a coordination number of 12 and an atomic packing factor of 0.74 [40, 41]. The length of the unit lattice cube contracts by decreasing the purity of the metal due to the formation of impurity segregations [40, 61]. Deformation in Al alloys happens by crystallographic slip on the {111} planes in the  $\langle 110 \rangle$  directions, which means there are 12 slip systems, resulting in high ductility [38, 41]. The melting temperature of Al is 660°C and its boiling temperature is 2520°C. Its mean specific heat for temperatures between 0 °C and 100 °C is 917 J.kg<sup>-1</sup>.K<sup>-1</sup> [41].

Al powders can be found in a wide range of particle sizes ranging between 0.015 µm and 17,000 µm, as well as different shapes such as spheres, thin flakes, or irregular powders. The powders are classified according to certain parameters such as apparent density, specific surface (surface area per unit weight), and oxide content [61]. There are various types of powders, such as: air atomized, spherical atomized, water atomized, acicular, grained, granulated,

ultra-fine, fibres, flakes, flitter, chopped and balled, shot particles, cut foil, brittle alloy, and machined particles [62].

### *Physical metallurgy of Aluminium and its alloys*

Pure Al has the lowest strength compared to its alloys, which is why Al is always used in the form of an alloy [38] despite the success of the studies on strengthening pure Al [62-64]. Pure Al is commonly used in electrical applications, such as conductor cables. The major alloying elements used are Cu, Mg, and Si as strengthening elements, Mn and Sb to enhance corrosion resistance, Ti and Cr for grain refinement, Ni for boosting the thermal strength, and Co, Fe, and Bi to improve machinability [38, 41, 42].

The addition of Si to Al to produce cast alloys improves several properties such as increasing the fluidity and reducing solidification contraction [16, 41]. The phase diagram of the Al-Si alloy system (the alloy of interest in this research) in **Figure 4** shows that the relationship between the two components has a eutectic reaction taking place at 12.6 % Si and a temperature of 577 °C [38, 41, 42].

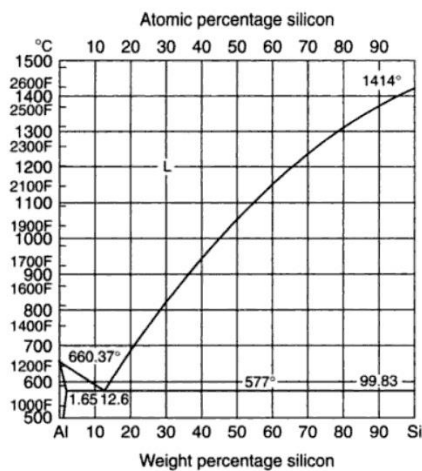


**Figure 4: The Al-Si alloy system phase diagram [42].**

It is difficult to machine Al-Si alloys because of the presence of the hard phase Si [41]. The addition of Mg to the Al-Si alloys strengthens the alloy by promoting the formation of Mg<sub>2</sub>Si precipitates and yields the alloy heat-treatable [16, 41]. Mg is also considered to be the most effective strengthening alloying element because of its high solubility [41]. Si and Mg are the main alloying elements for Al because they have atomic structures that are almost identical to Al, however, the crystal structures are different [38]. Si and Mg are the direct neighbours of Al in the periodic table of elements with an atomic number of 12 for Mg, 14 for Si, and 13 for Al. The crystal structures on the other hand are distinct since Al has FCC crystal structure, Si has a diamond type cubic crystal structure and Mg has a hexagonal close-packed structure.

Heat-treatable Al-Si-Mg alloys are usually treated by tempering (precipitation hardening T6) in a specific sequence that is [38, 41, 42]:

*a) Solution heat treatment (SHT):* at this stage the material is heated to a high temperature in the single phase region, not exceeding the solidus temperature (below the eutectic temperature) to avoid overheating or localized melting.

*b) Quenching:* the material is then quenched to room temperature, i.e. rapidly cooled to room temperature to obtain a super saturated solid solution (SSSS). Usually water is used for quenching large objects but for small and/or thin sections this might introduce residual stresses. The alternative then for a slower quenching rate is to use hot or boiling water or even air-cooling.

*c) Ageing or precipitation hardening:* Ageing could be either natural or artificial. The material is maintained at an elevated designated temperature(s) for a duration of time to allow the decomposition of the SSSS into finely

dispersed precipitates. Nucleation occurs at the Guinier–Preston (GP) zones or dislocations [40]. For a more pronounced ageing effect, sometimes the metal is cold worked before ageing to increase the dislocation sites (density of dislocations).

## **2.2. Aluminium powder for SLM**

### **2.2.1. Properties of powder**

Powders used in SLM are produced either by gas atomisation or plasma rotating electrode (plasma atomisation) with the former being more common [65]. The quality of the powder used is one of the SLM process variables [20]. Since the process constitutes successive deposition of uniform layers of powder, it requires the powder to have particular properties to enhance its flowability and packing density; these are controlled by the powder morphology and size distribution. In contrast to irregular particles, spherical particles mean better flowability [66] and higher packing density; two characteristic features that are pre-requisites in SLM [21, 67]. The same alloy can have different morphological properties based on the suppliers and how well they adhere to the standards. In addition, the chemical composition of the powder also affects the process. For instance, the presence of gas phase in the starting powder significantly suppresses densification [68]. Li *et al.* [21] compared the use of water-atomised 316L stainless steel to the gas-atomised powder and showed the superiority of the gas-atomised powder due to the lower oxygen content and higher packing density. The role of powder specifications has also been studied by Kempen *et al.* [54] who tested processing with AlSi10Mg with different morphological and chemical

properties. Their results confirmed that the choice of powder properties is critical as it affects the quality of the produced parts, in terms of porosity either due to chemical composition, morphology, or moisture. Upon irradiating the powders with a laser beam, there exists an energy balance between conductivity (K) and absorptivity (A). The absorptivity or reflectivity of the powder depends not only on the physiochemical properties of the powder but also on their granular morphology and apparent density. Hence, the properties of the powder in the solid state before starting the process of SLM highly affects processing [69]. Yadroitsev *et al.* [70] recommended pre-heating the powder before processing to improve its absorptivity. Weingarten *et al.* [71] attributed the presence of gas pores in AlSi10Mg SLM parts to the hydrogen content in the starting powder and showed that drying the powder before processing can reduce porosity by 50%. The sources of hydrogen in SLM are moisture on the surface of powder particles and the gases trapped in the voids in the powder particles. The amount of the latter depends on the powder atomisation process. Moisture on the powder surface also depresses its flowability [71].

The national Institute of Standards and Technology has developed a series of reports on “Materials Standards for Additive Manufacturing” with the standards developed via the ASTM Committee F42 on Additive manufacturing Technologies and the ISO TC261 committee on Additive manufacturing. The second report in this series covered the various standardised techniques that could be used to test the properties of metal AM powders [65]. Having standardised AM powder properties along with standardised methods of testing

and evaluation should minimize the process variability and improve repeatability.

### **2.2.2. Tailoring powders**

Although SLM is used for fabrication using readily available commercial alloys, the development of new powder mixtures specially tailored for SLM is of current interest. The Airbus group has developed a new Al-Mg-Sc alloy and gave it the name SCALMALLOY®RP. This alloy is specifically tailored for powder-bed manufacturing processes and is characterised by high corrosion resistance, high specific strength, and exceptional fatigue and toughness properties [72]. Blending metal powders with different properties is a promising route. The possibility of coating a material of high reflectivity with another of lower reflectivity could be a means for better material processability. For example, Sachs *et al.* [73] deposited Cu on Al particles using a fluidized bed reactor to be specifically used in SLM and reported intermediate values of absorptivity and reflectance compared to the original source elements, promoting their use in SLM. Olakanmi [74] has studied the effect of processing parameters on using pure Al, Al-Mg, and Al-Si powders in SLM and reported that the processing parameters were independent of the alloying elements, i.e. the use of different Al alloys did not alter the process window to produce dense samples but it did affect the surface morphology of the produced parts.

### **2.2.3. Alloy development and *in-situ* composite production**

SLM can be used for *in-situ* production of reinforced composites [75] as well as the production of amorphous/glassy (metallic glass), nanocrystalline, or ultrafine grained structures [67]. For instance, Dadbakhsh and Hao [76] have

successfully processed Al-5wt% Fe<sub>2</sub>O<sub>3</sub> *in-situ* powder blend using SLM and showed that this composite requires the use of large layer thickness to allow the decomposition of oxide layers formed during processing. In another study, Dadbakhsh and Hao [60] investigated the possibility of *in-situ* production of Al alloy metal matrix composites using SLM and reported that the alloy composition plays an important role in controlling the process. This contradicts Olakanmi's [74] statement that the alloy composition does not affect the process window. Gu *et al.* [77] produced novel Al-based composites from AlSi10Mg and SiC using SLM. With high energy densities, multiple reinforcements were formed leading to enhanced mechanical properties [77]. The laser energy density also controlled the structure of the reinforcements in the case of a TiC reinforced AlSi10Mg composite [78]. In another study, Gu *et al.* [79] produced TiC reinforced Al-Si-Mg based nano-composite from mechanically alloyed blend of AlSi10Mg and TiC. Also, mechanically alloyed Ti, Al, and graphite were selectively laser melted and a TiC reinforced composite was successfully produced [80].

#### **2.2.4. Powder recycling**

One of the appealing advantages of SLM is that the process is resource-efficient, with the ability of re-using the leftover powder (recycled powder). Recently, a method and apparatus were patented by O'Neill [81] that could be used to de-oxidise residual metal powder from additive manufacturing so that it could go back into the system with enhanced efficiency. This could be another boost to the process because although the use of recycled powder is quite common now, its effect on the part's quality is questionable due to oxidation. The oxidation reactions occurring during SLM of Ti-6Al-4V, AlSi10Mg, and

316L stainless steel were investigated by Simonelli *et al.* [82] demonstrating how different materials behave differently in this aspect.

### **2.3. The processing environment/media in SLM**

It is important to conduct SLM under an inert atmosphere to avoid oxidation during the process, especially when processing Al alloys that are highly susceptible to oxidation [2, 40, 83, 84]. The type of inert atmosphere under which the process is conducted was found to have no effect on densification by Wang *et al.* [84] when they investigated processing Al-12%Si using different purging gases (argon, nitrogen, and helium). However, the majority of SLM processes are conducted under argon [49, 51, 85, 86].

Purging an inert gas into the chamber means there is continuous gas circulation during processing. Ferrar *et al.* [17] investigated the effect of the gas flow rate within the processing chamber during SLM of Ti alloy and reported that slower flow rates remove less condensate, leading to the production of parts with higher porosity. Whether this applies to all material requires further investigation. The importance of studying the gas flow rate is because it affects the removal of spatter produced during processing. Spatter is produced due to the interaction between the laser beam and the target material. The amount of spatter produced on the other hand is controlled by the laser power and the laser beam spot size [10]. Inefficient removal of the spatter might lead to its entrapment as inclusions in the parts produced. Their structure and chemical composition was found to be different from the original powder for some materials but the same for others [82]. This acts as evidence that the effect of

the gas flow rate cannot be generalised for SLM and each material must be considered separately.

## **2.4. Single scan tracks using SLM**

### **2.4.1. The motivation behind studying single tracks**

The properties of the material to be processed with a laser beam have a dominant role on the process control. Examples of these properties are the absorption coefficient, absorptivity, specific heat capacity, thermal conductivity, density, thermal diffusivity, coefficient of thermal expansion, transformation temperatures, latent heat of melting, and latent heat of vaporization [16].

A laser beam radiated onto a surface might be absorbed, reflected, transmitted, or re-radiated depending on the absorptivity of the material. The absorptivity of a material during processing is influenced by the wave-length of the laser beam. Absorptivity of metals decreases with increase in wave-length [16].

The power density in the laser-material interaction controls the interaction mechanism. Power density is defined as the ratio between the laser power and the cross-sectional area of the laser beam. If the laser power is constant and the beam diameter is decreased, such as the example in **Figure 5**, the power density increases. At low power densities, the mechanism of interaction between the laser beam and the material leads to heating of the surface without achieving complete melting. Surface melting starts to take place with a gradual increase in the power density. Further increase leads to keyholing, where vaporisation occurs [16].

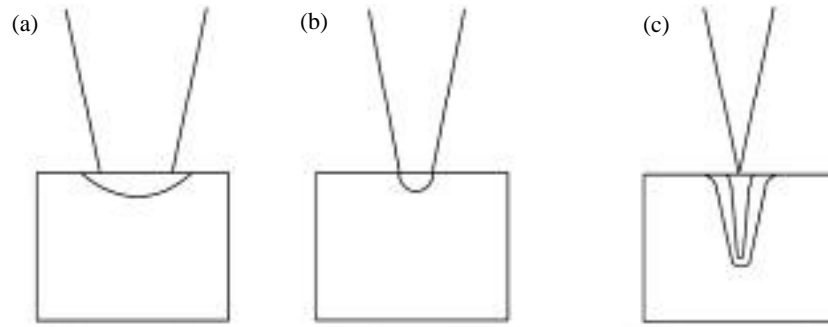


**Figure 5: The effect of power density on the laser-material interaction mechanism (a) surface heating, (b) surface melting, and (c) surface vaporisation/keyholing [16].**

The mechanism of laser-material interaction is not only dependent on the power density, but is also influenced by the interaction time or the exposure time [16], as demonstrated in the process chart in **Figure 6**. Considering the power density without attention to the interaction time can lead to undesirable results by switching the interaction mechanism.

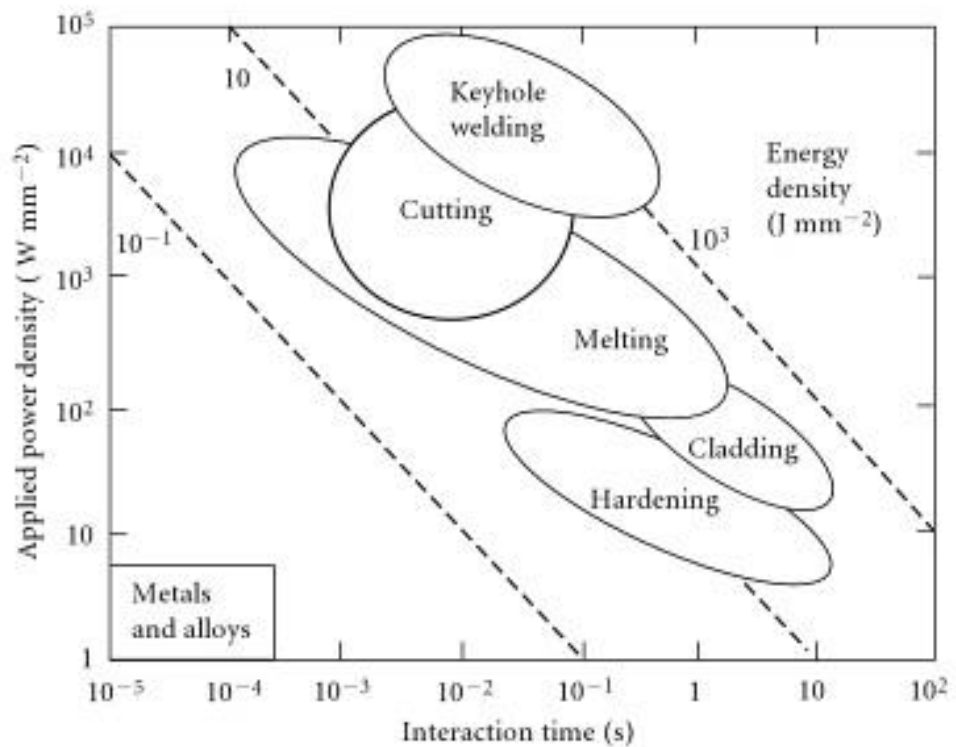


**Figure 6: Laser-material interaction mechanism based on the power density and interaction time [16].**

A thermal gradient is developed in material radiated by a laser beam. The coefficient of surface tension increases with temperature decrease [87, 88] and the surface tension gradient causes fluid to flow from the centre of the melt pool to the edges, in what is known as the Marangoni flow. Marangoni flow is the dominant mechanism of convection in laser-induced melt pools [16]. The thermal gradient and the surface tension of the material result in the formation of a melt pool that is a cylindrical segment. Detailed discussion of melt pool formation will be presented in the following chapters.

During SLM, the laser beam melts the powder line-by-line forming a melt pool. The melt pool usually takes the form of a circular or cylindrical segment. Stability of the melt pools is affected by the processing parameters, such as laser power, scan speed, layer thickness, substrate material, and properties of the powder [69]. Studies on the formation of single tracks are essential to help understand the melting and solidification behaviour in the process. This includes the response of the target material towards being irradiated with a laser beam. Several phenomena take place during SLM, including laser absorption and scattering, heat transfer, phase transformation, chemical reactions, fluid dynamics within the melt pool controlled by surface tension gradient, and evaporation and emission of material [69]. Solidification of a metal is controlled by the ability of the material to conduct the latent heat of solidification away from the solid/liquid interface [89]. When the laser beam is irradiated onto the target material, part of the energy is reflected from the material and the rest is conducted into it. The amount of energy reflected depends on numerous parameters, such as the beam angle of incidence, the refractive index of the atmosphere and the material as well as the material's

reflectivity and conductivity. The intensity of light transmitted into a material decays with depth due to absorption and this decay is dependent on the absorption coefficient of the material [90].

Considering a laser beam focussed onto a metal substrate (without powder), a cavity is created by ablation and plasma formation. This cavity is surrounded by molten material in the melt pool that is applying forces on the cavity due to surface tension and hydrostatic pressures. As the laser beam moves in its assigned path, the melt pool material flows into the cavity and solidifies in a characteristic chevron pattern on the surface. If the laser beam moves with a high speed, fast solidification of the molten metal occurs without completely filling the cavity leaving a void or a keyhole pore in place. Whereas slow speeds lead to the production of wide melt pools. In addition, the heat from the melt pool is transferred to the surrounding solid creating a heat affected zone [16].

#### **2.4.2. Single track experiments and parameters**

The stability, irregularity, and discontinuity zones seen in single track experiments help to narrow down the processing parameters, avoiding waste of material and time producing bulk samples at all possible combinations of parameters. These experiments are usually designed in a systematic procedure. First, a layer of powder of a defined thickness is deposited onto a substrate material. Second, a laser beam scans the powder layer to form single tracks (lines) deploying different combinations of scan speeds and laser powers. Although the layer thickness is usually pre-defined, some experiments use inclined/tilted platforms in order to continuously change the layer thickness, i.e. changing the scan speed, laser power, and layer thickness simultaneously

[91, 92]. The third stage of these experiments is to analyse the developed scan tracks. The scan track analysis usually comprises; (I) evaluating the presence of irregularities and distortions along the length of a scan track, i.e. defining zones of continuity, and (II) measuring the depth and width of each melt pool from the cross-sections of a scan track. Comparison of the results from (I) and (II) at different processing parameters leads to a narrowing down of the process window by finding the most uniform and consolidated scan track. According to Kempen *et al.* [54], there are some requirements that need to be fulfilled in the formation of single tracks for a successful SLM process, these are: (1) the deposition of a continuous track, (2) each layer must penetrate the previous layer, (3) each layer has to be high enough to build up the part cumulatively, and (4) the connection angle with the previous layer should be close to 90°.

Using single tracks experiments, Kempen *et al.* [54, 93] defined an energy density range for processing AlSi10Mg, above which irregularities were observed and below which insufficient melting and lack of bonding between the current layer and the layer underneath occurred. A good bond between a layer and the following will minimize the possibility of cracking or pore formation. Bonding of a layer to the one below is controlled by wettability, i.e. molten powder spreading over the substrate or the previous layer rather than balling [20, 70]. In general, the laser power and scan speed are the two factors mainly affecting the width and depth of the melt pool, whereas its length is mainly governed by the laser power and the material's absorptivity [94]. The use of slower scan speeds means higher temperature within the melt pool, with lower viscosity so the liquid spreads out improving bonding (wettability), as reported by Li and Gu [39]. Similarly, Ahuja *et al.* [95] showed the dependence

of the quality of single tracks from Al-Cu alloys on scan speed. Bartkowiak *et al.* [6] conducted single track experiments to validate the feasibility of producing new blends of powder especially tailored for SLM as well as to determine if there was oxidation of the surface during the processing of bulk parts.

There is not much work on single tracks of Al alloys but the literature is rich with studies on other materials. For instance, Yadroitsev *et al.* [69] reported the depth and width of stainless steel grade 304 scan tracks to decrease with decreasing the scan speed, which progressed until the inter-layer bonding diminished. This was attributed to heat loss due to conduction promotion with the reduced scan speeds. Increasing the speed beyond a certain limit resulted in the formation of discontinuous scan tracks, *i.e.* instability zones, owing to the lack of heat sink into the substrate material [69]. This finding opposes another study, by Yadroitsev *et al.* [20], stating that the width of 904L stainless steel (an austenitic stainless steel) scan track decreased with increasing scan speed. Matilainen *et al.* [10] observed single tracks of 17-4 PH stainless steel to deepen rather than widen with increasing energy density. This variation in material response towards altering the laser power or scan speed in SLM shows that findings from one material cannot be generalised for the process as a whole.

Investigations on the irregularity along the length of a stainless steel grade 304 scan track by Yadroitsev *et al.* [69] showed that using relatively high laser power along with low scan speed results in increasing melt volume and decreasing the melt viscosity. At this point melt hydrodynamics (driven by Marangoni effect) become important and irregularity is observed. On the other

hand, using low laser power along with low scan speed led to the disappearance of penetration into the substrate (re-melting of the substrate) and was the reason for distortion in the scan track. Further reduction in laser power can result in a scan track that is a sequence of discrete drops [69]. The use of high laser power was also reported to allow a higher degree of freedom for the scan speeds employed since the lack of enough energy to maintain the boiling and evaporation behaviour of the melt pool will result in irregularities and distortions [24].

The importance of defining a suitable layer thickness to be used in SLM to ensure bonding of one layer to the preceding arises from the variation in the depth of penetration of the scan tracks and remelted regions with the processing parameters [24, 91]. Experiments using 316L stainless steel by Yadroitsev *et al.* [24] showed that increasing the layer thickness reduces the maximum scan speed that can be used after which the scan track is transformed into a sequence of droplets rather than a consolidated line.

Another aspect that should be considered when studying single tracks is the formation of satellites. Satellites are re-molten drops sticking to the layer having contact with the scan track. They are formed by spattering or partial re-melting of the powders in the peripheral zone of the laser spot. These satellites promote the creation of pores and worsen the surface roughness [70].

In order to obtain a 3D object with high quality, i.e. minimal porosity if any, the stability of the geometrical characteristics of the single track has to be ensured and a good bond between each layer and the previous one must be achieved [20, 70]. Besides the geometrical and surface features of SLM scan

tracks, single tracks can be used to trace the mechanisms of porosity formation. King *et al.* [96] visualised three-dimensional porosity and its distribution in single tracks of 316L stainless steel using synchrotron radiation microtomography. They reported evidence for keyhole mode melting rather than conduction melting and observations of trails of voids [96]. When keyhole mode melting dominates, the material becomes susceptible to keyhole instability that could contribute to porosity. Kamath *et al.* [94] differentiated between the modes of melting and stated that the transition from conduction mode melting to keyhole mode melting is dependent on the energy density. When this transition occurs, the power density is enough to cause evaporation of the material and the formation of what is like a drilled hole. The collapse of metal in this cavity results in keyhole pores. The presence of voids in single tracks indicates the possibility of their growth and accumulation during multi-layer processing.

#### **2.4.3. Thermal behaviour within melt pools**

It is essential to understand the thermal behaviour of a material during SLM, however, it is difficult to study this experimentally. Therefore, numerical simulation models have been developed. Li and Gu [39] developed a model to simulate SLM of AlSi10Mg and reported that the melt pool depth and length decrease with either increasing the scan speed or decreasing the laser power. Loh *et al.* [97] utilised data from single tracks experiments with Al6061 to develop a simulation model that could (1) predict temperature distribution in a melt pool and its variation with the laser power and scan speed and (2) predict suitable combinations of processing parameters to fabricate dense parts. In their study, the authors considered several phenomenon taking place in the melt

pool, such as material shrinkage due to escape of gases trapped in the powder, evaporation due to exceeding the boiling point of the metal, and removal by the argon gas flow within the processing chamber [97].

In terms of tracing porosity using modelling, Dai and Gu [68] proposed a hypothesis based on modelling the SLM process of copper matrix composites. Their hypothesis was that gaseous bubbles are formed within the molten pool leading to gas pores according to the energy density used and its effect on the bubbles' motion promoted by Marangoni convection due to surface tension. A schematic presentation of their hypothesis is shown in **Figure 7**. At the lowest energy density (15 KJ/m), most of the bubbles are trapped within the melt pool (below the surface) after solidification. As the energy density increases (17.5 KJ/m), the speed of the bubbles increases, allowing them to escape from the melt pool, thereby reducing porosity. However, further increase in the energy density (20 and 22.5 KJ/m) leads to the development of a flow vortex that traps the bubbles inside the melt pool, resulting in an agglomeration of pores [68]. However, this hypothesis lacks experimental evidence in the form of micrographs of the melt pools' cross-sections to support (or defy) their scenario. Panwisawas *et al.* [98] conducted a study on the evolution of porosity with changing processing parameters when selectively laser melting Ti-6Al-4V and indicated that the shape of the pore formed changes with the scan speed employed. At slow scan speeds, the pores are mostly spherical, however, they change to irregularly shaped at high speeds. This was attributed to the change in the flow dynamics within the melt pool represented by the vapour pressure as well as the gravitational and capillary forces.

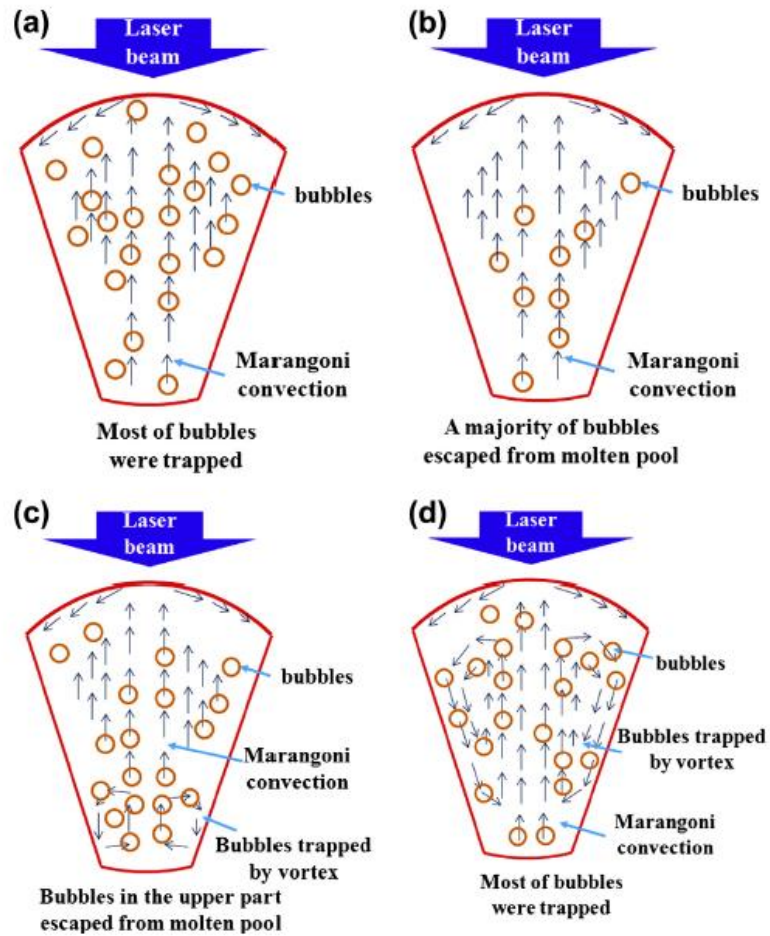


Figure 7: Schematic presentation for gaseous bubbles motion within a melt pool during SLM at increasing energy density (a) 15KJ/m, (b) 17.5 KJ/m, (c) 20 KJ/m, and (d) 22.5 KJ/m, as illustrated by Dai and Gu [68].

## 2.5. Overlap of scan tracks in SLM

### 2.5.1. Overlap into single layers

Single tracks experiments partly aim at determining the maximum layer thickness that can be processed. But they are also important to work out the optimal hatch spacing. For instance, the shape of the melt pool of a single track can impose limitations on the scan spacing, as has been shown by Pupo *et al.* [92] in a study on CoCrMo. It is then important to study the overlap of single tracks forming a single layer before proceeding to multi-layers fabrication. Su

and Yang [99] studied the overlap between single scan tracks with stainless steel to determine sources of porosity, whether inter-layer or intra-layer. They [99] asserted that the hatch spacing is highly influential to ensure the formation of a consolidated and defect-free layer. Ciurana *et al.* [91] designed a sloped platform to investigate the effect of changing the scan speed whilst continuously changing the layer thickness that was also used by Pupo *et al.* [92] to study multi-tracks or single layers of CoCrMo, i.e. investigating layer continuity. They [92] concluded that the hatch spacing value controls the overlap between the scan tracks and affect the morphology of the surface produced. This agrees with the work by Yadroitsev and Smurov [100] using stainless steels. The morphology of the surface is affected by the hatch spacing since the height of the scan track is reduced for the tracks following the first one. This is because less material is melted since the already solidified material acts as a heat sink for the energy, i.e. the laser beam melts more material in the first scan than it does in the following ones. There are some studies concerned with single tracks and multi-layered parts with fewer studies on single layers such as [100]. Particularly for Al alloys, no studies can be found in this field, so far, although it could help define the means of porosity formation and develop a methodology to reduce porosity.

### **2.5.2. Overlap into thin walls**

Another benefit from conducting single tracks experiments is determining the feasibility of producing thin walls, such as the work by Krauss and Zaeh [101] on Inconel 718. The poor roughness of single tracks was an indicator for the limitations that would hinder the fabrication of thin walls made up of stacked single tracks [101]. Ahuja *et al.* [95] produced thin walls by simply

overlapping single tracks in the vertical direction to narrow down the process window. Their method allowed them to define suitable laser power and scan speeds. Also, based on the successful combination, the thickness of the wall was used to determine the optimal hatch spacing [95]. These experiments are also helpful for studies on the production of lattice structures that are of interest for weight reduction [34].

## **2.6. Material qualification research**

### **2.6.1. Parameters and experimental approaches**

The SLM process can be divided into a series of steps, including powder deposition and laser scanning [2]. The basic components of an SLM system are illustrated in **Figure 8**. SLM is conducted within a controlled-atmosphere chamber to enable processing under inert atmosphere so as to avoid oxidation [102]. The procedure to fabricate a part is illustrated in **Figure 9** and can be summarised as follows:

- I. The 3D-CAD file of the part to be fabricated is first sliced into layers of pre-defined thickness using appropriate software. Then by means of a computer connected to the SLM machine, the sliced-part file is transferred to the machine.
- II. The build plate is heated (temperature is material dependent) to aid in heat dissipation by lowering the thermal gradient [103]. Also, heating the platform is important to avoid part warping/curling or cracking during processing [67], i.e. to reduce distortions in the part due to non-uniform thermal expansion [104].

- III. A layer of powder from the powder feeder (hopper) with a predefined thickness, equal to the thickness of each slice, is spread over the heated build plate using the wiper blades. The uniformity of the deposited layer is crucial to avoid the formation of defects.
- IV. A laser beam focussed onto the powder-bed is carried through an optical fibre and radiated onto the layer of powder. The beam, moving in the x-y plane, selectively melts the regions of interest on the currently deposited powder layer. The information attached to each layer is used to guide the laser-beam across the powder-bed [16].
- V. The build plate – controlled by a piston – is then moved downwards a distance equal to the predefined layer thickness to allow the deposition of another layer of powder.

This sequence is then repeated a number of times equal to the number of slices the part has been divided into [21, 94] until the full part is built layer-by-layer [5, 6, 20, 53]. Each scan penetrates deeper than the powder layer thickness leading to metallurgical bonding of one layer to another [71]. The time consumed to build a full part is divided into primary and auxiliary times. The primary time is that needed to scan/melt the powder so this depends on the scan speed and the hatch spacing, whereas the auxiliary time is that required for build plate lowering and powder deposition [13, 25].

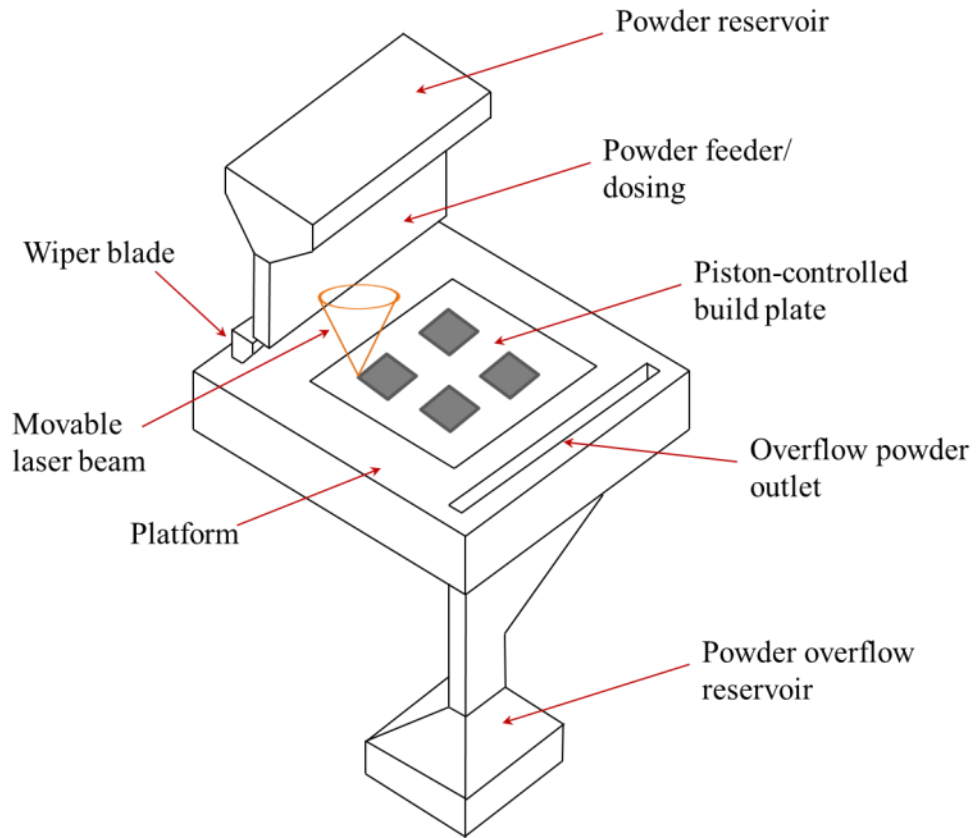


Figure 8: Simplified schematic presentation of an SLM machine.

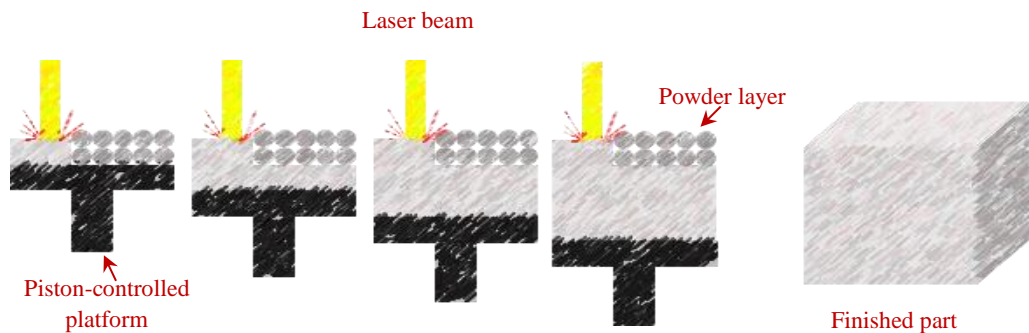


Figure 9: Schematic presentation of the SLM process.

The SLM process is governed by over 130 parameters [92] but only some of them are considered of main importance. The main set of parameters controlling SLM [2] is illustrated in **Figure 10**. The major parameters involved in the process are: the scan speed of the laser beam (defined by the point distance and the exposure time), the hatch spacing (the distance between each

two adjacent laser scans), the laser power, the layer thickness, and the laser beam and its properties in terms of laser power and spot size. Some of these parameters are not only selected for adjusting/controlling the process of building, but also because they can affect the surface finish, microstructure, mechanical properties, and the production time and cost. The geometrical features, demonstrated in **Figure 11**, are point distance/sequence, hatch distance/geometry, border geometry, and layer thickness. Numerous investigations have been conducted considering these parameters to enhance part density and overall quality [25, 53, 54, 74, 94]. Another parameter that offers a large degree of freedom to the SLM process is the scan strategy. The scan strategy includes the scan pattern and the scan orientation. The scan pattern is used to refer to the scan direction per layer, whereas the scan orientation refers to the scan alignment from one layer to its subsequent. Examples of possible scan patterns are the unidirectional scan, the meander scan, and the checkerboard scan, as illustrated in **Figure 12**. The scan orientation describes rotation of the scan pattern a certain degree from one layer to another, for example in the alternating scan each layer is rotated 90° with respect to its preceding, as shown in **Figure 13**. The scan strategy should also define the number of scans per layer, if each layer is to be scanned more than once. Read *et al.* [49] conducted a response surface study alongside analysis of variance (ANOVA) and stated that the most important processing parameters are the laser power, scan speed, and hatch spacing.

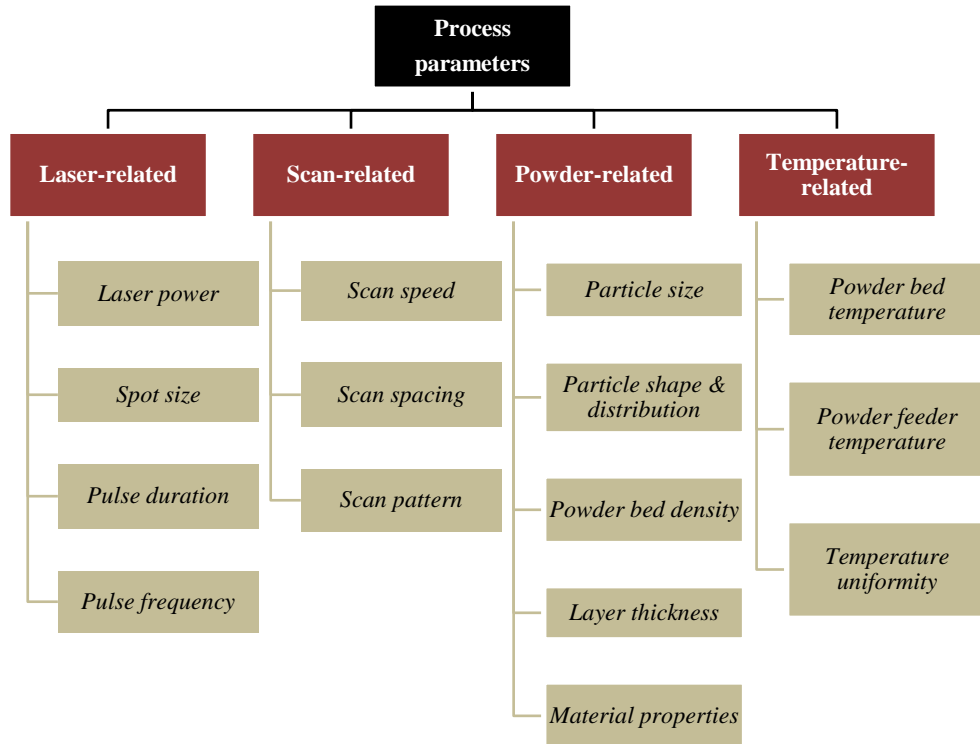


Figure 10: Controlling parameters in SLM process [2].

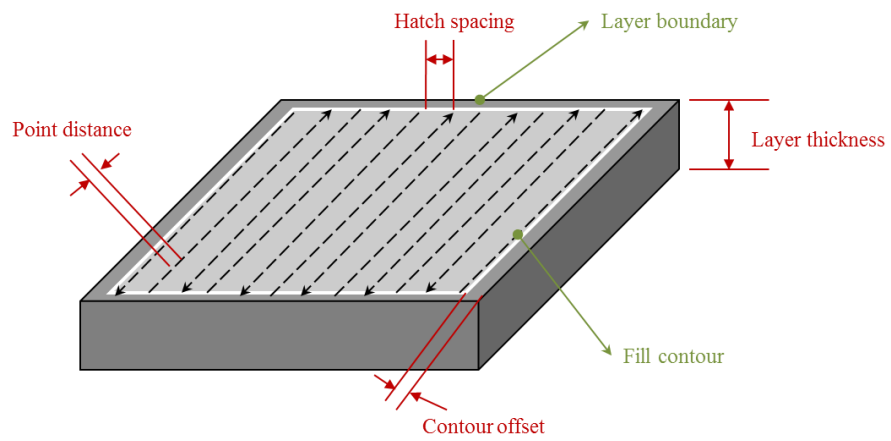
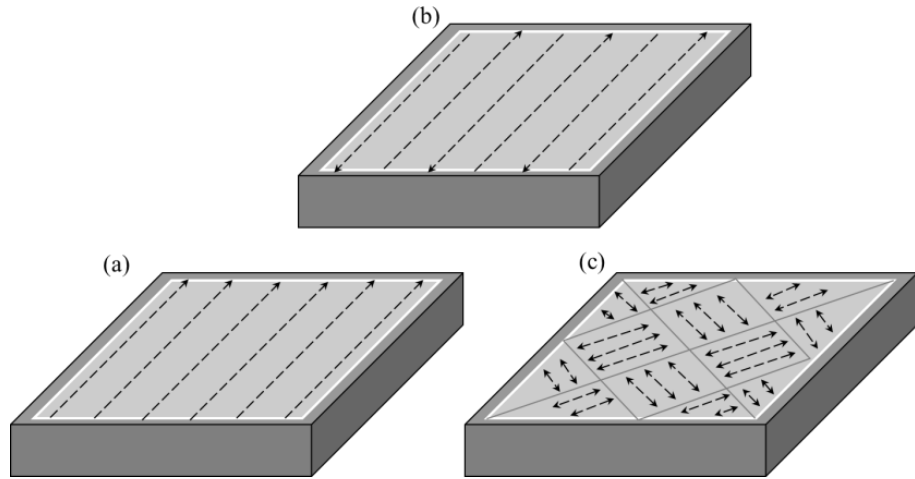
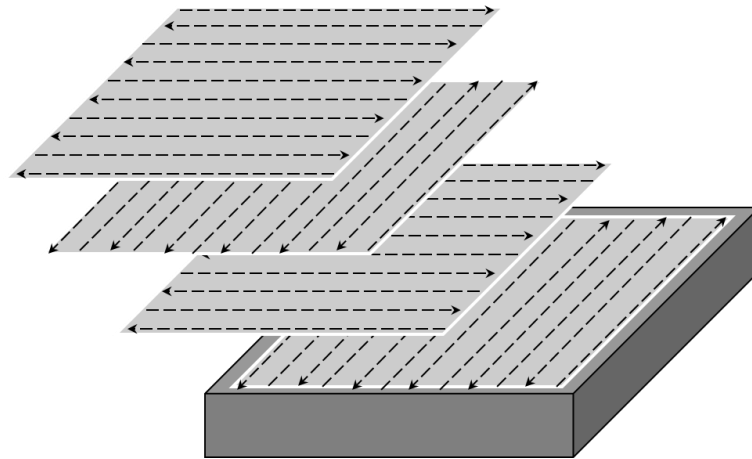


Figure 11: Geometrical parameters in the SLM process.



**Figure 12: Examples of scan patterns (a) uni-directional, (b) meander, and (c) checkerboard scans.**



**Figure 13: Altering the scan orientation 90° per layer.**

Optimisation of the numerous process parameters, controlling the SLM process and affecting the quality of the produced parts, is being extensively studied. A compromise between these parameters is essential to fully melt the layer without introducing cracks, balling, voids, or pores [94]. The selection of an inappropriate combination of processing parameters leads to several defects in the produced part [39]. The optimised process parameters vary from one machine to the other and between materials. This is why there is a field of research known as “Material Qualification Research” [10, 13] in SLM. For

instance, Zhang *et al.* [19] optimised the processing parameters for Mg-9%Al alloy to produce 82% dense parts. Also, Kamath *et al.* [94] incorporated the use of simulation models with single scan tracks and bulk samples processing to find the best parameters to process 316L stainless steel.

Material qualification is a crucial part for the success of the SLM process. Experiments for material qualification are lengthy but systematic. At first, random combinations of parameters are used to fabricate small cubes, preferably after narrowing down the process window using single tracks experiments (see section 2.4). The relative density of these cubes is determined and the results are used as feedback to alter the parameter combinations and find the best process window. The most commonly used techniques/methods for determining the relative density are either (1) *cross-sectioning*: the cube is cross-sectioned, polished, imaged using optical microscopy, and the optical micrographs are analysed using an image processing software to quantify porosity [25, 49, 51], or (2) *Archimedes method*: weighing the cube in air and in a liquid and determining the relative density through the difference in weights [5, 53, 84]. The problem with the cross-sectioning method is that one cross-section per sample will not be representative of the whole batch. Also the degree to which the sample is polished controls whether all trapped un-melted powder was removed or not (such as the case in **Figure 14**) and this shall in its turn mislead density measurement via image processing. Whereas the drawback of using the Archimedes method is that it will not consider voids filled with un-melted/un-bonded powders as pores. The use of X-Ray micro-computed tomography ( $\mu$ CT) is gaining popularity in characterising SLM parts as an effective and non-destructive means of quantifying porosity. Tuck *et al.*

[105] used this technology not only to evaluate the degree of porosity in AlSi10Mg parts produced by SLM but also to determine the pores' shapes, sizes, and position distribution with high precision.

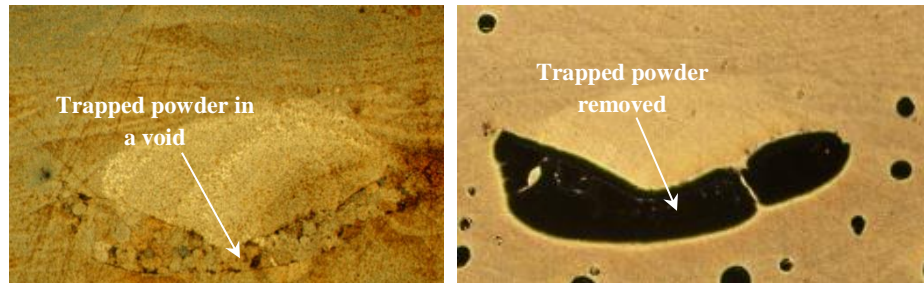


**Figure 14: AlSi10Mg sample processed by SLM (a) polished without removing the trapped powder, and (b) the same sample polished until the removal of the sintered powders.**

### **2.6.2. Parametric investigations to produce near fully dense samples**

Although the literature is full of material qualification studies for Ti alloys, Ni alloys, and stainless steels such as [106], [107], and [21, 94], respectively, to name a few, the investigations on Al alloys are quite limited due to the difficulties facing their processing. The most commonly used Al alloys in SLM are AlSi10Mg and Al6061 [9]. Louvis *et al.* [53] studied Al6061 and attributed the difficulty of processing to the formation of thin oxide films on tracks' surfaces that promote porosity. Their attempts to produce dense parts were not successful since their highest reported relative density was slightly less than 90%. Ahuja *et al.* [95] managed to optimise the processing parameters for two SLM Al-Cu alloys to fabricate near fully dense parts, reporting the role of supporting structure geometry in decreasing porosity by reducing heat transfer, rather than building directly on the substrate.

The selection of the hatch spacing is dictated by the width and depth-shape of the scan track and the laser beam spot size, to ensure sufficient overlap so as to

yield a consolidated part. Small hatch spacings mean a slower rate of production by increasing the primary time but allows more freedom in selecting the scan speed used [49]. Large hatch spacing will impose a limitation on the maximum layer thickness in which the part can be sliced [99] thus increasing the auxiliary time. Extremely large hatch spacing leads to the formation of gaps between the scan tracks due to the lack of intra-layer bonding.

Because of their high reflectivity and thermal conductivity, the use of a high laser power is usually recommended when processing Al alloys by SLM [19] to broaden the process window [93, 94]. Buchbinder *et al.* [25] stated that using high laser power, up to 1 kW, when processing AlSi10Mg increases the degree of freedom of the usable scan speed range.

In terms of the scan speed, it is advised to use slower speeds for better densification during SLM [39] along with high laser power. The slower the scan speed, the more molten material, producing deeper and wider melt pools [21, 92, 108]. This agrees with the results reported by Read *et al.* [49]. The problem with using a slower scan speed is that the industry prefers fast build rates. Buchninder *et al.* [25] were able to process AlSi10Mg with high scan speeds (up to 2100 mm/s) without depressing the relative density by using higher laser power (900 W), with results demonstrating the possibility of going faster as long as the power is further increased (up to 1 kW). Read *et al.* [49] adopted a statistical experimental design to optimise the processing parameters used to produce dense AlSi10Mg using SLM. Increasing the scan speed with decreasing the laser power promoted porosity due to the lower energy density induced in the material leading to incomplete solidification. They

recommended the use of high laser power, slow scan speed, and small hatch spacing to mitigate porosity when processing Al alloys by SLM.

The scan strategies are mainly designed with the aim of minimizing the residual stresses developed during processing. It is believed that the interlayer stagger scan strategy, where each layer is scanned shifted from its preceding to scan the overlap between each two scan tracks, reduces the heat accumulation [99]. Thijs *et al.* [4] investigated processing using various scan strategies from a metallurgical perspective by monitoring the influence of the strategy on the crystallographic texture produced. Furthermore, altering the scan strategy can be used to amend defects formed in a layer, as a means to reduce porosity. For instance, a double scan strategy was used to process Ti-6Al-4V [47] in order to fabricate near fully dense parts. Yadroitsev *et al.* [24] recommended two scan strategies to achieve a part with a higher relative density when processing stainless steels; (a) two zone scanning, where the layer is scanned twice, with the second scan scanning the overlap between two melt pools, and (b) cross-hatching scan strategy, which is to scan each layer with a 90° rotation with respect to the previous layer to avoid the creation of a wave that would be magnified with further layers. Two-zone scanning was also recommended by Su and Yang [99]. Li *et al.* [109] used a double scan strategy, re-scanning with low energy density, to avoid the formation of cracks in Al-based metallic glass/nanocrystalline alloys. Lijing *et al.* [86] scanned each layer twice with the second scan rotated 90° from the first using the same processing parameters when processing Al-8.5Fe-1.3V-1.7Si alloy. However, porosity in their [86] samples was around 10 %, which they attributed it to oxidation.

Besides the problem of porosity in SLM parts from Al alloys, balling on the surface of each layer is another defect that must be avoided as it depresses the relative density of the produced part [68]. Islam *et al.* [7] investigated this phenomenon while processing stainless steel and defined boundaries for the energy density to be employed outside which balling is promoted. However, they did not register a relationship between the scan speed and the amount of balling.

## **2.7. Microstructure of the selectively laser melted material**

Parts produced by SLM go through a series of thermal experiences [9]. The material is molten after interaction with the laser beam and during melting and solidification it is subjected to directional heat transfer (the presence of a thermal gradient). Solidification of the material occurs at a very fast rate [71]. After this, the material is remelted more than once due to the penetration of the laser beam and heat transfer in subsequent scans. This thermal history affects the microstructure of the part.

Rapid solidification of Al-Si alloys produces a fine microstructure in the form of smaller grain size, smaller eutectic spacing, and smaller dendritic arms, compared to slowly solidified material in conventional casting. In addition, metastable phases are formed [45]. Li and Gu [39] stated that the fine microstructure produced by SLM is attractive as an alternative to conventional casting techniques with their slow solidification rates that lead to microstructural coarsening. In some cases, the effect of laser-material interaction in the process of SLM and the rapid solidification lead to microstructural modifications that yield enhanced material properties [60], as

reported by Kempen *et al.* [54] when processing AlSi10Mg. Thijs *et al.* [4] reported the microstructure of AlSi10Mg to be made up of fine grains, coarse grains, and heat affected zones (HAZ), as shown in **Figure 15**. Along the building direction, the grains at the melt pool boundaries were elongated in the direction of thermal gradient with finer equiaxed grains at the cores, as can be seen in **Figure 16**. On the plane perpendicular to the building direction, the grains were equiaxed with finer microstructure at the melt pool core and coarser microstructure at the melt pool boundary [4]. The grain orientation in SLM AlSi10Mg in the planes parallel and perpendicular to the build direction is shown in the EBSD map in **Figure 17**. Similarly, Lijing *et al.* [86] selectively laser melted Al-8.5Fe-1.3V-1.7Si alloy and observed a fine cellular dendritic microstructure in the melt pool core surrounded by spherical nano-scale particles in the heat affected zone.

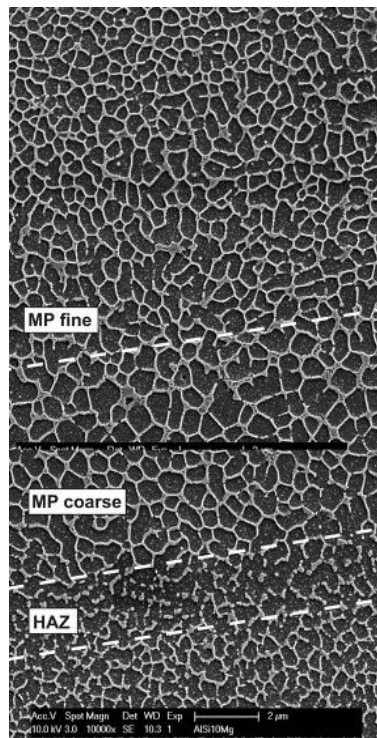


**Figure 15:** Microstructure of SLM AlSi10Mg as observed from the plane normal to the build direction [4].

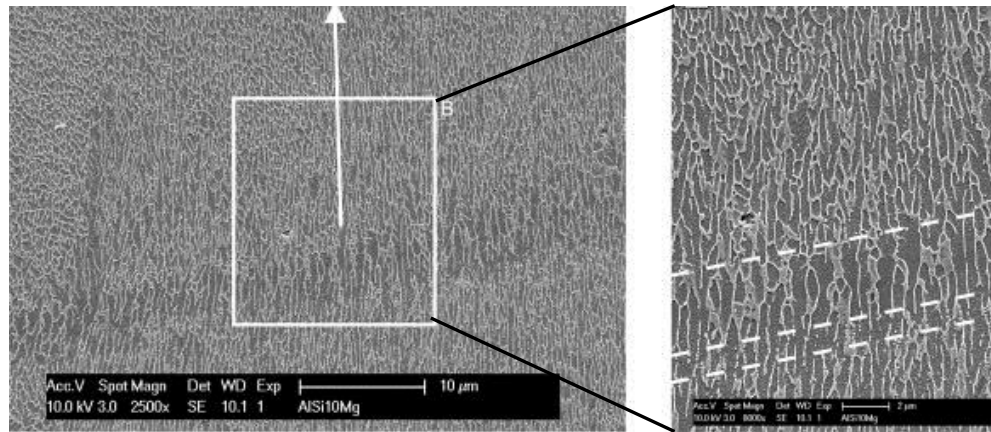


Figure 16: Microstructure of SLM AlSi10Mg as seen on the plane parallel to the build direction at (a) low and (b) high magnifications [4].

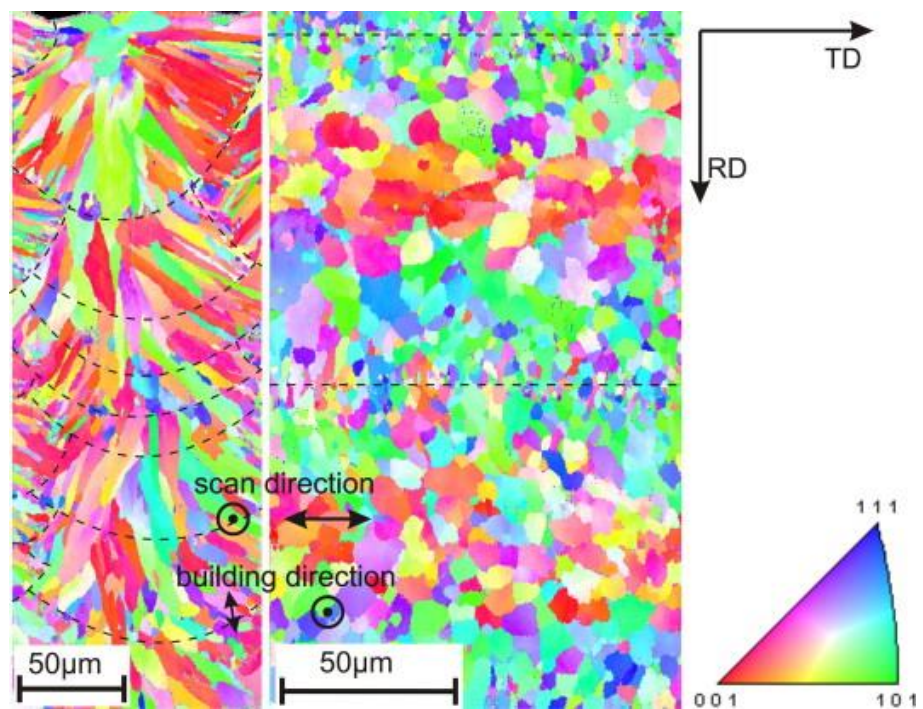
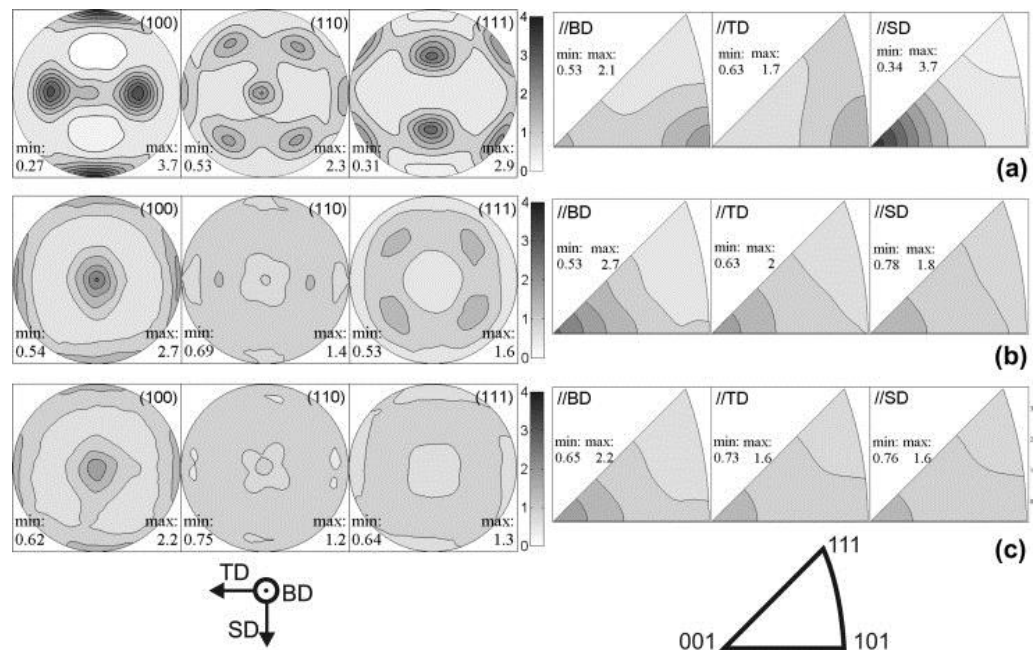


Figure 17: EBSD orientation maps showing the grains orientation in SLM AlSi10Mg in two perpendicular planes.

During solidification of the molten metal, there are preferred orientations in which a fraction of the grains grow faster than others, i.e. formation of a crystallographic texture. This crystallographic texture is controlled by the processing technique. The formation of textured material when processing by SLM has been previously reported for Ti-6Al-4V [47, 48, 110] and Inconel 939

[111]. Since, Al is an FCC metal, columnar grains usually have  $\langle 100 \rangle$  axes [42]. A textured microstructure has been observed for AlSi10Mg, which changed from a strong fibre texture to a weak cubic texture by changing the scan strategy (rotating each layer  $90^\circ$  from the previous) [4], as demonstrated in **Figure 18**. It has also been reported [4] that the texture was significantly reduced when using a checkerboard scan strategy.



**Figure 18:** The pole figure and inverse pole figures showing the change in the crystallographic texture of SLM AlSi10Mg with the scan strategy (a) unidirectional scan strategy, (b) alternating scan strategy with  $90^\circ$  rotation per layer, and (c) checkerboard scan strategy [4].

In SLM Al-Si alloys, Si segregates at the grain boundaries of  $\alpha$ -Al in the form of continuous segregations [85]. The characteristic microstructure developed by SLM in Al alloys suggests that their response to heat treatment will be unlike conventionally manufactured parts. Ma *et al.* [112] annealed SLM AlSi20 at various annealing temperatures and demonstrated microstructure coarsening with heat treating. During annealing, Si diffused to form particles that coarsened with further annealing. This finding agrees with those reported

by Prashanth *et al.* [85] from annealing AlSi12. Brandl *et al.* [18] heat-treated SLM AlSi10Mg following a peak hardening regime and the microstructure developed was similar to that achieved by annealing where Si diffused into spherical particles.

## **2.8. Mechanical performance of selectively laser melted parts**

Fabricating load bearing parts using SLM is becoming more commonplace. Consequently, studying the mechanical performance of these parts is gaining further attention [5, 18, 25, 111, 113-118]. This is important in order to cope with the widely expanding popularity for this process as a flexible manufacturing technique to fabricate complex structures [68]. Generally, parts produced by SLM are characterised by high residual stresses arising from the high energy density induced and rapid solidification rates [23], cracks, pores, and characteristic microstructure [4] that depend on the processing parameters [98]. All these features affect the mechanical properties of SLM parts and yield them different from conventionally manufactured ones [49]. For instance, porosity depresses the mechanical behaviour of the parts [18]. The influence of the processing parameters on the crystallographic texture [4] of the produced parts is expected to impact the anisotropy in mechanical properties [5, 111].

There are several aspects of the process that require consideration when studying the mechanical behaviour of SLM parts. The effect of the build orientation has been reported to be influential on the tensile properties of several alloys other than Al [116, 119, 120]. The building direction has been reported to affect the mechanical properties of SLM Al parts by numerous researchers, such as Brandl *et al.* [18], Kempen *et al.* [5], and Buchbinder *et al.*

[25]. Kempen *et al.* [5] reported the properties of vertical AlSi10Mg samples to be worse than horizontal ones. But Read *et al.* [49] observed no significant effect for the build direction on tensile strength of AlSi10Mg samples – it mainly affected anisotropy of the elongation per cent under tensile loading [5, 49]. Similarly, Kanagarajah *et al.* [111] reported that the density of dislocations in SLM parts (using INCONEL 939) is dependent on the build orientation, which affects the material's properties. Also, the energy density used during processing was found to affect the tensile behaviour of SLM material with regards to AlSi12 [84].

Various mechanical properties of SLM parts made from Al alloys have been covered in the literature, such as tensile behaviour [49, 84, 85, 121], creep resistance [49], micro-hardness [5, 84], impact resistance [5], and fatigue performance [18, 121]. A higher hardness in the SLM material, compared to cast counterparts, was reported by Buchbinder *et al.* [25], Kempen *et al.* [5], Bartkowiak *et al.* [6], and Thijs *et al.* [4] for AlSi10Mg, Wang *et al.* [84] for AlSi12, and Lijing *et al.* [86] for Al-8.5Fe-1.3V-1.7Si. Buchbinder *et al.* [25] and Read *et al.* [49] observed good tensile strengths in SLM AlSi10Mg, also superior to die-cast equivalents, as shown in **Figure 19**, agreeing with results published by Wang *et al.* [84] and Prashanth *et al.* [122] for SLM AlSi12. These improved mechanical properties were attributed to the finer microstructure developed by SLM [4]. Although several studies reported higher tensile strength for SLM parts, it cannot be overlooked that these parts are brittle. However, annealing was found to significantly recover a fraction of the lost ductility by sacrificing the high strength [112]. Comparing the properties of AlSi10Mg parts processed by SLM to die cast ones in creep [49]

and impact [5] resistance have yielded good results since the behaviour was either comparable or even better with SLM.

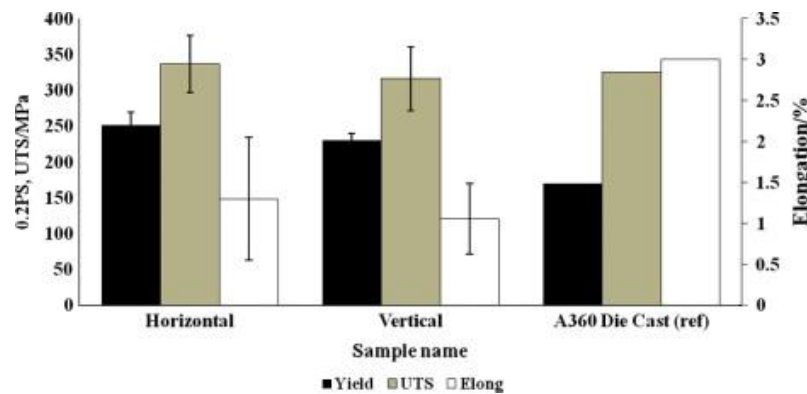


**Figure 19: Tensile behaviour of SLM AlSi10Mg samples built in two different orientations and compared to the die cast equivalent [49].**

The presence of un-bonded regions (regions containing un-melted powder) in SLM parts has been reported by Read *et al.* [49] for AlSi10Mg and Louvis *et al.* [53] for Al6061. Although these regions are relatively small, meaning that they will not significantly reduce the load bearing area in the case of tensile loading, they might be influential on fatigue properties. Recent studies have mainly considered the static tensile properties of the parts, with little attention so far to fatigue performance [18]. Fatigue performance is susceptible to defects commonly present in SLM parts, such as porosity, residual stresses, build orientation, and surface roughness [23, 111, 123]. The fatigue life of flawed parts, such as those manufactured from cast alloys, is affected by pores and second phase particles, i.e. inclusions and precipitates [44]. Defects in parts produced by SLM, such as pores, non-molten spots, or surface roughness, cause stress concentrations (notch effect) that depress the fatigue life of parts as fatigue cracks grow and nucleate at these sites [18, 23, 44, 124, 125]. Edwards and Ramulu [23] recommended hot isostatic pressing (HIP'ing) to improve

fatigue performance as it consolidates the part, reducing porosity and stress relieves the material. Siddique *et al.* [121] recommended using double scan strategies to enhance fatigue life by re-melting regions that might suffer the presence of un-bonded material. The sensitivity of fatigue properties to surface defects, accentuated by the poor surface roughness of SLM parts, has been widely reported [9], such as the study by Chan *et al.* [126] on Ti alloy. The effect of surface roughness of Ti-6Al-4V samples produced by SLM on the fatigue life was investigated by Edwards and Ramulu [23] when they compared the fatigue life of samples as-built and machined. The authors affirmed that the poorer the surface roughness of the sample, the worse its fatigue properties by showing that the fatigue performance of machined samples was better than the as-built ones. Results by Riemer *et al.* [123] for 316L stainless steel further support these findings. Wycisk *et al.* [15] tested Ti-6Al-4V additively manufactured samples and reported improving the surface roughness to nearly double the fatigue endurance limit by testing as-built and polished samples. Frazier [9] states that when the surface roughness increased from 3 to 1000 R<sub>a</sub>, the fatigue life reduced by an order of magnitude. But it is worth noting that although machining helps in enhancing fatigue life, it cannot be overlooked that porosity may still be the primary site for crack initiation. Brandl *et al.* [18] conducted uniaxial cyclic loading tests to evaluate the high cycle fatigue (HCF) behaviour of SLM AlSi10Mg. In their work, they investigated the effect of changing the build orientation, the platform temperature, and peak hardening on the fatigue properties of the material. They reported that the building orientation/direction has a small influence on the material properties as opposed to peak hardening that was found to yield samples with higher fatigue

strength, as shown in **Figure 20**. The improved strength was attributed to the transformation of the Si dendrites to spheroids capable of hindering crack initiation and propagation. Heating the platform was found to not affect the mean fatigue strength of the material but rather reduce the scatter in results [18]. Siddique *et al.* [121] asserted that the use of a heated platform (200 °C) when processing AlSi12 diminished the residual stresses to the extent that post-processing stress relieving treatment did not have a significant effect on the mechanical properties. The influence of stress relieving by heat treatment or HIP'ing on the fatigue properties of SLM 316L stainless steel parts was examined by Riemer *et al.* [123], who reported stress-relieving the samples to yield fatigue properties that were the same as, or even outperform those of, conventionally manufactured samples [123]. Edwards and Ramulu [23] recommended peening to induce compressive residual stresses at the surface since they found SLM parts to have tensile residual stresses .

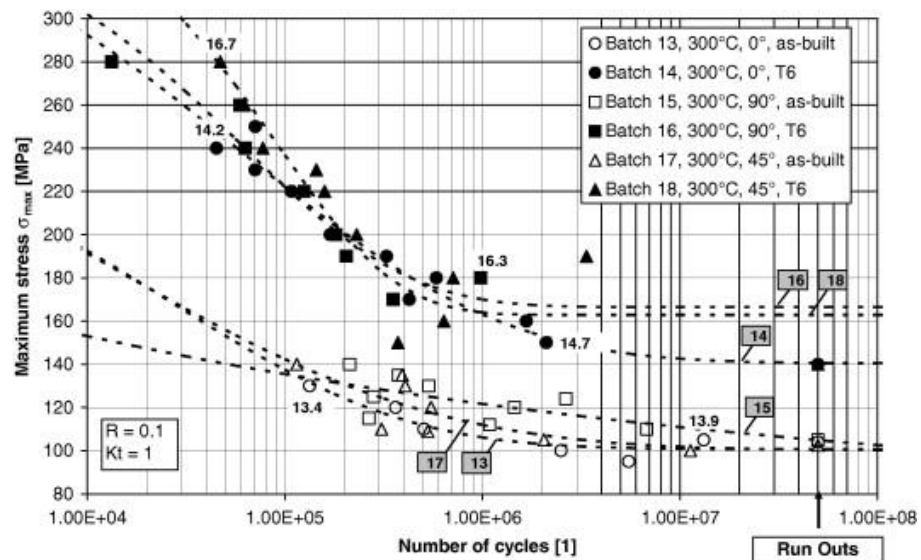


**Figure 20:** Fatigue performance of SLM AlSi10Mg samples in their as-built and heat treated (T6) conditions. The samples were built in various orientations (0°, 45°, and 90°) with respect the build plate [18].

Altering the mechanical properties of SLM material by heat treatment usually follows the same procedures that have been developed for conventionally manufactured materials, with no special attention to the distinct microstructure that SLM produces. For AlSi10Mg, the alloy of interest in this study, annealing is usually used to promote ductility, whereas, it is conventionally strengthened through precipitation hardening (T6 heat treatment). Prashanth *et al.* [85] reported microstructure coarsening and material softening when annealing SLM AlSi12, which is a similar response as conventional cast material. Precipitation hardening of AlSi10Mg is divided into two steps; (1) solution heat treatment (SHT) followed by quenching and (2) artificial ageing (AA) at 423-453 K (150-180 °C) [127]. Each step is conducted over duration of time, which is generally provided as a range. The durations are based on studies conducted on conventionally manufactured components from AlSi10Mg that have microstructures that are entirely different from those developed during the SLM process [4]. The duration for each step is of crucial importance to avoid underaging or overaging, which results in reducing hardness. An example of the importance of the ageing process was shown by Brandl *et al.* [18] where the fatigue resistance of AlSi10Mg SLM parts was enhanced following a hardening regime. However, whether Brandl *et al.* [18] selected the most appropriate SHT and AA durations for optimal fatigue resistance requires further investigation. This raises the question of the validity of the conventional heat treatments when it comes to SLM materials, and what would be the effect of these heat treatments on the overall mechanical behaviour.

Research to date has focussed on either the micro- or macro-scopic mechanical properties of SLM material, while little work has examined the nano-scale

properties, such as nano-hardness. The advantage of using nanoindentation is the very small indentation area and depth of penetration, which are helpful in characterising materials with very fine microstructure such as SLM AlSi10Mg [4, 51]. The application of this technique in SLM is not yet common and it has been mainly used to test the hardness of larger bulk parts, such as in the work by Biedunkiewicz *et al.* [128] on metal matrix composites processed by SLM. Also, Prashanth [67] used nanoindentation to determine the hardness of individual phases in an  $\text{Al}_{85}\text{Nd}_8\text{Ni}_5\text{Co}_2$  alloy processed by SLM, which then aided in defining the deformation, cracking, and failure mechanisms at the macroscopic level.

## **2.9. Further aspects in selective laser melting**

Numerous studies concerned with material qualification can be found in the literature, however, material qualification on its own is not going to help AM in the industry. This is because aside from the material variability, it is important to understand the machine-to-machine variability, as pointed out by Frazier [9]. In other words, optimising the parameters for a material on a machine does not mean that these parameters can be generalised for this material and the need to optimise the parameters for each material on each specific machine (make or model) is a setback for AM.

In addition to the areas of research detailed in this thesis, there is an important aspect in the SLM process that deals with the process efficiency. This includes researching the feasibility of the process and the effectiveness of its use [10, 13]. For instance, Matilainen *et al.* [10] investigated controlling the process parameters to yield an effective build rate. They concluded that limitations on

the scan speed and layer thickness are imposed by the available laser power, whereas the laser beam spot size adds the constraint to the hatch spacing variation, agreeing with [13]. Although increasing the laser power would increase the build rate, doing so without increasing the laser beam diameter will cause increased intensity, which leads to evaporation of elements and production of spatter, as well as promoting keyholing. Significant increase in laser beam diameter means loss of accuracy [13]. However, research like this will remain hindered by the immaturity of the process that is significant in the degree of variability and inconsistency in production. Only when these issues are tackled and it becomes possible to reduce the scatter in data from material variability (depending on the source or supplier that controls the properties of the powders) and machine variability (variation of results from machine to machine based on manufacturer) will efficiency-related research find its way.

Besides material qualification and process parameters investigations, there is ongoing research into the feasibility of using additive manufacturing in several applications. This aims at showing that metal additive manufacturing can be used to fabricate complex structures that are difficult with conventional manufacturing. For example, Wits *et al.* [129] successfully manufactured a high-pressure micro-pump for space applications by SLM of Ti-6Al-4V. Osakada and Shiomi [3] reported promising results for their attempts to manufacture dental crowns and artificial bones from Ti using SLM. One of the promising aspects of research in SLM of Al alloys is the production of lattice structures to replace bulk parts in order to achieve drastic weight reduction [37].

## **2.10. Summary**

Selective laser melting involves numerous parameters that control its success. The work that has been undertaken in studying the most important parameters in the literature has been reviewed in this chapter; starting from the powders used in the process to characterising the produced parts. Besides highlighting what has already been covered in the literature, this chapter has also pinpointed the research areas that require further investigation for better understanding of the SLM processing of Al alloys. This further understanding should not only be pursued for the sake of knowledge but also to help open up further opportunities for the alloy in industry.

Although there are numerous studies investigating the different aspects of single track formation, little can be found on Al alloys. As has been established from the literature, the melt pools in SLM are governed by the laser-material interaction, which is dependent on the target material properties, so the outcome of the study would vary based on the material. Most studies are concerned with the formation of single tracks from powder without paying enough attention to the response of the substrate material to laser radiation and how it is contributing to the overall form of the single tracks. Moreover, verifying the hypothesis of porosity formation within individual melt pools, and it progressing to become porosity in the 3D parts, requires consideration through a study of single tracks, layers, and then multi-layered samples. This cumulative approach will help define the stage at which pores form and minimize them.

Process parameters optimisation to produce near fully dense parts from Al alloys usually recommended the use of high laser power to account for the

material's high reflectivity as well as low scan speeds. The use of different scan strategies is usually studied in terms of the effect on microstructure and mechanical properties. From the author's perspective, there might be an underestimation of the role of scan strategies, as they might also be designed in a way that could help remedy the problem of porosity. Also, there are further parameters that are not given much attention, although they might be influential to the process. For example, there is the role of powder properties that is known to promote porosity if they do not comply with the recommended properties related to morphology, particle size distribution, and chemical composition. Finding a means to amend defects that could be induced by using powders with poorer properties will also improve the SLM process. Moreover, there is the effect of the gas flow rate within the processing chamber, which has previously been reported as an important factor when processing Ti alloys. The use of a stronger gas flow rate within the chamber helped remove more condensate material leading to better densification. Whether this would apply to Al alloys as well requires attention.

SLM of Al alloys results in a material with characteristically fine microstructure. Although this has been reported in the literature already, the evolution of the microstructure starting from single tracks until reaching the stage of having a multi-layered part is important and is yet to be published. The response of the microstructure to annealing has been reported for AlSi12 and found to be different from the response of conventional material. Thus the response of the SLM material to different heat treatments requires investigation. For instance, conventional T6 heat treatment procedures are used to strengthen AlSi10Mg – the alloy of interest in this study – as Brandl *et al.*

[18] have done to enhance the fatigue performance of this alloy after SLM. Since the procedure and parameters of the T6 heat treatment were originally developed for conventional materials with different microstructures, using it for SLM without conducting an investigation in this matter might be misleading. Therefore, a thorough study to define the optimum combination of T6 heat treatment parameters is needed.

Published studies investigating the mechanical properties of SLM parts from Al alloys focussed on either the micro or the macroscopic properties such as micro-hardness, tensile behaviour, impact and creep resistance, and fatigue performance. The work in the nano-scale properties is quite limited. The effect of a heat treatment such as T6 (solution heat treatment and ageing) on the various mechanical properties has not yet fully been studied. The work on fatigue in the literature for this alloy investigated the influence of the T6 heat treatment on the fatigue life but a more comprehensive study incorporating the effects of heat treatment and machining might better draw the bigger picture. To the author's knowledge, the compressive behaviour of solid SLM AlSi10Mg has not yet been reported since attention is mainly directed towards compressive behaviour of their latticed structures [37].

The gaps in the literature that require attention are:

- A lack of knowledge as to which mode of melting dominates the SLM process according to the laser-material interaction.
- It is unknown pores start to form at which stage of processing. The effect of the various process aspects such as scan strategies and powder properties on porosity formation and reduction is not addressed to date.

- The evolution of the microstructure during the overlap of scan tracks and layers requires investigation to aid understand the mechanical behaviour as well as the response of SLM material to the conventional heat treatments.
- The variation of the local mechanical properties due to the progressive nature of fabrication is not yet confirmed or annulled.
- The compressive behaviour of solid SLM material needs to be documented for prediction and simulation models referencing.
- A comprehensive study on the fatigue performance and the effect of various parameters in the material's behaviour in terms of surface quality and heat treatment needs to be developed in order to promote the outcomes of this study to be of help to the industrial sectors.

This thesis aims at targeting the abovementioned gaps in order to contribute to developing a comprehensive understanding of the various SLM process aspects towards a more reliable and controlled production process.

## CHAPTER (3): Materials & Methods

This chapter lays the ground for the following chapters since it includes descriptions of all the materials and equipment used in this research as well as the experimental procedures employed. The various experimental studies are mapped in **Figure 21**.



**Figure 21: Mapping the various experiments conducted in this thesis.**

### 3.1. The formation of single tracks and layers

The study on the formation of single tracks and layers is divided into two sections. The first section considers the creation of fusion lines onto a substrate material without any powder by means of a laser beam, whereas the second section considers the formation of single scan tracks and layers from

AlSi10Mg powder. A schematic presentation of these experiments is shown in **Figure 22**. These experiments were conducted using a Realizer SLM-50 (Germany) selective laser melting machine equipped with a 100 W Yttrium fibre laser (YLM-100-AC). The spot size of the focussed laser beam is 20  $\mu\text{m}$ . The machine processes under argon atmosphere with a 0.1% oxygen level.

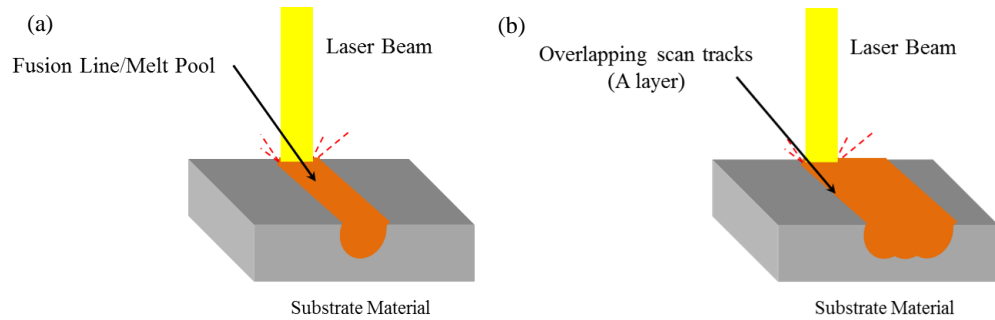


**Figure 22: Schematic presentation for the fusion lines experiments (a) single and (b) overlapping.**

In the first section, single and overlapping fusion lines were created onto the surface of an LM6 (AlSi12) as-cast substrate by irradiation of the substrate without powder. The LM6 as-cast ingot was supplied by Nigel Smith Alloys LTD (UK). The standard chemical composition for this alloy is 10-13 wt% Si, 0.6 wt% Fe, 0.1 wt% Cu, 0.5 wt% Mn, 0.1 wt% Ni, 0.1 wt% Zn, 0.2 wt% Ti, and the balance is Al [41]. Prior to irradiating the laser beam onto the substrate, the surface was polished then cleaned with acetone. Fusion lines were created using six different scan speeds (250, 500, 750, 1000, 1250, and 1500 mm/s) at a fixed laser power (100 W).

In the second section, single and overlapping scan tracks (single layers) were formed using gas (argon) atomised AlSi10Mg powder supplied by TLS Technik GmbH & Co. Spezialpulver KG (Germany) onto an LM6 as-cast polished substrate. AlSi10Mg powder had a particle size range between 20 –

63  $\mu\text{m}$  and a chemical composition of 86.96 wt% Al, 12.58 wt% Si, and 0.46 wt% Mg. The layer thickness was varied to be once 40  $\mu\text{m}$  and once 400  $\mu\text{m}$ . Three scan speeds were examined; these were 250, 500, and 750 mm/s at a fixed laser power (100 W). Similar to producing the overlapping fusion lines, overlapping scan tracks (a single layer) were formed using a hatch spacing of 50  $\mu\text{m}$ . This process is similar to the process of cladding [16]. Summary of the experimental plan is shown in **Table 2**.

**Table 2: Summary of the experimental plan for the single tracks experiments.**

Experiment	With (w) or without (w/o) powder	Laser power (W)	Speed range (mm/s)	Speed increment (mm/s)	Layer thickness ( $\mu\text{m}$ )	Hatch spacing ( $\mu\text{m}$ )
Fusion lines	(w/o)	100	250-1500	250	N/A	N/A
Overlapping fusion lines	(w/o)	100	250-750	250	N/A	50
Scan tracks	(w)	100	250-750	250	40 & 400	N/A
Single layers	(w)	100	250-750	250	40 & 400	50

The morphology of the fusion lines and scan tracks was investigated using a Philips XL30 scanning electron microscope (SEM). Fusion lines, scan tracks, and single layers were cross-sectioned and polished to study their transverse views using a Nikon Eclipse LV100ND optical microscope. The geometrical features of the melt pools, in terms of penetration depth and track width, were measured from the optical micrographs using the open source software ImageJ 1.46r [130] to establish their response to changing the scan speed and in case of using powder, changing the layer thickness. For single tracks, the factors used to define their stability are the depth of penetration, track width, and the continuity. The microstructure of the melt pools was revealed by etching in Keller's reagent [131].

### **3.2. Process parameter investigations to produce near fully dense parts**

Gas (argon) atomised AlSi10Mg powder supplied by LPW Technology (UK) was processed by SLM to produce test cubes using a Realizer SLM-50. The particle size distribution for the powder was determined using a Malvern Mastersizer 3000. The Malvern Mastersizer 3000 (UK) uses laser diffraction to measure the size of particles through measuring the intensity of light scattered as a laser beam passes through a dispersed particulate sample. Data is then analysed to calculate the size of the particles that created the scattering pattern [132]. A Philips XL30 SEM was used to evaluate powder morphology and an energy dispersive X-ray (EDX) detector was used for chemical composition analysis. The powder was also cross-sectioned and polished according to the Struers tips for metallographic preparations of Al alloys [133] to investigate the presence of inherent pores using a Nikon Eclipse LV100ND optical microscope. Powder was first dried/pre-heated at 70 °C for 20 minutes to improve its laser absorptivity [70].

The test cubes produced were 5 mm x 5 mm x 5 mm (see **Figure 23**). The size of the cubes was selected as it was commonly used in the literature and the cubes are small enough to enable faster production of the samples. The SLM process was conducted under an argon atmosphere (below 0.5% O<sub>2</sub>). The platform on which the test cubes were built was kept at 200 °C to maintain the part at an elevated temperature so as to prevent it from warping due to non-uniform thermal expansion [70]. In order to study the effect of the various building parameters on pore creation, the study was divided into the three phases, namely (1) the hatch spacing study, (2) the scan speed study, and (3) the scan strategy study. The window of process parameters investigated in this

study was narrowed down using the results from the study on single tracks formation in chapter (4).

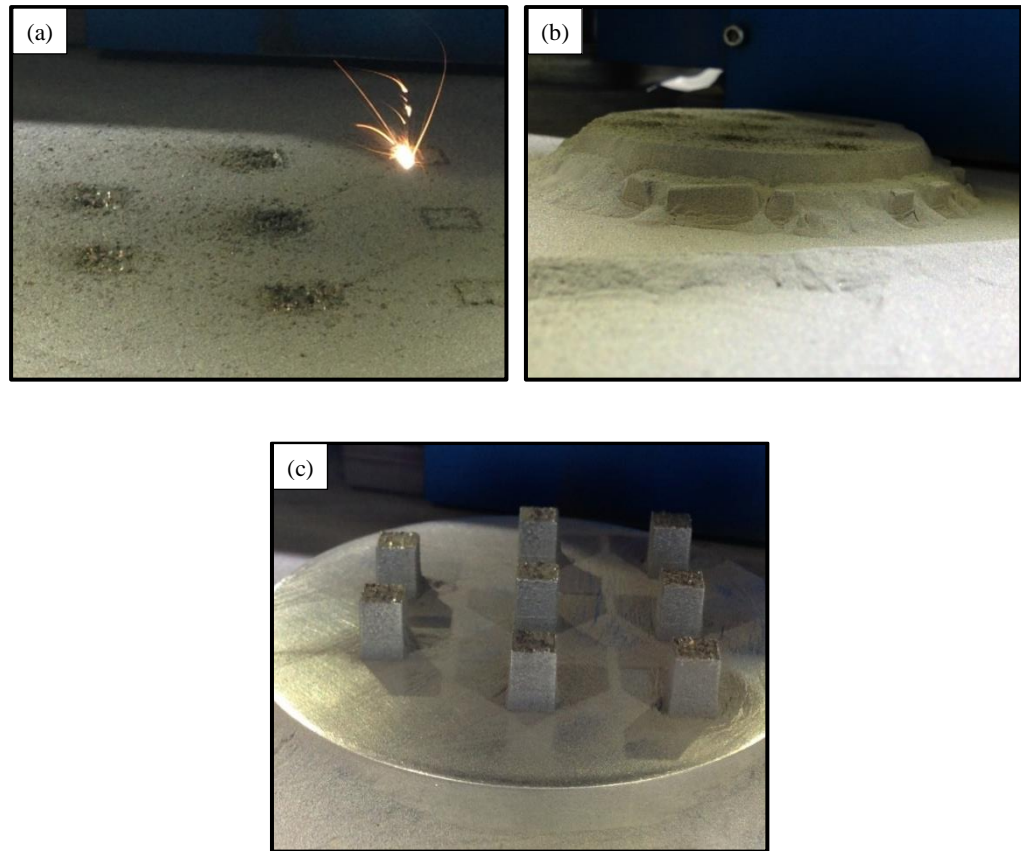


**Figure 23: Selective laser melting of AlSi10Mg (a) in process, (b) process completed, and (c) test cubes on the platform.**



### **3.2.1. Hatch spacing study**

Five sets of samples were produced, each using a different hatch spacing (50  $\mu\text{m}$ , 100  $\mu\text{m}$ , 150  $\mu\text{m}$ , 200  $\mu\text{m}$ , or 250  $\mu\text{m}$ ). Other parameters were kept constant for all samples in this batch:

- Layer thickness = 40  $\mu\text{m}$ ,
- Scan speed = 500 mm/s,
- Laser power = 100 W.

The scan strategy in this study was a unidirectional X-axis scan. This was used to simplify the structure of the bulk sample in order to aid in tracing the mechanisms behind the pores and cavity development. The combinations of parameters used to produce each of the five sets are presented in **Table 3**.

**Table 3: Processing parameters combinations used in the hatch spacing study.**

Set #	Hatch spacing ( $\mu\text{m}$ )	Laser power (W)	Scan speed (mm/s)	Layer thickness ( $\mu\text{m}$ )	Scan strategy
1	50	100	500	40	Uni-directional
2	100	100	500	40	Uni-directional
3	150	100	500	40	Uni-directional
4	200	100	500	40	Uni-directional
5	250	100	500	40	Uni-directional

### 3.2.2. Scan speed study



In the scan speed study, the layer thickness and laser power were kept constant at 40  $\mu\text{m}$  and 100 W, respectively, during processing. The scan speed was varied between 250 mm/s and 1000 mm/s with 250 mm/s intervals, along with varying the hatch spacing between two values that are 50  $\mu\text{m}$  and 100  $\mu\text{m}$ . The combinations of parameters used in the scan speed study are shown in **Table 4**.

**Table 4: Combinations of processing parameters used in the scan speed study.**

Set #	Hatch spacing ( $\mu\text{m}$ )	Laser power (W)	Scan speed (mm/s)	Layer thickness ( $\mu\text{m}$ )	Scan strategy
1	50	100	250	40	Uni-directional
2	50	100	500	40	Uni-directional
3	50	100	750	40	Uni-directional
4	50	100	1000	40	Uni-directional
5	100	100	250	40	Uni-directional
6	100	100	500	40	Uni-directional
7	100	100	750	40	Uni-directional
8	100	100	1000	40	Uni-directional



### 3.2.3. Scan strategy study

The layer thickness was fixed at 40  $\mu\text{m}$  for the scan strategy study. The samples built were divided into three batches according to the scan speed used (500, 750, and 1000 mm/s). The scan strategies investigated for each batch are listed in **Table 5**. The “X” denotes a unidirectional scan with a single scan per layer. The “2X” is similar to “X” but each layer is scanned twice. The “alternating” scan is rotating the orientation of scan per layer 90° from its preceding. The “X&Y 2HS” indicates that each layer was scanned twice having each scan perpendicular to the one before and with different hatch spacing values for each scan. The “pre-melt” scan is to first scan the layer with half the power followed by a second scan with full power. In the “overlap” strategy, each layer was scanned twice with the second scan melting the overlap between each two adjacent scan tracks. The idea of utilising different scan strategies for densification is to avoid the propagation of a pore formed in one layer into the subsequent layers, forming an interconnected void, through hindering its progression [24].

**Table 5: Scanning strategies variable parameters**

Scan Strategy	No. of scans per layer	Uni or bi-directional	1 <sup>st</sup> Scan		2 <sup>nd</sup> Scan	
			Power (W)	HS ( $\mu\text{m}$ )	Power (W)	HS ( $\mu\text{m}$ )
X	1	Uni	100	50	-	-
2X	2	Uni	100	50	100	50
Alternating	1	Bi	100	50	-	-
X&Y 2HS	2	Bi	100	100	100	50
Pre-melt	2	Uni	50	50	100	50
Overlap	2	Uni	100	50	100	50

### 3.2.4. Evaluating the quality of the produced samples

The test specimens were cross-sectioned, mounted, and polished [133]. Post polishing, the samples were etched using Keller's reagent [131] through immersion etching for microstructural examination using optical and electron microscopes. The relative density of each of the built samples was determined by image processing of the optical micrographs using the open source software ImageJ 1.46r [130].

Energy dispersive x-ray (EDX) analysis was carried out to determine the chemical composition of the built parts to decide whether some elements were more vulnerable to being lost or scattered by evaporation during processing. For a comprehensive understanding of the chemical composition and its evolution from the powder phase to the bulk phase, four types of samples were studied. These were:

- *Fresh powder*: This is the AlSi10Mg powder as received from the supplier.
- *Recycled powder*: This sample denotes the powder that is not used during a build and is sieved to go back into the cycle of the SLM machine.
- *Bulk sample*: This represents the test cubes produced by SLM. The sample surface was polished and cleaned with ethanol before analysis.
- *Laser spatter*: As the laser beam is irradiated onto the powder, laser spatter is produced [82] in the vicinity of the part being built, as seen in **Figure 24**. This spatter is characterised by dark colour and relatively large size. Since the spatter represents elements that are being lost

during SLM, it was the fourth sample examined by EDX for elements' evaporation tracing.

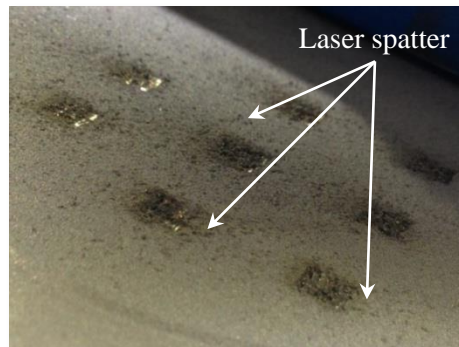


**Figure 24: Laser spatter shown as darker particles surrounding the cubes being built.**

### **3.3. Investigating further parameters in the SLM process**

#### **3.3.1. Powder quality effect**

Processing with two batches of AlSi10Mg powder from two different suppliers was investigated to determine the influence of powder properties on the processability, referred to hereafter as powder LPW and TLS. The latter is specially produced for AM to comply with the process requirements. The morphology of the powder was examined using a Philips XL30 SEM. The powder was also cross-sectioned, polished, and imaged using a Nikon Eclipse LV100ND optical microscope. EDX served to analyse the chemical composition by means of a detector attached to the SEM. Particle size distribution was analysed using a Malvern Mastersizer 3000. Flowability was tested using the Hall flowmeter funnel following the ASTM standard B213 [52] and the apparent density was calculated in accordance with the ASTM standard B212 [134].

Cubic samples ( $5 \times 5 \times 5 \text{ mm}^3$ ) were fabricated using the Realizer SLM-50 machine. Two sets of samples were produced using the two batches of powder. SLM was conducted under argon to limit contamination and oxidation, with an oxygen level below 0.5%. The build platform was kept at  $200 \text{ }^\circ\text{C}$  to maintain the part at an elevated temperature to avoid deformation by curling due to residual stresses. Samples were processed using a 100 W laser power,  $50 \text{ }\mu\text{m}$  hatch spacing,  $40 \text{ }\mu\text{m}$  layer thickness, and a scan speed of 500 mm/s. In each set, half the samples were processed using a uni-directional single scan strategy and the other half was processed using a pre-melt scan strategy (for description see section 3.2.3). The cubic samples were cross-sectioned, polished, and imaged using optical microscopy. The relative density was determined through image processing of optical micrographs using the open source software ImageJ 1.46r [130].

### **3.3.2. Gas flow within the processing chamber**

Experiments to study the effect of the gas flow within the processing chamber were conducted using a Realizer SLM-50 machine. Since the gas circulation within the processing chamber is controlled by the filter in use, it was decided to install a new filter into the machine and then build a set of cubic samples ( $5 \times 5 \times 5 \text{ mm}^3$ ) with different processing parameters. The fixed processing parameters were  $40 \text{ }\mu\text{m}$  layer thickness, laser powder 100 W, hatch spacing  $50 \text{ }\mu\text{m}$ , along with the variable parameters being the scan strategy (overlap or pre-melt – for description see section 3.2.3 of this thesis) and the scan speed (500, 750, and 1000 mm/s). A schematic presentation for the gas flow within the processing chamber in the Realizer SLM-50 is shown in **Figure 25**. Each set of samples was repeated five times using the same filter and then the

relative density of the samples with similar processing conditions built at different rates of filter usage was compared to determine the trend. The relative density was determined using the same protocol employed in section 3.3.1. The rate of filter usage was denoted by the time for which it had been functioning, i.e. the first build was at time zero since the filter was new and the fifth build was at time 280 minutes since each build takes 70 minutes. The more the filter is used, the older it is, the slower the gas flow based on visual observation of the amount of spatter removed away with the flow.

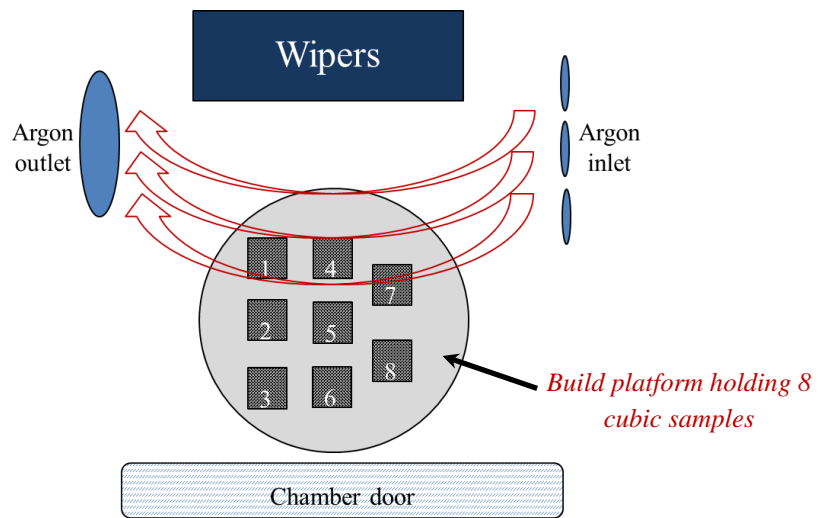


**Figure 25: Schematic presentation for the top view of the processing chamber in the SLM machine showing gas circulation.**

### **3.4. Fabricating and characterising AlSi10Mg SLM samples**

#### **3.4.1. Microstructural investigations**

Near fully dense AlSi10Mg cubic samples ( $5 \times 5 \times 5 \text{ mm}^3$ ) were produced for the microstructural investigations using a Renishaw AM250 (UK) SLM machine from AlSi10Mg powder supplied by LPW technology (UK). The Renishaw AM250 SLM machine is equipped with a 200 W Yb-Fibre laser ( $\lambda =$

1064 nm). The spot size of the laser beam at the focus position is 70  $\mu\text{m}$ . The machine processes under argon atmosphere (below 0.1%  $\text{O}_2$ ). The processing parameters can be found in **Table 6**. This point onwards, the Renishaw AM250 machine was used instead of the Realizer SLM50 because the former is equipped with a 200 W laser and a larger beam spot size that together enable faster fabrication through using a single scan per laser and larger hatch spacing. It is worth noting that the parameters on both systems are optimised to yield parts that are nearly 99.8 % dense. Furthermore, the Renishaw AM250 was more convenient to use to benefit from the larger build plate that can accommodate the larger samples needed for macro-mechanical properties tests.

**Table 6: Processing parameters (set 1) using Renishaw AM250 to produce near fully dense parts.**

Laser power	Layer thickness	Scan speed	Hatch spacing	Scan strategy
200 W	25 $\mu\text{m}$	318 mm/s	80 $\mu\text{m}$	Checkerboard

The surface roughness and surface texture of a cubic sample was determined using an Alicona InfiniteFocus SL system. Samples were cross-sectioned, mounted, and polished [133]. The microstructure of the samples in three planes (XY, YZ, and XZ – see **Figure 26** – Z parallel to the build direction) was revealed by immersion in Keller’s reagent [131] and imaged using a Nikon Eclipse LV100ND optical microscope and a Philips XL30 SEM operating at 20 kV. Also, elemental mapping was conducted using an EDX detector attached to the SEM and the INCA software was used for data analysis. A Bruker D8 Discoverer with  $\text{CuK}\alpha$  X-rays was used for X-ray diffraction and crystallographic texture analysis.

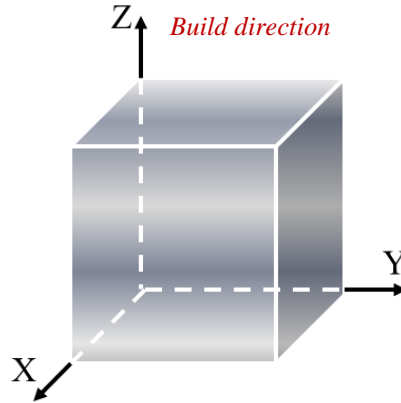
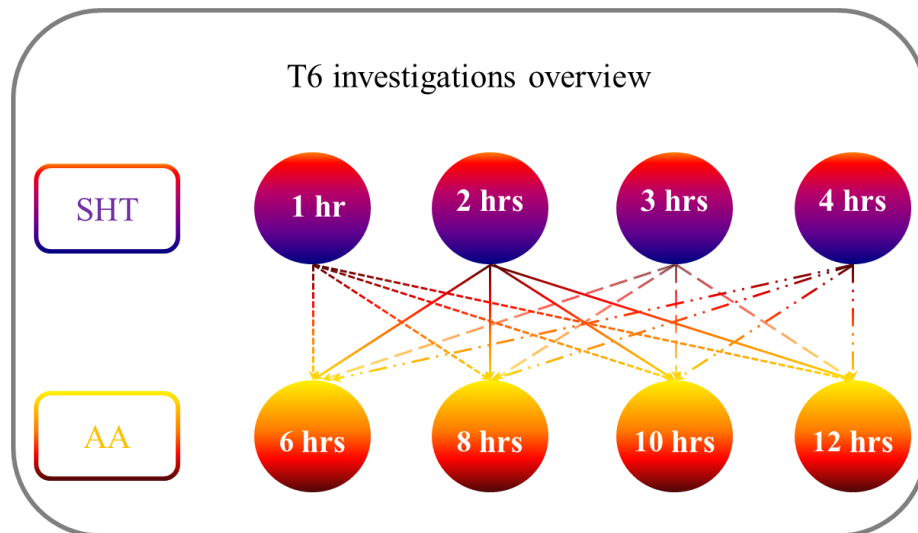


Figure 26: Planes of a cubic sample with layers in the XY-plane stacking up in the building direction (Z-axis).

### 3.4.2. Heat treatment study

For the heat treatment study, 21 cylindrical samples of 13 mm diameter and 5 mm height were produced using the same set up in section 3.4.1 and the parameters in **Table 6**. This study is to explore the effect of a T6 heat treatment on the SLM material. The plan for this experiment is illustrated in **Figure 27**. One sample was considered the reference sample that remained in the as-built condition. Four samples were only solution heat treated at 520 °C. The soaking time for solution heat treatment was varied between 1, 2, 3, and 4 hrs. Sixteen samples were subjected to a full T6 heat treatment, solution heat treatment (SHT) at 520 °C followed by water quenching to room temperature then artificial ageing (AA) at 160 °C. These samples were divided into four groups (4 samples each) based on the SHT soaking time (1, 2, 3, and 4 hrs). For each group, four ageing durations were employed that are 6, 8, 10, and 12 hrs. The heat treatment was conducted in an air furnace since the time gap between solution heat treatment and water quenching must be minimised and this would not be possible with a controlled atmosphere furnace.



**Figure 27: T6 heat treatment investigations study plan.**

The samples (as-built and heat-treated) were cross-sectioned, mounted, polished [133], and etched using Keller’s reagent [131] for 20-25 seconds and the change in microstructure was studied using a Nikon Eclipse LV100ND optical microscope. The chemical composition distribution was mapped using the EDX detector attached to the Philips XL30 operating at 20 kV. The influence of the different treatment durations on mechanical properties was represented by micro-hardness testing using a Buehler Vickers hardness tester. A load of 3 N was applied for 10 indentations per sample to be averaged.

### 3.4.3. Nanoindentation

The nanoindentation study was designed to investigate nano-hardness profiles across individual melt pools as well as single layers and multi-layered samples. Therefore, this study is divided into the following sections:

- *Single tracks*

A single track from AlSi10Mg powder supplied by TLS Technik GmbH (Germany) was formed on a polished LM6 (AlSi12) as-cast

substrate using a Realizer SLM-50. The single tracks were formed using 100 W laser power, 40  $\mu\text{m}$  powder layer thickness, and 500 mm/s scan speed.

- *Single layers*

On the polished surface of an LM6 (AlSi12) as-cast substrate, an individual layer from AlSi10Mg powder supplied by TLS Technik GmbH (Germany) was created using the Realizer SLM-50. The layer was formed using 100 W laser power, 40  $\mu\text{m}$  powder layer thickness, 500 mm/s scan speed, and 50  $\mu\text{m}$  hatch spacing.

- *Multi-layered samples using different scan strategies*

The Realizer SLM-50 was used to manufacture two samples (**Figure 28**) with 10 x 10 x 5 mm<sup>3</sup> dimensions using different scan strategies; one using a uni-directional scan and the other using a pre-melt scan strategy. The remaining processing parameters were the same as those used to produce the single layers. For the sake of investigating the microstructural-hardness interrelation around pores, these samples were fabricated from the LPW Technology (UK) powder.



**Figure 28: Samples for nanoindentation.**

- *Multi-layered samples with and without heat treatment*

Near fully dense samples were fabricated from AlSi10Mg powder supplied by LPW Technology (UK) using the Renishaw AM250 (UK) using the parameters in **Table 7**. One of these samples was tested in its as-built condition whereas the other one was heat treated by solution heat treatment for 1 hr at 520 °C followed by water quenching and then artificial ageing for 6 hrs at 160 °C.

**Table 7: Processing parameters (set 2) using Renishaw AM250 to produce near fully dense parts**

Laser power	Layer thickness	Scan speed	Hatch spacing	Scan strategy
200 W	25 µm	570 mm/s	80 µm	Chessboard

All the above mentioned samples were cross-sectioned, polished [133] to mirror finish, and the surfaces to be tested were cleaned by ethanol in preparation for the nanoindentation experiments. A MicroMaterials LTD Nanotest™ NTX Platform3 nanoindenter was used to measure the nano-hardness of the various samples. The loading head in this nanoindenter is perpendicular to the instrument's frame, this provides thermal stability during testing [135]. The indenter tip and sample set up can be seen in **Figure 29**. The loading setup is enclosed in an isolated chamber to maintain temperature stability during the tests. The nanoindenter is placed on isolated ground to avoid the influence of surrounding vibrations on the results. Moreover, the chamber enclosing the loading head and the sample is on an air table for the same reason.

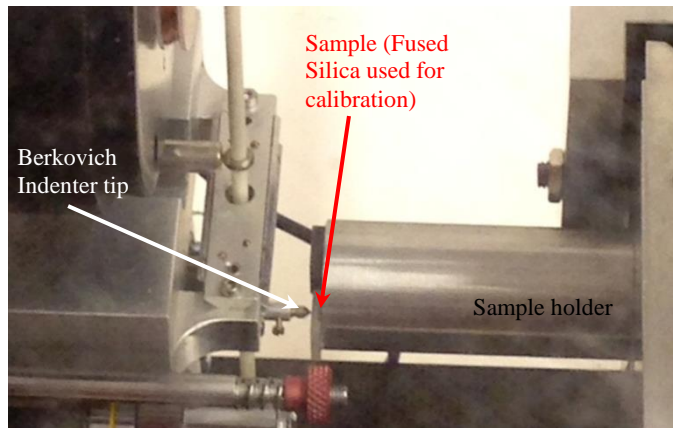


**Figure 29: Nanotest™ indenter tip-sample setup.**

A Berkovich tip was used for indentation with the indenter tip shape factor taken into account in the analysis. Tests were performed in accordance with the ASTM standard E2546-07 [136] in a load-controlled mode. The maximum indentation load was 7.5 mN. For each indentation, the load was applied with a gradual increase, at a constant rate of 0.3 mN/s, until the maximum designated force was achieved then this load was held for 20 seconds before unloading to allow any relaxation needed. Unloading was also gradual at a constant rate (0.3 mN/s) down to 10% of the maximum load, when unloading was paused to account for thermal drift (thermal drift data collection). The thermal drift data was collected before and after each indentation. The thermal drift data correction is automatically executed by the machine's software. The main idea behind thermal drift data collection is that although the tests are conducted in a sealed chamber, i.e. controlled temperature, thermal drift due to sensitivity of the depth sensing capacitor might still have an effect. Not all the data collected for thermal drift are considered in the correction since the first few data are discarded in order not to be biased by viscoelastic recovery at the beginning of load pause [135]. The horizontal and vertical spacing between each two

adjacent indentations was 10  $\mu\text{m}$  and 15  $\mu\text{m}$ , respectively, to avoid one indentation affecting the results from the subsequent one.

#### 3.4.4. Tensile behaviour

Dog-bone tensile test samples with 50 mm gauge length and 9 mm gauge diameter (see **Figure 30**) were manufactured using a Renishaw AM250 (UK) SLM machine. The samples were built vertically with their axes parallel to the build direction. The processing parameters used were the same as in **Table 7**. Six samples were produced, half of which were heat-treated by solution heat treatment for 1 hr at 520 °C followed by water quenching and then artificial ageing for 6 hrs at 160 °C.

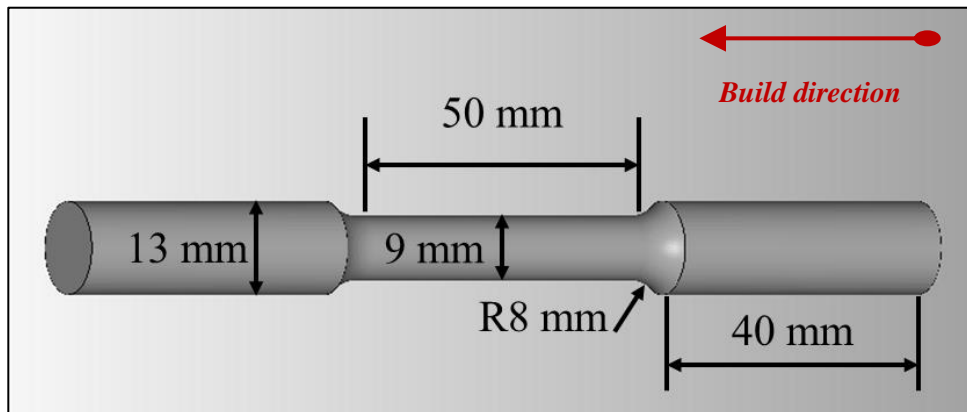


Figure 30: Tensile test sample.

Monotonic uniaxial tension tests were conducted using an Instron 5581 universal testing machine with a load cell that has a maximum capacity of 50 kN. The tests were carried out in accordance with the ASTM standard E8/E8M [137]. The cross-head speed was 0.5 mm/min employing a strain rate of  $1.8 \times 10^{-4} \text{ s}^{-1}$ . A random spatter pattern was applied to the surface of the tensile samples using white and black spray paint to collect strain data using a video gauge. The fracture surfaces of the tensile samples were imaged using a

Philips XL30 SEM. Also, they were cross-sectioned and polished [133] then imaged using the optical microscope and a Hitachi TM3030 SEM equipped with a backscatter electron detector operating at 15 kV and the chemical composition distribution was mapped by means of an EDX detector.

### 3.4.5. Compressive behaviour

The Renishaw AM250 SLM machine was used to fabricate cylindrical compression test samples with a 22 mm diameter and a 62 mm height using the parameters in **Table 7**. These cylinders were then machined by turning, to reduce the surface roughness and ensure flat parallel surfaces being loaded, until the final dimensions became 20 mm and 60 mm for the diameter and height, respectively (see **Figure 31**). The samples were built vertically with their axes parallel to the build direction. Uniaxial compression tests were conducted using an Instron 5985 universal testing machine equipped with a 250 kN load cell. The test was conducted following the ASTM standard E9 [138]. The testing speed was 0.3 mm/min, resulting in a strain rate of  $8.3 \times 10^{-5} \text{ s}^{-1}$ . The strain data was collected using a linear variable displacement transducer (LVDT). The test was stopped when the load reached 230 kN as limited by the machine's capabilities.

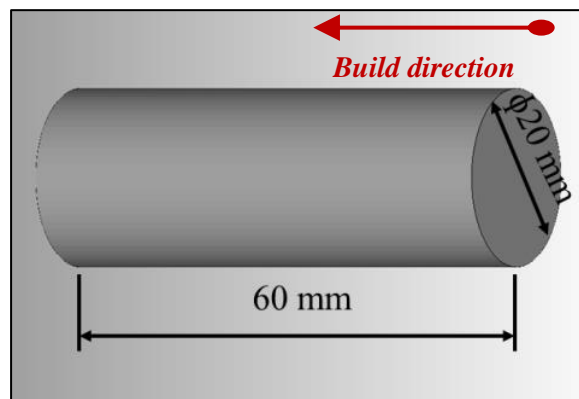


**Figure 31: Compression test specimen.**

### 3.4.6. Fatigue behaviour

Two batches of standard dog-bone fatigue test samples (**Figure 32**) with continuous radius between the ends were manufactured for fatigue tests using a Renishaw AM250 SLM machine employing the parameters in **Table 7**. The samples were of a minimum diameter of 6 mm and a gauge length of 36.8 mm (see **Figure 33**). The samples were built vertically with their axes parallel to the build direction. The first batch was tested without machining and the second one was machined to reduce the surface roughness; machining allowance was taken into consideration when building the samples by accounting for extra material removal. Half the samples in each batch were heat-treated by solution heat treatment for 1 hr at 520 °C followed by water quenching to room temperature and then aged for 6 hrs at 160 °C. A Bruker D8 Discoverer with CuK $\alpha$  X-rays was used to measure the residual stresses in the material with and without heat-treatment.



**Figure 32: Fatigue test samples.**

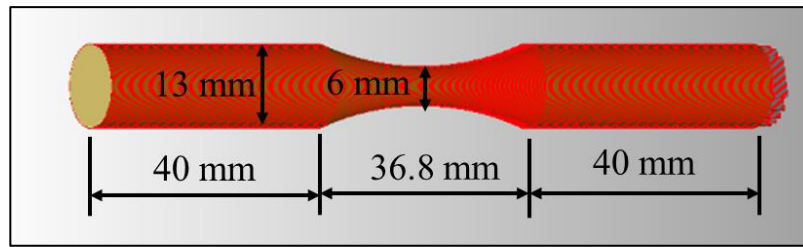


**Figure 33: Fatigue test specimen.**

Fatigue tests were conducted in a stress-controlled testing mode following the ASTM standard E466 [139]. Before testing, the machined samples were inspected visually by unaided eyes as well as by low power magnification using optical microscopy to ensure they are free of abnormalities such as cracks, machining marks, or undercuts. The specimens were also cleaned with ethanol prior to testing to remove any surface oils or fingerprints. An Instron 8801 servo-hydraulic fatigue testing machine with a 100 kN load cell was used for axial high cyclic fatigue tests. Tests were conducted in atmospheric air at room temperature. The cyclic loading followed a sine wave. The frequency used was 30 Hz and the R-value was 0.1. The effect of frequency variation when testing Al alloys for fatigue behaviour is reported to be non-significant [140]. The samples were loaded until failure and samples exceeding  $3 \times 10^7$  cycles were considered run-outs. Fracture surfaces of the samples were imaged using a Philips XL30 SEM then cross-sectioned, polished [133], and imaged using a Nikon Eclipse LV100ND optical microscope.

## **CHAPTER (4): Single tracks and layers in selective laser melting**

Although the majority of studies in the field of selective laser melting of Al alloys to date have considered the development of load bearing objects, in particular porosity reduction and mechanical characterization of the parts, it is also important to study the single tracks formed during the process as they form the building blocks of the parts. In other words, it is required to understand the response of a material whether in the form of a substrate or metal powders to being irradiated with a laser beam. This chapter studies the effect of changing the scan speed on the formation of fusion lines and single tracks from AlSi10Mg, as well as their overlap to form single layers using various powder layer thicknesses. The geometrical features of the melt pools as well as the boundaries of continuity and/or irregularities were defined.

### **4.1. Fusion lines on a substrate material**

Fusion lines on an LM6 as-cast polished substrate created using different scan speeds (250, 500, 750, 1000, 1250, and 1500 mm/s) at 100 W laser power are shown in **Figure 34**. Increasing the scan speed from 250 mm/s up to 1500 mm/s reduced the width of track, also known as the powder consolidation zone, by slightly over 50%. The fusion lines showed evidence of irregularities and discontinuities when increasing the scan speed beyond 500 mm/s. The increase in the scan speed is equivalent to the reduction in the energy density.

The formation of defects with the decrease in the energy density has been previously reported [54]. Thinning of the fusion lines with increasing scan speed is due to shorter exposure time to the laser beam at a specific location or point.

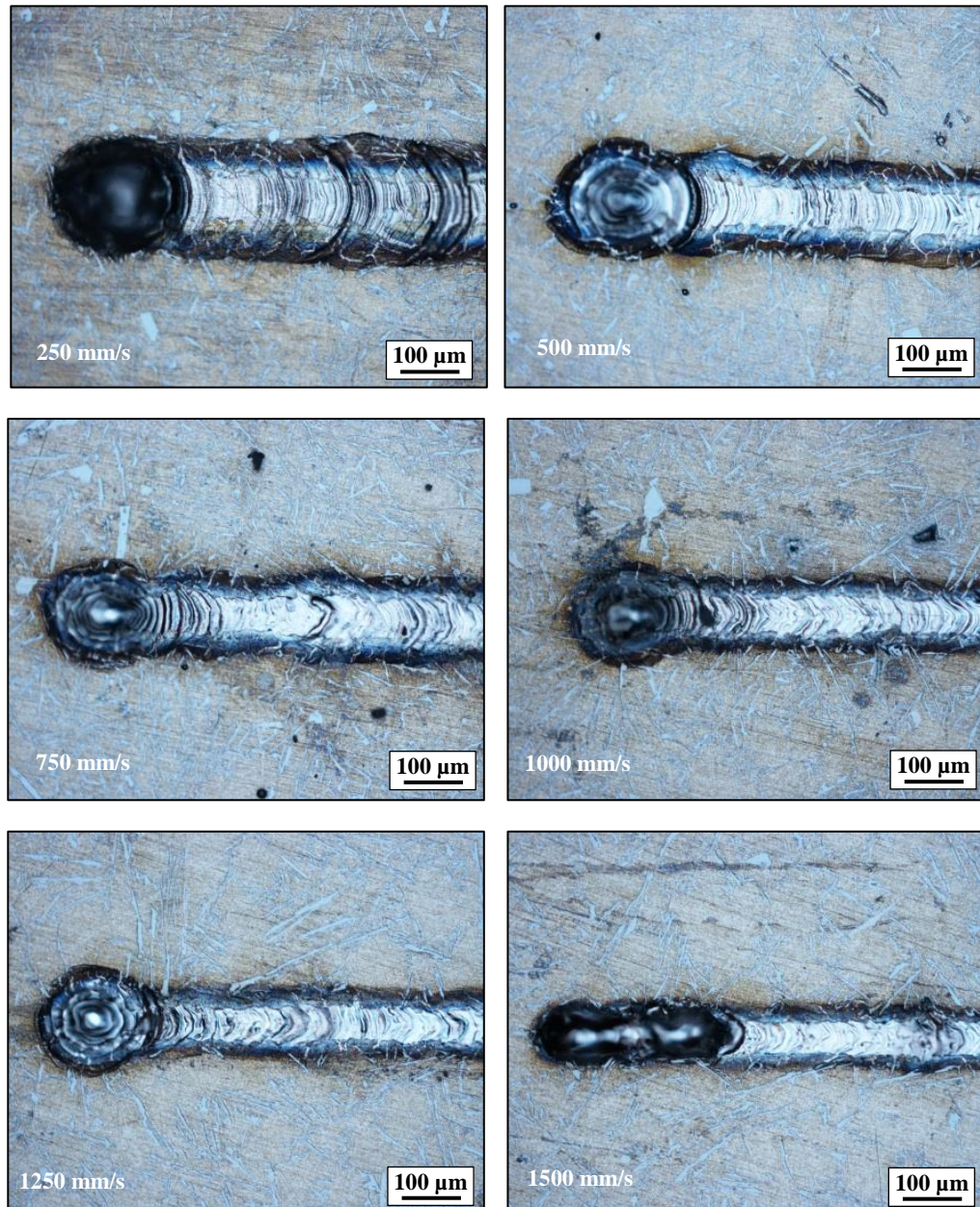


**Figure 34: Thinning of fusion line with increasing the scan speed.**

A fusion line is comprised of a melt pool (fusion zone) with an adjacent heat affected zone (HAZ); a structure similar to that of laser welds [141]. As well as

the widths of the fusion lines, the thickness of the HAZ was reduced by increasing the scan speed, as can be seen in **Figure 35**, which also, in addition to **Figure 36**, shows the irregularities promoted by increasing the scan speed. Irregularities along fusion lines are expected to lead to the formation of gaps between the adjacent scan tracks when producing a layer since sufficient overlap will not be ensured along the length of the track. Quantitative analysis of the change in width trend with the scan speed with further discussion is provided later on in this chapter.

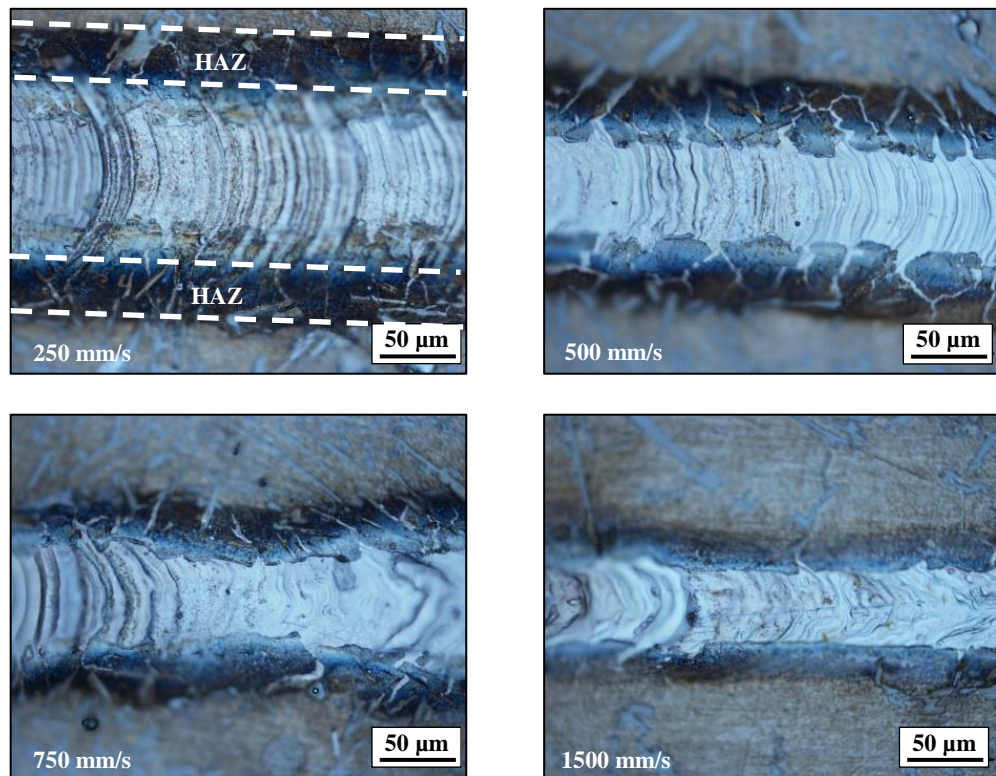


**Figure 35: Reduction in HAZ thickness with increasing scan speed.**

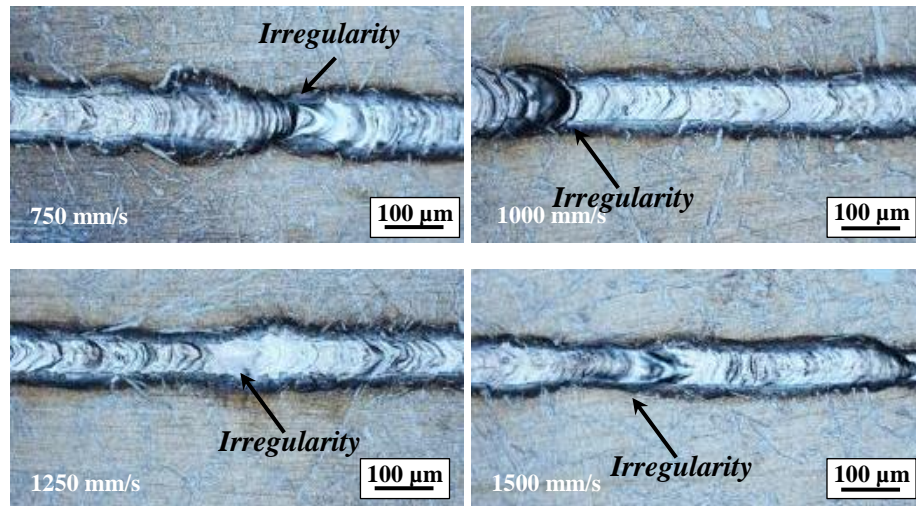


**Figure 36: Irregularities in fusion lines using 750, 1000, 1250, and 1500 mm/s.**

Higher magnification of the fusion lines revealed the presence of micro-porosity, approximately 2 - 6  $\mu\text{m}$  in size, in the HAZ at scan speeds of 750 mm/s and above, as can be seen in **Figure 37**. Micro-porosity was not observed at the slower scan speeds. The fraction of the micro-pores formed in a fusion line (based on observations of the top view) increases with increasing the scan speed. These pores are thought to have formed during the solidification of the molten metal due to trapped gases that were not allowed enough time to escape the melt pool because of the lower energy density [68] accompanied by a fast rate of solidification. The energy density during the formation of single tracks via SLM is the ratio between the laser power and the scan speed employed (energy density ( $\text{J}/\text{mm}$ ) = laser power (W) / scan speed ( $\text{mm}/\text{s}$ )). Although SLM is conducted under an inert atmosphere with reduced oxygen content within the processing chamber, an amount of entrapped gases could be inherent in the cast material (the substrate) that is ejected upon melting with the laser beam [71]. Conventional casting of Al alloys produces high degrees of porosity and the substrate used in this study was found to contain a high fraction of spherical and irregularly shaped pores. An example

of the spherical pores in the cast substrate is shown in **Figure 38**. Also, these pores could be attributed to the turbulence and vortex within a melt pool during solidification that is mainly governed by Marangoni convection and the vaporisation pressure of the alloying elements [43]. According to the work conducted by Dai and Gu [68], discussed in chapter (2) on densification of Cu matrix composites during SLM, as the energy density increases the gaseous bubbles are trapped by vortices at the lower section of the melt pool, as was shown in **Figure 7**. As the energy density decreases (which is equivalent to increasing the scan speed if other parameters are kept constant), the gaseous bubbles tend to move upwards towards escaping the melt pool affected by Marangoni convection [68]. Although this hypothesis justifies the presence of micro-pores observed on top of the melt pools, it cannot be verified without investigating the transverse cross-sectional views of the fusion lines.

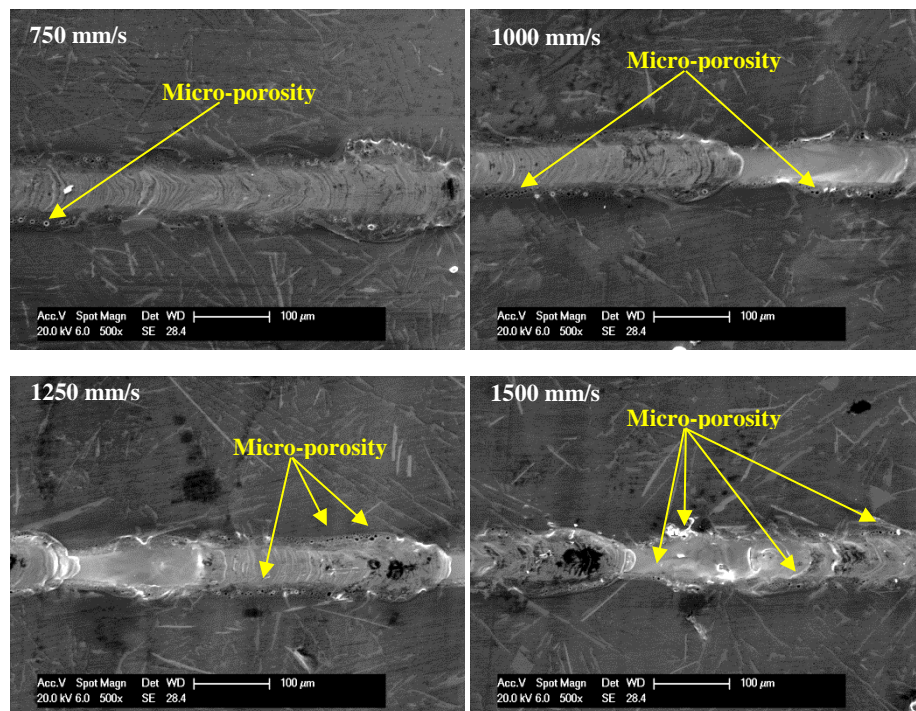


**Figure 37:** Fusion lines produced using different scan speeds showing evidence of micro-porosity.

The transverse cross-sections of the fusion lines' melt pools at different scan speeds are shown in **Figure 38**. The widths of the fusion lines as well as their depths of penetration decreased with the increasing scan speed. The measurements for these geometrical parameters are represented in the plot in **Figure 39**, showing the clear trend of decreasing size with increasing the scan speed, i.e. wider and deeper scan tracks are formed at higher energy inputs [101] due to an increase in melt volume or melt efficiency. This behaviour is similar to what happens in the case of laser welding [108].

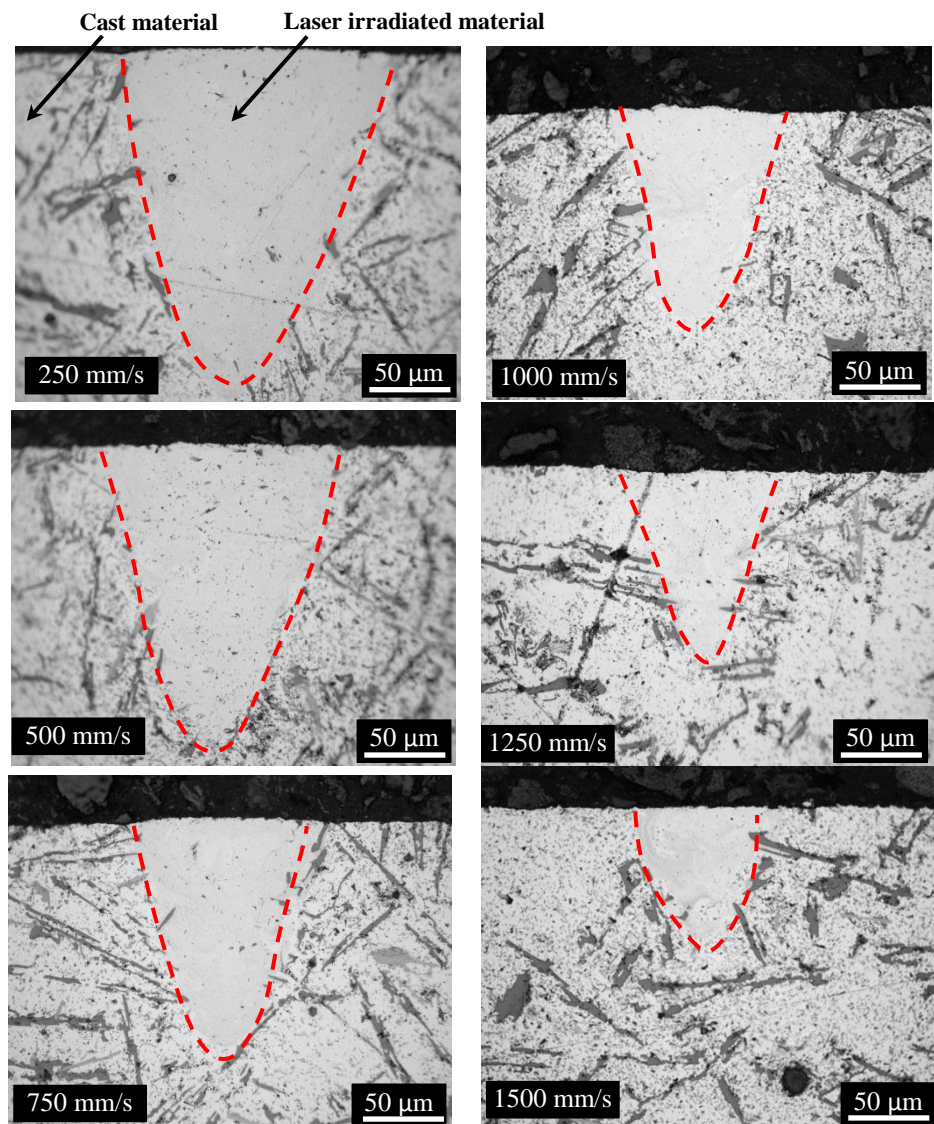


**Figure 38:** Cross-sectional view of the polished fusion lines at different scan speeds.

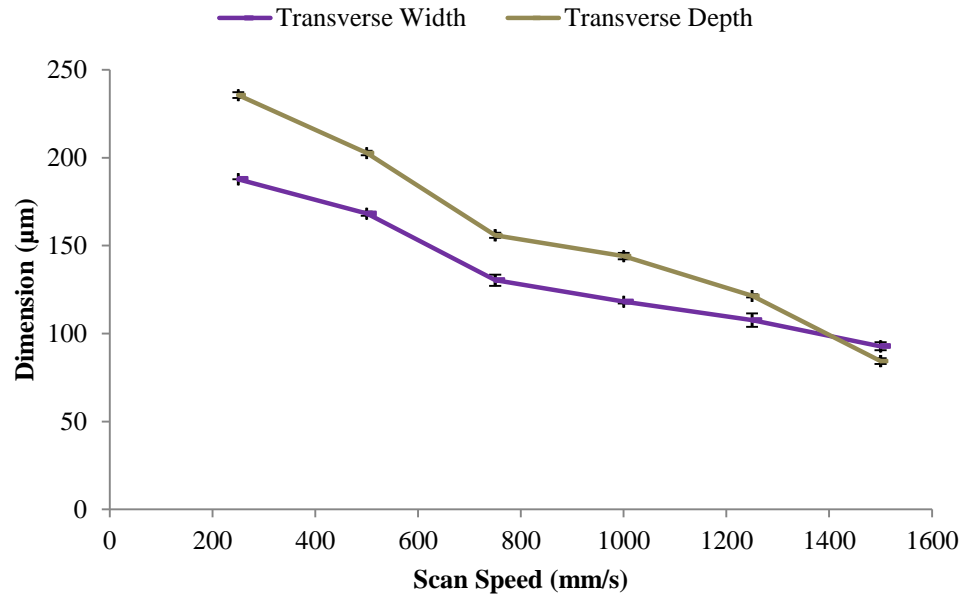


**Figure 39: Effect of scan speed on width and depth of penetration of the fusion lines (with error bars showing standard error).**

The AlSi10Mg melt pool was conical – see **Figure 38** – rather than spherical unlike other SLM candidate materials, such as stainless steels [70]. The larger depth of the melt pool compared to its width indicates keyhole mode melting rather than conduction mode melting. Keyhole mode melting is identified by having a melt pool of a depth that is larger than half its width [96]. When a metallic material is irradiated by a laser beam, it melts either adopting a conduction mode melting or a keyhole mode melting. The adopted mechanism depends on the energy transfer efficiency during the process. According to Zhao *et al.* [43], the energy transfer efficiency is defined by the ratio between the laser energy absorbed by the target material and the laser power used. If the energy transfer efficiency is equal to the material’s absorptivity, conduction mode melting dominates. But if the energy transfer efficiency is larger than the material’s absorptivity due to high reflectivity within the melt pool, keyhole mode melting rules. This justifies why melt pools of Al fusion lines

demonstrated domination of keyhole mode melting. Keyhole mode melting implies that scan tracks of AlSi10Mg are susceptible to keyhole instabilities that are means for formation of pores when producing bulk samples through multi-layer processing.

#### **4.2. Overlap of fusion lines**

The hatch spacing 50  $\mu\text{m}$  provided sufficient overlap between adjacent fusion lines at the three scan speeds examined (250, 500, and 750 mm/s), as can be seen in **Figure 40**, to yield a consolidated layer. This outcome was predicted based on the widths of the fusion lines that ranged between 180  $\mu\text{m}$  and 130  $\mu\text{m}$  depending on the employed speed. The hatch spacing increase led to reducing the overlap. For instance, at 150  $\mu\text{m}$  hatch spacing the fusion lines were barely touching and in some regions gaps started to form between the adjacent lines at a scan speed of 750 mm/s that already showed irregularities along the corresponding fusion lines, as explained earlier (see **Figure 41**).

Discolouration was observed on the surface of the layer formed using the slowest speed (250 mm/s), as can be seen in **Figure 40 (a)**. This was attributed to the longer time during which each spot is exposed to the laser beam [142] and the formation of oxides. This discoloration decreased with increasing the scan speed to 500 mm/s and 750 mm/s. Oxide creation is promoted at slower scan speeds since the material remains molten for longer duration – due to the increase in the laser exposure time – increasing the likelihood of oxidation despite the low oxygen content (less than 0.5%) in the processing chamber. The oxygen content originally in the substrate material and the powder (in the case of processing with powders) contributes to increasing the content in the

processing environment upon melting [71] as the trapped gases escape the melt pool whilst it is solidifying.

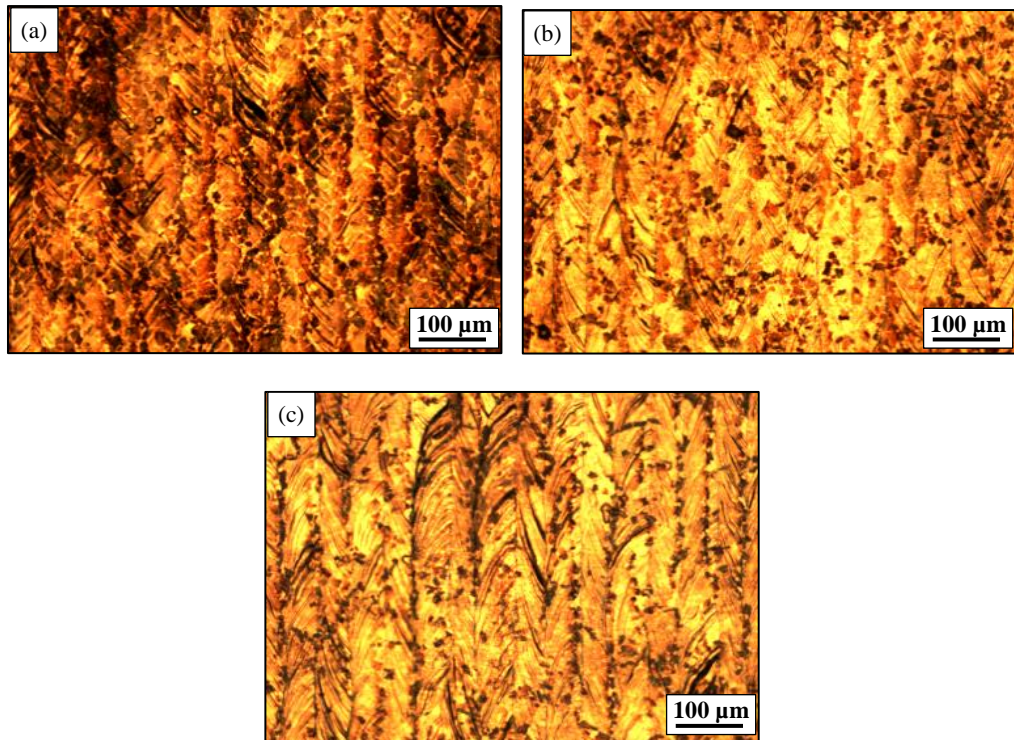


Figure 40: Overlap of fusion lines with 50  $\mu\text{m}$  hatch spacing using (a) 250, (b) 500, and (c) 750 mm/s.

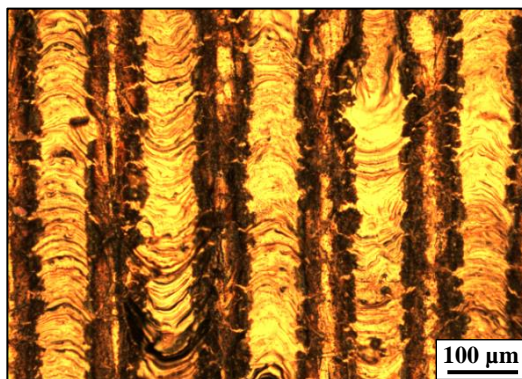
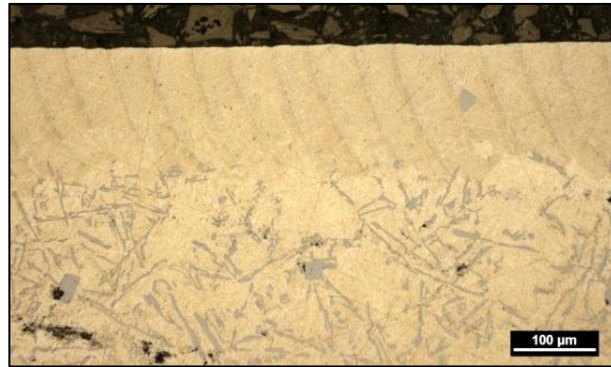


Figure 41: Lack of overlap between fusion lines at 750 mm/s and 150  $\mu\text{m}$  hatch spacing.

A hatch spacing of 50  $\mu\text{m}$  at a speed of 500 mm/s yielded a homogeneous layer in terms of depth of penetration as shown in the transverse view in **Figure 42**.

This indicates that this combination of processing parameters is promising in

terms of producing near fully dense bulk samples. Despite the presence of inherent porosity in the as-cast substrate used in these experiments, porosity in either the fusion lines or their overlaps was not evident. This suggests that SLM has reduced the original pores in the as-cast substrate, by allowing the gaseous bubbles enough time to escape the molten material.



**Figure 42: Transverse view showing overlap of fusion lines processed using a speed of 500 mm/s and a hatch spacing of 50 µm.**

### **4.3. Single tracks from AlSi10Mg powder**

#### **4.3.1. Single tracks from 40 µm thick powder layer**

In SLM, a moving heat source is used to melt the material. As a result of this motion, the material flows in the assigned path of the laser beam. Thus single tracks in SLM solidify with a characteristic chevron pattern observed on top of the track. The characteristic chevron pattern denotes the direction of motion of the heat source (laser beam in this case) [143], as shown in the micrographs in **Figure 43**.

Creating scan tracks from a 40 µm thick powder layer on the LM6 as-cast polished substrate was successful. Similar to the geometry of the fusion lines, the scan tracks' widths decreased with increasing the scan speed, as

demonstrated in the top view images in **Figure 43** at the scan speeds from 250 mm/s up to 750 mm/s, accordingly. No distortion in the scan tracks was detected. Irregularities started to form at elevated scan speeds, as can be seen for the scan speed of 750 mm/s in **Figure 43** (c). However, discontinuities, if described as complete disconnection in the scan track, were not observed in any of the tracks. The presence of irregularities along a scan track imposes a limitation on the hatch spacing to be used when processing a layer or a multi-layer part. Irregularities in a scan track might also lead to the formation of gaps or pores in a bulk part. These defects act as obstacles on the way of validating the process of SLM and taking it to commercialisation. Moreover, the presence of these defects when producing latticed structures will depress their feasibility and mechanical behaviour.

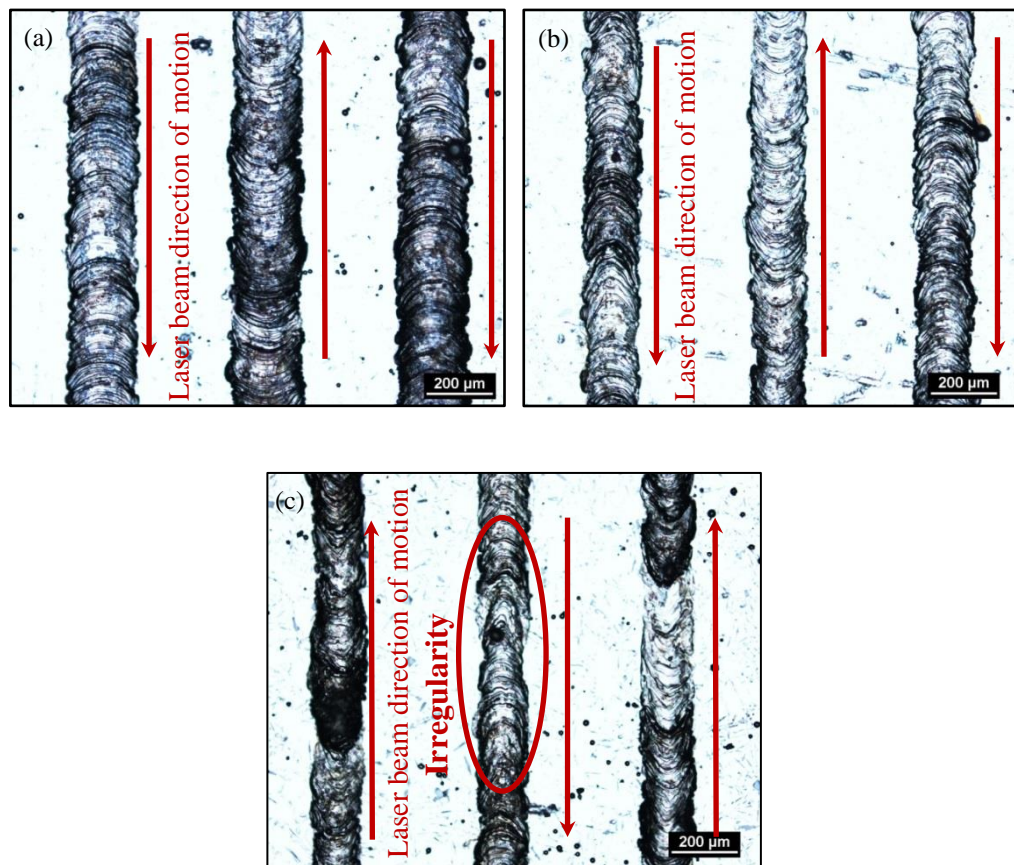


**Figure 43:** Single tracks of AlSi10Mg from 40 μm thick layers at (a) 250, (b) 500, and (c) 750 mm/s.

In the cross-sectional views of the tracks in **Figure 44**, the overall height of the scan track can be divided into two sections; (1) the height above the substrate surface and (2) the depth of penetration into the substrate material (remelted depth). The height above the substrate surface increased with increasing scan speed, whereas the remelted depth decreased with increasing the scan speed, i.e. an opposite trend is seen for the remelted depth compared to the height above the substrate surface. This suggests that further increase in scan speed might lead to significantly small depth of penetration resulting in a lack of contact between the track and the substrate material, i.e. de-cohesion of the layers from one another in multi-layer processing.

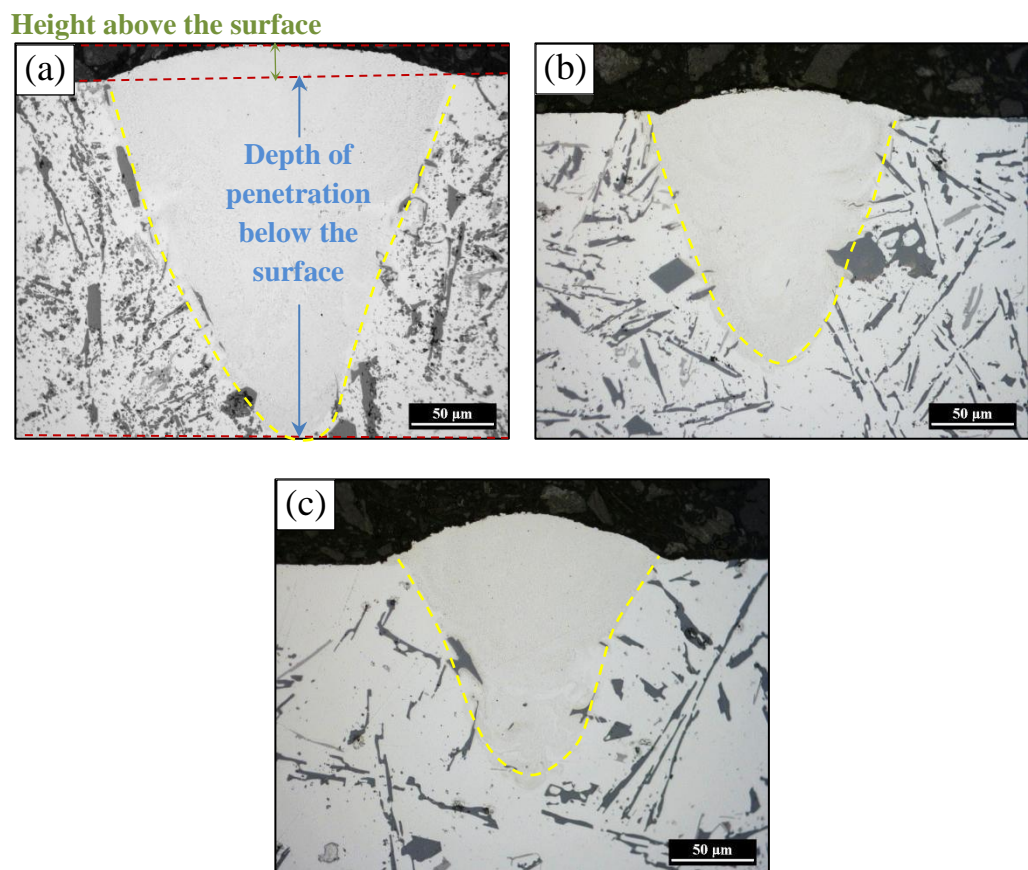


**Figure 44:** Cross-sectioned single tracks processed from a 40 μm thick powder layer at (a) 250 mm/s, (b) 500 mm/s, and (c) 750 mm/s.

The examined processing conditions showed no evidence of balling on the surface of the scan tracks. This indicates good wettability with the substrate material which is a crucial factor affecting the bonding of a layer to the one below since a flat layer is required to enable processing the next layer [1]. Wetting in SLM means that the molten material has spread over the substrate or the previous layer rather than balling [70] and it is also related to the material's viscosity and surface tension [1]. Al is a metal of high surface tension, so it is susceptible to balling instabilities. The presence of Si and Mg in the alloy contributes in reducing its overall surface tension [43].

The measurements for the geometrical features of the melt pools of the scan tracks from the transverse cross-sections are presented in **Table 8**. These numbers support the observations made from the optical micrographs of the top views. The width of a scan track decreased with increasing the scan speed from 250 mm/s and up to 750 mm/s. This agrees with simulation predictions for this material made by Li and Gu [39].

**Table 8: Geometrical dimensions of AlSi10Mg single tracks.**

Scan speed (mm/s)	Track dimensions ( $\mu\text{m}$ )		Depth-width aspect ratio
	Depth	Width	
250	$238 \pm 7$	$212 \pm 4$	1.13
500	$172 \pm 8$	$164 \pm 6$	1.04
750	$165 \pm 1$	$156 \pm 3$	1.06

On comparing the width of the melt pool of a scan track (**Table 8**) and that of a fusion line (**Figure 39**), it can be deduced that the width of the former is larger. This is because the width of a scan track is increased by denudation, which is

the existence of particles sticking to the sides of the scan track [99]. Also, another aspect contributing to increasing the width of a scan track over that of a fusion line is the presence of powder in the former and their wettability, as explained earlier. Since the width of a melt pool changes along its depth (getting narrower as the depth increases), the width at the top of a melt pool (widest zone) is what is referred to as the width of track. As the powder material spreads out on the top surface, it contributes to increasing the width. The depth of a melt pool – considering the overall height of the scan track – also decreased with increasing the scan speed similar to that of the fusion lines. The difference between the geometrical dimensions of the scan tracks and fusion lines is also attributed to the laser-material interaction in SLM. In case of the fusion lines, the laser beam is irradiated onto a bulk material (substrate material). In case of the scan tracks, the laser beam is irradiated onto a powder material. The absorptivity and reflectivity in each case varies (bulk material absorbs less incident laser energy [100]), hence the variation in the laser-material interaction. Again, the depth-width aspect ratio in **Table 8** indicates the domination of keyhole mode melting.

Another aspect that should be considered when studying single tracks is the presence of satellites. These satellites worsen the surface roughness promoting the creation of pores [70]. The presence of satellites was minimal in all the tracks processed from a 40  $\mu\text{m}$  thick powder layer.

#### **4.3.2. Single tracks from 400 $\mu\text{m}$ thick powder layer**

The 400  $\mu\text{m}$  thick powder layer yielded tracks that incorporated several defects on the surface. These can be seen in the scanning electron micrographs in **Figure 45**, **Figure 46**, and **Figure 47** at the scan speeds 250 mm/s, 500 mm/s,

and 750 mm/s, respectively. For instance, at a speed of 250 mm/s (**Figure 45**), the tracks were no more uniform as was the case for the 40  $\mu\text{m}$  thick powder layer (**Figure 43**). At all three scan speeds examined, the tracks were made up of series of balls, i.e. balling phenomenon occurred.

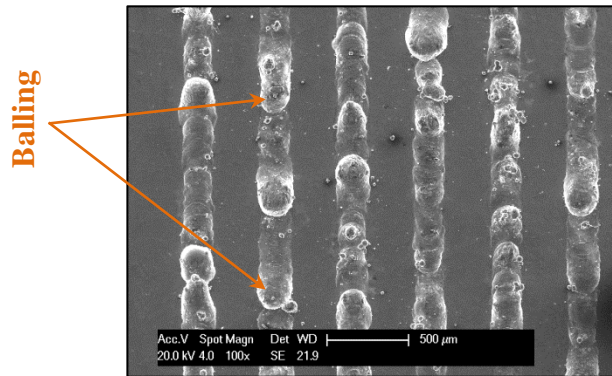


**Figure 45:** Single tracks of selective laser melted AlSi10Mg (250 mm/s and 400  $\mu\text{m}$  layer thickness).

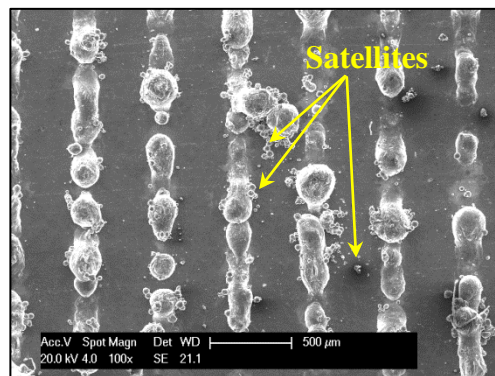


**Figure 46:** Single tracks of selective laser melted AlSi10Mg (500 mm/s and 400  $\mu\text{m}$  layer thickness).

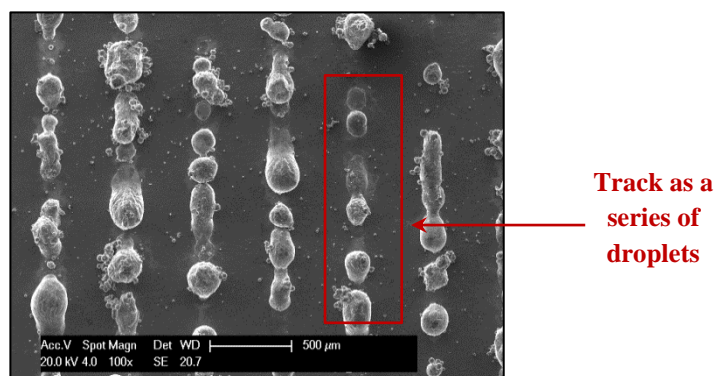


**Figure 47:** Single tracks of selective laser melted AlSi10Mg (750 mm/s and 400  $\mu\text{m}$  layer thickness).

Although 400  $\mu\text{m}$  is considered a relatively thick layer, discontinuities (if defined as absolute disconnection in the scan track, i.e. absence of the remelted depth) were not observed at the slowest scan speed (250 mm/s). This is attributed to the keyhole mode melting that the alloy adopts when irradiated with the laser beam, which results in a significantly deep melt pool. This means that processing a consolidated track from AlSi10Mg powder using SLM even at relatively large layer thicknesses is possible but will suffer severe balling on the surface, i.e. poor surface quality/roughness. Discontinuities formed at 500 mm/s and 750 mm/s yielded tracks in some regions that were just a series of droplets/balls (**Figure 47**). Minimal satellites were observed at the slowest scan speed (250 mm/s). An excessive amount of satellites formed at scan speeds 500 mm/s and 750 mm/s (**Figure 46** and **Figure 47**) that could be attributed to the increased amount of spatter produced at high scan speeds.

The cross sectional views of the tracks processed from a 400  $\mu\text{m}$  thick powder layer revealed the structure of the regions that are flat and those incorporating balls formed on the surface, as shown in **Figure 48**. When a ball is formed, due to increased surface tension as the temperature decreases during solidification [43], the majority of the energy is absorbed by the amount of material forming a ball conducting minimal energy to the substrate. This leads to reduction in the remelted depth with the possibility of totally diminishing it, which means lack of bonding between the track and the substrate. The stability of a melt pool is promoted by good adhesion between the scan track and the substrate, i.e. enough depth of penetration beyond the melt pool depth and into the substrate.

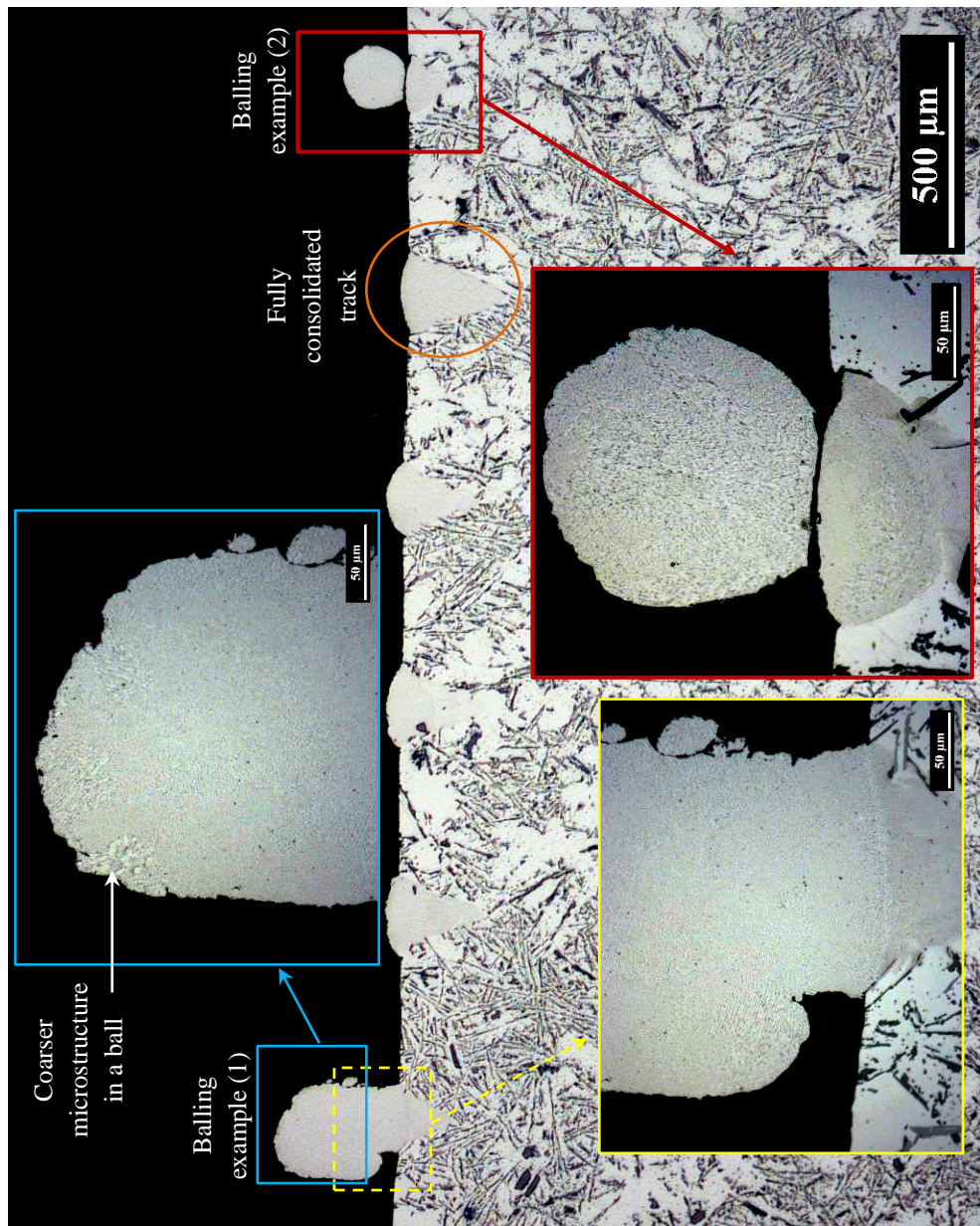
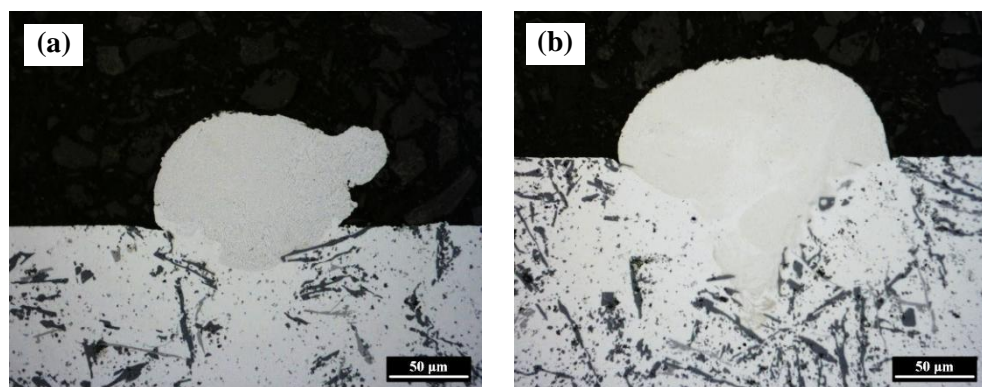


Figure 48: Cross-sections of single tracks formed using a layer thickness of 400 μm with a 250 mm/s scan speed.

It cannot be overlooked that some of the tracks processed at 250 mm/s were fully consolidated into the substrate, such as the one circled in **Figure 48**, however, the fraction of balls formed on the surface preclude the possibility of using large layer thicknesses.

At the scan speeds 500 mm/s and 750 mm/s, the cross-section of the tracks was either in the form of a free circular cylinder (with a large contact angle and

small remelted depth – see **Figure 49 (a)** and **Figure 50 (a)** for examples) or a segmental cylinder (with a smaller contact angle and larger remelted depth – see **Figure 49 (b)** and **Figure 50 (b)** for examples). For the former, the remelted depth was circular whereas for the latter it was conical. This could be attributed to reduction of the heat sink into the substrate. Melt pools that have the shape of segmental cylinders are reported to be more stable than free circular ones [69].



**Figure 49: Different forms of single tracks processed at 500 mm/s using a 400 μm layer thickness**  
(a) free circular cylinder and (b) segmental cylinder.

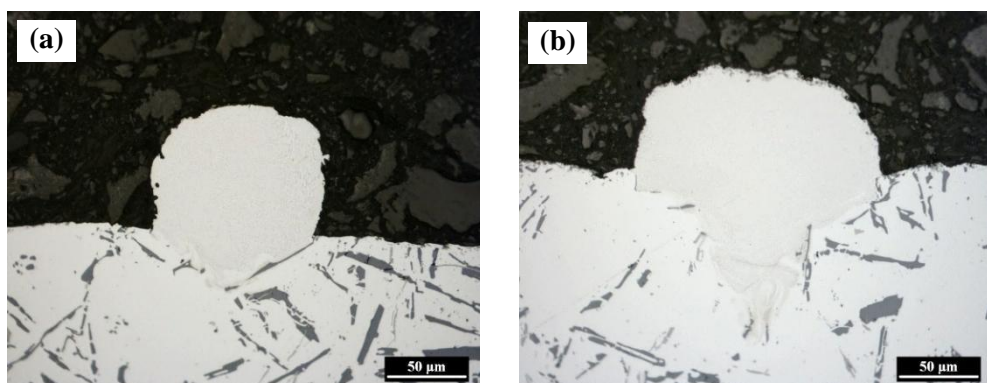


**Figure 50: Different forms of single tracks processed at 750 mm/s using a 400 μm layer thickness**  
(a) free circular cylinder and (b) segmental cylinder.

Although the microstructure of the single tracks and their metallurgy will be studied in details in chapter (6), it is worth noting that the microstructure of a ball is slightly coarser than the rest of the melt pool. A coarse dendritic

microstructure can be observed in the micrograph in **Figure 48**. This could be attributed to the difference in thermal conductivities between argon in the processing chamber (with which the ball is surrounded) and the substrate material surrounding the melt pool. The lower thermal conductivity of argon compared to Al enforces a slower rate of solidification allowing enough time for the microstructure to coarsen.

According to the results presented so far, it can be concluded that there must be limitations on the thickness of the powder layer to be used during SLM. These limitations define both the minimum and maximum values of thickness that are suitable for use. The minimum layer thickness should be high enough that it would ensure building the part cumulatively [54]. The maximum layer thickness requires considering different factors for a suitable decision to be made. First, the thickness should not be larger than the value that would lead to diminishing of the remelted depth to guarantee consolidation of each layer to its preceding and promote vertical overlap and metallurgical bonding. Second, the characteristic shape of the melt pool in case of Al was found to be conical rather than spherical. This means that the layer thickness is crucial in terms of the horizontal overlap between the scan tracks into a layer whilst processing. This implies that the use of a large layer thickness will lead to lack of overlap between the scan tracks towards the bottom of the layer resulting in porosity. Third, when using excessively large layer thicknesses, several defects develop in the track formed such as balling, discontinuity, irregularity, and lack of bonding. Also, while designing the SLM process and selecting a layer thickness, the material's shrinkage upon solidification has to be considered [24].

### **4.3.3. Distinction between balling and satellites**

Balling and satellites are surface defects, among others, that are commonly reported with SLM [1]. The distinction between balling and satellites is important at this point of discussion. The micrograph in **Figure 51** demonstrates the difference between balling and satellites from a topographical perspective. The presence of both defects on the surface of a layer affects the process-ability of the following layers negatively. Improper melting of satellites or laser spatter by the following scans will lead to inclusions in the parts. The term balling is used to refer to the formation of a large ball of material, with a fraction of this ball fully incorporated in the processed layer, i.e. the powder was molten and then solidified in the form of a ball. This means that a ball is not a distinct entity on the surface but rather a form in which the surface solidified, as demonstrated in the cross-sectioned layer in **Figure 52**. Balling is scan speed dependent and is formed due to instability promoted by high scan speeds and the material's surface tension when using large powder layer thicknesses. Surface tension plays an important role in the crystal growth and porosity formation of a metal during solidification [144]. At high temperatures when the metal is in the molten state, its surface tension stays constant but as soon as solidification starts, the surface tension of the material increases [145] so balling occurs.

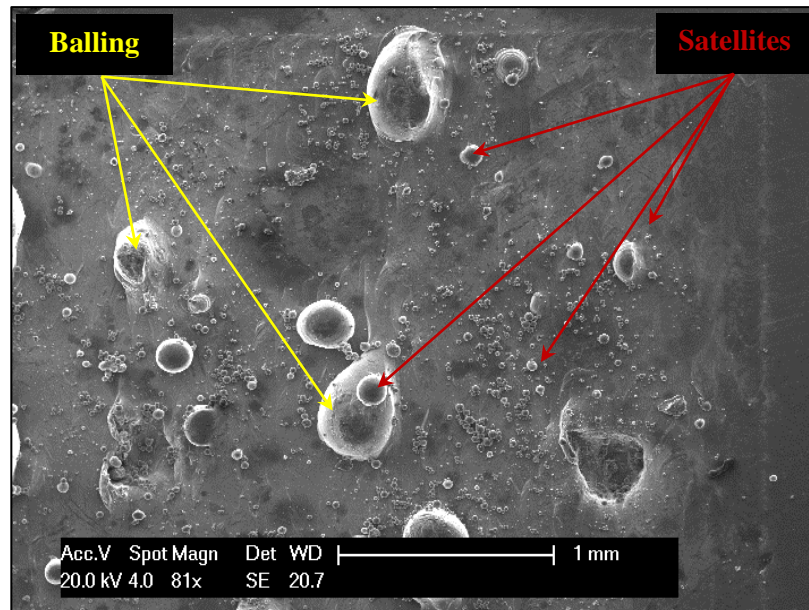


**Figure 51: Topography of a 400  $\mu\text{m}$  thick single layer of selective laser melted AlSi10Mg using 750 mm/s scan speed and 50  $\mu\text{m}$  hatch spacing.**

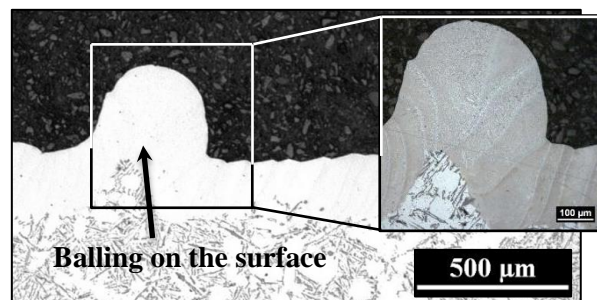


**Figure 52: Cross-sectional view of a polished single layer with balling on the surface with the inset showing the balling region after etching.**

A satellite on the other hand, as defined by Yadroitsev *et al.* [70], is a particle sticking to the surface of the processed material having contact with the scan track. It is formed by spattering or partial re-melting of the powders in the peripheral zone of the laser spot [70]. A satellite could be fresh powder or laser spatter [82] ejected during processing. A satellite that was spotted on the track processed using 250 mm/s was cross-sectioned, polished, etched and imaged using optical microscopy and can be seen in **Figure 53 (a)**. The satellite had a coarser microstructure compared to the SLM material in the scan track/melt

pool (**Figure 53 (b)**). The microstructure of the satellite was similar to the as-received (fresh) powders (**Figure 53 (c)**). The rate of solidification during fabricating the powder produces a solid solution of relatively coarse Si particles or dendrites segregated at the grain boundaries of the  $\alpha$ -Al (**Figure 53 (c)**). Although the SLM material also solidifies at a fast rate, its microstructure is significantly finer than that of the as-received powder. The different microstructure of the satellite compared to the scan track suggests that satellites are formed by the spatter of particles on the single track towards the end of its solidification with less energy transferred to the particle; not enough to melt it and incorporate it into the melt pool. Spatter of material during SLM occurs due to laser-material interaction and could have drastic effects on the processability. Satellites promote the creation of pores and worsen the surface roughness [70].

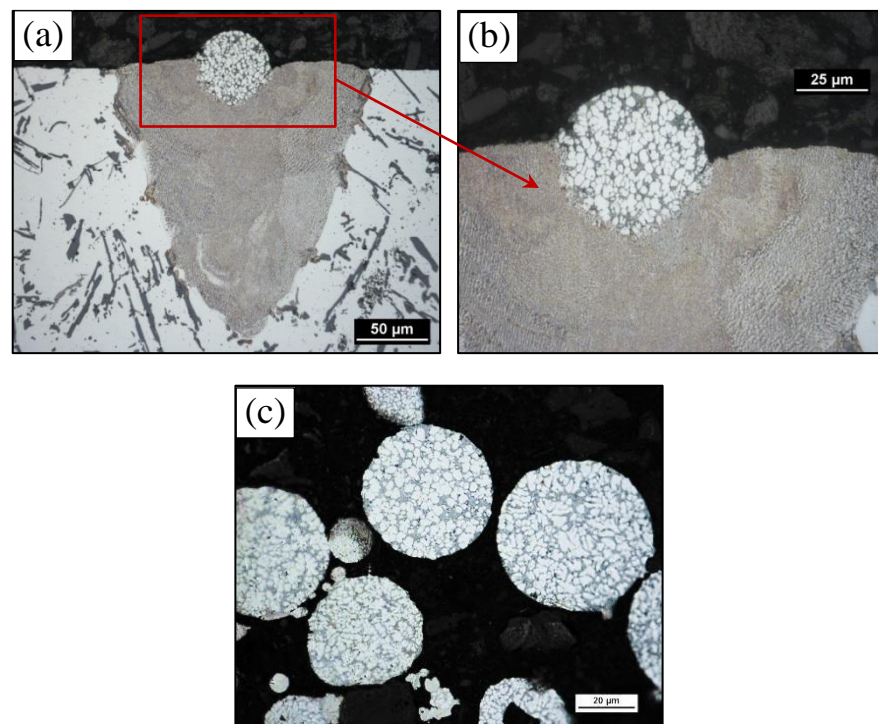


**Figure 53:** A satellite on top of a single track processed from a 40  $\mu\text{m}$  thick powder layer using 250 mm/s (a) low and (b) high magnification, and (c) showing cross-sectioned as-received powder.

## 4.4. Single layers

### 4.4.1. Single layer topography

Similar to the fusion lines, the 50  $\mu\text{m}$  hatch spacing yielded a layer with adequate overlap between each two neighbouring tracks using a 40  $\mu\text{m}$  thick powder layer at all examined scan speeds (250 mm/s, 500 mm/s, and 750 mm/s), as can be seen in **Figure 54**, **Figure 55**, and **Figure 56**, respectively. This is in agreement with the widths of the corresponding scan tracks at these speeds (**Figure 44** and **Table 8**). The amount of overlap was sufficient to provide a consolidated layer with no gaps seen on the top surface. Discoloration of the surface of the layer formed using the slowest speed (250 mm/s) was observed that decreased with increasing the scan speed. The chevron pattern in which each scan track in the layer solidifies can be observed on the top surface of the layers in **Figure 54**, **Figure 55**, and **Figure 56** with alternating directions due to using the meander scan strategy.

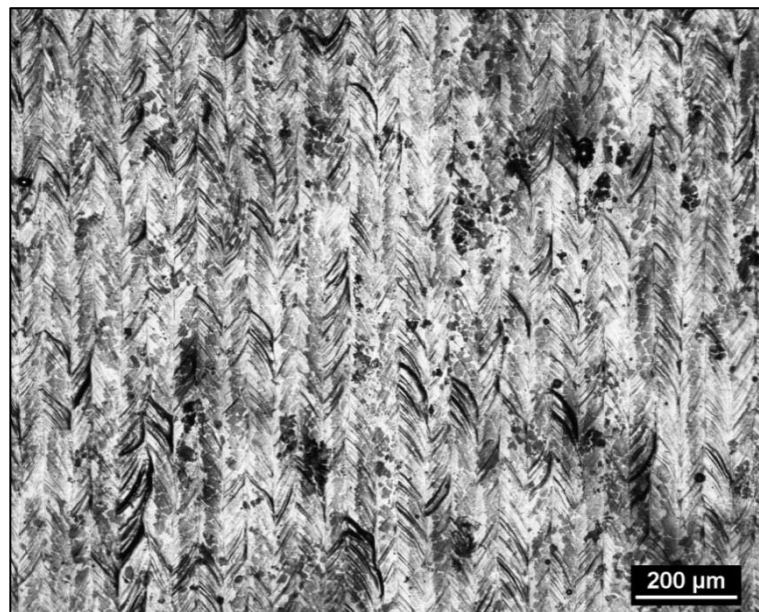


**Figure 54: Topography of a 40  $\mu\text{m}$  thick single layer of selective laser melted AlSi10Mg using 250 mm/s scan speed and 50  $\mu\text{m}$  hatch spacing.**

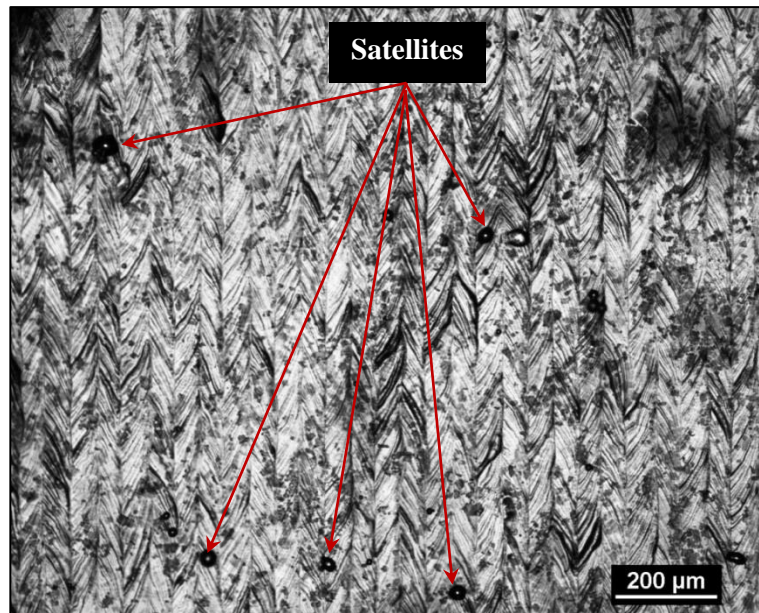


Figure 55: Topography of a 40  $\mu\text{m}$  thick single layer of selective laser melted AlSi10Mg using 500 mm/s scan speed and 50  $\mu\text{m}$  hatch spacing with arrows pointing to small satellites.

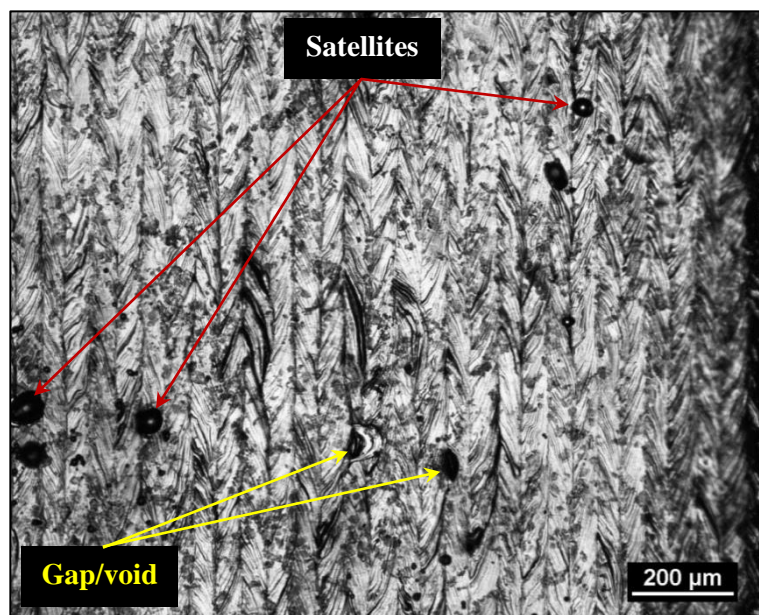


Figure 56: Topography of a 40  $\mu\text{m}$  thick single layer of selective laser melted AlSi10Mg using 750 mm/s scan speed and 50  $\mu\text{m}$  hatch spacing with arrows pointing to larger satellites and gaps or voids in the layer.

Minimal satellites were seen on top of the layer processed using 250 mm/s. More satellites started to show as the scan speed was increased to 500 mm/s

and 750 mm/s. It is quite noticeable that the maximum size of a satellite was larger with the higher scan speed. This might be because the turbulence within the melt pool at higher scan speeds is more vigorous due to higher instability [146] ejecting more spatter that is deposited in the vicinity of the melt pool, i.e. a nearby region of the layer being processed or even on top of the melt pool. As the spatter increases, the probability of the presence of satellites increases. Moreover, for the investigated parameters, balling on the surface did not occur for a single layer. However, this cannot guarantee no balling when processing a bulk sample with these parameters since balling could occur as further layers accumulate. Surface quality worsening with layer progression has been previously reported for 316L stainless steel [99].

In addition to the presence of balling and satellites at the highest scan speed (750 mm/s), evidence of surface porosity or gaps was observed on this layer as well. This is justified by the presence of irregularities along the length of the scan track processed using this high speed that could lead to lack of overlap at some regions while processing. Gaps formed between scan tracks in a layer are most likely to progress with following layers and span over a few of them. This means that a void or a large pore will be developed. Porosity in SLM parts must be avoided because it limits the opportunities for the process to be used in structural and load bearing applications.

Both balling and satellites were heavily existent on the surface of the layers formed using a 400  $\mu\text{m}$  thick powder layer, which was expected due to the poor quality of their corresponding single tracks. These defects are shown in the scanning electron micrographs in **Figure 57**, **Figure 58**, and **Figure 59**.

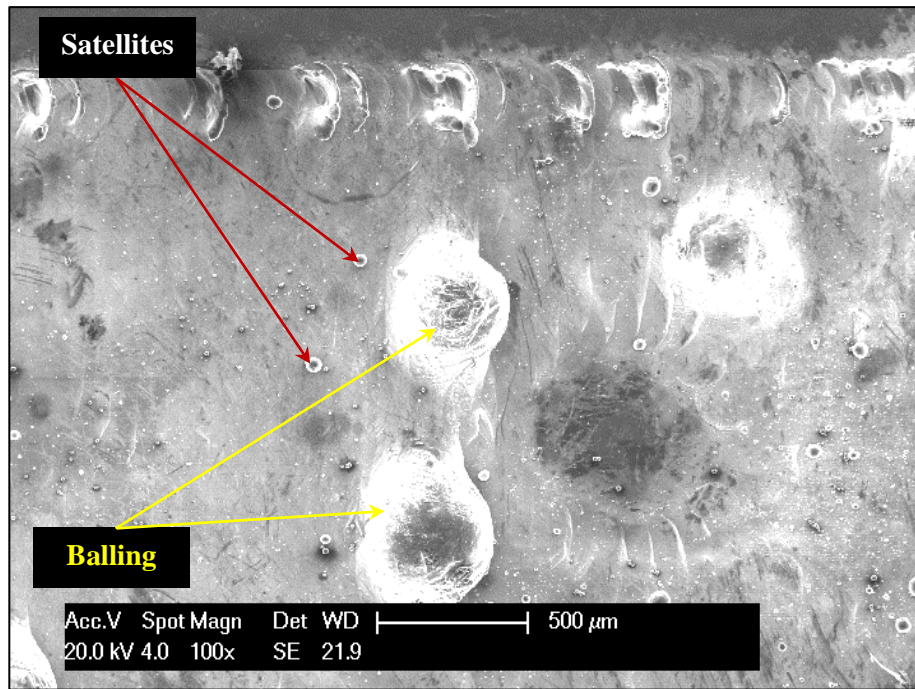


Figure 57: Topography of a 400  $\mu\text{m}$  thick single layer of selective laser melted AlSi10Mg using 250 mm/s scan speed and 50  $\mu\text{m}$  hatch spacing.

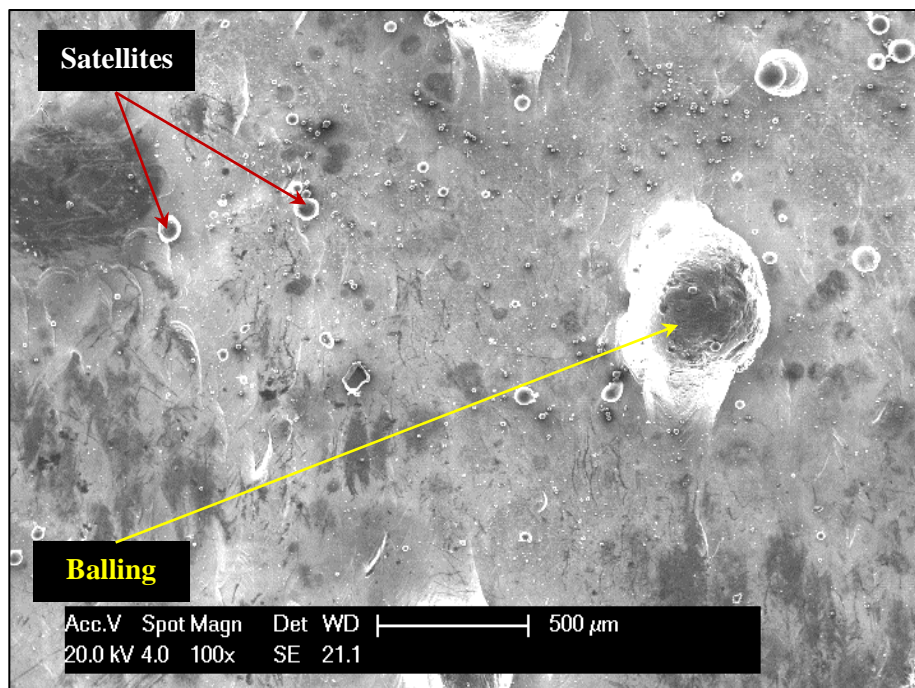
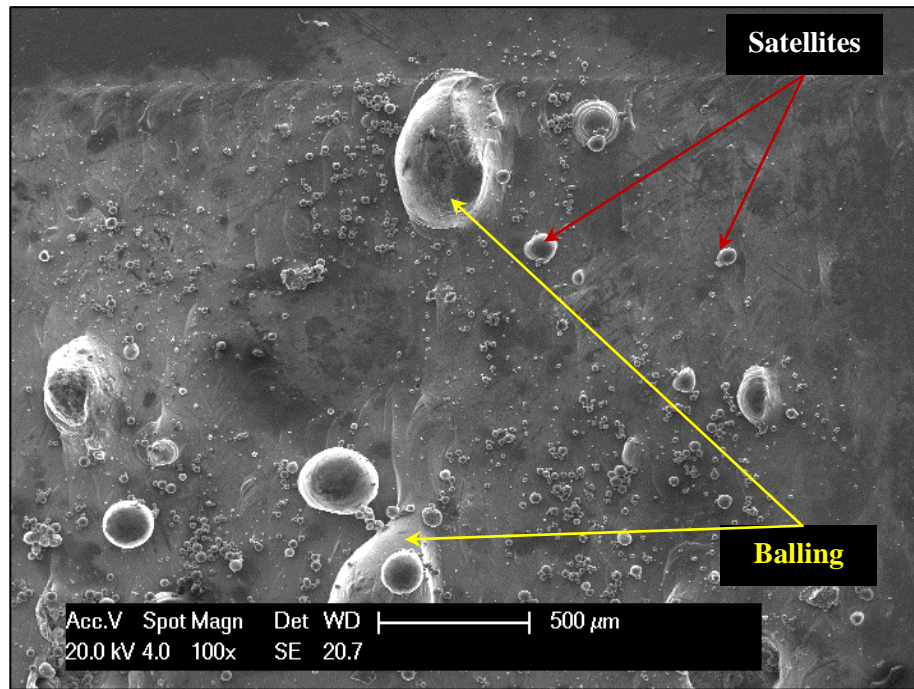


Figure 58: Topography of a 400  $\mu\text{m}$  thick single layer of selective laser melted AlSi10Mg using 500 mm/s scan speed and 50  $\mu\text{m}$  hatch spacing.



**Figure 59:** Topography of a 400  $\mu\text{m}$  thick single layer of selective laser melted AlSi10Mg using 750 mm/s scan speed and 50  $\mu\text{m}$  hatch spacing.

#### 4.4.2. Single layer cross-sections

The cross-sectional views of the layers at a range of scan speeds were considerably similar in terms of being sufficiently overlapping, thus returning consolidated layers. Examples for the cross-sections of the layers processed from 40  $\mu\text{m}$  thick layers of powder are shown in **Figure 60**. Observations of the height of the tracks building up the layer with respect to the substrate, considering the substrate surface as the datum, showed that the first few tracks were always relatively higher than the following ones, i.e. the first track is higher than the second and so on. A similar phenomenon has been previously reported by Yadroitsev *et al.* [100] for stainless steel grade 904 and Pupo *et al.* [92] for CoCrMo. This is attributed to the substrate denudation due to the difference between the absorptivity of the metal powder (current scan track) and the remelted material (previous scan track) that changes the melt volume.

The drawback of such surface morphology is that it can lead to internal porosity when producing multi-layered samples [100] by hindering the proper deposition of a uniform layers of powder, particularly if the same scan pattern is repeated for all layers. Moreover, it can negatively affect adhering to the accuracy of the dimensions required for the final part when producing a bulk sample, i.e. the surface of the bulk sample will be inclined if this behaviour persists. Altering the scan pattern can even out the defected surface morphology per layer and improve the quality.

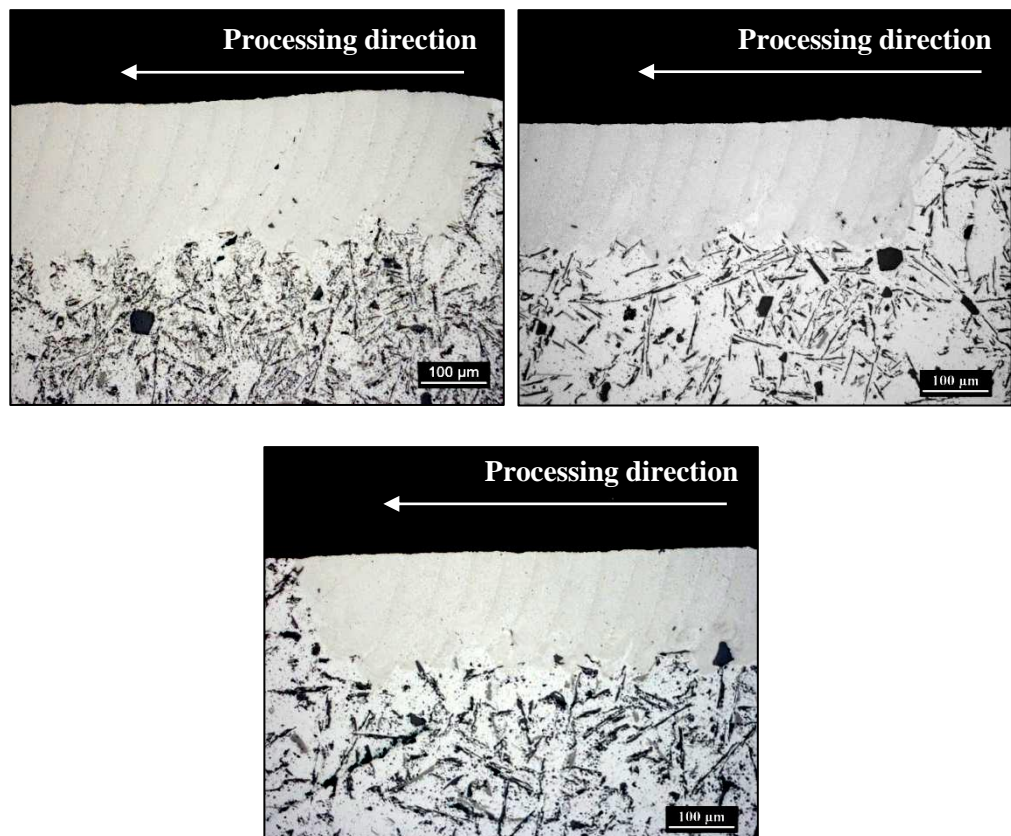


**Figure 60:** A single layer of 40  $\mu\text{m}$  thick selective laser melted AlSi10Mg formed using a hatch spacing of 50  $\mu\text{m}$  and a scan speed of (a) 250 mm/s, (b) 500 mm/s, and (c) 750 mm/s.

The same observation regarding the decrease in the height of the scan tracks after the first few tracks was made for the layers processed from a 400  $\mu\text{m}$  thick powder layer, as can be seen in **Figure 61**. The difference in track height

is even more magnified in case of using the larger layer thickness, as demonstrated in **Figure 61** for the layer processed at a scan speed of 250 mm/s. The height of the layer is significantly consistent in its ending and mid-sections. This layer was cross-sectioned at the location where balling was observed (**Figure 61**) showing how the balling region has the same structure as the layer. In other words, there is no distinction between the ball and the layer unlike the cross-section in **Figure 53** that showed the laser irradiated material and the satellite as separate entities with different microstructures.

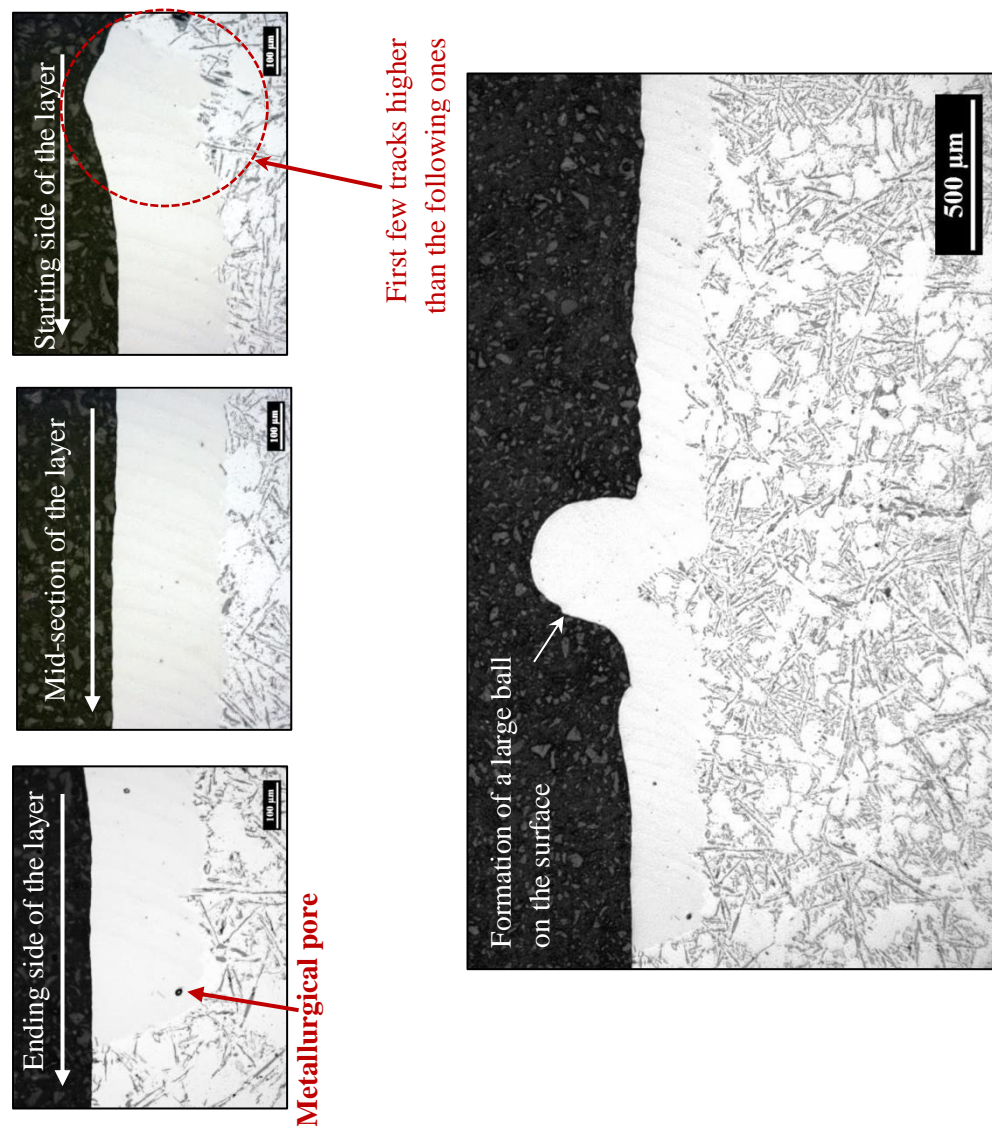


**Figure 61:** A 400  $\mu\text{m}$  thick single layer of selective laser melted AISi10Mg (250 mm/s scan speed and 50  $\mu\text{m}$  hatch spacing).

It is noticeable that the layer processed at 250 mm/s, the slowest investigated scan speed, had a considerably smooth or flat surface. On the contrary, the layers processed at the higher scan speeds, 500 mm/s and 750 mm/s, had irregular rough surfaces incorporating peaks and valleys (see **Figure 62**). The number and size of balls formed on top of the high scan speed layers increased significantly. The regions incorporating balling were high enough to significantly alleviate the penetration of the laser beam to the substrate material as well as diminishing it totally at some points. Generally, the results from processing 400 µm thick layers of powders into tracks or layers prove that it is not feasible to use layer thicknesses above the limitations that would yield a consolidated layer.

Laser beam welding is usually used as a reference to understand the behaviour of the material irradiated by laser in SLM. The particular alloy considered in this study (AlSi10Mg) has good weldability since it is not as susceptible to cracking during welding due to the presence of Si and Mg within the allowable limits. If the amount of  $Mg_2Si$  exceeds 1wt %, the alloy becomes susceptible to cracking [147] in welding. Thus this alloy did not suffer cracking during SLM. It has also been reported for laser welding of Al alloys, by Braun [147], that the presence of Mg promotes the formation of metallurgical pores and its increase leads to more metallurgical pores. It is important to note that porosity was not at all observed in all the tracks and layers formed in this study except for very few metallurgical (spherical) pores across a 5 mm layer. For example, a few metallurgical pores in the layer processed at 250 mm/s are shown in **Figure 61**. A metallurgical pore is a small spherical pore that is primarily formed due to

entrapment of gases within the melt pool that was not allowed enough time to escape. This could be attributed to the high volatility of Mg.

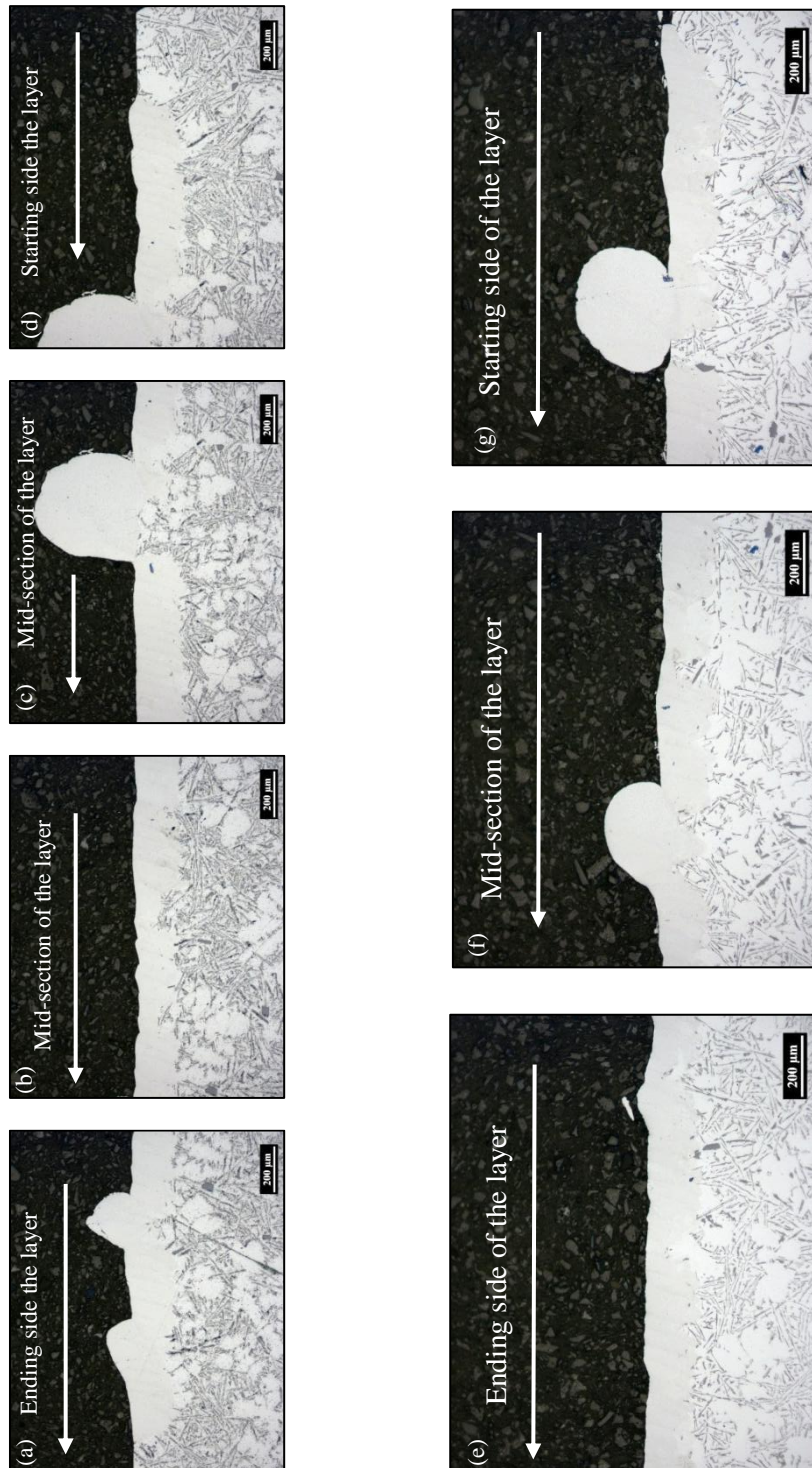


Figure 62: Single layers of selective laser melted AlSi10Mg (a-d: 500 mm/s) and (e-g: 750 mm/s) using 50 μm hatch spacing and 400 μm layer thickness.

Further discussion of this issue will be presented in chapter (5). This indicates that pores created in SLM parts from AlSi10Mg, especially the irregularly shaped ones, are developed with layer progression, i.e. re-melting and re-solidifying of the layers as well as their overlap in the vertical direction (parallel to the build direction). This issue will be further investigated in the chapter (5) dealing with processing near fully dense bulk parts from AlSi10Mg powder using SLM.

#### **4.5. Summary**

This chapter has contributed to available research on single tracks made by SLM in various aspects. The work available in the literature does not provide sufficient attention to single tracks from Al alloys, except for few works, such as the paper by Kempen et al. (2011). The work in the literature focussed mainly on stainless steels. The response of the material to being irradiated by a laser beam varies according to the physical properties of the target material and so results from investigation on one material cannot be generalised for all materials. So the literature lacked information on the melting and solidification response of Al alloys to laser irradiation in SLM. Based on the results from this chapter, the following is concluded:

- The speed with which the laser beam scans the metal powder during SLM along with the properties of the target material control the shape of the melt pool as they define its width and depth. In case of AlSi10Mg, increasing the scan speed, meaning less exposure time, led to less amount of molten material. Therefore, the width and depth of a melt pool decreased with increasing the scan speed.

- The conical shape of the melt pool in case of Al alloys requires a small hatch spacing when developing a layer to ensure sufficient overlap between the adjacent scan tracks. The sufficient overlap is required to avoid the formation of gaps at the base of the melt pools that induce porosity [21, 99]. Based on the conducted experiments, a 50  $\mu\text{m}$  hatch spacing was found to meet this criterion. Although increasing the hatch spacing means faster fabrication, it cannot be overlooked that larger hatch spacings impose the use of smaller layer thickness which will add to the manufacturing time [99]. In other words, a large hatch spacing means having to slice the part into layers of smaller thickness to ensure sufficient consolidation and this will increase the auxiliary time of processing; the time needed for platform lowering and powder spreading. Whereas using small hatch spacing means slower scanning, increasing the primary time of processing.
- The shape of the melt pool is governed by the mode of melting; keyhole mode melting dominated the melting and solidification behaviour. The mode of melting adopted is dictated by the physical properties of the target material, AlSi10Mg, that influence the laser-material interaction. This finding opposes results published in the literature for stainless steel, for instance, that becomes deeper with increasing the scan speed.
- The work on Al single tracks by Kempen et al. (2011) used 170-200 W laser power, whereas the current study limited the laser power to 100 W, which is expected to affect the process window and the range of parameters at which defects form. Yadroitsev et al. (2010) has shown

that the change in laser power can drastically change the form of the stainless steel scan tracks.

- Kempen et al. (2011) focussed on developing the process window for producing a consolidated single track, i.e. processing-focussed. The current study presents novel results in being the first to report on the distinct microstructure of single tracks and layers and its influence on the local mechanical properties.
- The distinction between balling and satellites reported in this chapter, in terms of morphology and microstructure, has not been published to date.
- There are very few publications available on the overlap of single tracks into individual layers. Most studies in the literature focus on the formation of single tracks and multi-layered parts with very little attention to the single layers. This chapter traced porosity in single track and layers and the results contradicted claims [68] that pores form in single tracks.
- Considering the topology of the scan tracks, defects in the form of irregularities were observed as the scan speed increased.
- As for the single layers of AlSi10Mg, they followed the same trend as the tracks regarding the geometrical features and formation of irregularities on the top layer. Increasing the scan speed did not much alter the consolidation of the layer because of using relatively small hatch spacing.
- Increasing the powder layer thickness by 10 fold, aiming at an extreme for a magnified observation of the defects formed, was shown to

introduce several defects in both the tracks and layers such as balling and satellites. Balling and satellites do not only worsen the surface quality of a layer but they promote porosity depressing the overall quality of the part. Although it was possible to develop a layer from the magnified layer thickness, it is not recommended to use larger layer thicknesses in production due to the several defects developed that will not ensure stability with multi-layer processing.

- The height of a layer decreased from one track to its following one. Continuation of this phenomenon with layers progression could affect the quality of the final product and an approach to mitigate could be altering the scan strategy as will be investigated in the coming chapters.
- Cracking was not observed for the laser irradiated Al alloy because the amount of the alloying elements was within the allowable ranges. The single tracks and layers were porosity free suggesting porosity in multi-layered parts to form with layer accumulation. A few metallurgical pores were observed in the single layers processed using the slowest scan speed. Their formation was attributed to the presence of Mg in the alloy with its high volatility.

## **CHAPTER (5): Selective laser melting parametric studies to produce near fully dense parts**

In this chapter, the parameters window required to produce near fully dense parts from AlSi10Mg powder using SLM are investigated. The best combination of parameters in terms of hatch spacing, scan speed, and scan strategy whilst keeping the laser power and layer thickness constant was determined to produce AlSi10Mg parts with minimal porosity. The different types of pores formed during processing were defined. The major microstructural features in the vicinity of pores and the overall grain structure within the melt pools in the near fully dense fabricated SLM parts were investigated. In addition, the evolution in the chemical composition from the powder phase to the bulk phase as well as in the laser spatter was established. The role of powder properties on the processability of an alloy in SLM was also examined since the process requires successive deposition of uniform layers of powder, which is hindered if the powder does not flow well. In this aspect, two batches of AlSi10Mg powder with different specifications were characterized in terms of morphology, composition, size distribution, flowability, and apparent density. Bulk samples were created from the powders and the relative densities were compared. This chapter also reports a successful approach to avoid defects and porosity induced by powder quality. This approach could pave the way for successfully overcoming poor quality powder effects. Lastly, the effect of gas flow rate within the processing chamber on the

relative density of the produced components was investigated in order to question inter-build variability. The variation in the amount of laser spatter formed and ejected was monitored and related to the density.

### **5.1. Powder characterisation**

The particle size distribution of the LPW AlSi10Mg powder in **Figure 63** shows that the size distribution is slightly positively skewed. The particle size range as advised by the supplier is 20-63  $\mu\text{m}$  but the experimentally determined particle size distribution verified the presence of particles outside this range and mainly larger. However, this result could be influenced by the orientation of the particle during data collection if its morphology is not spherical. The morphology of the particles was irregularly shaped and elongated rather than being spherical, as can be seen in **Figure 63**. This morphology is expected to negatively affect the process of SLM since it is favoured neither for efficient powder packing density nor for flowability. Hence, the deposition of a uniform layer of powder would be poor. Also, the skewed particle size distribution could be attributed to this morphology. The chemical composition of the alloy (see **Table 9**) was within the standard range [148]. The cross-sectioned particles showed evidence of inherent porosity in the powder annotated by arrows in **Figure 64**, which suggests the presence of trapped gases that might contribute to porosity in the bulk samples to be produced [71]. The internal microstructure of the AlSi10Mg powder was revealed in the cross-sections in **Figure 65** as cellular-dendritic.

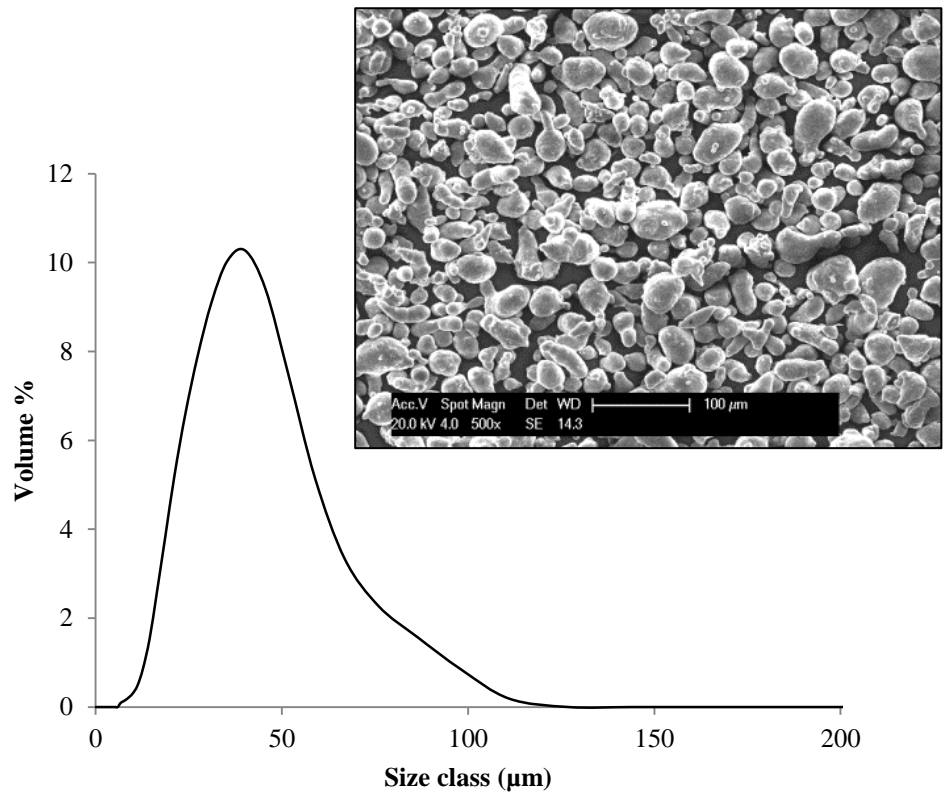


Figure 63: Particle size distribution of AlSi10Mg powder supplied by LPW technology with the inset showing the morphology of the powder.

Table 9: Chemical composition of LPW AlSi10Mg powders in relative weight%.

Supplier	Mg	Si	Al
LPW	0.48	10.67	88.85
Standard [148]	0.2-0.45	9.0-11.0	Balance

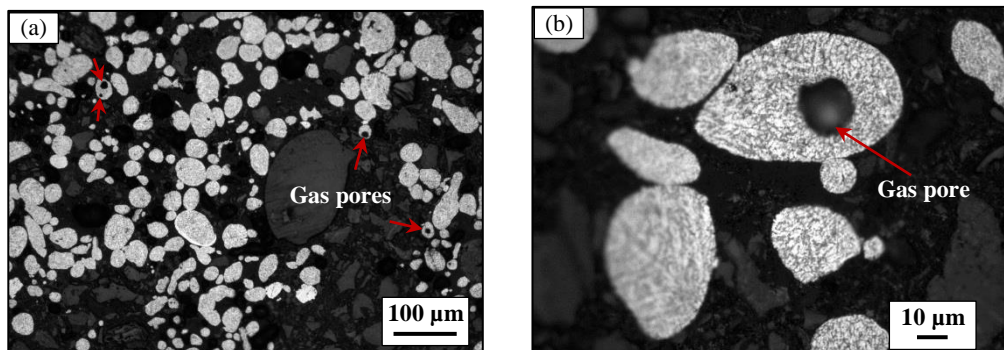
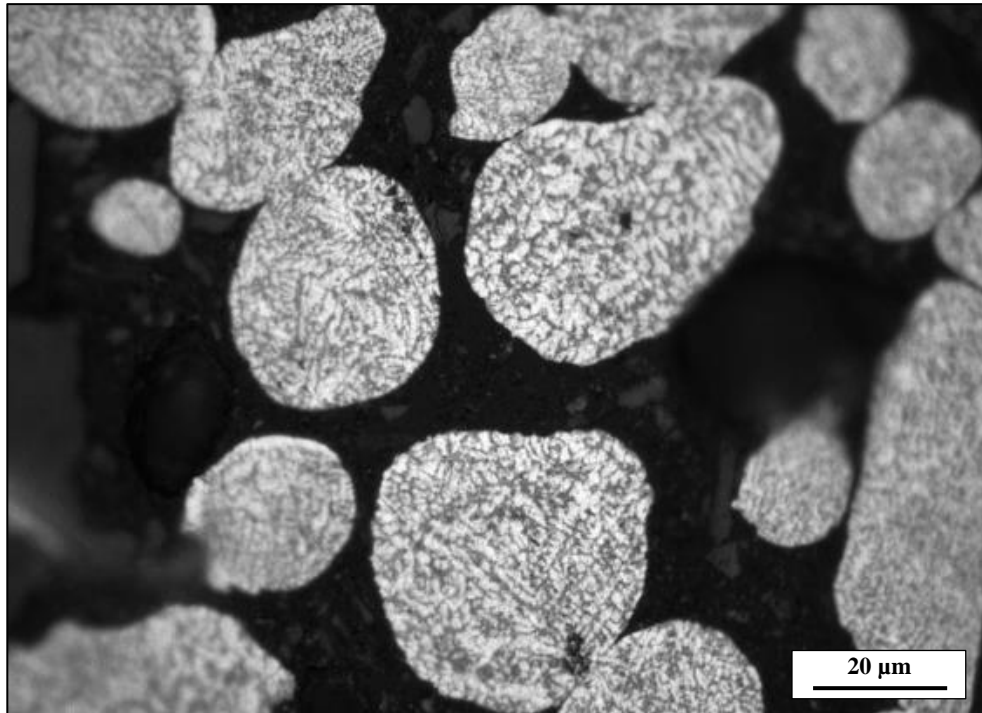


Figure 64: Cross-sectioned AlSi10Mg powder supplied by LPW Technology showing evidence of inherent porosity at (a) low and (b) high magnification.



**Figure 65: Cellular-dendritic microstructure in the cross-sectioned AlSi10Mg powder.**

## **5.2. Hatch spacing study**

At the smallest hatch spacings (50 and 100  $\mu\text{m}$ ), the surface of the test cubes was observed to be fully consolidated despite the poor surface quality in terms of surface morphology (see **Figure 66**). When the hatch spacing was increased to reach 150  $\mu\text{m}$ , gaps started to form between adjacent scan tracks, as seen in the surface topography micrographs of the test cubes, i.e. the uppermost layer of the sample, as demonstrated in the high magnification SEM images in **Figure 67**. Further increase in the hatch spacing beyond 150  $\mu\text{m}$  has led to the development of more gaps.

Excessive balling was observed on the surface of all processed samples at this stage although these parameters did not show balling when creating a single track or single layer as was shown in chapter (4). This indicates that balling can

form during layer accumulation. The balling phenomenon will be further discussed in the following section covering the scan speed study.

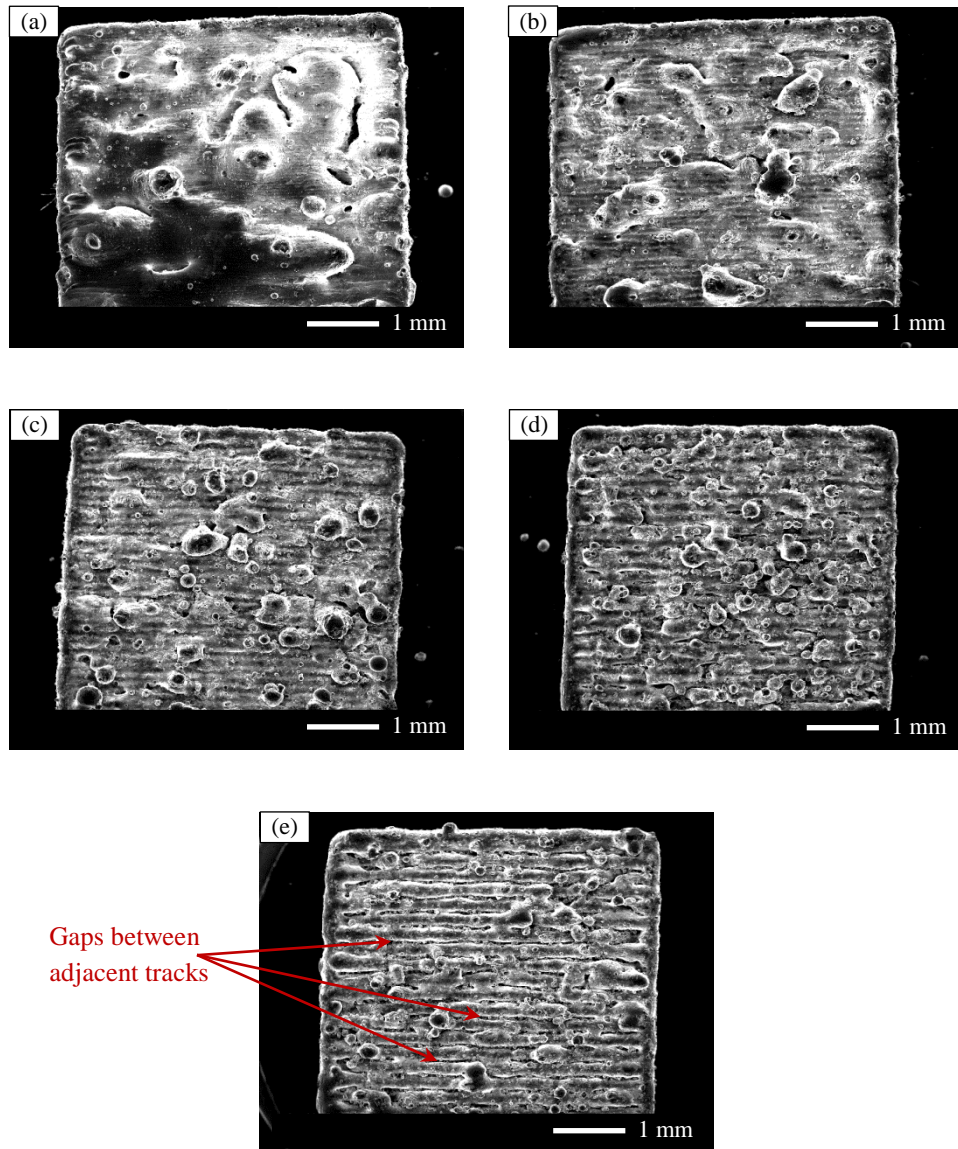


**Figure 66:** Low magnification images for the surface topography of AlSi10Mg test cubes produced by SLM using different hatch spacing values (a) 50  $\mu\text{m}$ , (b) 100  $\mu\text{m}$ , (c) 150  $\mu\text{m}$ , (d) 200  $\mu\text{m}$ , and (e) 250  $\mu\text{m}$ .

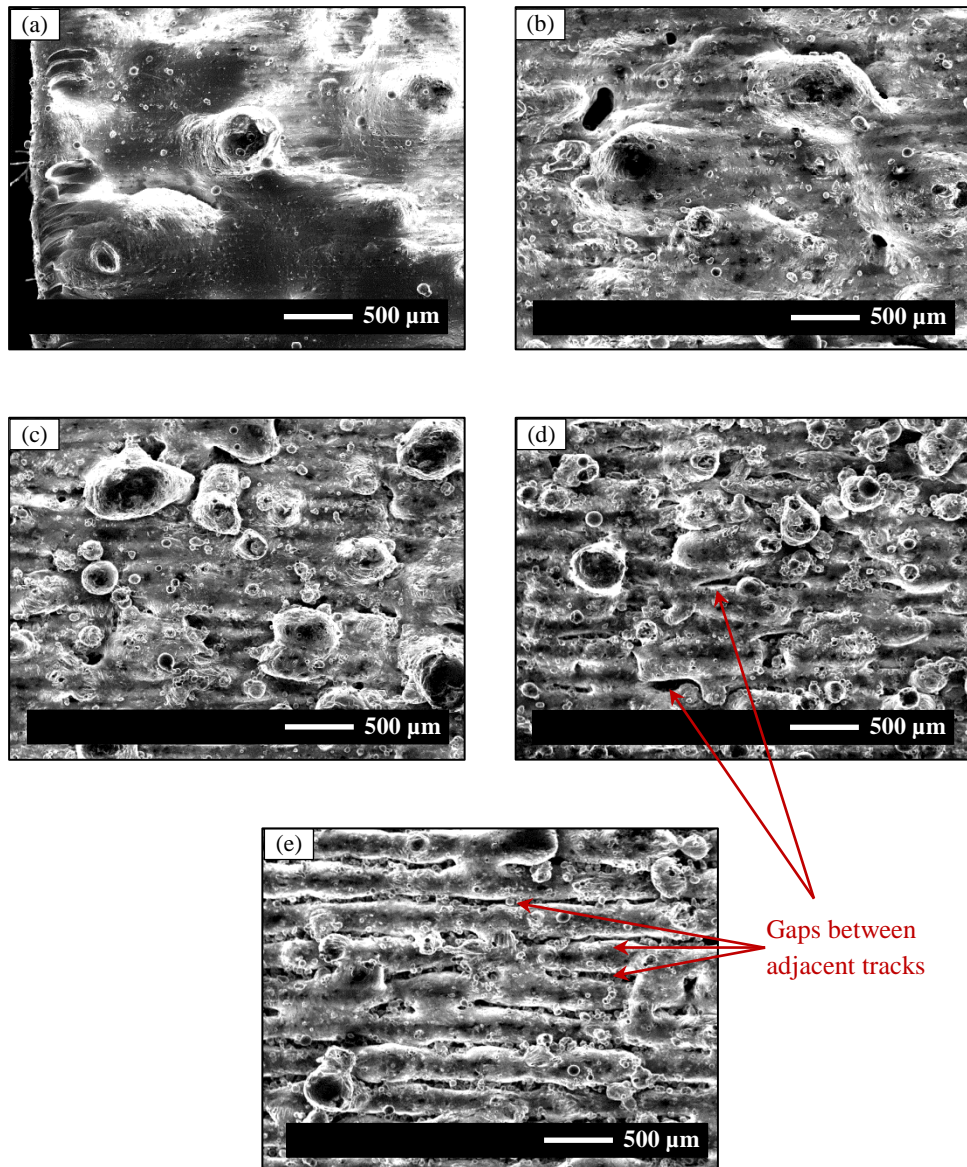
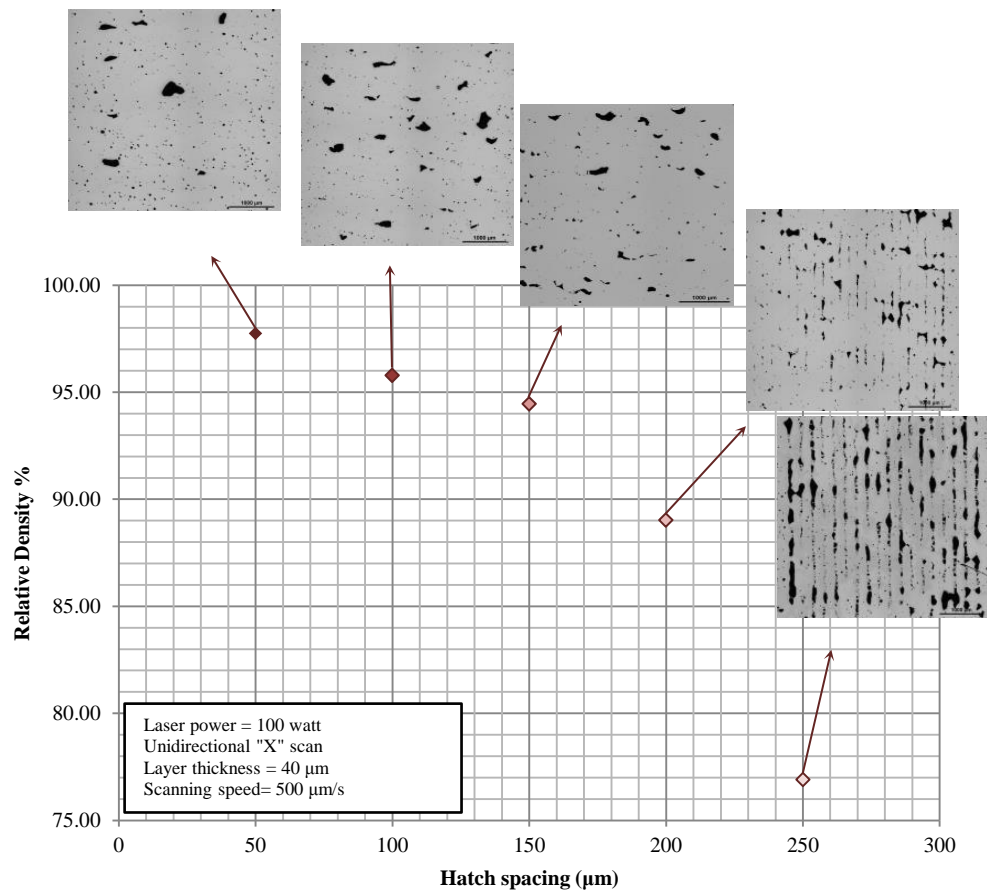


Figure 67: High magnification images for the surface topography of AlSi10Mg test cubes produced by SLM using different hatch spacing values (a) 50 μm, (b) 100 μm, (c) 150 μm, (d) 200 μm, and (e) 250 μm.

The subsequent increase in porosity with increasing the hatch spacing is demonstrated in **Figure 68**, along with the insets showing the optical micrographs that demonstrate the increase in the fraction of pores and gaps created with the hatch spacing increase, as seen in the polished samples and in cross-sections. The relative density represents the area fraction not including pores. These gaps act as pockets of non-molten powder that was removed

during grinding and polishing (sample preparation). These gaps are formed due to lack of overlap between the scan tracks [21], as has been established from the single tracks study in chapter (4).



**Figure 68: Effect of changing the hatch spacing on the relative density represented by the pore area fraction on micrographs determined using ImageJ.**

As the hatch spacing increases, the intra-layer overlap diminishes and the part is held together mainly through interlayer bonding. Although building with a large hatch spacing is a means for faster fabrication, it should be noted that a larger hatch spacing will require smaller layer thicknesses to ensure overlap between adjacent melt pools along the melt pool depth given their conical shape shown chapter (4), i.e. the parts will be sliced into extra number of layers, and hence further time is added. Also, heat accumulates within the melt

pool when using a small hatch spacing, which leads to a slightly slower cooling rate for the layer resulting in a more homogeneous and continuous layer [92]. A compromise between the energy density and the speed of fabrication should be pursued [99]. Based on the aforementioned results, it can be concluded that the best overlap was achieved when using hatch spacing values of either 50  $\mu\text{m}$  or 100  $\mu\text{m}$  (the smallest within the investigated range) given that the scan speed is fixed at 500 mm/s. Consequently, these were the values carried forward to the scan speed study.

### 5.3. Scan speed study

The average relative density values for each combination of scan speed and hatch spacing are in **Table 10**. The difference in relative density between using a hatch spacing of 50  $\mu\text{m}$  or 100  $\mu\text{m}$  for the same speed was not significant since both yielded sufficient overlap between the scan tracks, as established earlier in the hatch spacing study.

**Table 10: Relative density values (%) at different combinations of hatch spacing and scan speed.**

Hatch spacing ( $\mu\text{m}$ )	Scan speed (mm/s)			
	250	500	750	1000
50	96 $\pm$ 1	97.7 $\pm$ 0.2	97 $\pm$ 2	97 $\pm$ 2
100	96.3 $\pm$ 0.6	96 $\pm$ 1	97 $\pm$ 1	96 $\pm$ 3

All the samples in this particular study showed porosity between 2 % and 5 % according to the results in **Table 10**. However, meticulous investigation of the samples suggested that porosity values by themselves do not tell the whole story. Porosity could be categorized as metallurgical pores and keyhole pores. Metallurgical pores, also known as hydrogen porosity, are spherically shaped and small in size (less than 100  $\mu\text{m}$ ), whereas keyhole pores are irregularly

shaped and large in size (above 100  $\mu\text{m}$ ) [108, 149, 150]. This categorisation is similar to that of pores formed in case of laser welding of Al alloys [150]. It was deduced that metallurgical pores are created at slow scan speeds and this is attributed to gases being trapped within the melt pool or evolving from the powder during consolidation. Keyhole pores arise from keyhole instabilities, which can be attributed to rapid solidification of the metal without complete filling of gaps with molten metal leaving voids and defects [16, 149, 150]. The optical micrographs in **Figure 69** show that metallurgical pores existed in samples built using a scan speed of 250 mm/s but they were reduced significantly with increasing the scan speed up to 1000 mm/s; whereas keyhole pores started to form at a scan speed of 500 mm/s and they further increased with increasing the speed up to 1000 mm/s. Thus two samples could have the same relative density numerically but with different types and causes of the porosity. This indicates how critical it is to evaluate the samples processed by SLM both quantitatively and qualitatively. For example, scan speeds of 250 mm/s and 1000 mm/s both show an amount of porosity in the range of 5%. Nevertheless, the 250 mm/s porosity was made up only of metallurgical pores, whereas in the case of the 1000 mm/s a majority of keyhole pores was observed, as seen in **Figure 69**, in addition to a smaller fraction of metallurgical pores.

The numerous of metallurgical pores at relatively slow scan speeds could also be attributed to the high energy density induced in the material. In order to confirm this hypothesis, extra samples were processed using scan speeds below 250 mm/s employing a hatch spacing of 50  $\mu\text{m}$ , i.e. 100 mm/s, 150 mm/s, and 200 mm/s. Porosity in these samples was found to be made up entirely of only

metallurgical pores with no evidence of keyhole pores in any of them, as can be seen in **Figure 70**; a result that supports the hypothesis.

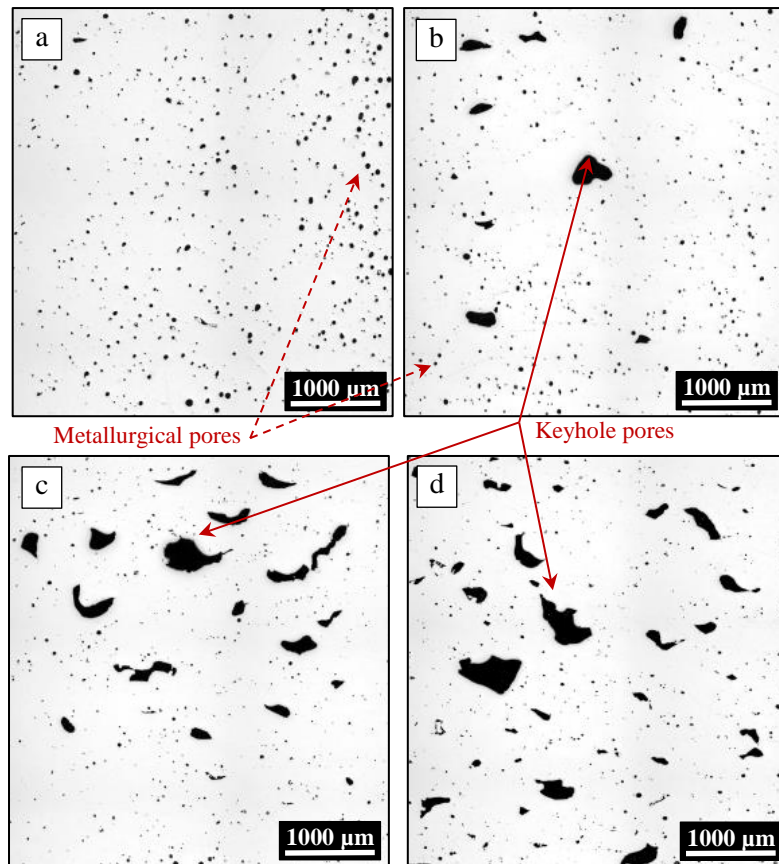


**Figure 69:** Evolution of pores with scan speed (a) 250, (b) 500, (c) 750, and (d) 1000 mm/s.

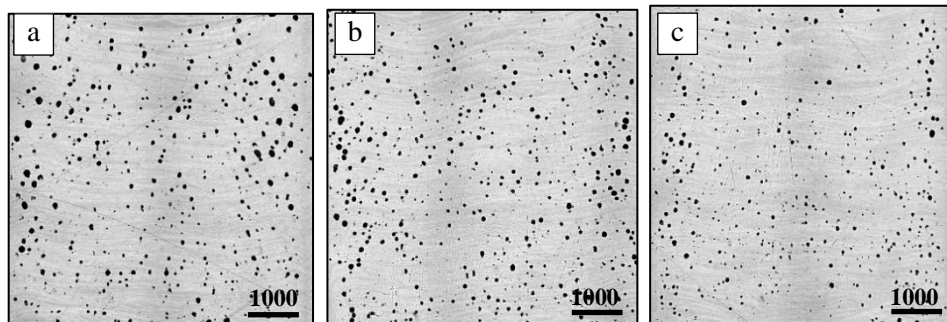


**Figure 70:** Extensive presence of metallurgical pores only at scan speeds below 250 mm/s (a) 100 mm/s, (b) 150 mm/s, and (c) 200 mm/s.

The areal energy density for the process of SLM was calculated in this study using the formula below:

$$ED (J/mm^2) = \frac{P (W)}{HS (mm)*SS(mm/s)} \quad (1)$$

Where **ED** refers to the areal energy density in J/mm<sup>2</sup>, **P** refers to the laser power used in Watt, **HS** is the hatch spacing in mm, and **SS** is the scan speed in mm/s. Usually researchers [54, 91] calculate the volumetric energy density when studying SLM in which the formula considers the layer thickness (LT) in mm to obtain the energy density in J/mm<sup>3</sup>. In this case the formula changes to be:

$$ED (J/mm^3) = \frac{P (W)}{HS (mm)*SS(mm/s)*LT(mm)} \quad (2)$$

In their investigations, Krauss and Zaeh [101] preferred to use the linear energy density over the areal and volumetric energy densities. This could be driven by avoiding to misrepresent the results when using the hatch spacing since the overlap between scan tracks is not accounted for in these cases. This overlap means that certain regions will be remelted more than once in the SLM process. Furthermore, the linear energy density avoids misleading the results by not considering the effect of the change in reflectivity and absorptivity of the material irradiated for the first time and the remelted region. The linear energy density can be calculated using the following formula:

$$ED (J/mm) = \frac{P (W)}{SS(mm/s)} \quad (3)$$

However, in the current study it was decided to use the areal energy density by employing equation (1) instead of using the volumetric energy density. The

problem with using the volumetric energy density in SLM studies from the author's point of view is that considering the layer thickness is not as accurate as the remaining parameters since the credibility of estimating the right value for the layer thickness is questionable for several reasons such as;

- the fact that practically laying down a layer of powder of uniform thickness all across cannot be guaranteed owing to the powder packing density that is influenced by the powder's morphology
- each layer is not melted once only but probably more than once due to the penetration of the energy or its transfer from the currently melting layer to the preceding one(s)

The variation in the degree of porosity (quantitatively) in a sample with the areal energy density used in processing is demonstrated in the plot in **Figure 71**. Although a clear trend cannot be observed from these results, it is worth noting that the relative density cannot be solely interpreted as a function of energy density without considering the type of porosity, as discussed earlier. The parameters combined to deliver this energy density to the material while processing are crucial. For instance, as can be observed in **Figure 71**, an energy density of  $4 \text{ J/mm}^2$  can be achieved by fixing the scan speed to  $500 \text{ mm/s}$  and changing the hatch spacing between  $50 \text{ }\mu\text{m}$  and  $100 \text{ }\mu\text{m}$  and each combination of these two produced parts with different average relative density.

In case of fixing the scan speed and changing the hatch spacing (the hatch spacing study in section 5.2), as the energy density increases the relative density of a part increases until a certain limit after which a plateau is

observed. Below the threshold energy density, there is not enough energy to fully melt the powder [84].

Relating the formation of keyhole pores to the energy density from the results of this study, it could be concluded that for energy densities less than  $4 \text{ J/mm}^2$  (based on  $P = 100\text{W}$ ,  $HS = 0.05 \text{ mm}$ , and  $SS = 500 \text{ mm/s}$ ), keyhole pores are promoted. An increase in energy density leads to diminishing keyhole pores but extensively introduces metallurgical pores.

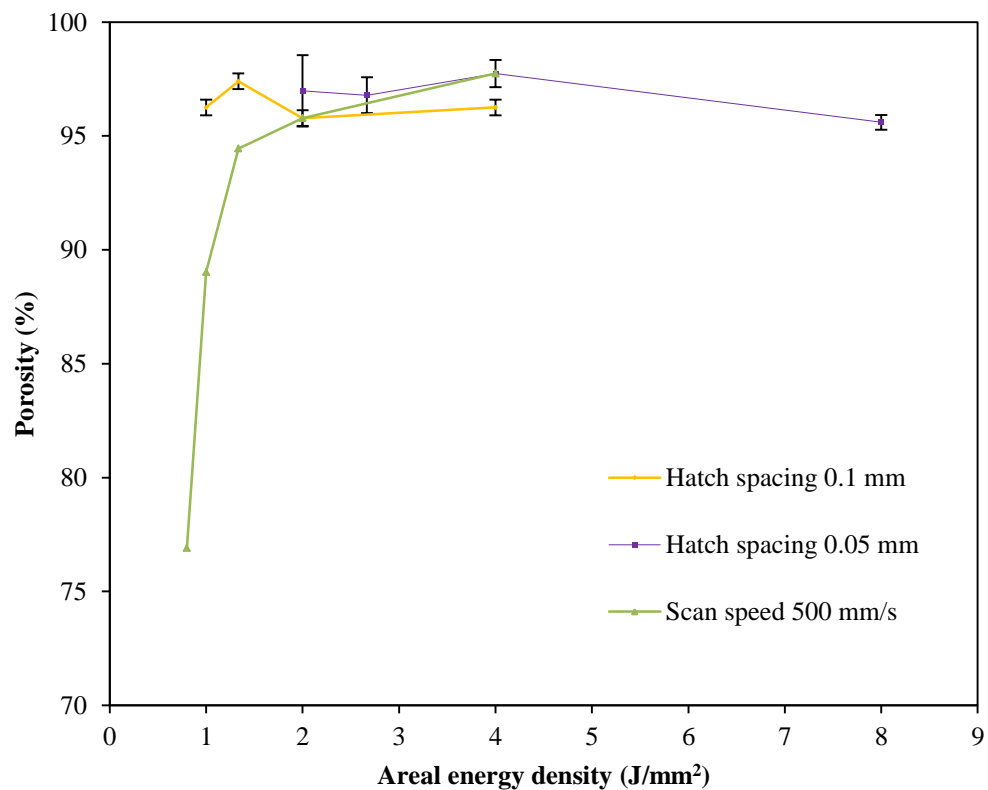


**Figure 71: The influence of energy density variation on a sample's degree of porosity.**

Aside from using the quantitative and qualitative estimation of porosity in SLM AlSi10Mg samples to find the range of scan speeds that would yield dense samples, the morphology of the surface of the test cubes (samples' topography) was also of interest. Not only because they will obstruct the way

of topology optimisation work and make it difficult to adhere to dimensions or surface quality of the produced parts but also because they affect processing. An irregular surface will hinder the deposition of a uniform layer of powder over its surface. In addition, a surface defect, like balling and gaps, will act as a pocket trapping powder inside it or underneath it that might not be melted with the following laser scan. A gap on the surface can also be considered a void, and once a void is formed in a layer it progresses into several subsequent layers creating a larger pore. It was observed that balling occurs on the top surface of the samples with increasing scan speeds from 250 mm/s up to 1000 mm/s, as evident in **Figure 72**. Balling occurs at increased speeds because high speed promotes capillary instability in the molten metal pool leading to the splashing of small liquid droplets on the surface [19, 69]. Also, balling is exacerbated by the use of powder with large particle size [74]. As pointed out by Osakada *et al.* [3], these balls are formed due to non-linear solidification of the metal. Excessive balling results in an irregular surface and hence inhomogeneity in the following layer(s), i.e. various regions having different melting and solidifying behaviours. Balling phenomenon on the surface of each layer processed using SLM must be avoided as it depresses the relative density of the produced part [68].

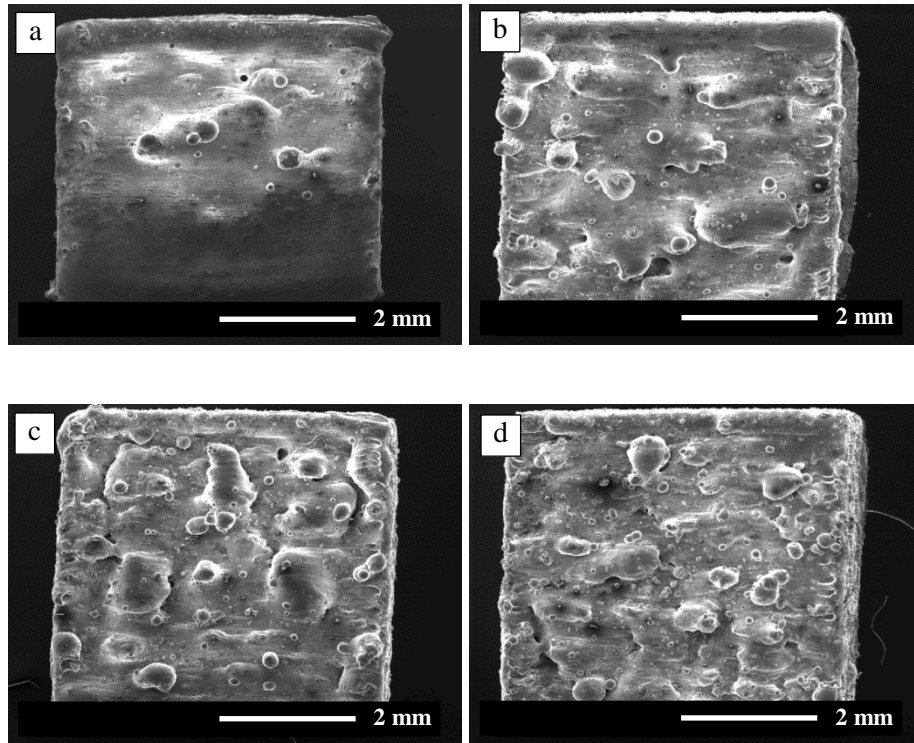


**Figure 72:** Balling increases with the increase in scan speed (a) 250, (b) 500, (c) 750, and (d) 1000 mm/s.

#### 5.4. Scan strategy study

The effect of changing the scan strategy on porosity, in terms of amount fraction or type of pore, can be easily traced in the optical micrographs of the  $5 \times 5 \text{ mm}^2$  cross-sections in **Figure 73**. At a scan speed of 500 mm/s, scanning each layer twice (2X, overlap, X&Y 2HS, or pre-melt) was effective in reducing the keyhole pores (**Figure 73**) but the keyhole pores still existed when scanning the layer once like in the alternating scan (**Figure 73**). In the case of the overlap scan, the keyhole pores were reduced but not eliminated. The double scan per layer, whether in the form of 2X, X&Y 2HS, pre-melt, or overlap significantly reduces (if not eliminates) the keyhole pores at all scan speeds investigated (500, 750, and 1000 mm/s). However, the excessive energy induced per layer as a result of scanning more than once led to the extensive

formation of metallurgical pores at the slower speeds, i.e. the elimination of keyhole pores was at the expense of introducing metallurgical ones. Yet this was not the case when using the pre-melt scan strategy at 500 mm/s, possibly because the first scan was done with a lower laser power (50 W). At 500 mm/s, when using the pre-melt scan strategy the keyhole pores were successfully eliminated without the introduction of metallurgical pores, i.e. this combination of parameters showed the least fraction of both metallurgical and keyhole pores.

At a speed of 750 mm/s, the largest fraction of keyhole pores was observed for samples with the X scan strategy (**Figure 69 (c)**), but they were drastically reduced by changing the scan strategy, as can be seen in **Figure 73**. Unlike the samples produced using a speed of 500 mm/s, the metallurgical pores were not significant with the double scans at this speed (750 mm/s) owing to the lower energy density in this case. Similar observations were evident for the 1000 mm/s scan speed, as seen in **Figure 73**.

The quantified relative density of the various samples, as shown in the bar chart in **Figure 74**, was found to agree with the observations stated above. Starting with a highest average relative density of  $(97.74 \pm 0.09)$  % originally using a 500 mm/s speed with a single unidirectional scan, the scan strategy study has shown that a relative density of  $(99.76 \pm 0.07)$  % was achieved using a double unidirectional scan with different laser powers for each scan (pre-melt strategy) at the same speed. According to Weingarten *et al.* [71], the first scan with reduced power is basically a stage of laser drying of the powder during which hydrogen, in the form of moisture on the surface of the powder, is released reducing the metallurgical pores.

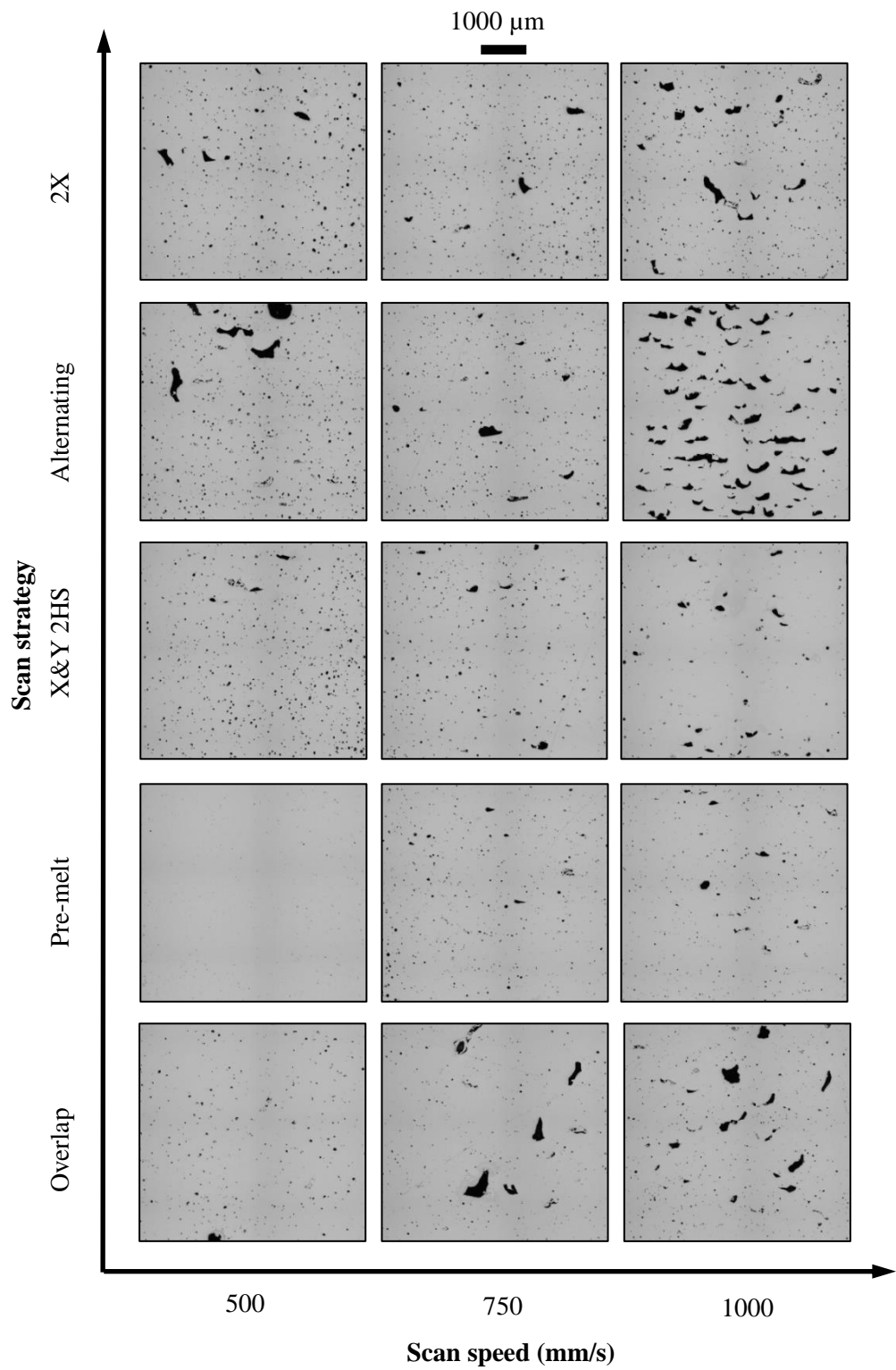
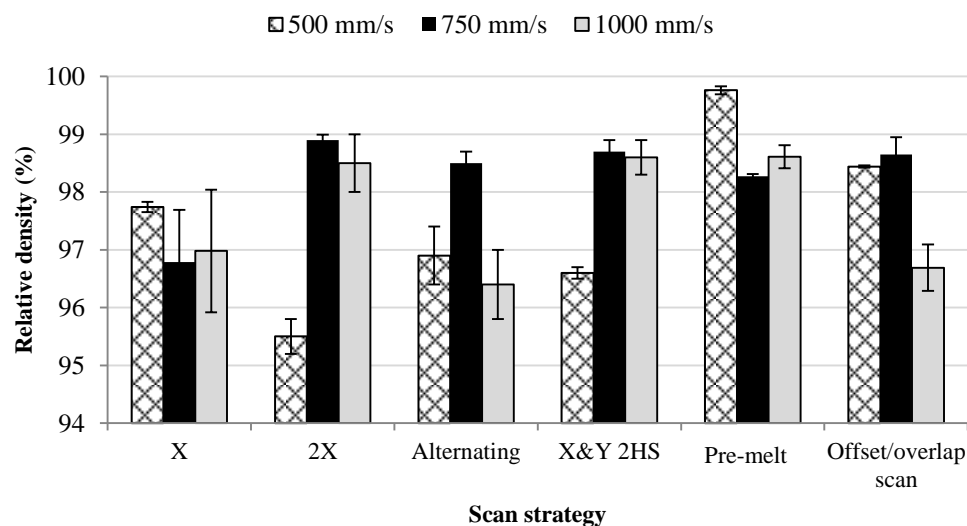


Figure 73: Porosity evolution in samples processed using different combinations of scan speeds and scan strategies.

The significance of understanding the influence of energy density at this stage becomes ambiguous. It is difficult to calculate the energy density when using one of the scan strategies where each layer is scanned more than once because the solid material absorbs less laser energy compared to powder [92, 100]. Whereas the molten pool has higher reflectivity with respect to the solid material [100], so the interaction between the laser beam and the target material is not easily understood since the state at which the second scan finds the material is not known.



**Figure 74: Influence of scan strategy on relative density for each of the scan speeds investigated 500 mm/s, 750 mm/s, and 1000 mm/s.**

### 5.5. Microstructural investigation of melt pools and pores

The cross-sectioned, polished, and etched samples revealed that there are two different forms of grain structures in the defect-free melt pools of the AlSi10Mg samples produced by SLM, as demonstrated in **Figure 75 (a)**. This sample is processed using a 100 W laser power, 50  $\mu\text{m}$  hatch spacing, 500 mm/s scan speed, 40  $\mu\text{m}$  layer thickness, and a single unidirectional scan

strategy. The core of the melt pool is characterised with a fine microstructure of equiaxed grains, whereas moving towards the melt pool boundary, the grains become coarser and elongated rather than equiaxed. This microstructure at the melt pool boundary is due to the longer time this region stays at high temperature since being at the overlap of two adjacent melt pools results in a slower solidification rate.

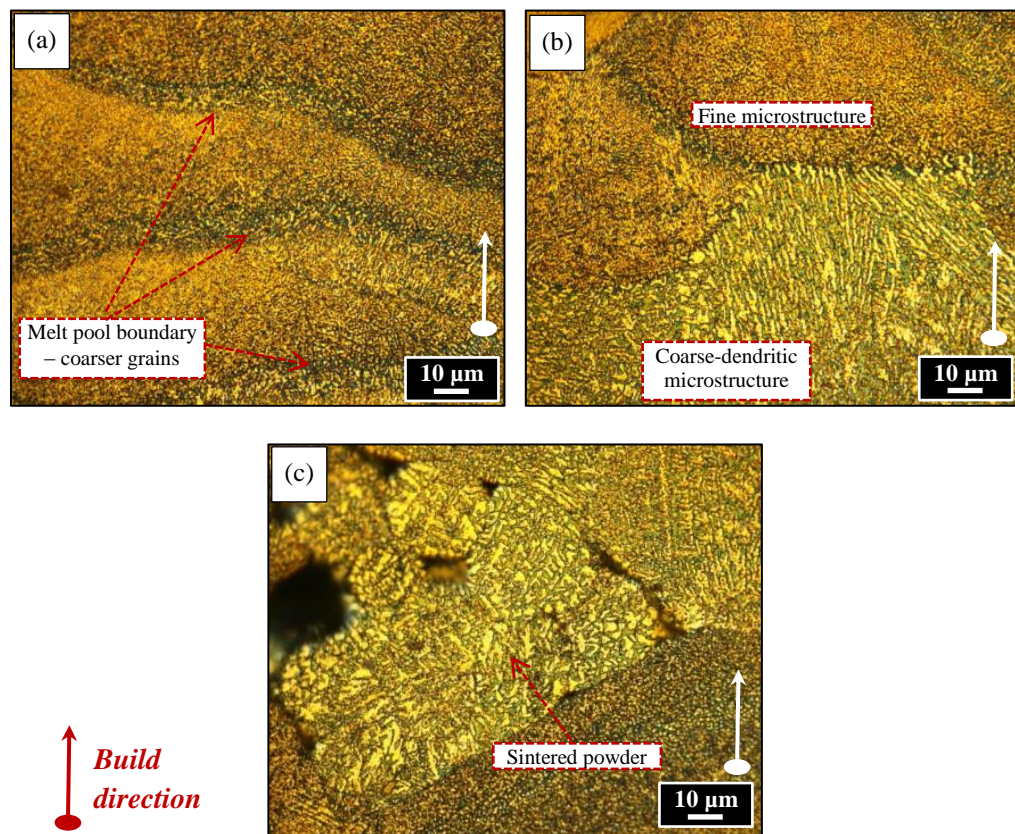


**Figure 75:** Microstructure of etched samples (HS 50  $\mu\text{m}$ , SS 500 mm/s, and unidirectional single scan): (a) adjacent melt pools, (b) vicinity of a keyhole pore where the pore (not shown) is below the coarse microstructure, and (c) keyhole pore enclosing non-molten powders.

Studying the regions containing defects such as keyhole pores; a coarse-dendritic microstructure was observed in the vicinity of keyhole pores (**Figure 75 (b)**). This characteristic microstructure is attributed to the difference between the thermal conductivity of the gas (argon) trapped within the keyhole

pore and that of the solid material, i.e. solidifying AlSi10Mg. Also, the keyhole pores were found to contain powder that was not fully melted and hence complete diffusion of the powder particles did not take place leaving particles as definite entities, i.e. sintered powder, as shown in **Figure 75 (c)**.

Scanning electron microscopy was first used to find supporting or contradicting evidence that the powder trapped inside the keyhole pores is sintered powder. An example of what is trapped inside a keyhole pore is demonstrated in **Figure 76** that is considered supporting evidence that there is non-molten powder inside the keyhole pores. This observation indicates incomplete melting of the particles at these points leading to agglomeration of powder. These defects contribute to depressing the relative density of the part produced.

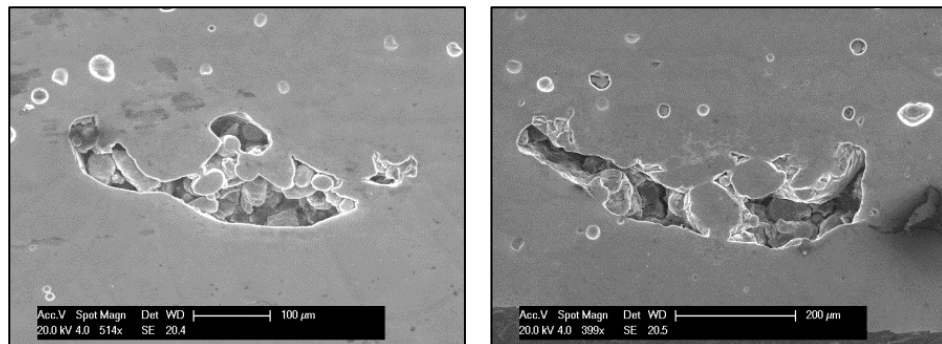


**Figure 76: Keyhole pore enclosing non-molten powders.**

Moreover, the scanning electron microscope was used to study the microstructure of an etched sample to investigate the grain structure. **Figure 77 (a)** shows the orientation of the dendritic cells to be elongated and pointing towards the centre of the melt pool (i.e. the heat source) because of solidification in the direction of the thermal gradient [42]. Also it is illustrated in **Figure 77 (b)** and **(c)** that the melt pool is comprised of regions of fine cellular structure (~500 nm), regions of coarse cellular structure (~650 nm), in

addition to heat affected zones (HAZ), an observation previously reported by Thijs *et al.* [4]. The fine microstructure is at the core of the melt pool since this is the region experiencing the fastest rate of solidification, then coarsening starts to show moving farther from the centre-line, because this represents the overlap region of two neighbouring or adjacent melt pools, until reaching the heat affected zone at the borders.

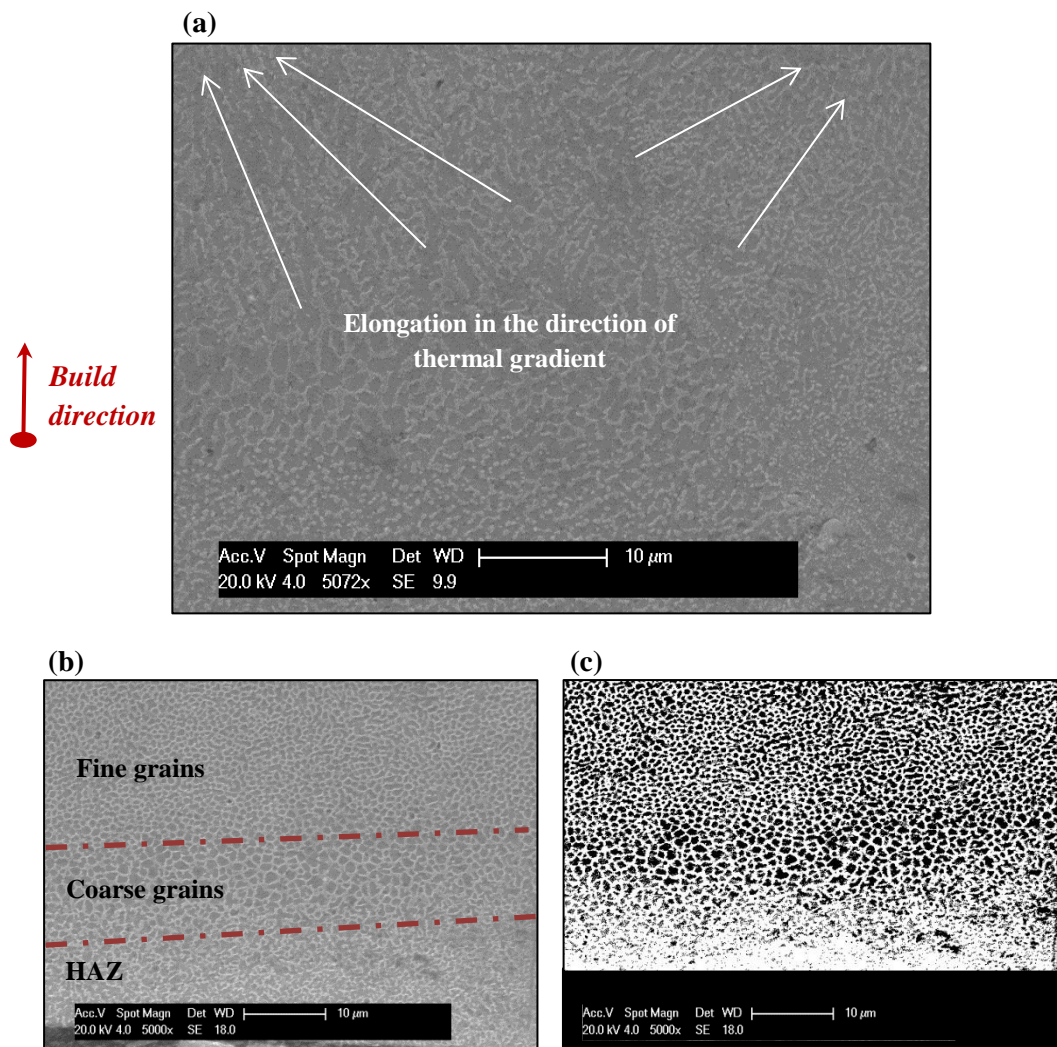
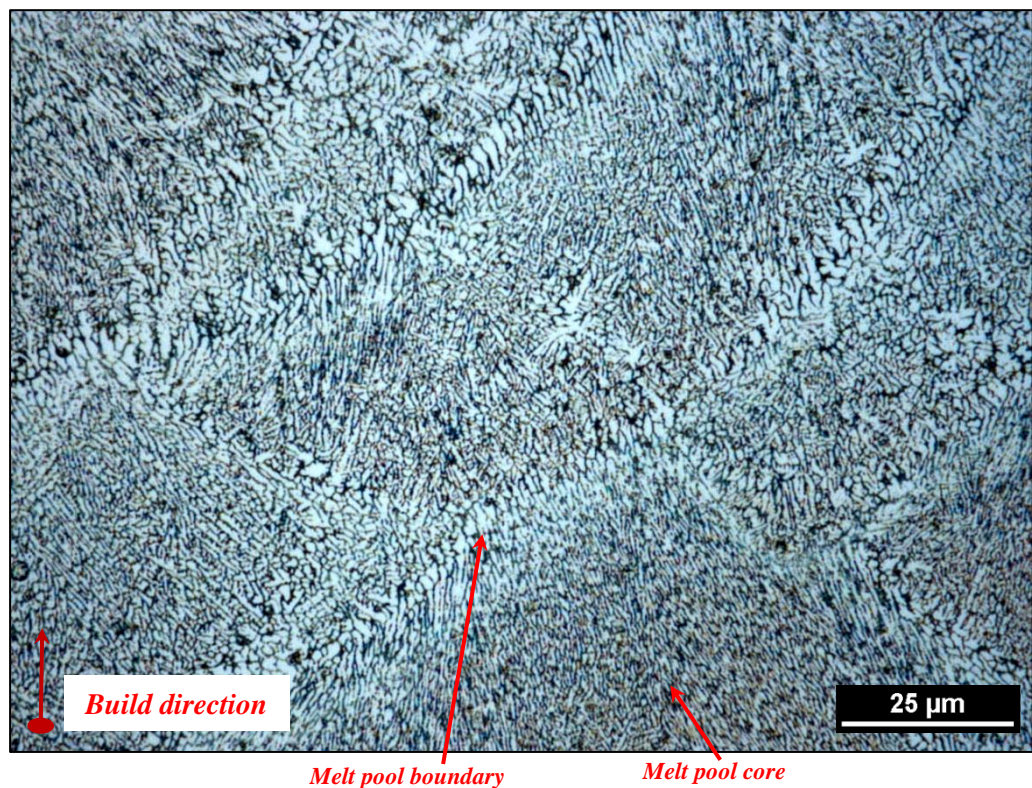


Figure 77: Microstructure of the melt pools demonstrating (a) cell orientation, (b) morphology, and (c) grain size distribution.

Since the pre-melt scan strategy was found to resolve the porosity issue (to a satisfactory extent) when using 500 mm/s scan speed, it was important to study what this scan strategy does to the material in terms of microstructure as well.

The optical micrograph of the etched sample in **Figure 78** shows the same distribution across the melt pool explained earlier in case of the single scan with finer cellular structure at the melt pool core and coarser one at the melt pool boundary. The structure of the cells at the melt pool boundary was clearly seen to be cellular-dendritic growing in the direction pointing towards the heat source. Further investigations on the microstructure of AlSi10Mg parts processed by SLM will be explained in chapter (6).



**Figure 78:** Microstructure of an AlSi10Mg sample produced by SLM using the pre-melt scan strategy at 500 mm/s.

## **5.6. Comparative chemical composition analysis for powder versus bulk samples**

Comparison of the chemical composition of the fresh and recycled powder (**Table 11**) suggests that the use of recycled powder would not be expected to negatively affect the quality of the produced samples since there is no

significant change to the chemical composition between both samples and they both lie within the acceptable ranges of the standardised values (refer to **Table 9** for the standard chemical composition).

**Table 11: Chemical composition of powders and bulk sample in relative weight %.**

Sample	Al	Si	Mg
Fresh powder	88.85	10.67	0.48
Recycled powder	88.60	10.90	0.49
Bulk sample	89.37	10.35	0.28
Laser spatter	85.8	13.00	1.10

It can also be seen in **Table 11** that there is a substantial difference between the chemical composition of the bulk sample and the fresh powder, as the amount of Mg in the bulk has dropped to almost half its original value suggesting that Mg is being lost or scattered out of the melt pool during processing, which could be occurring due to the high laser power hitting the powder bed with Mg being a light element. Since Mg has low vaporisation temperature, its evaporation with laser processing causes porosity, as has been previously reported for laser welding [16, 43, 108]. Although the laser power (100 W) used is considered as relatively low power, the laser beam diameter (~ 20  $\mu\text{m}$ ) is relatively small leading to a high energy density. This high energy density is expected to promote evaporation of the material [10]. There is also a slight decrease in the amount of Si in the bulk sample when compared to the fresh powder. The decrease in the fraction of the alloying elements in the bulk samples might have an effect on the overall mechanical properties. The findings regarding the loss of Mg and Si from the bulk sample agree well with the chemical composition of the laser spatter, which can be seen to be rich in both elements; Mg and Si when compared to the fresh powder. The production

of laser spatter when selectively laser melting AlSi10Mg was studied by Simonelli *et al.* [82] and attributed to selective oxidation reactions occurring in the process. **Figure 79** shows that the sizes of the particles in the laser spatter sample are much larger than the fresh powders. The size of the laser spatter particles ranges from 200  $\mu\text{m}$  to 500  $\mu\text{m}$ , whereas the size distribution of the fresh powder ranges from 20  $\mu\text{m}$  to 63  $\mu\text{m}$ . This supports that the particles entrapped in the keyhole pores in **Figure 76** are clusters of fresh powders and not laser spatter.

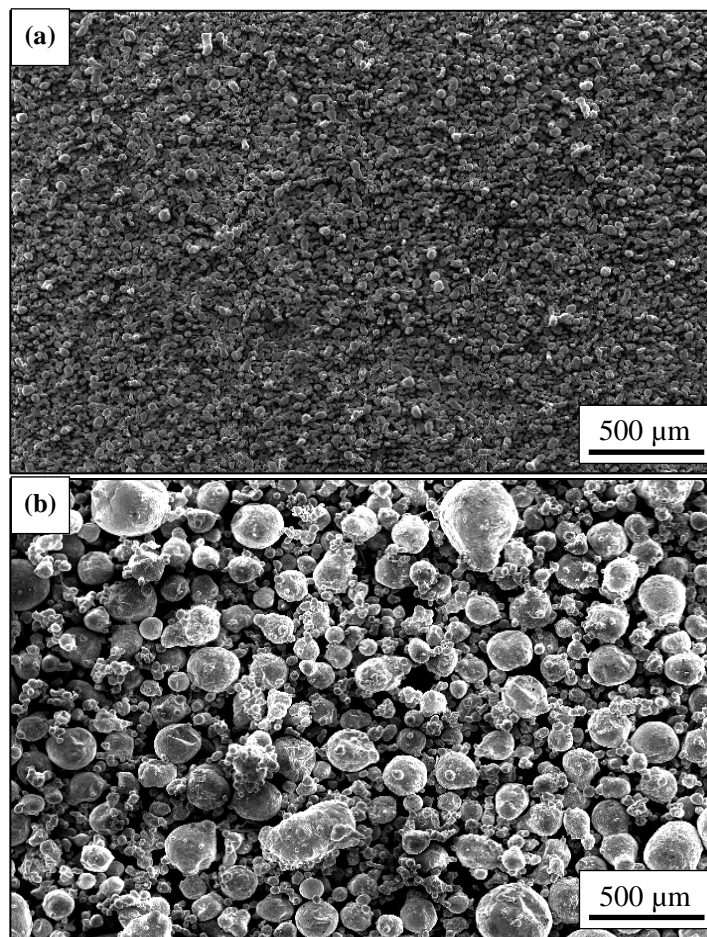


**Figure 79: Morphology of (a) fresh powder and (b) laser spatter.**

## 5.7. Further parameters in selective laser melting

### 5.7.1. The role of powder properties on the processability of AlSi10Mg

#### *Powder characterisation*

The batches of powder in this study were named after their suppliers, i.e. powder supplied by LPW Technology will be referred to as LPW hereafter and powder supplied by TLS Technik will be referred to as TLS. The morphology of the powder is shown in **Figure 80** and **Figure 81**. The LPW powder was a mixture of elongated particles and irregularly shaped particles. The TLS powder was largely spherical, which is favoured for SLM requirements. This difference in morphology is expected to grant superiority to the TLS powder since the spherical shape allows better flowability and packing density [21]. Some satellites were observed in the micrograph for the TLS powder with almost none observed in the examined batch of the LPW powder.

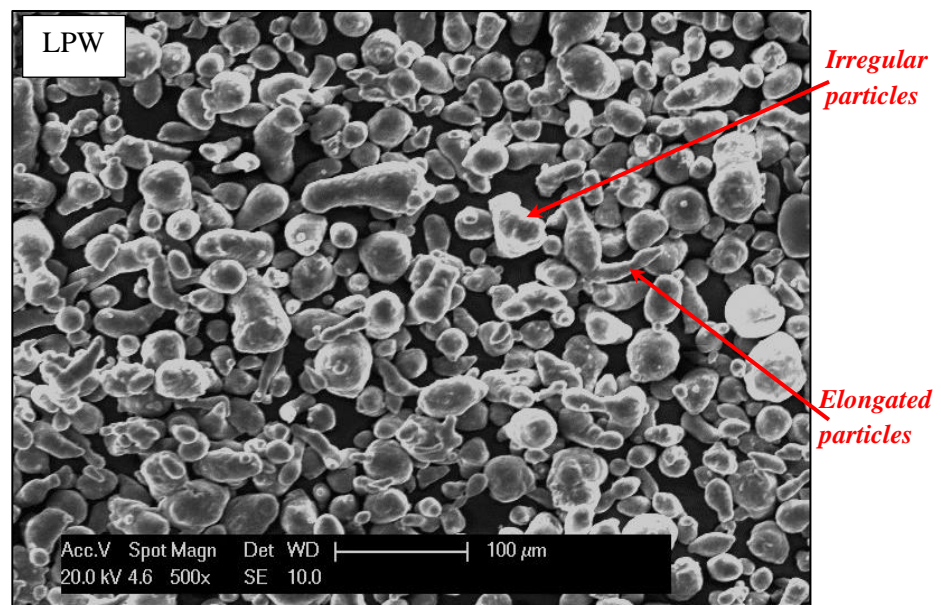


**Figure 80:** Elongated and irregular particle morphology in the LPW powder.

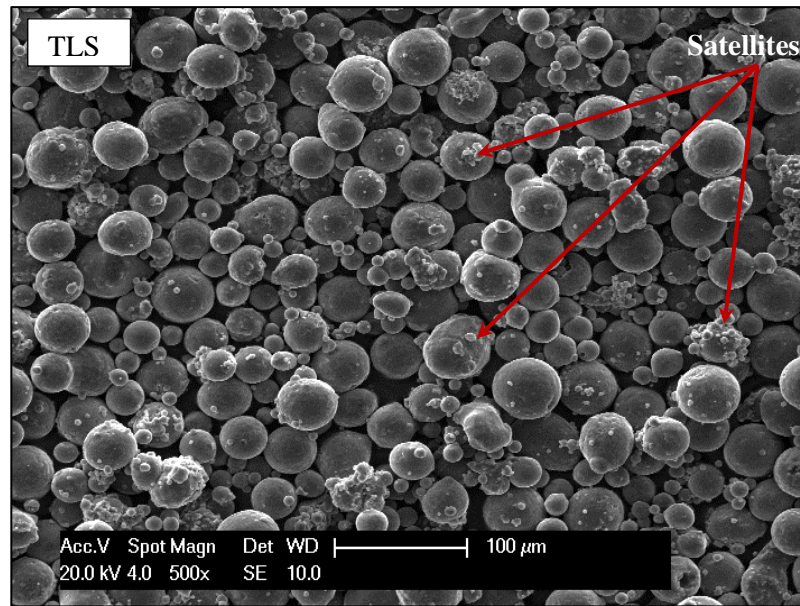


**Figure 81:** Particles in the TLS powder were mostly spherical with observed satellites.

The microstructure of the LPW powder, as demonstrated in the cross-section in **Figure 82 (a)**, contained Si dendrites. The TLS powder's microstructure, in **Figure 82 (b)**, was a solid solution of cellular  $\alpha$ -Al with Si segregated on the Al grain boundaries. Comparison of the two microstructures indicates that the TLS powder cooled faster than the LPW during the atomisation process. Minimal inherent porosity was observed in the cross-sections of both powders. Inherent porosity in the powder suggests trapped gases that might promote porosity in processed parts. Gas pores (metallurgical pores) have been reported in SLM parts fabricated from AlSi10Mg earlier in this chapter and attributed to moisture on the powder particle surface as well as gases dissolved in the particles [71].

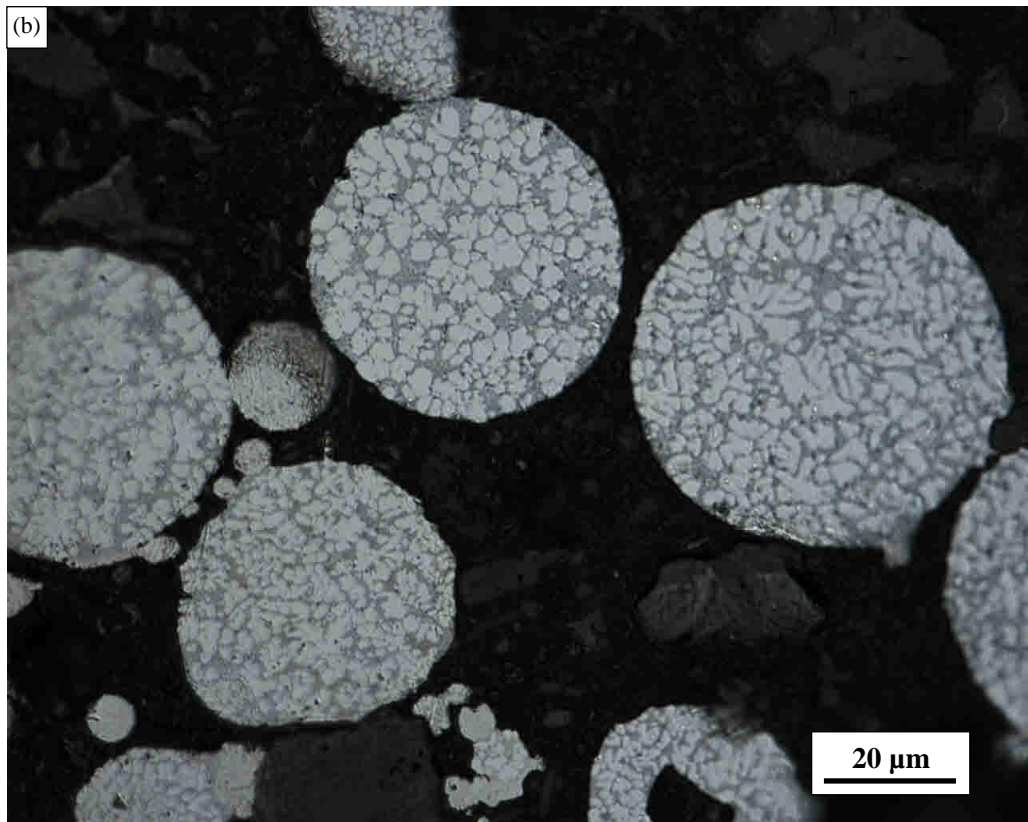
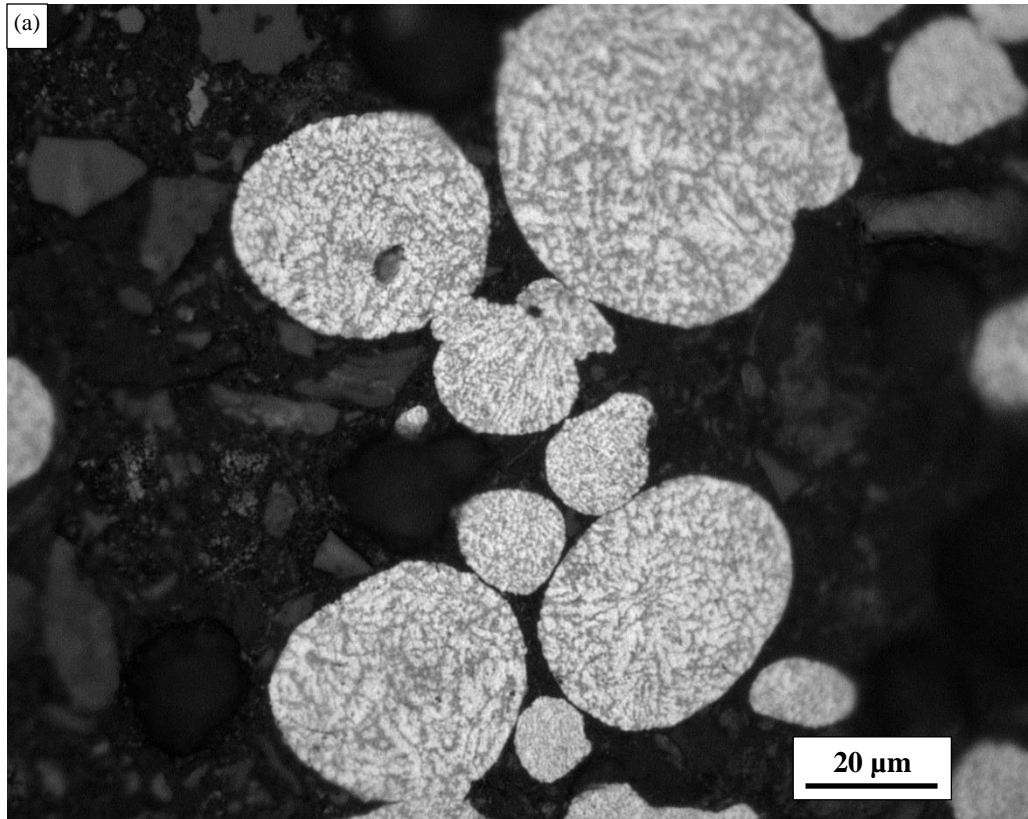


Figure 82: Microstructure of the cross-sectioned powder from batch (a) LPW and (b) TLS.

The chemical composition of the LPW and TLS powder with respect to the standard composition is listed in **Table 12**. The LPW powder had Si content within the standard range. The TLS powder, on the other hand, had higher Si content. The higher Si content in the TLS powder makes it a eutectic alloy whereas that of the LPW powder is a hypo-eutectic composition [151]. This difference in Si amount will affect the melting and solidification behaviour during SLM. Higher Si content enhances laser absorption [93], which is beneficial since Al has low absorptivity and high reflectivity compared to other SLM candidate materials (see chapter (1) of this thesis, section 1.3). In addition, Si increases the metal's fluidity [108] enhancing its wettability. The drawback of the higher Si content is that it affects the material's mechanical behaviour. Si is added to Al alloys for strengthening, however, in the range close to the eutectic composition it promotes the formation of platelets, which act as sites for crack nucleation under cyclic loading [152], hence reducing the fatigue life. This issue requires investigation, bearing in mind the distinct microstructure developed by SLM [4]. The magnesium content is not significantly far from the standard range [60] for both batches of powder.

**Table 12: Comparing chemical composition of powders from different suppliers - in weight %.**

Powder batch	Mg	Si	Al
LPW	$0.48 \pm 0.01$	$11.2 \pm 0.2$	$88.3 \pm 0.2$
TLS	$0.43 \pm 0.02$	$12.36 \pm 0.09$	$87.2 \pm 0.1$
Standard [60]	0.2 – 0.45	9 - 11	Balance

The particle size distribution in **Figure 83** shows that the TLS powder has a more uniform distribution as the LPW powder is positively skewed. This skew

could be caused by not only the presence of larger particles, but also by the elongated morphology of the particles. The device used for analysis operates by means of measuring the intensity of light scattered as the laser beam passes through the dispersed particulates. This means that the measurement is influenced by the material's refractive index and the projected surface of the particle; i.e. particle orientation during data collection will mislead the data for non-spherical particles.

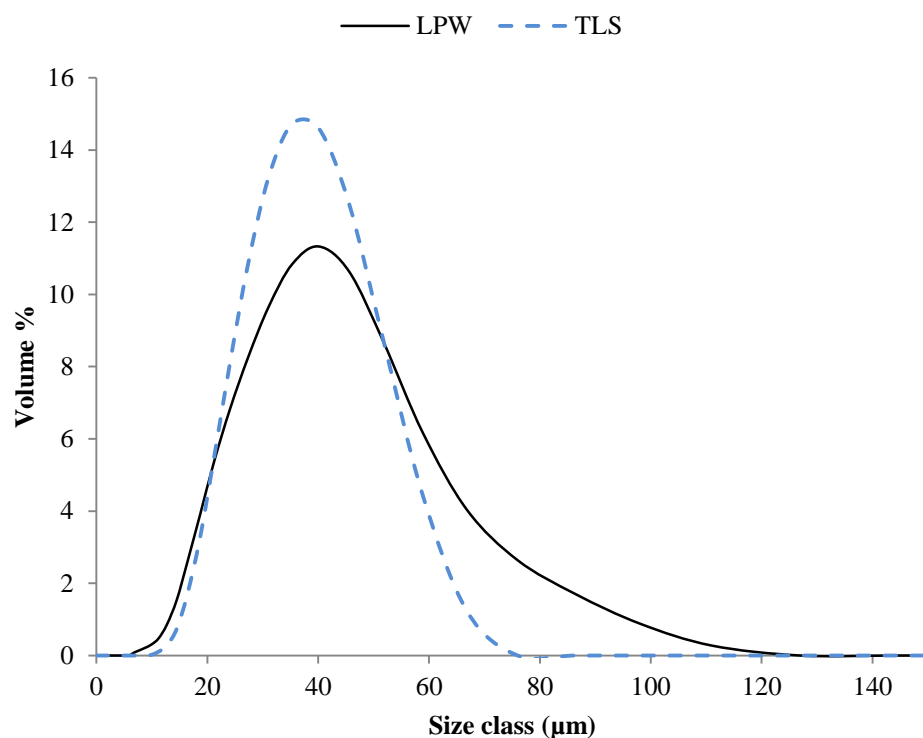


**Figure 83: Particle size distribution for AlSi10Mg powders supplied by LPW and TLS.**

Regarding the powder flowability, the LPW powder did not flow through the Hall flowmeter funnel, indicating poor flowability that cannot be quantified. Poor flowability means that depositing a uniform layer will be challenging during processing. The flow rate of the TLS powder was 62 s/50 g. Flowability of a metal powder is governed by its morphology and size distribution and this

explains why the flowability of the TLS powder was better than the LPW powder. The LPW powder had an irregular morphology in addition to a skewed particle size distribution. Also, the presence of moisture on the particle's surface would likely contribute to suppressing the powder's flowability. Drying the powder before processing by pre-heating can help overcome this problem in addition to enhancing the powder's laser absorptivity [70]. The apparent density of the TLS powder was  $1.456 \text{ g/cm}^3$ . The apparent density of the LPW powder was not determined since the powders did not flow, but lower apparent density was expected because of the irregular morphology of the particles. The better the packing density, the higher the particle contact area, i.e. better consolidation during processing.

#### ***Effect of powder properties on bulk samples (3D parts) quality***

**Figure 84** shows the effect of using different powder (from the same alloy) on the quality of SLM samples. When using the same combination of processing parameters, the TLS powder yielded denser parts compared to the LPW powder. In the single scan strategy, the TLS powder showed a relative density of  $(99.6 \pm 0.2) \%$ , which is an improvement compared to the  $(97.74 \pm 0.09) \%$  relative density achieved by using the LPW powder. These results act as evidence that the properties of the powder used in SLM strongly affect the relative density of the parts produced. The TLS powder surpassed LPW by producing parts of higher relative density and this is attributed to the powder properties and these are:

- The spherical morphology that leads to better flowability [21] and higher packing and apparent densities

- The particle size distribution that supports better flowability of the powder
- The higher Si content resulting in better laser absorption [93]
- Containing higher Si content meaning smaller difference between the solidus and liquidus temperatures [6] that should influence the solidification behaviour [54]
- The higher Si content enhancing the metal fluidity [16, 41, 45, 108] as it reduces the metal's surface tension [43, 144]

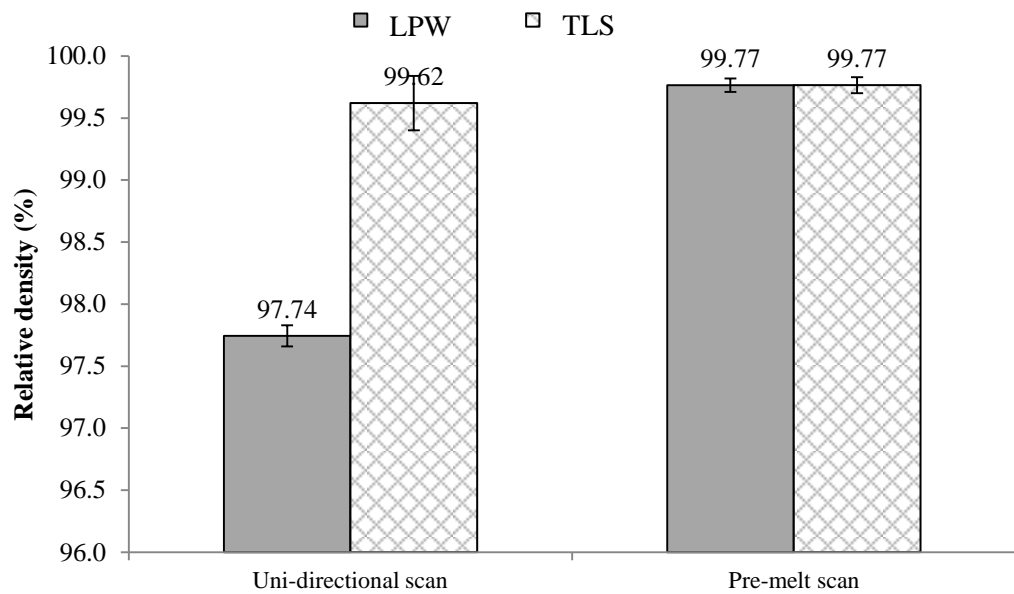


**Figure 84: Relative density of SLM samples processed using different scan strategies and powders with error bars representing the standard error.**

However, it is important to note that the pre-melt scan strategy, in which each layer is scanned twice with different laser power per scan, has yielded samples with high relative densities using either powder batches. There was no significant difference between the densities of parts from the different powders when using the pre-melt scan strategy; where LPW and TLS powder yielded samples that were  $(99.77 \pm 0.06) \%$  and  $(99.77 \pm 0.07) \%$  dense, respectively.

It is quite noticeable as well that the standard error was reduced when using the pre-melt scan strategy, which implies better repeatability of results. This suggests that it is possible to process powder with lower quality – to an extent – or else powder with specifications that do not fully comply with the SLM process requirements without losing the part's quality by means of altering the scan strategy. Powder with poor morphological properties will not allow deposition of a uniform powder layer to be processed by SLM. Thus each layer will suffer defects and irregularities. Sintering the powder in the first scan reduces the chances for defects formation in the full power scan. In this way, defects are remedied, returning a denser layer and consequently a denser part.

### **5.7.2. Gas flow within the processing chamber**

The influence of the rate of gas flow within the processing chamber in the SLM machine on the relative density of the built samples is demonstrated by the bar chart in **Figure 85**. It is clear that the longer the filter is used, the higher the relative density of the samples. These results are also supported by visual observations as the amount of laser spatter removed was found to decrease as the filter gets older, i.e. the gas flow is slowed down. It was also observed that the pre-melt strategy produces less scatter compared to the overlap strategy at all times yielding higher density, this is attributed to the less power (50 W) used for the first scan in case of pre-melt where the powder is first sintered and then melted by the following full power scan.

There are two scenarios for the ejection of material that is being removed by the gas flow rate during processing. The first is that balling occurs on the surface being selectively laser melted [3, 68] due to high surface tension of the material. The balls formed are not fully integrated into the processed layer,

however, they are supposed to be stagnant in place for the following scan to melt them and homogenise the surface altogether. But due to the high speed of the gas flow when the filter is still new, these balls are susceptible to be carried away from the surface of the sample with the laser condensate. The usage of the filter leads to its gradual partial blocking so the gas flow is slowed down and becomes unable to remove larger particles from the surface. The second scenario is that the spatter is produced due to the interaction of the laser beam and the target material. When the power density is high, keyholing is promoted, which is somewhat similar to drilling a hole in the layer, i.e. scatter of material. The scattered material is then carried away with the gas flow within the chamber and based on the speed of the flow where the spatter is deposited can be defined. The effect of gas flow on the parts' porosity as demonstrated by **Figure 85**, contradicts what has been previously reported by Ferrar *et al.* [17] for Ti alloys. This could either be due to the difference in material or the machine set up used in the experiments. This issue requires further investigation but this is beyond the scope of this thesis.

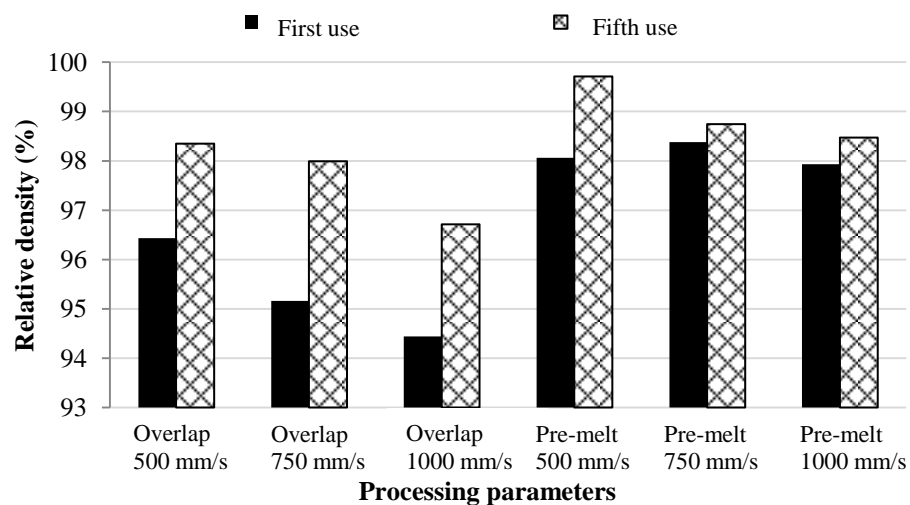


**Figure 85: Effect of gas circulation on the relative density of SLM Al parts showing inter-build variability.**

The laser spatter ejected during processing was much larger than the starting/fresh powders, as can be seen in the SEM micrographs in **Figure 79**. Moreover, the spatter was mostly spherical where on the other side, the LPW starting powders was elongated and irregularly shaped, as was demonstrated in **Figure 80**. A comparison between the chemical composition of the fresh LPW AlSi10Mg powder and the laser spatter was already shown earlier in this chapter in **Table 11**. It was noted that the spatter showed a higher content of Si and Mg with respect to the fresh powder. This finding along with the results from section 5.6 in this chapter that showed the bulk samples to be short of Mg and Si supports findings published by Simonelli *et al.* [82] on the selective oxidation reactions that occur during SLM where a thorough investigation of the laser spatter can be found.

## 5.8. Summary

The study conducted in this chapter is summarised in the schematic diagram in **Figure 86**. The findings of the study are:

- Based on the hatch spacing investigations, it was found that sufficient overlap between adjacent melt pools was achieved at either a hatch spacing of 50  $\mu\text{m}$  or 100  $\mu\text{m}$ . As indicated by Pupo *et al.* [92], heat accumulation in the melt pool occurs when using smaller values of hatch spacing since it allows slow cooling of the layer giving a homogeneous and continuous layer. Consequently, it was recommended to use the smaller hatch spacing, i.e. 50  $\mu\text{m}$ .

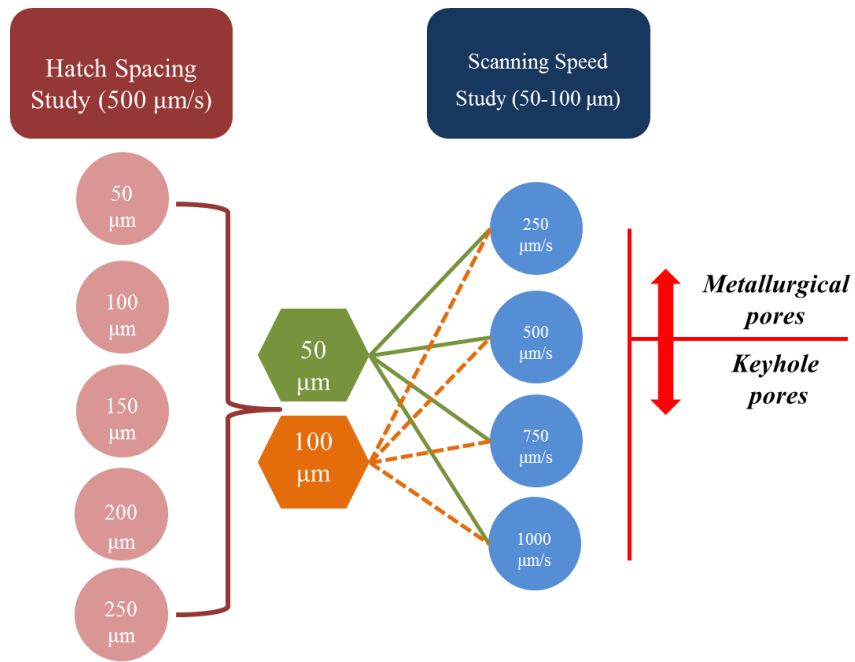


**Figure 86: Summary of the study and findings.**

- The effect of the scan speed variation was investigated at the two values of hatch spacing that were reported successful in the hatch spacing study, i.e. 50 μm and 100 μm. The scan speed study showed that the speed used not only affects the fraction of pores formed but also the type of pore.
- Metallurgical pores tend to be formed at lower speeds whereas keyhole pores are created with increasing scan speed, along with a reduction in metallurgical pores. The bordering speed for the shift between metallurgical and keyhole pores was 500 mm/s.
- Keyhole pores enclose non-molten powder and their formation is parameter-dependent. Irregularities on the surface, such as balling, that occur with increasing scan speed promote the capture of powder that is not fully melted by the laser beam scanning the following layer; hence a keyhole pore is created. This scenario is supported by the effect of

altering the scan strategy since scanning the same layer twice has resolved this issue specially using the pre-melt scan strategy that flattens the surface, by sintering the powder particles, before the second scan.

- Altering the scan strategy to a double scan at high speeds was an alternative to solely reducing the scan speed in pursuit of keyhole pore prevention, as the latter introduces metallurgical pores. Some metallurgical pores were still seen at high speeds but it is worth noting that a fraction of the pores (metallurgical) could be inherent porosity in the powder.
- Surveying the windows of parameters, the best combination was found to be a speed of 500 mm/s, hatch spacing 50  $\mu\text{m}$ , and 100 W laser power whilst using a layer thickness of 40  $\mu\text{m}$  and employing the pre-melt scan strategy yielding a relative density of  $(99.77 \pm 0.08) \%$ .
- It is worth noting that the achieved relative density using a 100 W only laser power is high compared to the values reported in the literature where similar densities were achieved using a minimum of 200 W laser power, such as the work by Thijs *et al* [4], and up to 900 W as shown by Buchbinder *et al.* [25].
- Two categories of microstructure are created in the melt pool; the first is a fine microstructure at the centre of the melt pool and the second is a coarse structure at the melt pool boundary. The grains were seen to be elongated in the direction of the thermal gradient, i.e. the heat source. Moreover, coarse dendritic structures were formed in the vicinity of keyhole pores.

- The use of recycled powder can be recommended since the chemical composition of the recycled powder was found to be the same as the fresh powder with no alterations. This in fact is an advantage of using SLM in manufacturing rather than conventional manufacturing for the minimal to zero waste.
- Magnesium, as the lightest element in the studied alloy, had a higher susceptibility to evaporation or scatter resulting in the production of parts with reduced Mg content compared to the raw virgin powder; this was confirmed by the excess amount of Mg found in the laser spatter. Although Mg as an element does not affect the melting and solidification behaviour of the material, the effect of this change in composition on precipitate formation and consequently mechanical properties needs further investigation.
- It is generally supposed that the quality of the powder plays an important role in the success of SLM because the powder morphology alongside its size distribution governs the formation of gas pores and controls the flowability. This study has demonstrated the variability between the properties and specifications of metal powders from one supplier to another. Attention has to be paid to the specifications of powder to be used in SLM as powder with irregular morphology will not allow deposition of a uniform layer of powder. The chemical composition of the powder can alter the melting and solidification behaviour during processing. Although this study has shown that the properties of the powder control the degree of porosity in SLM parts, an

approach to reduce porosity using altered scan strategy, using the pre-melt scan strategy, has proved successful.

- Evidence supporting the hypothesis that the density of the parts processed using SLM is influenced by both the processing parameters and the gas flow within the chamber was shown in this study. The excessive scatter of laser spatter due to high gas flow rate promotes porosity when processing AlSi10Mg.

## **CHAPTER (6): Microstructural characterisation of selectively laser melted AlSi10Mg**

In this chapter, the microstructure of selectively laser melted AlSi10Mg single tracks, layers, and multi-layered parts is studied by means of optical and electron microscopy. In addition, energy dispersive X-ray mapping was implemented to show the chemical composition distribution in the material. The quality of the samples' surfaces was evaluated by microscopy and surface roughness measurements. Also, X-ray diffraction identified the distinct phases in the material and crystallographic texture analysis is revealed. Besides defining the grain structure of the material produced using selective laser melting, the effect of a conventional T6 heat treatment on the SLM characteristic microstructure was also studied. A range of solution heat treatment and ageing durations was employed to determine the evolution of the microstructure.

### **6.1. Microstructure of single tracks**

The samples used in this section were the single tracks prepared in chapter (4). The microstructure of the as-cast material in the substrate and the laser irradiated material were compared. The developed microstructure after laser irradiation is influenced by the rate of solidification. For instance, in case of conventional casting, the slow rate of cooling develops Si with a coarse flake-like microstructure, as can be seen in the as-cast region in **Figure 87**. As for

chill casting, the faster cooling rate in which the material solidifies results in a fibrous morphology instead [153]. The latter mechanism occurs when irradiating the Al-Si substrate with the laser beam and hence produces a finer fibrous microstructure, as shown in **Figure 87** in the region of the selectively laser melted material.

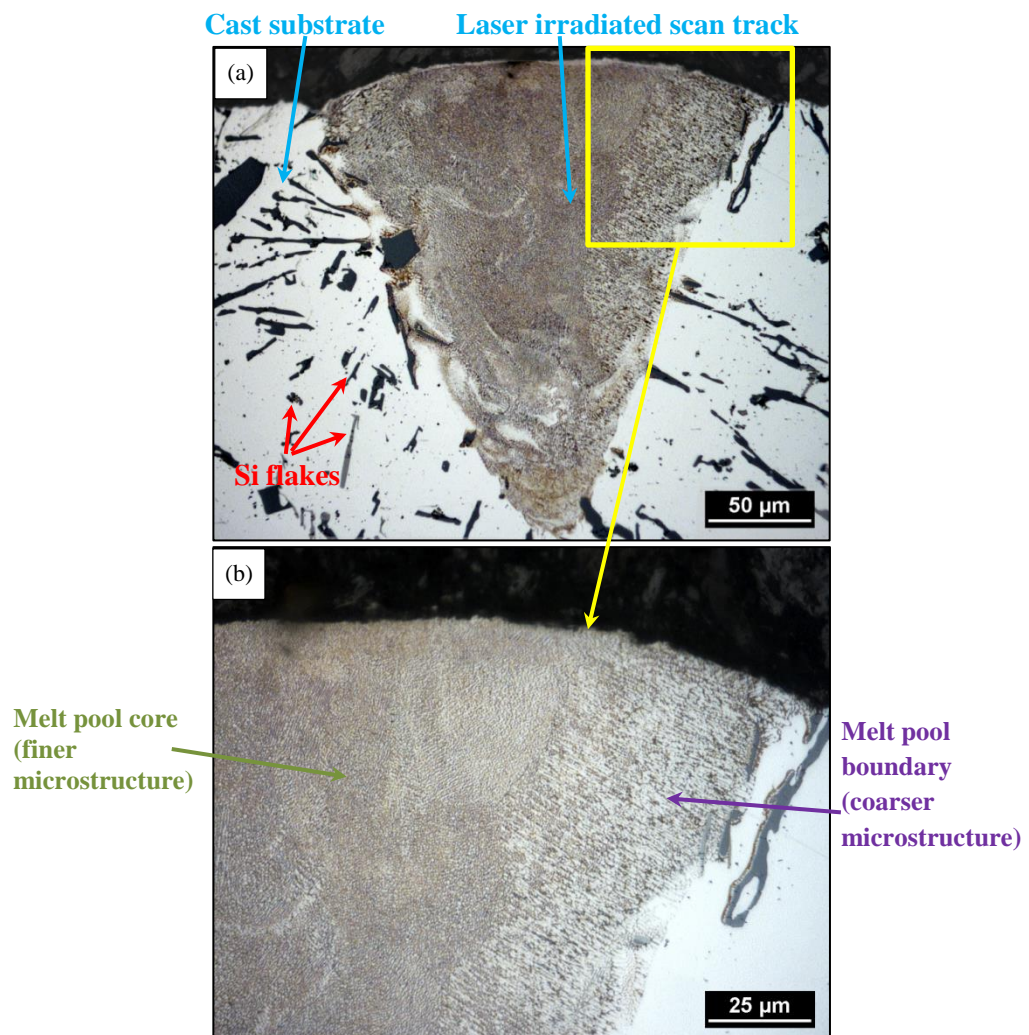


**Figure 87: Microstructure of a single track processed using 250 mm/s revealed using Keller's reagent at (a) low and (b) high magnification.**

The alloying elements in the cast material (Si, Mn, and Fe) were in the form of flakes in the Al solid solution. The cast material solidifies at a slow rate that allows for the alloying elements to diffuse and form these flakes. When a material is irradiated by a laser beam, it encounters a series of thermal

experiences. The phases forming in the zones of a melt pool are controlled by these thermal cycles experienced [16]. The melt pool formed during SLM is not much different from that formed during laser welding. After irradiation with the laser beam, the flake-like structure has dissolved from the melt pool region. The rapid solidification hinders the diffusion of the alloying elements and instead they are located on the boundaries of  $\alpha$ -Al.

The melt pool of an AlSi10Mg single track is divided into two zones, as shown in **Figure 87** for a single track processed using 250 mm/s scan speed. The inner zone – towards the core – was characterised by an ultrafine microstructure. The grains in this region were equiaxed with Si located on the boundaries of the  $\alpha$ -Al cellular structure. The outer zone – towards the boundaries of the melt pool – had relatively coarser grains. Grains at the melt pool boundary were elongated in the direction of the thermal gradient, i.e. columnar grains observed at the melt pool boundary. This microstructure is similar to that reported for weld pools in laser welding of Al alloys [154]. The distinction between the microstructure of the laser irradiated and cast material was that the former was much finer. The microstructure refinement was driven by the rapid solidification. Si flakes in the as-cast material are promoted by maintaining low temperatures for relatively long durations (slow solidification) [89].

The cross-section of the track processed using a 500 mm/s scan speed is shown in **Figure 88**. Although the difference between the microstructure of the tracks processed at 250 mm/s or 500 mm/s is not significant, a slightly coarser microstructure was obtained using the slower scan speed, especially in the melt pool boundary. This is in agreement with findings reported by Buchbinder *et*

al. [155] who asserted that the slower scan speed imposes slower solidification, which in its turn results in coarsening the grain structure.

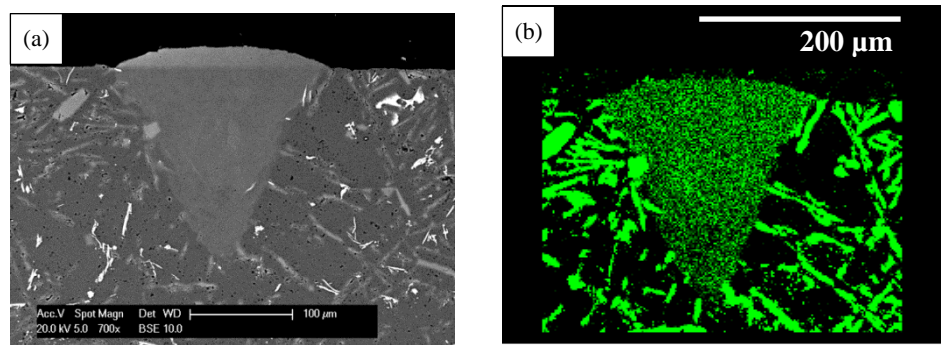


Figure 88: Microstructure of a single track processed using 500 mm/s revealed using Keller's reagent.

The higher scan speed means more turbulence within the melt pool that is accompanied by faster solidification [98, 146]. This not only controls the microstructure in terms of grain size coarsening or refinement but also controls the orientation of the grains. The SLM material in **Figure 88** looks as if the Marangoni flow or the turbulence within the molten material during processing was frozen in place by the rapid solidification.

The chemical composition distribution of Si within the melt pool of a single track is shown in **Figure 89**. The more homogenous distribution of Si in the laser irradiated material with respect to the cast counterpart is evident. During melting and solidification of an Al alloy, some elements are susceptible to vaporisation, such as Mg in AlSi10Mg, as has been reported in section 5.6. When a melt pool is created, the alloying elements tend to move towards the top of the liquid melt pool. If for some elements the energy supplied is

equivalent to their heat of vaporisation, which is the energy needed to break down the bonds between an atom and its neighbour so that it becomes free to move from the solid to the vapour [156], vaporisation occurs at the liquid-vapour interface and elements start to leave the melt pool as spatter into the surrounding media. This is further promoted by the vigorous fluid circulation within the melt pool [43]. This means that the amount of Mg decreased with laser processing compared to the starting powder, to levels that could not be accurately mapped with the EDX detector's capabilities.

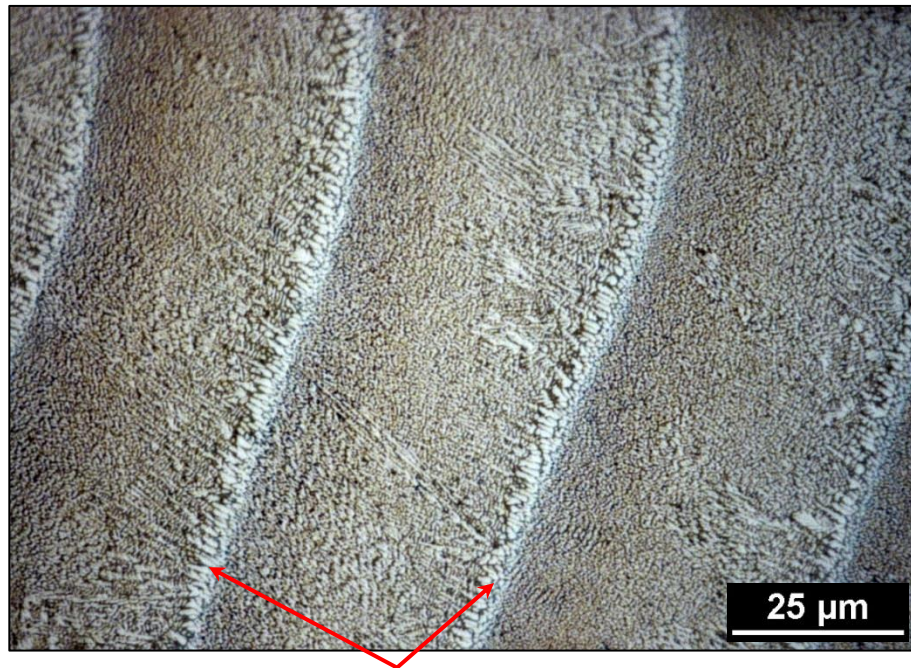


**Figure 89: Mapping the chemical composition of Si in (a) a scan track processed from a 40 µm powder layer at 250 mm/s scan speed with Si in (b) presented by the green colour.**

The distinctive Si distribution in the laser irradiated material was also formed due to rapid solidification of the material since this does not allow enough time for the alloying elements to diffuse and form the particles or flakes characteristic of the cast material. The good dispersion of the alloying elements along with the fine microstructure suggests enhanced mechanical properties may be found. Mechanical characterization is reported in chapter (7). There was no compositional gradient observed from the top of the bottom of the melt pool. This could be attributed to the fact the chemical composition of the laser irradiated powder and the substrate material is almost the same; containing 12 wt% Si.

## 6.2. Microstructure of single layers

The overlapping melt pools in the single layers had a similar microstructure to the corresponding single melt pools, as can be seen in **Figure 90** and **Figure 91** for single layers processed using 250 mm/s and 500 mm/s scan speeds, respectively.

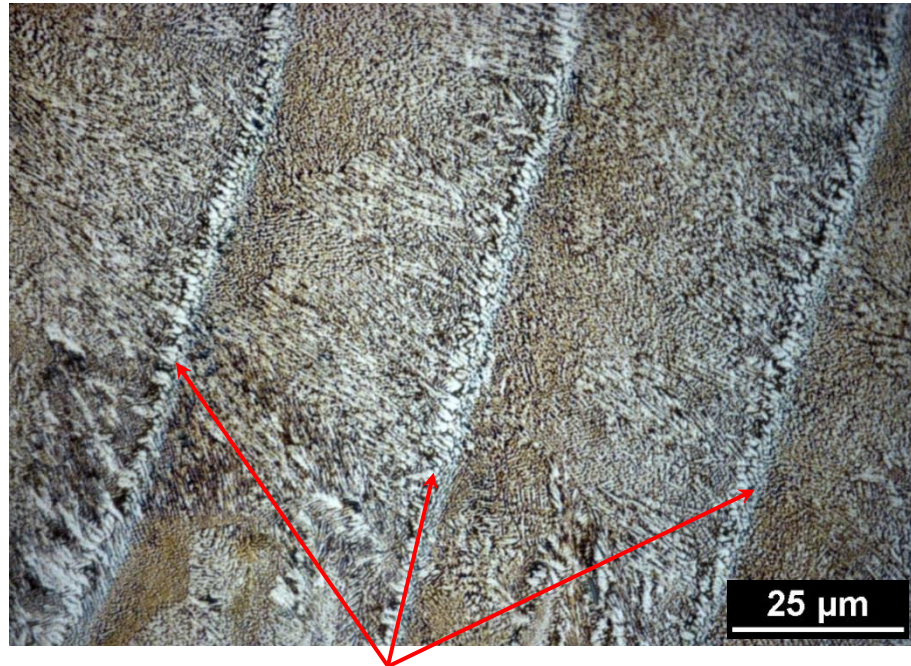


### Melt pool boundaries

**Figure 90:** Microstructure of overlapping melt pools in a single layer processed at 250 mm/s revealed by Keller's reagent.

Grains at the melt pool core were equiaxed whereas those at the boundary were coarser and elongated along the direction of the heat flow, i.e. pointing towards the heat source. Cellular dendrites of  $\alpha$ -Al and inter-dendritic Si are observed at the melt pool boundary in **Figure 90**. The cellular-dendritic growth of grains within the melt pools is also clear in **Figure 91**. The border between two overlapping melt pools was rich in Al compared to the rest of the melt pool, as per these micrographs represented by the lighter shade. This is because during solidification Si precipitated on the boundaries of the cellular dendritic Al

[157] and having coarser grains at the melt pool boundaries means less grain boundary area, i.e. less Si content in these regions. The areas with coarser dendritic  $\alpha$ -Al between the overlapping melt pool boundaries represent the heat affected zones [18].



**Melt pool boundaries**

**Figure 91: Microstructure of overlapping melt pools in a single layer processed at 500 mm/s revealed by Keller's reagent.**

### **6.3. Analysis of 3D bulk samples**

#### **6.3.1. Topography**

One of the downsides of the SLM process is the poor surface quality of the parts produced, either due to the formation of a surface with an irregular morphology or the presence of satellites or balling, as explained earlier in section 4.3.3. This is clearly evident in the micrographs in **Figure 92** where satellites sticking to the surface of a sample can be seen. The presence of surface defects and irregularities on the surface of the parts might depress various mechanical properties of parts such as fatigue life by developing notch

sensitivity. Frazier [9] stated that the fatigue life of SLM Ti-6Al-4V parts decreased by an order of magnitude when the surface roughness increased from 3 to 1000  $R_a$ . The effect of surface roughness on the fatigue performance of SLM AlSi10Mg is presented in chapter (7).

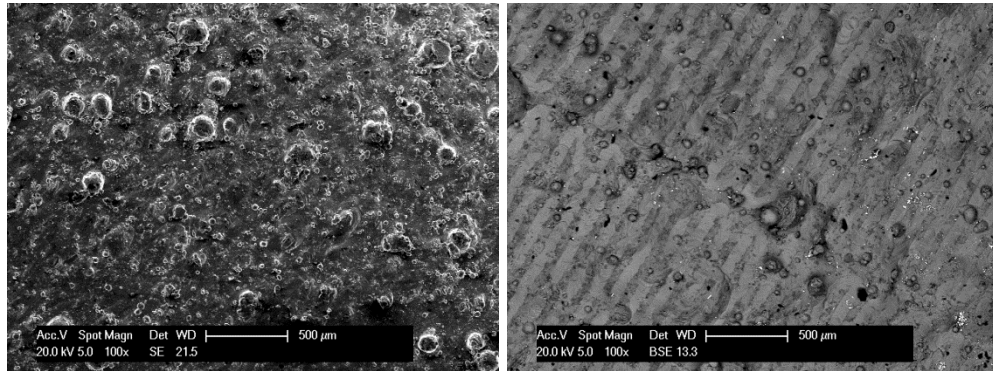


**Figure 92:** Morphology of the top surface of an AlSi10Mg part produced by SLM as seen by (a) secondary electrons detector SE and (b) backscatter electrons detector BSE (surface perpendicular to the building direction).

The surface roughness ( $R_a$ ) of the dense AlSi10Mg samples fabricated in this study was 10.3217  $\mu\text{m}$ , as determined by an Alicona infinitofocus SL. The profile of the sample surface is shown in **Figure 93**. The poor surface quality of SLM parts is a setback for the process as a net shape manufacturing technology since post-fabrication processing might be needed to reduce the surface roughness. Although post-processing machining might not be an issue for some parts, it might even be impossible in case of fabricating parts that cannot be machined using conventional technologies. Examples are topology optimised parts and latticed structures that would have complex shapes where machining might not be an option. So it is important to investigate the effect of the processing parameters on the surface morphology of the parts to remedy such defect at the source.

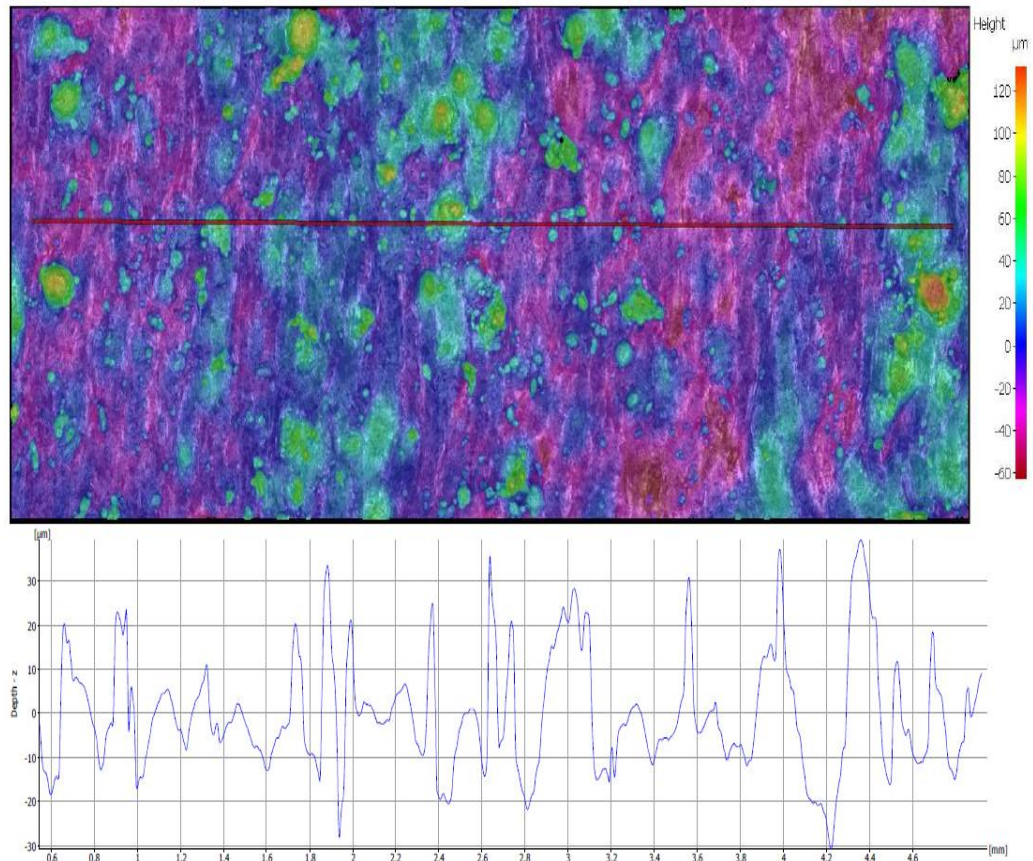


**Figure 93: Profile measurement for the surface of an AlSi10Mg SLM part.**

### 6.3.2. X-ray diffraction and crystallographic texture

The X-ray diffraction pattern of the SLM material in **Figure 94** shows the characteristic (111), (200), (220), and (311) peaks of the face-centred-cubic Al, in addition to the diamond-like cubic Si (111) peak, which suggests a two phase material and that Si is not completely dissolved within the Al phase. When the solubility of Si in the  $\alpha$ -Al is exceeded during solidification, Si crystals ( $\beta$ -crystals) start to precipitate [157]. No  $Mg_2Si$  peaks were detected although the alloy has to ability to precipitate it.

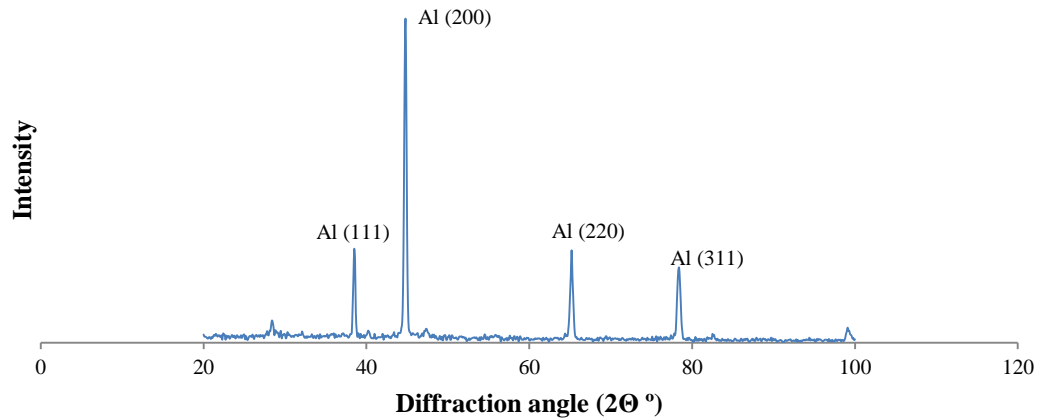


**Figure 94: XRD pattern for AlSi10Mg samples processed by SLM.**

During solidification of the molten metal, there are preferred orientations in which a fraction of the grains grow faster than others, i.e. formation of a crystallographic texture. This crystallographic texture is controlled by the processing technique, solidification, deformation, annealing, and phase transformation [158]. Accordingly, the type of texture is named, i.e. there is solidification texture, deformation texture, grain growth and recrystallization texture, and transformation texture. A textured material is one where the crystallites occupy a preferential orientation, whereas a texture-less material is when the orientations are generally random [158]. Since, Al is an FCC metal, columnar grains usually have  $\langle 100 \rangle$  axes [42, 158], i.e. fibre texture in the  $\langle 100 \rangle$ . Texture is categorised as macro-texture and micro-texture. There are several techniques to measure macro-texture such as diffraction of X-rays, electrons, or neutrons or using synchrotron X-rays. As for the micro-texture, this could be determined using scanning electron microscopy-based electron backscatter diffraction (SEM-EBSD) or transmission electron microscopy-based orientation imaging microscopy. Macro-texture, investigated in this study, is either represented by orientation distribution functions (ODF) or pole

figures. The pole figures, obtained using X-ray diffraction, giving the distribution of the orientations for the (100), (110), and (111) peaks in the selectively laser melted AlSi10Mg sample in **Figure 95**, indicate the presence of a preferred orientation for the unit cells within the grains with the (100) strongly aligned with the build direction. The pole figures were obtained from a cross-section of the plane parallel to the build direction. According to the microstructure reported in chapter (5), see **Figure 77**, the selectively laser melted AlSi10Mg material is made up of equiaxed grains at the melt pool core, grains elongated in the direction of the thermal gradient at the melt pool boundary, and the heat affected zone. This structure is quite comparable to the structure produced by laser welding and casting, so the texture developed in casting [158] will be used for an analogy. The equiaxed grains are expected to show a weak texture but the elongated ones will be dominated by a strong texture. The heat affected zone, resembling the chill zone in casting, will have a random texture.

The formation of a strong texture in the build direction has been reported by Buchbinder *et al.* [155]. The strong texture in this direction is attributed to the thermal gradient direction being the highest along the build direction. The magnitude of the resultant texture is magnified with faster rates of solidification [155].

The texture produced in an SLM material is controlled by the processing parameters [110]. Rotating the scan pattern from one layer to another reduces this texture, as reported by Thijs *et al.* [4]. The presence of a strong crystallographic texture, i.e. most grains have the same orientation, renders the material anisotropic in the mechanical properties [158]. The presence of a

preferred orientation (strong texture) in metals can also lead to a material with superior mechanical properties [156]. This will be investigated in chapter (7).

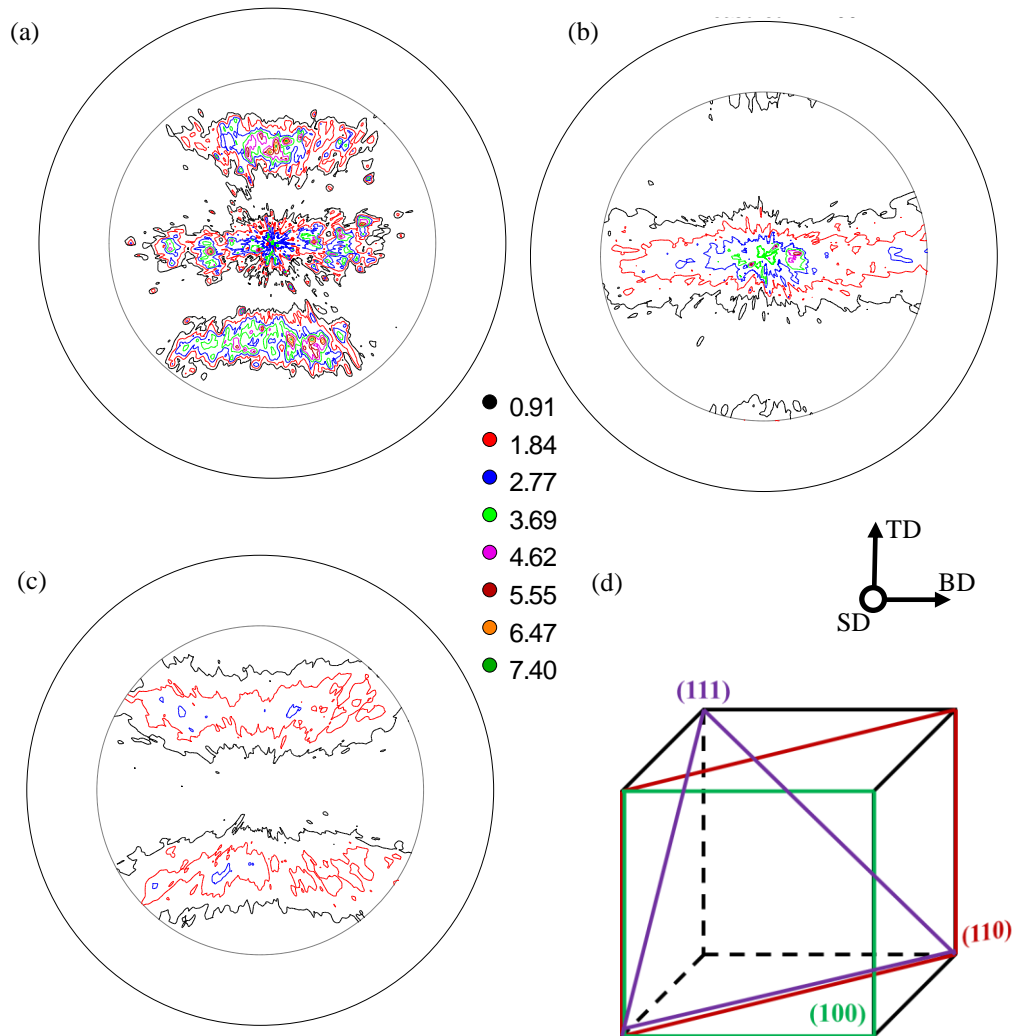


**Figure 95:** The (a) (110), (b) (100), and (c) (111) pole figures with (d) unit cell demonstrating the mapped planes. Note the build direction (BD), the scanning direction (SD), and the transverse direction (TD).

### 6.3.3. Microstructure and the effect of heat treatment

A part fabricated by SLM is made up of overlapping scan tracks in both the vertical and horizontal directions. Microscopic examination revealed the stacked layers on the sides of the cubic samples shown in **Figure 96** (XZ and YZ planes).

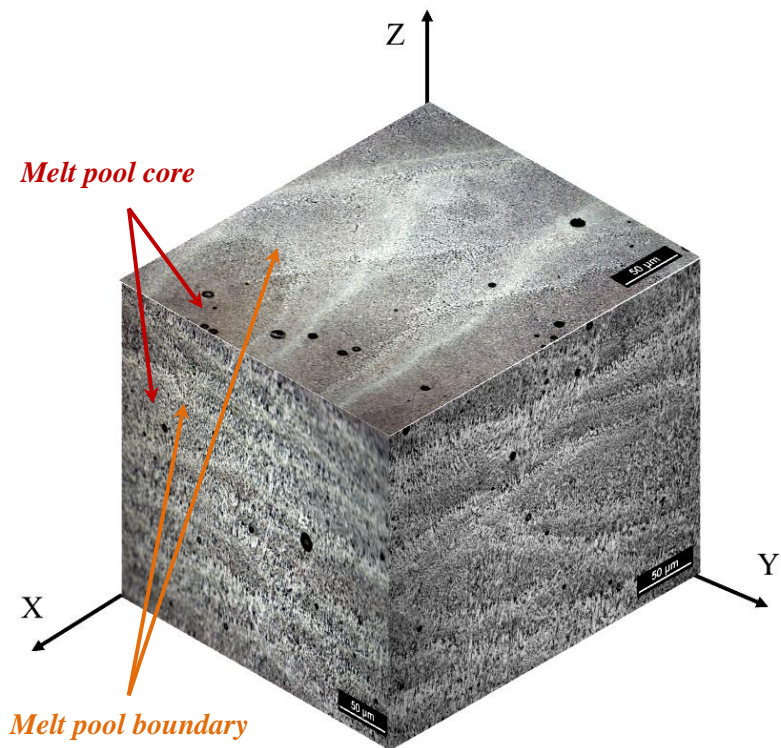
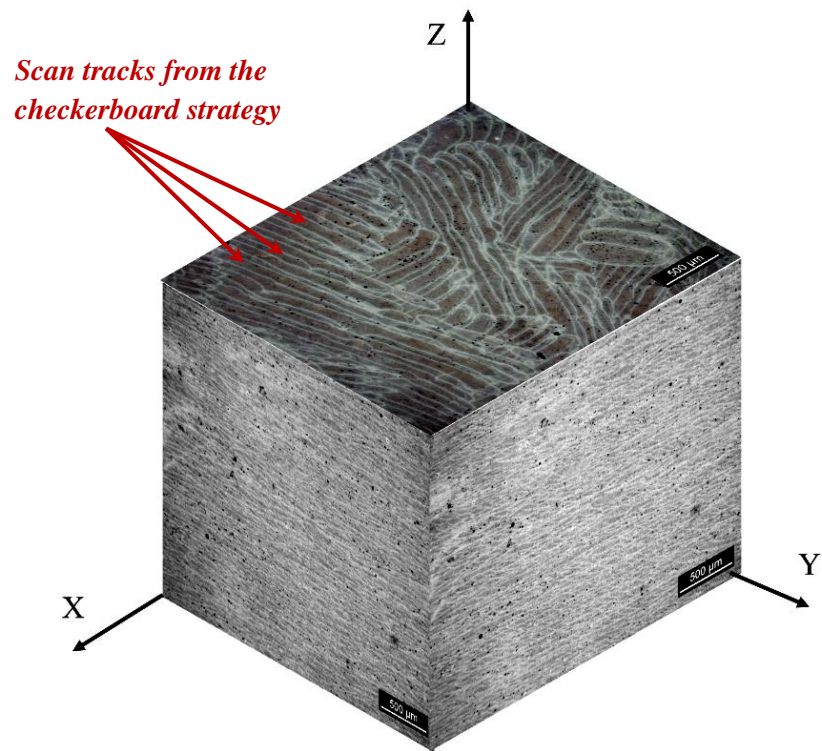


Figure 96: Microstructure of as-built AlSi10Mg sample produced by SLM showing XY, XZ, and YZ planes with lower magnification (top) and higher magnification (bottom).

The scan pattern, which in this case is a checkerboard scan pattern, can be seen on the top view (XY plane) of the cubes in **Figure 96** (both low and high magnifications). Each scan track is outlined by the melt pool boundary that has a coarser microstructure along with being Al-rich, as demonstrated by having the lighter shade. As has been already stated in chapter (5), the microstructure of SLM AlSi10Mg is divided into three zones; namely, melt pool core, melt pool boundary, and heat affected zone. This structure has been previously reported for AlSi10Mg [4] and Al-8.5Fe-1.3V-1.7Si alloy [86]. Grains in the XY plane, which is perpendicular to the build direction, were equiaxed, as can be seen in **Figure 97 (a)**. Due to the fast rate in which the material solidifies in SLM, Si dendrites segregated on the boundaries of the columnar  $\alpha$ -Al, a microstructure previously reported by Thijs *et al.* [4]. According to **Figure 97 (b)**, the grains in each melt pool, as viewed in the YZ plane, had two different orientations. The grains at the melt pool core were equiaxed whereas those at the melt pool boundary were columnar/elongated in the direction of thermal gradient, i.e. pointing towards the heat source (laser beam). This is the characteristic microstructure for SLM parts, as has been previously reported for this alloy [4, 159]. This agrees with results shown in chapter (5) and earlier in this chapter for the microstructure of the single tracks and the single layers. Grains at the melt pool boundaries were coarser and generally had a columnar morphology indicating cellular-dendritic growth during solidification, as demonstrated in **Figure 98**. This is attributed to this region being in contact with readily solidified Al that has lower thermal conductivity – compared to the molten metal – imposing slower solidification. When the liquid metal solidifies on a flat solid surface, unidirectional solidification is adopted rather

than equiaxed solidification [157]. In the unidirectional solidification, the layer of the molten metal grows forming crystals into cellular-like grains and then transition to the dendritic form occurs. Conventional processing of AlSi10Mg, being a hypo-eutectic alloy, results in a forest of Al dendritic structure surrounded by inter-dendrite Al-Si eutectic. The form of Si in the alloys changes depending on the cooling rate, such as quench modification, thermal modification, or chemical modification through the addition of modifiers like Na, Sr, Sb, or P. Fast solidification of Al alloys results in microstructure refinement [45].

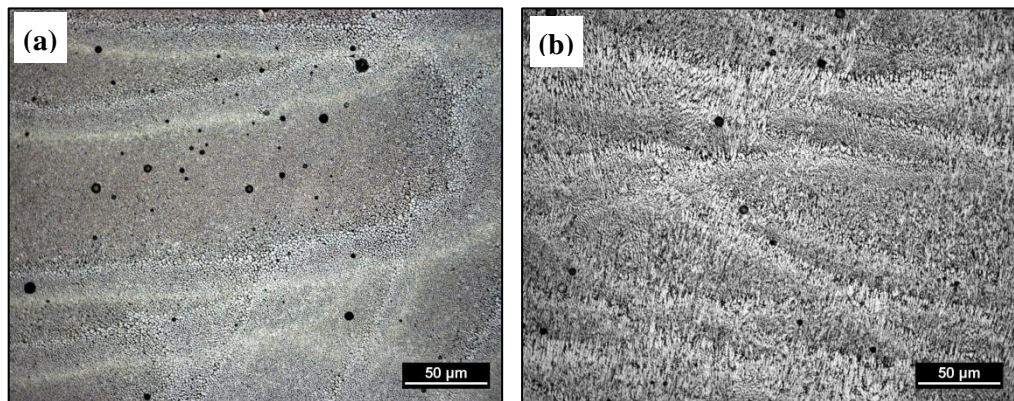


Figure 97: Microstructure of AlSi10Mg part processed by SLM (a) XY-plane and (b) YZ-plane.

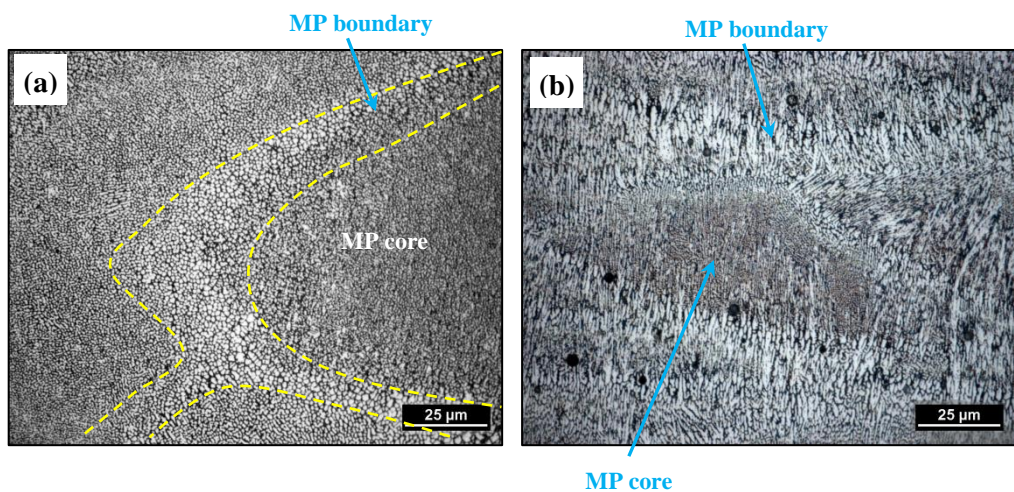
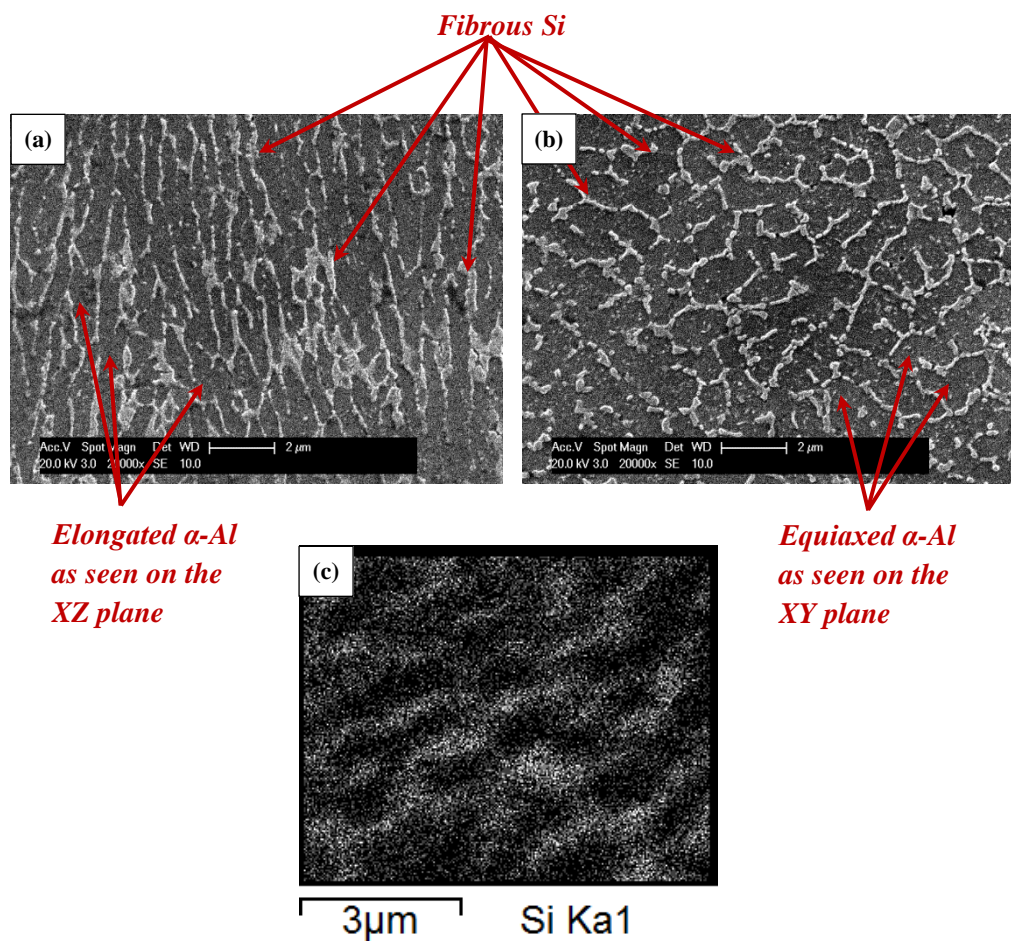


Figure 98: Coarser grains observed at the melt pool boundary in the (a) XY-plane shown as (b) cellular-dendritic grains in the YZ-plane.

Coarsening of Al at the melt pool boundaries reduces the fraction of grain boundaries in this region, which means fewer sites for Si segregation. This is why the melt pool boundaries were rich in Al whereas the cores were rich in Si. EDX confirmed that during solidification Si is located at the Al boundaries (see **Figure 99**). Fast cooling reduces the amount of Si rejected into the liquid by extending the solubility of Si in Al [160], so  $\alpha$ -Al solidifies first in the preferential cellular structure leaving the residual Si at the boundaries [85].



**Figure 99:** Microstructure of (a) as-built sample XZ plane, (b) as-built sample XY plane, and (c) EDX composition map for Si in the as built sample XY plane.

Hot cracking was not observed when selectively laser melting AlSi10Mg because of the presence of Si and its content being in the range between 7 wt% and 12 wt%. This composition means the solidification time is short and the eutectic amount is large [161]. Also, the presence of Si in the alloy reduced shrinkage during solidification because during changing phases from liquid to solid it expands [161]. (It is the low shrinkage of the Al-Si alloy system that grants it its commercial importance in casting and welding [45].)

Since AlSi10Mg is a hardenable alloy [162], heat treatment using a conventional T6 heat treatment was studied. At the first step of heat treating the SLM part (solution heat treatment), the material is fully homogenised. Solution heat treatment (SHT) involves maintaining the material at an elevated temperature (520 °C) for duration long enough in order to obtain a homogenous supersaturated solid solution after quenching. For conventional cast Al-Si alloys, too short SHT durations mean that not all the alloying element present in the material might have enough time to dissolve. Whereas SHT of too long a duration means adding more energy than necessary [162]. In order to preserve the supersaturated structure, the material is then quenched to room temperature. Rapid quenching using water is recommended in order to obtain the best combination of strength and ductility [162] and so this was applied in the current study. The material is then aged at a temperature of 160°C. The metallic compound  $Mg_2Si$  and Guinier-Preston I (GP I) zones form at early stages of ageing. Then Guinier-Preston II (GP II) zones form at regions containing metallic compounds rather than the solid solution with further ageing [38]. Following the formation of GP II zones (in the form of rods), a  $\beta'$  intermetallic phase is formed (also in the form of rods or needle-like structures), which is

followed by the intermetallic phase at equilibrium that is  $\beta$ -phase “ $\text{Mg}_2\text{Si}$ ” (in the form of plates) [89].

When the SLM material was solution heat treated for 1 hr, the microstructure coarsened and Si started diffusing to form particles (spheroidisation) instead of being segregated around the boundaries of the  $\alpha$ -Al (see **Figure 100 (a)**). Diffusion in materials is driven by the aim of reducing Gibbs free energy [89]. High temperatures (during heat treatments) provide the activation energy required for diffusion rates to increase. A material with fine grain structure has higher diffusion rates since the small grain size means the presence of large grain boundaries areas and grain boundaries favour diffusion due to their high energy states owing to the higher density of lattice defects (eg. vacancies and dislocations) [38, 42]. Further increase in the solution heat treatment duration (4 hrs) promoted diffusion, leading to the formation of larger particles (see **Figure 100 (b)**). Agglomerates of Si particles were observed at the melt pool boundaries. The preferential growth of Si particles at the melt pool boundaries could be seen because these regions were remelted more than once during processing since they lie at the overlap of two hatches. Solution heat treatment for more than two hours significantly dissolved the scan tracks even before ageing, as shown in **Figure 100 (b)** for the sample that underwent solution heat treatment for 4 hrs. The scan tracks that were not dissolved during solution heat treatment diminished upon ageing, yielding a more homogenous microstructure (**Figure 100 (c)** and **(d)**).

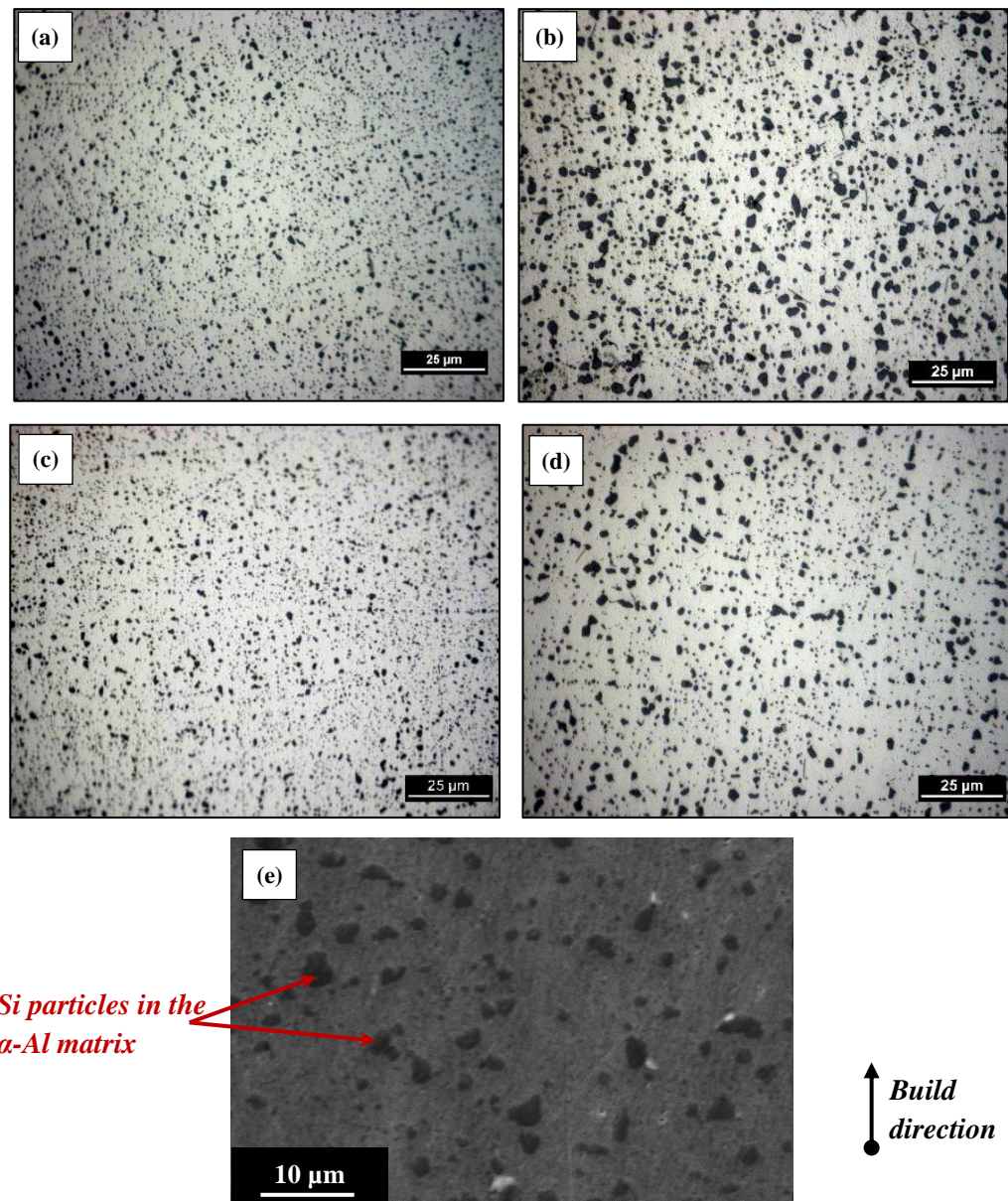


**Figure 100:** Microstructure of SLM samples (a) XY plane after 1 hr SHT, (b) XZ plane after 1 hr SHT and 12 hrs AA , (c) XZ plane after 4 hrs SHT, (d) XZ plane after 4 hrs SHT and 6 hrs AA, and (e) higher magnification image of XZ plane after 1 hr SHT and 6 hrs AA showing the morphology of Si particles.

The observations made from the micrographs of the samples treated for different durations (**Figure 100**) were further supported by analysing the size of the Si particles and their density (using the open source software ImageJ 1.46r [130]). The particles' size and density in the as-built samples could not be quantified since the alloying elements were continuous segregations at the

grain boundaries without a definite shape (see **Figure 101**). However, at the early stages of solution heat treatment (1 hr), particles started to form with a specific size and spatial density.

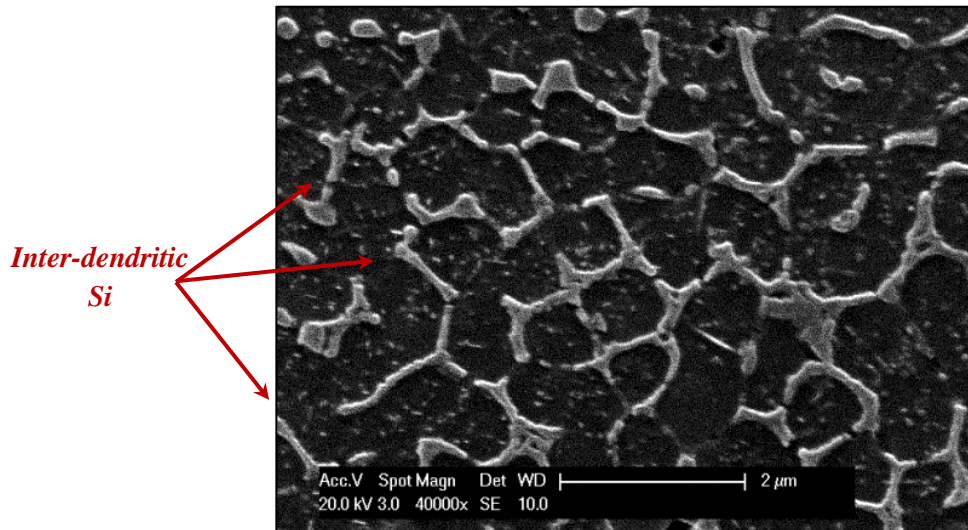


**Figure 101: Higher magnification SEM image clearly showing inter-dendritic Si around the  $\alpha$ -Al boundaries in the as-built sample.**

As solution heat treatment progressed, the average particle size increased until it reached a plateau in the range of 3-4 hrs, with average Si particle sizes of 1.40  $\mu\text{m}$  and 1.42  $\mu\text{m}$ , respectively, as demonstrated in **Figure 102**. The density of the particles decreased with increasing the solution heat treatment duration since the particles diffused to form larger particles, but the quantity of Si remained constant (**Figure 102**). When all samples subjected to different solution heat treatment durations were aged for 6 hrs, it was observed that the Si particle size and density were not significantly altered. The particles' size and density started to change with further ageing. It is important to note that during heat treatment, not only particle diffusion or dissolution occurred but also nucleation sites for the formation of needle-like  $\text{Mg}_2\text{Si}$  precipitates create that could influence the measurements of the particle size and density. In

addition, a fraction of these precipitates might not be adequately represented because their size is below the threshold of the image's resolution. Nevertheless they will be contributing to the overall hardness of the material. The effect of the conventional T6 heat treatment on the various mechanical properties will be discussed in details in chapter (7).

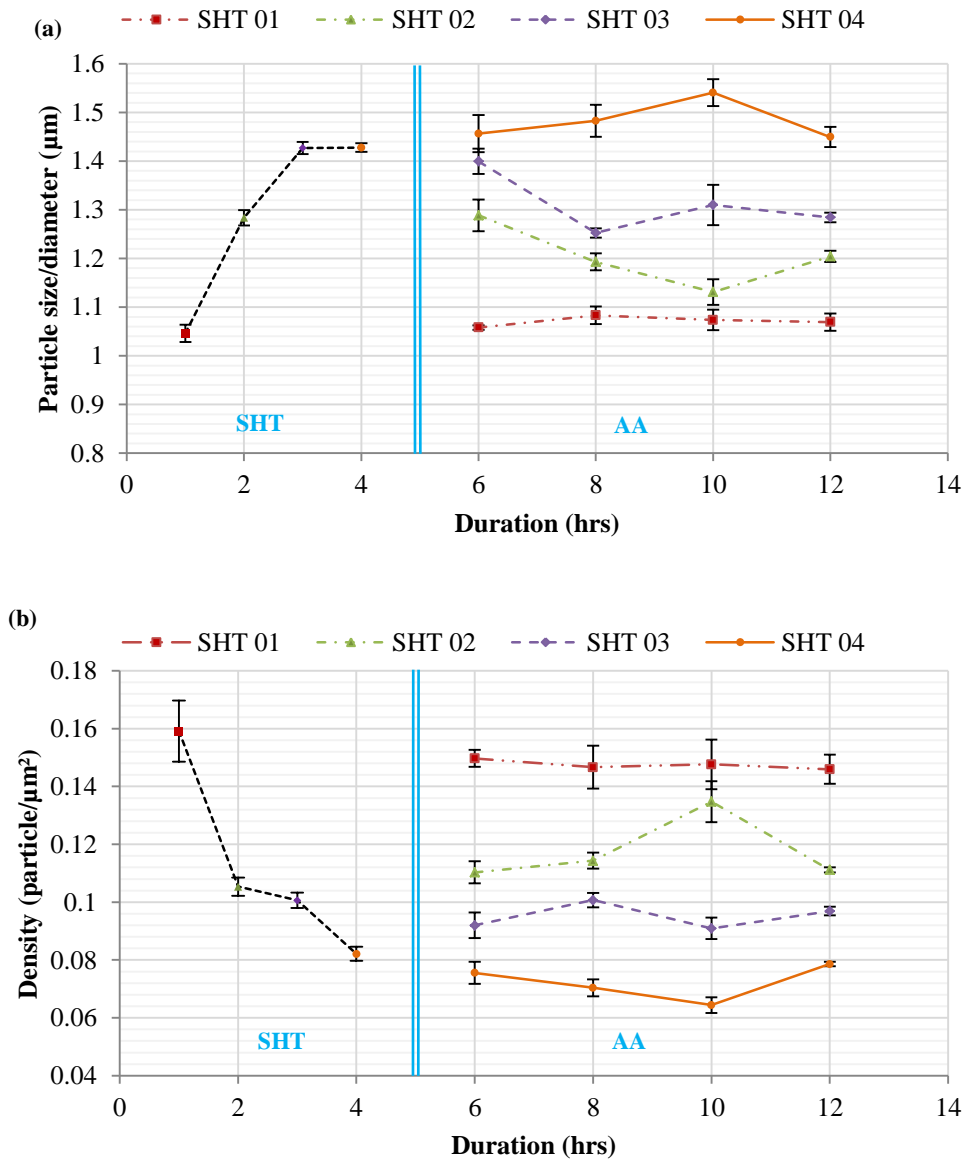


**Figure 102: Particles analysis showing change in (a) average particle size and (b) particle density with heat treatment duration with error bars representing the standard error.**

#### 6.4. Summary

- The material irradiated by the laser beam in selective laser melting experiences rapid solidification, which results in a finer microstructure when compared to the cast material for the same alloy.
- Melt pools of single tracks showed two distinct microstructures; a coarse elongated grain structure at the melt pool boundary with the grains oriented along the direction of the thermal gradient and a fine equiaxed grain structure at the melt pool core.
- The higher the scan speed, the faster the rate of cooling during solidification thus the microstructure is further refined. Nevertheless, the faster scan speed produced a more random grain orientation due to the high turbulence within the melt pool during processing.
- The rapid solidification also led to a good dispersion of the alloying elements within the SLM material, as was shown by energy dispersive spectroscopy.
- SLM material is characterised by a poor surface roughness due to the presence of satellites and irregularities on the surface.
- The alloy after selective laser melting processing was a two phase material as peaks for both Al and Si were observed in XRD patterns.
- The selectively laser melted AlSi10Mg was textured, which is common in materials processed by SLM because of the nature of the process and the associated directional solidification mechanism.
- In the SLM material, dendritic Si was in the form of continuous segregations on the grain boundaries of  $\alpha$ -Al. When the material was heat treated with a conventional T6 heat treatment, Si diffused to form

spheroids in the Al matrix. As the heat treatment duration increased, the density of Si in the material decreased and their particles sizes increased.

## **CHAPTER (7): Mechanical characterisation of selectively laser melted AlSi10Mg**

This chapter presents the mechanical properties of SLM AlSi10Mg at the nano, micro, and macro scales. The nano-scale level is represented by the nano-hardness and indentation modulus determined using nanoindentation aiming at understanding the local mechanical properties. For the microscopic level, micro-hardness is measured. Tensile, compressive, and fatigue behaviours are evaluated to reflect the properties of the material at the macroscopic level. In addition, the effect of a conventional T6 heat treatment on the mechanical properties is studied. Chemical composition mapping was conducted to relate the local mechanical properties to the chemical elements' distribution.

### **7.1. Nano-scale properties using nanoindentation**

Nanoindentation test, also known as Depth Sensing Indentation “DSI” or Instrumented Indentation Testing “IIT” [163], is used to determine the hardness of a material. In the conventional indentation testing, the area of the residual plastic impression left on the material is measured and used to determine the hardness, however in nanoindentation the depth of penetration is measured since the area is too small (in the nano-meter size range) to be measured. Given the known geometry of the indenter tip, the area of the impression is determined from the measured depth of penetration. Nanoindentation is not only used to determine a material's hardness, but it can

also be used to find several mechanical properties, such as its elastic modulus, strain hardening exponent, fracture toughness, internal residual stresses, and viscoelastic properties [163]. One of the advantages of using nanoindentation is that it can determine local mechanical properties rather than bulk properties and evaluate the mechanical performance of very small structures because of the small size of test specimen needed. The increasing interest in smaller sized components, such as lattice structures for instance, makes the use of nanoindentation to characterise the mechanical properties even more useful.

There are two modes of nanoindentation tests; load-controlled and depth-controlled with the former being more commonly used. Practically, the indenter moves towards the sample until contact is detected and then the loading cycle starts where the load is gradually increased until the maximum specified load is reached. At this point, the unloading cycle starts and towards the end of the unloading cycle, there is a dwell/hold period to collect data for thermal drift correction [163]. An illustrative example for a nanoindentation test with the load-depth curve can be seen in **Figure 103**.

In order to determine the hardness and indentation modulus of a material from the nanoindentation test results, the projected area of the impression has to be calculated. For a Berkovich indentation tip, the one used in the experiments in this study, the face angle is  $65.27^\circ$ . The formula to calculate the projected area is as follows:

$$A = \sqrt[3]{3h^2} \tan \theta = \sqrt[3]{3h^2} \tan 65.27 = 24.5 h^2$$

Where  $A$  is the projected area,  $\theta$  is the face angle, and  $h$  is the total depth of penetration below the sample surface. The hardness  $H$  can then be calculated using the maximum load  $P$  and the projected area  $A$  as follows:

$$H = \frac{P}{A}$$

The indentation modulus  $E$  is determined from the slope of the unloading curve

$\frac{dP}{dh}$  and the projected area  $A$  by:

$$E = \frac{1}{2} \frac{dP}{dh} \frac{\sqrt{\pi}}{\sqrt{A}}$$

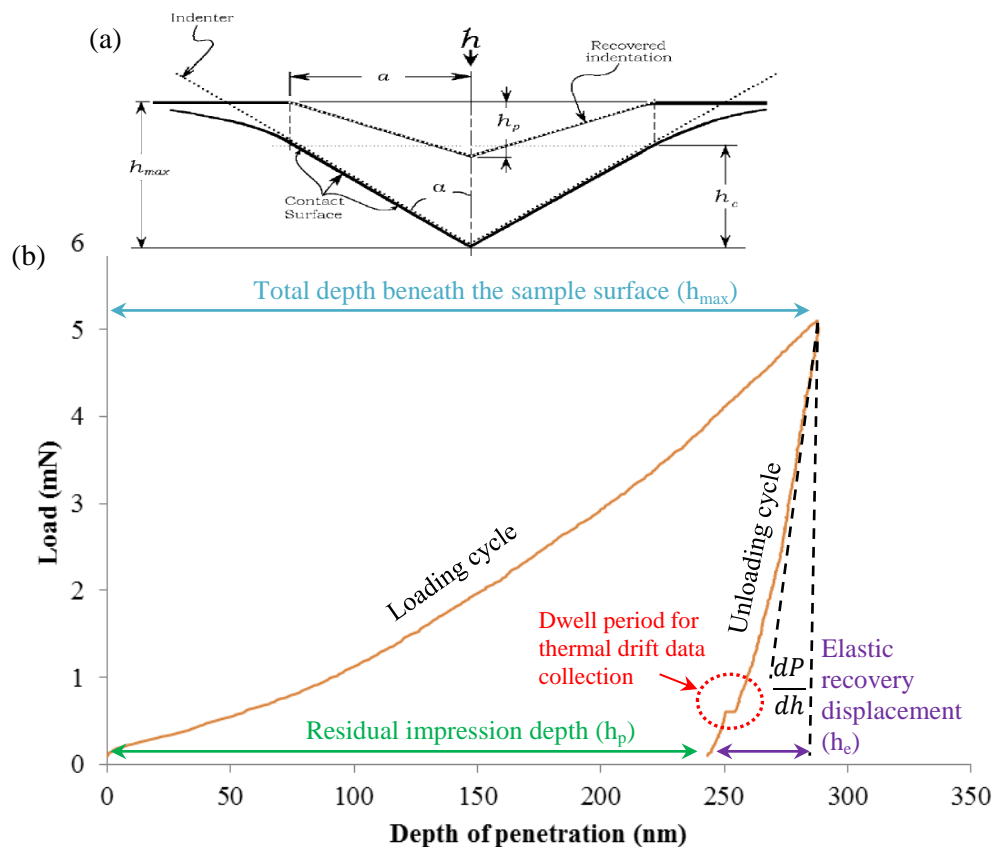
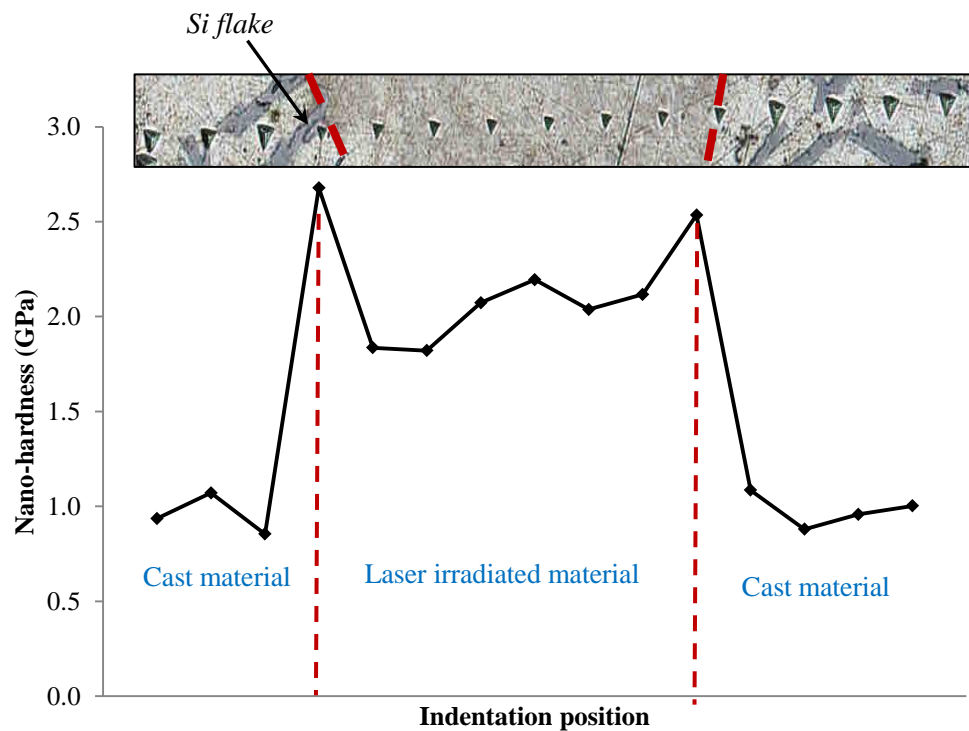


Figure 103: An illustrative example for loading and unloading in a nanoindentation test (a) schematic presentation for an indentation [136] and (b) load-depth curve.

### 7.1.1. Nano-hardness profiles across a single track

The finer microstructure developed in the laser irradiated material is thought to yield improved mechanical properties [164] when compared to the conventionally manufactured counterpart, e.g. through casting. This was evident in the nano-hardness profile across a melt pool of a scan track created on a cast substrate, as shown in **Figure 104**. The average nano-hardness in the cast material was  $0.97 \pm 0.03$  GPa, whereas the average nano-hardness in the laser irradiated material was  $2.2 \pm 0.1$  GPa. This means that an almost doubled nano-hardness is achieved via laser treatment owing to the characteristically fine microstructure and the good dispersion of the alloying elements, as was presented in chapter (6).



**Figure 104:** Nano-hardness profile of a line positioned at half the maximum height of a scan track spanning across both the laser irradiated material and the as-cast material.

It is worth noting that none of the indentations on the cast material in the row of indentations in **Figure 104** was coincident on a Si rich flake. Indentations on

the Si rich flakes in another array (not shown here) returned an average nano-hardness of  $9 \pm 1$  GPa. This shows that there is spatial variation in hardness in the cast material at the microstructural level. The finer homogenous microstructure in the laser irradiated material, however, provides a more uniform hardness profile. The indentations at the melt pool boundary (the first and last indentations within the melt pool) showed higher hardness than the core of the melt pool. This was seen to be high due to proximity to the Si flakes in the cast material upon investigation with an optical microscope (shown in the inset in **Figure 104**).

There are a number of strengthening mechanisms in the laser irradiated material under investigation, namely, grain size reduction, solid solution strengthening, and dislocation strengthening [165]. The grain size reduction is governed by the Hall-Petch equation where strengthening occurs due to the increased fraction of grain boundaries hindering the motion of dislocations [64]. The grain size reduction in the laser irradiated material is achieved by rapid solidification. The solid solution strengthening is due to the presence of the alloying elements and dislocation strengthening is due to the presence of the density of dislocations. High densities of dislocations in SLM materials have been previously observed and attributed to the rapid cooling rates in Iron [115] and rapid cooling rates in Al casting alloys such as the case in welding also produces dislocation cells and forests [166]. The effect of these strengthening mechanisms in SLM compared to cast material explains the higher nano-hardness.

The grid of indentations in **Figure 105** comprises 259 indentations spanning across the melt pool of the scan track and the cast material in the substrate.

This full grid supports the finding reported earlier about the difference in hardness between the laser irradiated and cast materials. As can be seen in **Figure 105 (a)**, the cast material shows spatial variation in nano-hardness that is related to the indented phase as indicated by the corresponding micrograph in **Figure 105 (c)**. In other words, the hardness map in **Figure 105 (a)** shows that at certain locations, hardness was significantly higher than the averaged range. Visual observation of the indentations suggests the hardness dependence on the indented phases. On comparing the map with the optical micrograph in **Figure 105 (c)**, it was found that the particularly high hardness was for the indentations coincident on Si flakes. The map in **Figure 105(b)** excludes the substrate and shows only the nano-hardness profile within the melt pool. The average nano-hardness within the scan track processed from AlSi10Mg powder at 500 mm/s scan speed was  $2.27 \pm 0.02$  GPa, as recorded in this array of indentations, without significant clear variation between the core and boundary nano-hardness.

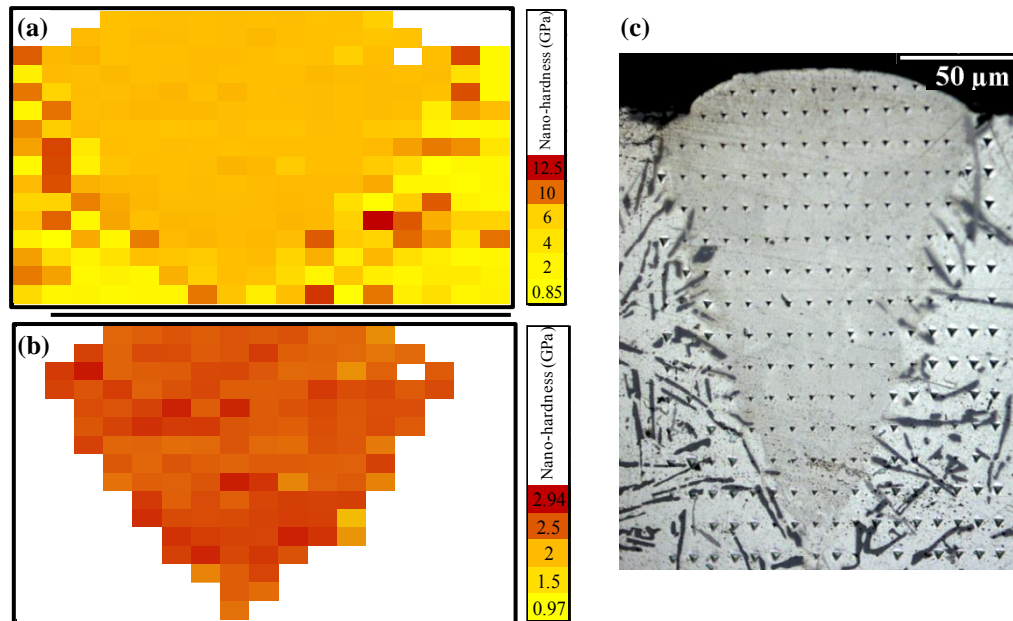


**Figure 105: The nano-hardness profile across the AlSi10Mg scan track (a) including the cast substrate and (b) excluding the cast-substrate. The array of indentations from which the nano-hardness map was retrieved is shown in (c).**

### 7.1.2. Nano-hardness profiles across a single layer

The hardness profile across overlapping melt pools, retrieved from an array of 272 indentations across a single layer, is demonstrated in **Figure 106**. The average nano-hardness across the melt pools was  $2.13 \pm 0.01$  GPa. Results from indentations on the cast substrate are not presented in this section to avoid duplication of similar findings presented in the previous section. Again a uniform hardness profile was seen. It is worth noting that the average nano-hardness within the single layer was 6% less than that within the single track. This softening could be attributed to microstructural coarsening driven by the re-melting of the material due to the overlap between the single tracks building up the layer. This partial re-melting leads to slower solidification, i.e. coarser microstructure hence the reduced nano-hardness at these regions.

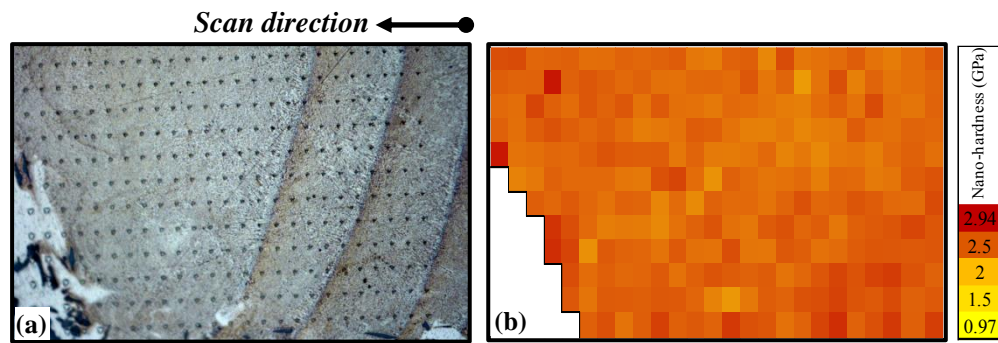


**Figure 106:** The array of indentations on (a) a series of overlapping melt pools in a single layer alongside (b) the corresponding nano-hardness profile.

By means of EDX and SEM, the chemical composition at specific indentations on the laser irradiated material and cast substrate was determined to relate the chemical composition to the mechanical property in terms of nano-hardness. **Figure 107 (a)** shows the chemical composition at two indentations within the SLM material. The origin of the amount of Fe detected in the material is the cast substrate since its material is AlSi12. The hardness profile across the melt pool was uniform, as was the chemical composition. This finding further supports the suggestion that the rapid solidification of the molten material results in the formation of a fine microstructure with the alloying elements uniformly dispersed. Also, the fast cooling rate does not allow sufficient time for the alloying elements (Si, Fe, and Mn in the case of the AlSi12 substrate) to diffuse and form flakes like those in the cast regions in **Figure 107 (b) to (d)**.

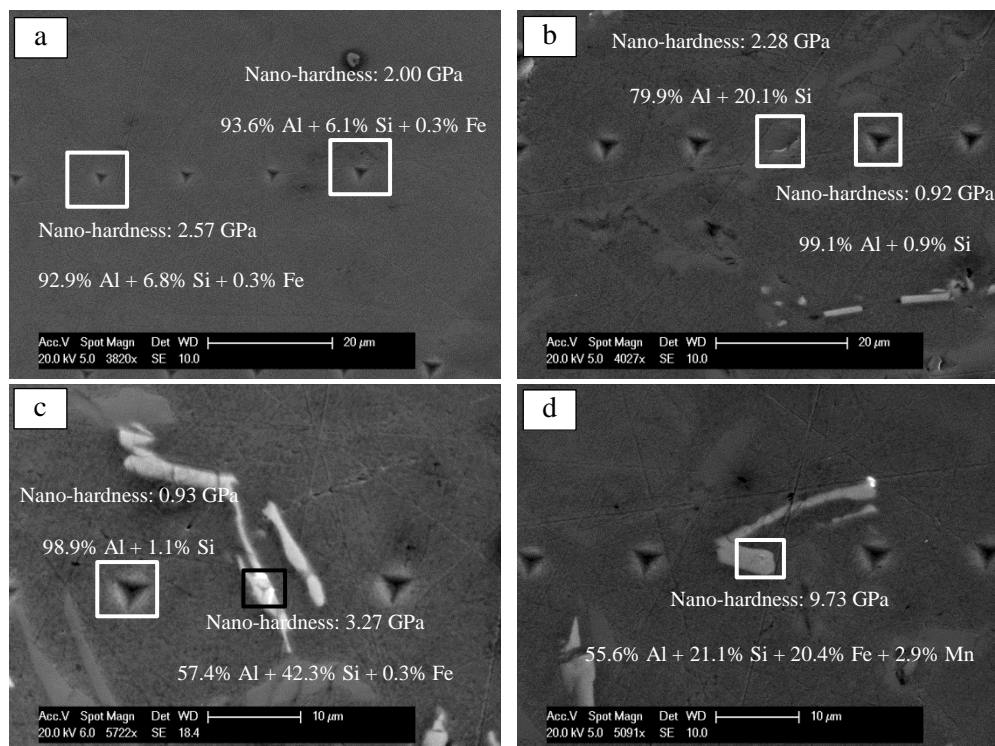


**Figure 107: SEM micrographs showing nano-indentations and corresponding chemical compositions within (a) the laser irradiated material (a) and at (b), (c), and (d) various points within the cast substrate.**

In case of the indentations on the cast substrate, the value of nano-hardness varied significantly according to the chemical composition at the indented region. For instance, indenting over an Al rich region in **Figure 107 (b)** yielded a nano-hardness of 0.92 GPa, whereas another point on the same figure with an increased Si content (20%) yielded a nano-hardness of 2.28 GPa. In **Figure 107 (c)**, the difference in nano-hardness between regions rich in Si and Fe and an Al-rich region is shown with the latter's nano-hardness of 0.93 GPa, whereas indenting a flake rich in Si and Fe increased the nano-hardness to 3.27 GPa. **Figure 107 (d)** shows the effect of Si and Fe in addition to Mn, where in this case, the nano-hardness increased to 9.73 GPa. The illustrated results show that the variation in chemical composition across the substrate material influences the nano-hardness values. Regions rich in Al were found to

be the softest, the hardness increases gradually with the increase in Si content, and furthermore with the presence of Fe and Mn. However, the hardness profile across the melt pools formed by laser irradiation was quite consistent in comparison to the substrate material due to the homogenous composition.

### **7.1.3. Nano-hardness profiles across multi-layered parts**

The scan strategy used to fabricate a part affects the produced microstructure specially in case of using single versus multiple scans per layer. The resultant microstructure when using a single scan strategy (**Figure 108 (a)**) was slightly coarser than that when using a pre-melt scan strategy (**Figure 109 (a)**) where each layer is scanned twice. In its turn, the variation in microstructure led to a variation in the mechanical response of the material towards nanoindentation, as shown in the nano-hardness maps in **Figure 108 (b)** and **Figure 109 (b)**. The material processed using a single scan possessed an average nano-hardness of  $1.70 \pm 0.03$  GPa, whereas using the pre-melt scan strategy yielded an average nano-hardness of  $1.96 \pm 0.01$  GPa. The variation in properties with the scan strategy can be understood from the change in the microstructure of the material. According to Thijs *et al.* [4], the use of a double scan strategy reduced the crystallographic texture in the material, however, in their study the orientation of the second scan was rotated by  $90^\circ$ , which could have a more pronounced influence on reducing the texture. The correlation between the scan strategy, crystallographic texture, and nano-hardness requires further investigation beyond the scope of this thesis.

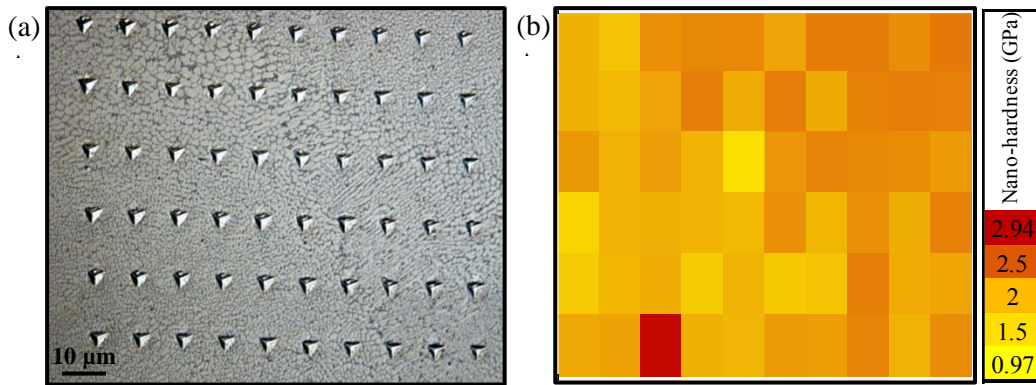


Figure 108: An array of indentations across layers in a part fabricated using a single scan strategy showing (a) the microstructure and (b) the corresponding nano-hardness map.

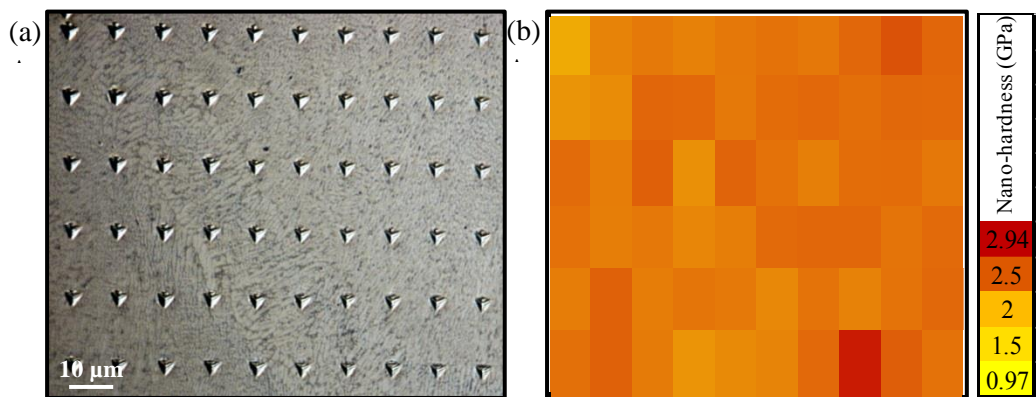


Figure 109: An array of indentations across layers in a part fabricated using a pre-melt scan strategy showing (a) the microstructure and (b) the corresponding nano-hardness map.

#### 7.1.4. Nano-hardness in the vicinity of keyhole pores

The discussion in chapter (5) stated that the regions in the vicinity of keyhole pores in multi-layered parts exhibited a coarser microstructure. This is also demonstrated by the coarsened microstructure in the top region in **Figure 110 (a)** above which a keyhole pore existed as well as the lower section in **Figure 111 (a)** below which the pore existed. In the case of the single scan strategy, the keyhole pore vicinity showed a nano-hardness of  $1.66 \pm 0.02$  GPa; indicating softness in these regions (**Figure 110**). Results from samples processed using a pre-melt scan strategy (**Figure 111**) agree with this finding where the nano-hardness was reduced to  $1.81 \pm 0.03$  GPa.

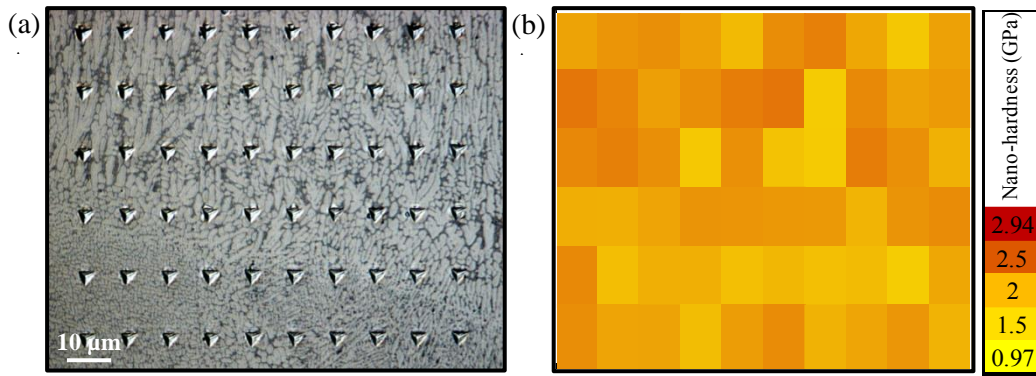


Figure 110: (a) Coarsened microstructure in the vicinity of a keyhole pore (towards the top) in a sample processed using a unidirectional scan strategy alongside (b) the corresponding nano-hardness profile.

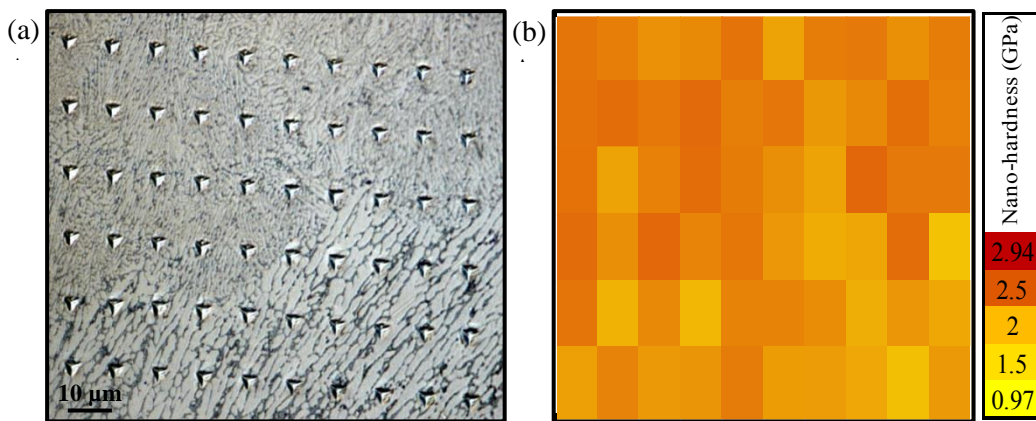


Figure 111: (a) Coarsened microstructure in the vicinity of a keyhole pore (towards the bottom) in a sample processed using a pre-melt scan strategy alongside (b) the corresponding nano-hardness profile.

In addition to material softening in the regions surrounding keyhole pores, a spatial variation in nano-hardness within the sample showed as a result of the modified microstructure. This variation in local mechanical properties is a setback for the reliability of the parts produced by SLM because the defected regions will be susceptible to premature failure in parts used in load bearing applications. This supports the need to minimize porosity in SLM parts, specifically the keyhole pores that lead to an altered microstructure in their vicinity.

### **7.1.5. Nano-hardness profiles across multi-layers and the effect of heat treatment**

It has already been established in chapter (6) that a conventional T6 heat treatment dramatically changes the microstructure of the SLM material. This change in microstructure will have an effect on the various mechanical properties of the parts manufactured using this material. The average nano-hardness of the as-built SLM material was 1.82 GPa ( $\pm 0.01$  GPa standard error), as retrieved from 104 indentations spanning over an area of  $130 \mu\text{m} \times 120 \mu\text{m}$ . The samples used in this section were manufactured using a different machine (Renishaw AM250) from the one used in sections 7.1.1 to 7.1.4 (Realizer SLM50) and so the processing parameters were also different. The aim of this change is to be able to tie in results from this section to the following ones (tensile, compressive, and fatigue properties) making use of the larger build platform in the Renishaw AM250 machine that is able to accommodate the test specimens for the macro-scale properties tests. This explains the slight variation in nano-hardness results from multi-layered parts in this section when compared to those in previous sections.

After the conventional T6 heat treatment (solution heat treatment for 1 hr at  $520^\circ\text{C}$  followed by ageing for 6 hrs at  $160^\circ\text{C}$  after water quenching), the average nano-hardness was reduced to 1.52 GPa ( $\pm 0.02$  GPa standard error) according to the same number of indentations. This indicates that the actual effect of this heat treatment on the material is one of softening rather than hardening as would have been the case in conventionally processed materials [167]. A t-test was performed to determine the statistical significance of the difference between both data sets with a confidence level of 95%. Since the t-

value (12.05) was greater than the critical t-value (1.97) for a two-tailed test, the null hypothesis that there is no difference between the as-built and heat-treated nano-hardness can be rejected. The nano-hardness maps over the sampled areas in the as-built and the heat-treated specimens are shown in **Figure 112 (a)** and **(b)**. The as-built material showed a uniform hardness profile whereas the heat-treated material displayed spatial variation within the tested region due to some indentations yielding significantly higher nano-hardness than the average. Examples of the indented regions along with the Berkovich nano-indenters are demonstrated in **Figure 112 (c)** and **(d)**.

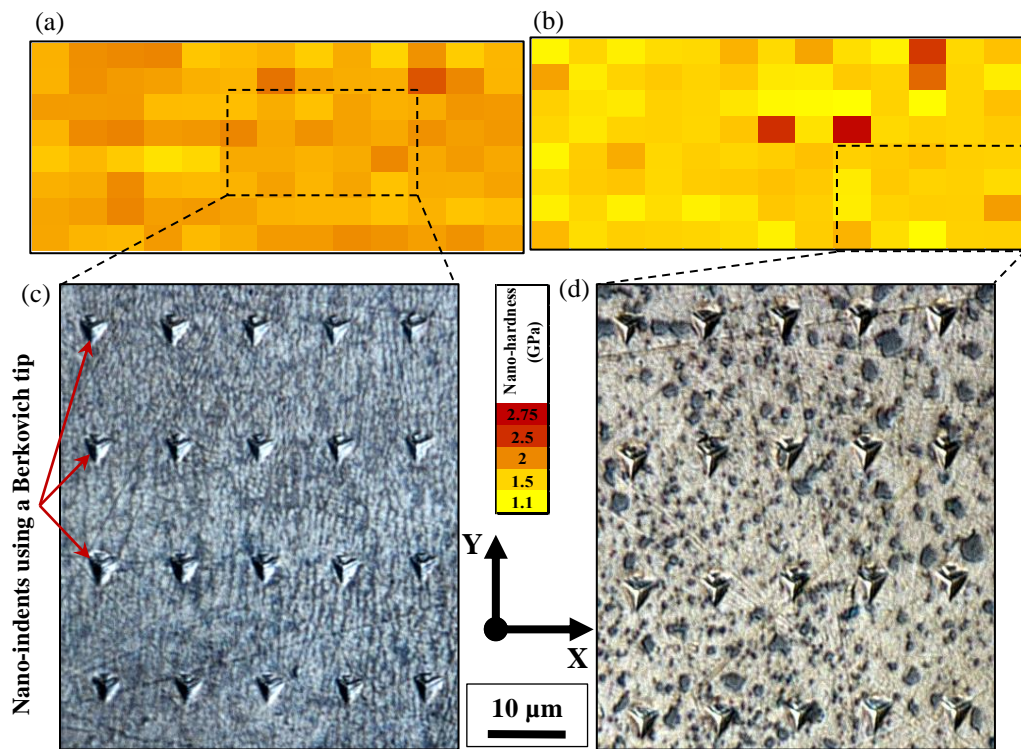


**Figure 112:** Nano-hardness map demonstrating the property profile within (a) as-built SLM AlSi10Mg and (b) heat-treated SLM AlSi10Mg, as well as examples of the nano-indenters on the tested surfaces (c) as-built SLM material and (d) heat-treated SLM material.

The uniform nano-hardness within the as-built material is attributed to the fine microstructure with the good dispersion of the alloying elements, as can be seen in **Figure 113 (a)**. Closer investigation of the microstructure of the

material, as can be seen in **Figure 113 (c)**, revealed the cellular-dendritic microstructure made up of  $\alpha$ -Al and fibrous Si. Similar microstructure has been previously reported by Thijs *et al.* [4]. This characteristic microstructure is driven by the fast cooling rate the material experiences during processing [121, 167] and the direction of the columnar dendrites is controlled by the thermal gradient. The spatial variation in the nano-hardness of the heat-treated material is due to phase transformation occurring during treatment that was explained in chapter (6). The solution heat treatment allows enough time for Si to diffuse and form particles/spheroids [85, 167], referred to as spheroidisation transformation, as shown in **Figure 113 (b)**, in addition to the microstructure coarsening. The presence of these Si particles along with the coarser microstructure produces nano-hardness sensitivity to the indented phases [168]. The decrease in the nano-hardness after heat treatment is attributed to the difference in the strengthening mechanisms due to the microstructural changes occurring during heat treatment. The main strengthening factor in the as-built material is the fine microstructure, whereas in case of the heat-treated material it is the presence of precipitates (Orowan strengthening) [167] since AlSi10Mg is capable of precipitating  $Mg_2Si$ . From these results, it can be deduced that the grain size reduction effect outweighs that of the dispersoids. The indentation modulus of the as-built samples was  $100 \pm 1$  GPa and that of the heat treated samples was  $105 \pm 1$  GPa.

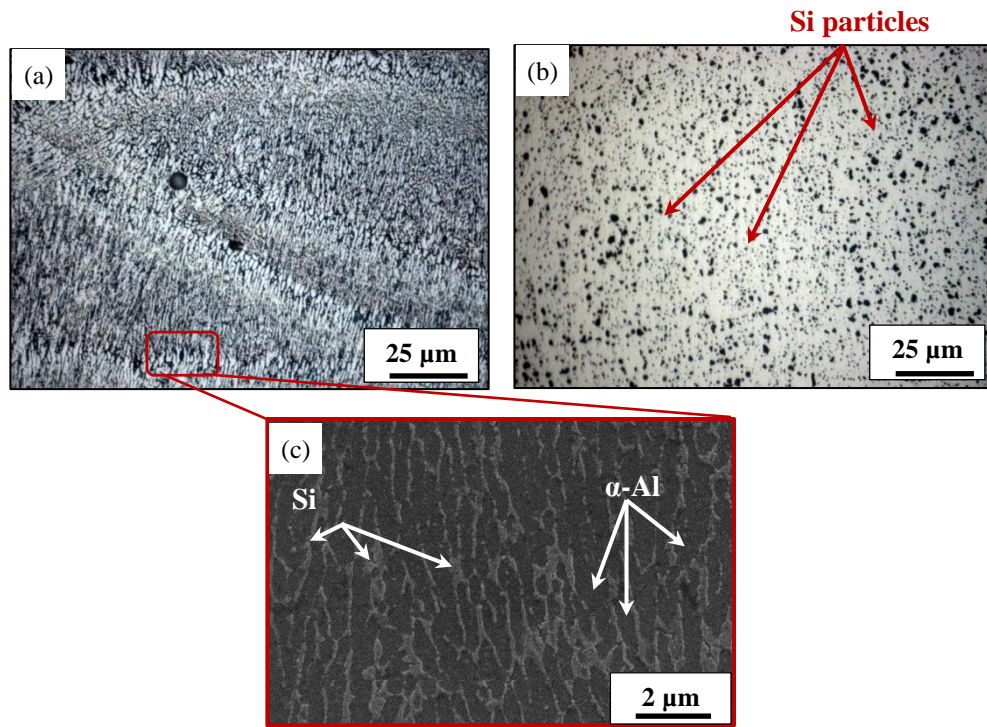


**Figure 113: Microstructure of the SLM AlSi10Mg (a) as-built and (b) heat treated, and (c) high magnification image for the as-built microstructure revealing the inter-dendritic Si within the  $\alpha$ -Al matrix.**

## 7.2. Micro-scale properties: micro-hardness

This section presents the effect of the conventional T6 heat treatment on the micro-hardness of the SLM material. Micro-hardness tests were conducted using a Vickers hardness tester with a load of 300 gf. The hardness of the prepared samples was expected to be influenced by the microstructure developed at different heat treatment durations as was the case in the nano-hardness results. In order to relate the evolution in the microstructure to the micro-hardness, these tests were conducted over a range of samples heat treated by the T6 treatment over a wide range of solution heat treatment and ageing durations. The evolution of hardness with changing the heat treatment duration can be found in **Figure 114**. The highest hardness was achieved with the as-built material. The material was significantly softened by solution heat treatment for one hour due to microstructure coarsening. Hardness started to

increase with further increase in solution heat treatment duration. This could be attributed to the increase in the size of the Si particles, as described in chapter (6) section 6.3.3. Hardness then increased when the material was artificially aged possibly due to the formation of  $Mg_2Si$  precipitates. However, it is quite noticeable that the maximum enhancement in hardness falls short compared to the as-built material; losing 12.3% of the original hardness. This is better understood by considering the various strengthening mechanisms in both the as-built and heat-treated material. In the as-built material, hardness or strength is mainly attributed to: (1) grain size reduction governed by the Hall-Petch equation  $\sigma_y = \sigma_0 + k (d)^{-1/2}$ , where  $\sigma_y$  is the yield strength,  $\sigma_0$  is a material constant denoting the stress required to start dislocation motion,  $K$  is the strengthening coefficient, and  $d$  is the grain size, (2) solid solution strengthening due to the presence of alloying elements, and (3) dislocation strengthening through the interaction of dislocations impeding each other's motion. On the other hand, strengthening in the case of the heat-treated material is dominated by the presence of precipitates or dispersoids, replacing the grain size reduction factor in the as-built material, in addition to the solid solution strengthening and dislocation strengthening [165]. In as-built samples the dislocation motion is mainly hindered by the increased volume of grain boundaries, whereas in the treated material the dislocation motion is obstructed by the dispersoids acting as obstacles. The mechanism of hardening by the T6 heat treatment in the alloys that are capable of precipitation (Orowan strengthening) is that the dislocation motion is hindered by the particulate (harder precipitate) that blocks its path. Consequently, for the dislocation motion to progress, shear stress is required to pass between the precipitates.

The closer the precipitates to each other, the stronger the material is, since the dislocation segment will exert more force to pass through [42]. During the T6 heat treatment, small precipitates are formed until a certain limit when a high density exists, a stage after which an increase in heat treatment temperature or duration will lead to the small precipitates coarsening to form large precipitates depressing the strength of the material [89]. For overaged materials, the strength decreases because the precipitates are bypassed by the dislocation, depressing the effect of Orowan strengthening [169]. This is because the increase in precipitate size requires more energy from the dislocation to shear through, so bypass is promoted [170]. The presence of precipitates in aged alloys is known to boost the material's hardness. This was evident in this study when comparing the samples subjected to solution heat treatment only, to those aged afterwards. However, this was not the case when comparing aged samples to as-built. This indicates that the effect of grain boundary strengthening (through grain size reduction) in the as-built samples outweighed the contribution of Orowan strengthening by the presence of dispersoids in the aged samples.

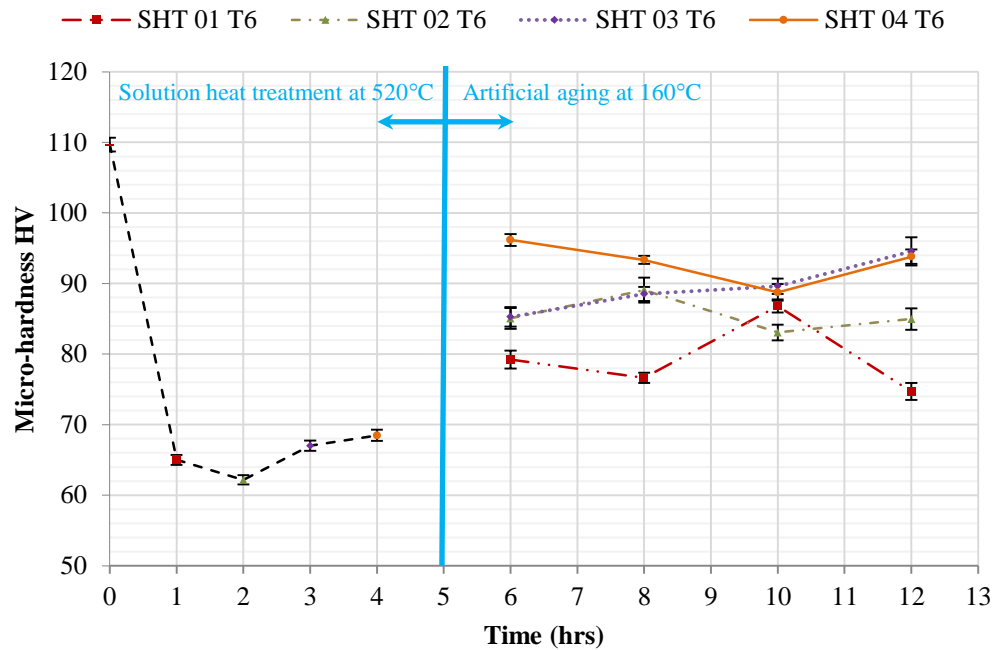


**Figure 114: Evolution of micro-hardness with heat treatment procedure with error bars representing the standard error.**

The importance of this study lies within the difference between the response of conventionally manufactured (e.g. casting) Al alloys and those fabricated by SLM. The response is typically a function of the microstructure. It has been previously reported that the ageing response of Al-Si-Mg alloys is independent of the solution heat treatment time in the case of casting [171]. However, the results discussed here showed that this is not the case for SLM materials, since the solution heat treatment duration significantly influenced the ageing response, as represented by the material's hardness. Moreover, the fineness of the microstructure dominates the selection of solution heat treatment times. For cast alloys, shorter times are needed to completely homogenize finer microstructures [172], but the characteristically fine microstructure of SLM parts required longer durations to stabilize the microstructure and enhance the mechanical response with and without ageing. Precipitation behaviour in coarse-grained Al alloys differs from that in ultrafine-grained Al alloys,

typically due to the difference in the density of dislocations and grain boundary area fraction in each case [173]. A study comparing the precipitation behaviour in coarse-grained and ultrafine-grained Al alloys has shown that the former requires longer durations because dislocations remained after treatment due to pinning of the solute atoms that attracts more dislocations [173]. Consequently, when dealing with Al alloys processed by SLM, it is crucial to bear in mind that it is an ultrafine-grained material rather than a conventional coarse-grained.

Now if we consider the combination of solution heat treatment and ageing durations that were applied to all the samples used in the various mechanical tests in this thesis (1 hr of solution heat treatment and 6 hrs of ageing), the overall micro-hardness, provided in **Table 13**, showed the same behaviour as the nano-hardness results. The hardness of the as-built material was reduced by nearly 28% after heat treatment. This is an indicator that hardening SLM AlSi10Mg requires the development of new procedures rather than following the heat treatments used for conventionally manufactured materials. The inapplicability of conventional heat treatments is driven by the characteristic microstructure developed by SLM [174]. The micro-hardness of the SLM material was higher than its die cast counterpart (95-105 HV [5]) by almost 10%. However, heat treating the die cast material using a conventional T6 treatment increases the micro-hardness to 130-133 HV [5], above that of the SLM material in the current study. This further supports the need to develop a novel heat treatment procedure to strengthen the SLM material as conventional T6 actually causes softening.

**Table 13: Comparing the micro-hardness of SLM AlSi10Mg with and without heat treatment**

SLM AlSi10Mg	As-built	Heat-treated (T6)
Vickers hardness (HV)	$110 \pm 1$	$79 \pm 1$

It is important to note that the micro-hardness ( $110 \pm 1$ ) HV was for indentations on the plane parallel to the build direction in the as-built material, but the plane perpendicular to the build direction showed an average micro-hardness of ( $99 \pm 2$ ) HV. The difference in hardness between the two planes indicates anisotropy in the mechanical properties. Anisotropy in the mechanical properties of SLM parts from Al alloys has been previously reported by [5, 49] and attributed to the layer-by-layer approach and the grain structure and texture developed as a result of the thermal gradient. Anisotropy was not observed in the material after heat treatment since the hardness in both planes reflected an average of ( $79 \pm 1$ ) HV, possibly due to the homogenized microstructure and evolution of the crystallographic texture.

### **7.3. Macro-scale properties: tensile behaviour**

The engineering stress-strain curves in **Figure 115** show that the as-built samples behave in a relatively brittle fashion under tensile loading. Heat treating the samples by a conventional T6 treatment (1 hr of solution heat treatment followed by 6 hrs of ageing) provided the material with enhanced ductility without a drastic loss in tensile strength, i.e. increasing the material's strain hardening capacity, as demonstrated by the extension in the plastic deformation region in the stress-strain curve. This result supports the earlier findings that the as-built material is stronger than the heat-treated.

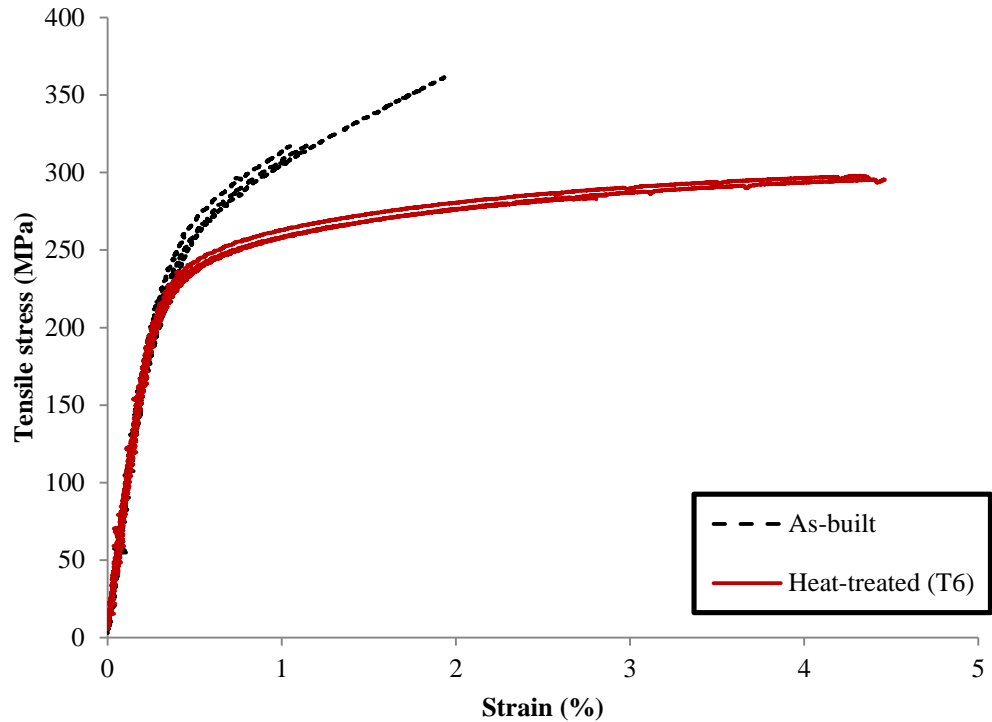


**Figure 115: Engineering tensile stress-strain curves comparing the behaviour of SLM AlSi10Mg with and without heat treatment.**

It is hard to categorise a material as ductile or brittle based on the elongation percent only [175], so the macroscopic features on the fracture surface were examined. Fractography revealed that failure always originated at a surface or sub-surface flaw, as shown in **Figure 116** and propagates along the plane perpendicular to the loading direction until the final fracture region where the shear lip inclined by 45° can be seen (**Figure 117**). This could be attributed to the poor surface roughness that is common in SLM parts and/or the presence of sub-surface defects, such as pores or laser spatter [82]. Macroscopically, the fracture surface was flat with a few regions showing the shear lips that are a sign of relatively brittle failure [175]. No significant necking was observed in any of the tested samples due to the process-induced brittleness. This was also demonstrated by the fracture stress being equal to the ultimate tensile strength.

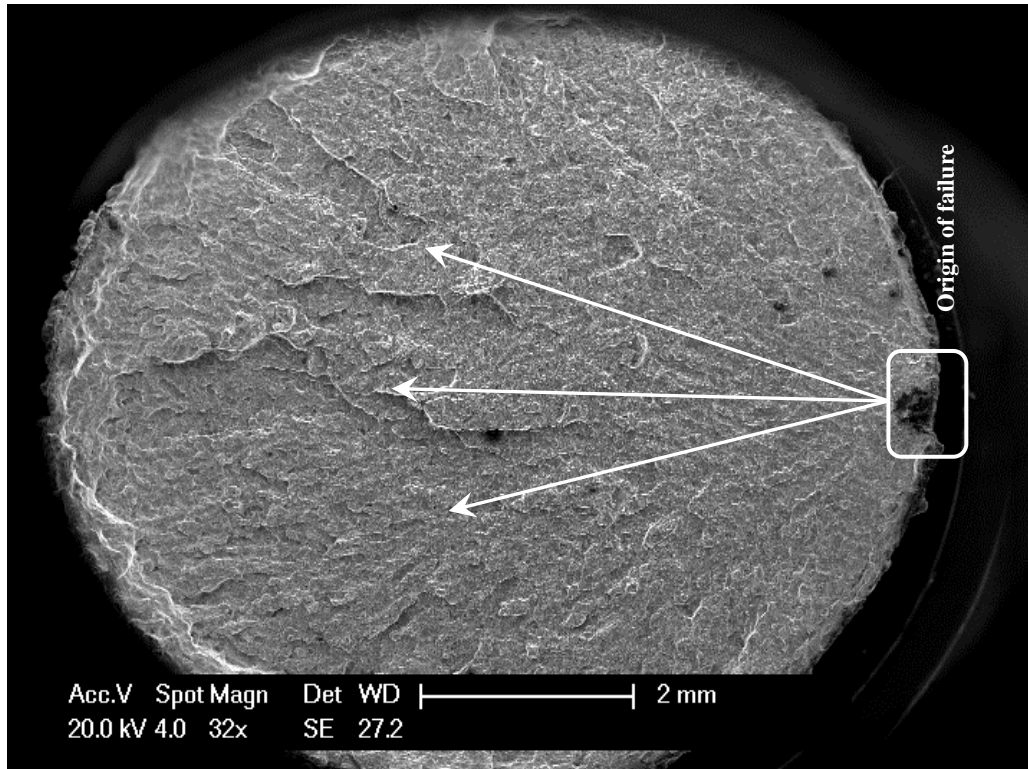


Figure 116: The overall fracture surface of a tensile sample with the origin of failure highlighted along with the direction of crack propagation pointed out by arrows.

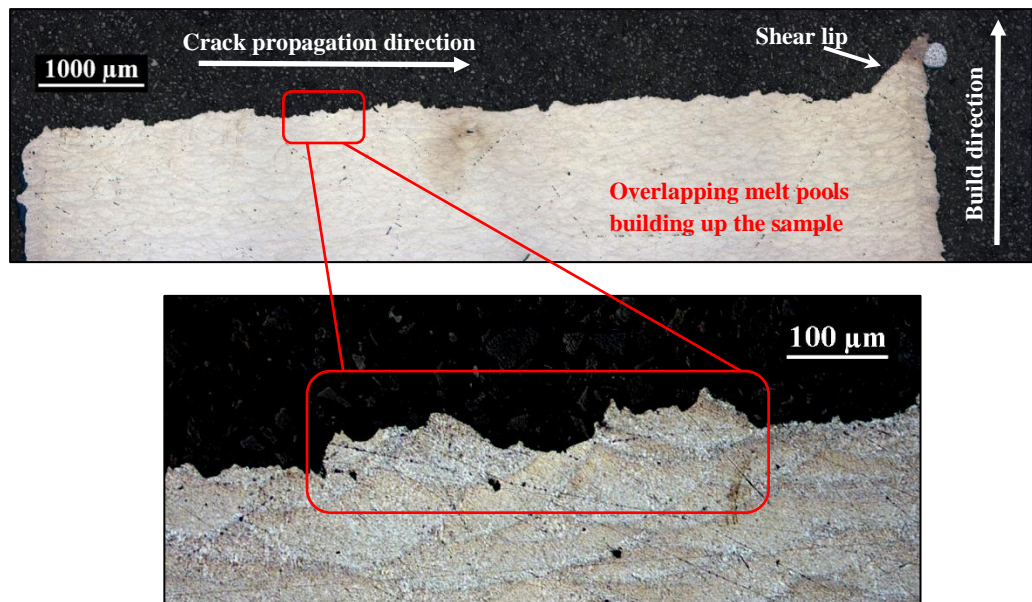
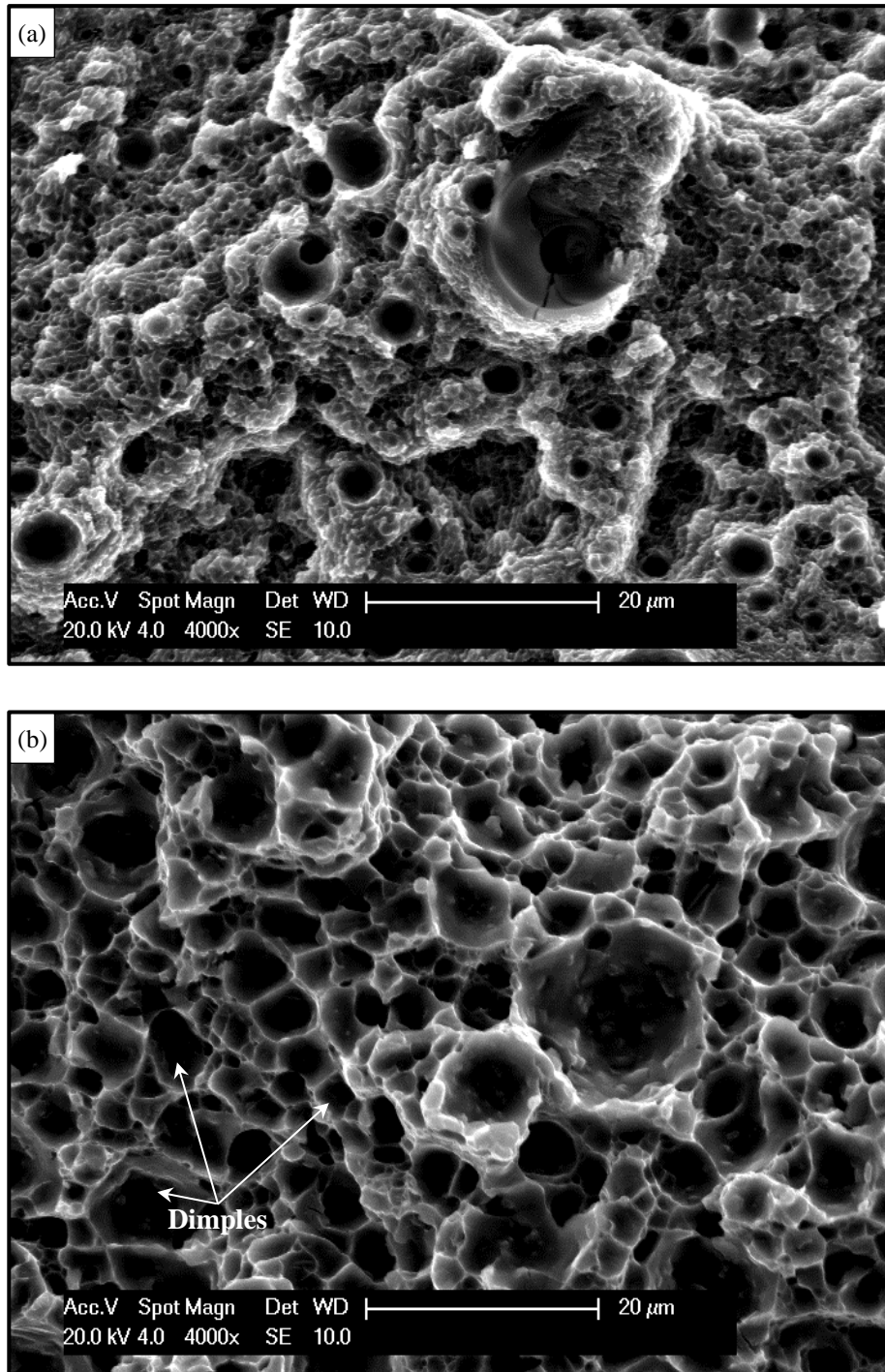


Figure 117: Cross-sectional view of the fracture surface of a tensile sample demonstrating crack propagation along melt pool boundaries.

The fracture surface of the tensile samples was shell shaped, i.e. the removed material is in the shape of a series of adjacent crescents, as shown in **Figure 117**. This suggests that the crack propagates along the boundaries between melt pools, i.e. failure through de-cohesion from one layer to another. This is because the crack follows the softer regions in the material, which are the melt pool boundaries, as explained earlier. This step-like failure morphology was also observed by Prashanth *et al.* [85] in SLM AlSi12.

The fine microstructure in the as-built samples is shown in **Figure 118 (a)**; this microstructure coarsens after heat treating, as seen in the dimpled surface in **Figure 118 (b)**. Failure in both cases was intergranular. Shallow dimples are seen on the surface of the as-built material (**Figure 118 (a)**), indicating failure in a relatively brittle mode [175]. Equiaxed dimples are clearly seen in the heat-treated sample (**Figure 118 (b)**), indicating micro-void coalescence and deformation by slip [175], which is a ductile failure feature [176].



**Figure 118: Fracture surface of SLM AlSi10Mg (a) as-built and (b) heat-treated T6.**

The failure mechanism can be further understood from the high magnification cross-sectional views of the fracture surfaces provided in **Figure 119**. In the as-built material (**Figure 119 (a)**), the crack propagates along the interface between the melt pool core and boundary for being the softer regions – this was consistent along the fracture surfaces. For the heat-treated material (**Figure 119**

(c)), voids nucleate at the Si particles by de-cohesion [177] then these voids coalesce and cracks propagate until complete separation occurs and the sample fails under tensile loading. The chemical distribution of the elements in the alloy (mapped in **Figure 119 (b) and (d)**) confirms the scenario of transformation of the Si segregates into randomly distributed spheroids with heat treatment as well as microstructural coarsening that was explained in chapter (6), section 6.3.3.

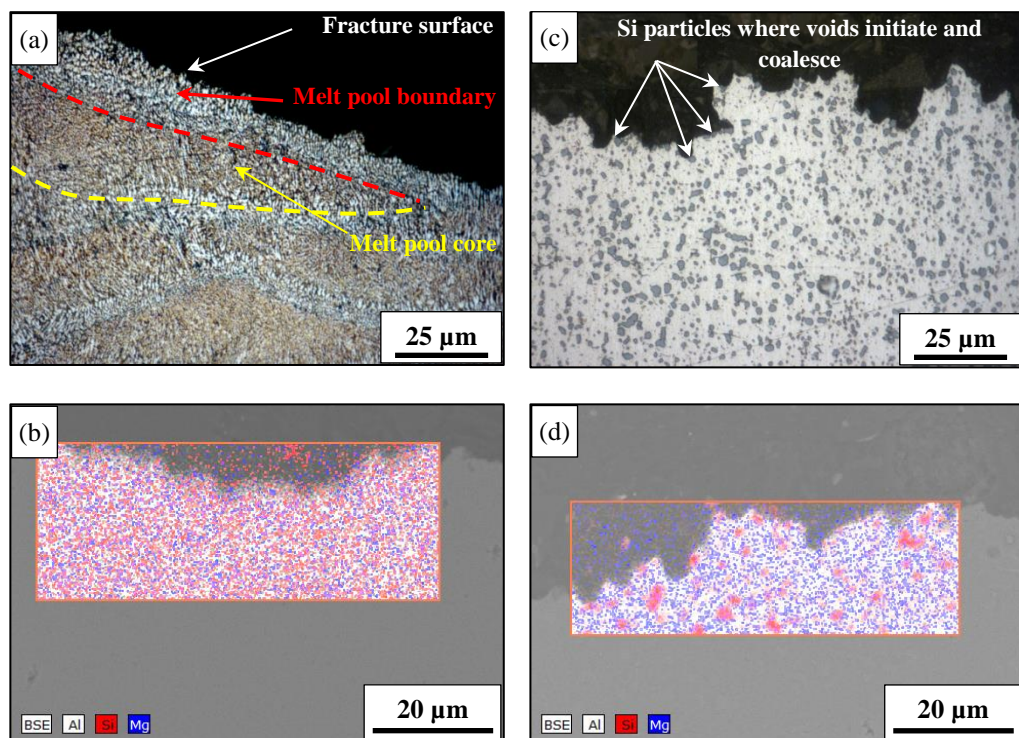


**Figure 119:** Cross-sectioned fracture surface of tensile samples: (a) as-built material with (b) the corresponding representative chemical composition mapping and (c) heat-treated material with the corresponding chemical composition mapped in (d).

The overall tensile properties of the samples with and without heat treatment can be found in **Table 14**. The decrease in the material's ultimate tensile strength, yield strength, and modulus of elasticity after heat treatment is attributed to the microstructural coarsening, as determined by the microscopic investigation, meaning reduction in the amount of grain boundaries that hinder

the motion of dislocations during deformation. Heat treatment reduced the ultimate tensile strength by almost 12%, whilst increasing the ductility by a factor of 2.8. The contribution of the precipitates to the overall strength is thought to be the main reason for the relatively small strength reduction.

**Table 14: Tensile properties of SLM AlSi10Mg developed in this study compared to results from the literature for SLM and die cast counterparts.**

Sample	Tensile yield strength (0.2% offset) MPa	Tensile modulus (GPa)	Ultimate tensile strength (MPa)	Elongation at failure (%)
SLM As-built	268 ± 2	77 ± 5	333 ± 15	1.4 ± 0.3
SLM – T6	239 ± 2	73 ± 4	292 ± 4	3.9 ± 0.5
SLM as-built [49]	~230	-	~318	~1.0
SLM as-built [178]	230	73	328 ± 4	4.1
SLM – T6 [178]	245	-	278	3.6
SLM as-built [5]	-	68	396	3.47
Conventional cast & aged [5]	-	71	300-317	3-5
High pressure die cast [5]	-	71	300-350	3-5
High pressure die cast (T6) [5]	-	71	330-365	3-5
A360 Die cast [179]	175	-	320	3.0

These results are an enhancement in the tensile behaviour of SLM AlSi10Mg with respect to the literature for this alloy [49]. The tensile strength of SLM AlSi10Mg supersedes that of the conventionally cast and is largely comparable to the high pressure die cast (**Table 14**). Typically, the higher strength in the SLM material was accompanied by a reduced ductility. The presence of Si in the alloy introduces a brittle phase that decreases the ductility of the material [161]. However, the ductility was improved by the T6 heat treatment for

applications that require higher elongation capabilities as a design consideration. The improved tensile properties in the SLM processed material when compared to its cast counterpart has also been observed for AlSi12 [121].

The moduli of elasticity determined from tensile tests (**Table 14**) were less than those determined using nanoindentation (section 7.1.3), which were around 100 GPa. Variation between absolute values of properties measured using tension tests and nanoindentation is common [164]. This is explained by the fact that the sampling area in nanoindentation is extremely small, as is the depth of penetration into the material. This means that nanoindentation would not detect the defects within the part, and hence the indentation modulus is usually higher than the bulk modulus.

#### **7.4. Macro-scale properties: compressive behaviour**

The compressive behaviour of the material before and after heat treatment is presented in the stress-strain curves in **Figure 120**. Neither the as-built samples nor the heat-treated ones fractured under compressive loading up to 230 kN, which is the maximum capacity of the machine used in these experiments. The inset in **Figure 120** shows examples of the samples before and after the compression test with buckling clearly observed in the tested as-built samples. The general compressive properties of the material are listed in **Table 15**. Heat treatment has significantly reduced the compressive yield strength, determined at 0.2% strain offset, of the material by ~150 MPa. The compressive yield strength of both the as-built and heat-treated material outperforms the cast counterpart (~100 MPa [180]). The compressive strain at fracture was not determined in these experiments due to limitations on the capacity of the load

cell used in testing along with the samples' buckling rather than fracturing for both the as-built and the heat-treated samples.

The SLM material possessed tension-compression asymmetry demonstrated by the higher compressive yield strength compared to the tensile yield strength. Also, tension-compression asymmetry of the elastic modulus was observed, as shown in **Table 14** and **Table 15**. Differences between Young's modulus of a metal alloy between tension and compression have been previously reported [181]. This could be attributed to the finer microstructure compared to conventionally processed materials, which leads to the material being categorised as an ultrafine-grained material. The tension-compression asymmetry phenomenon is quite common in ultrafine-grained materials [62, 182, 183]. Moreover, the presence of a crystallographic texture promotes tension-compression asymmetry [181] and SLM is known to produce strongly textured AlSi10Mg [4].

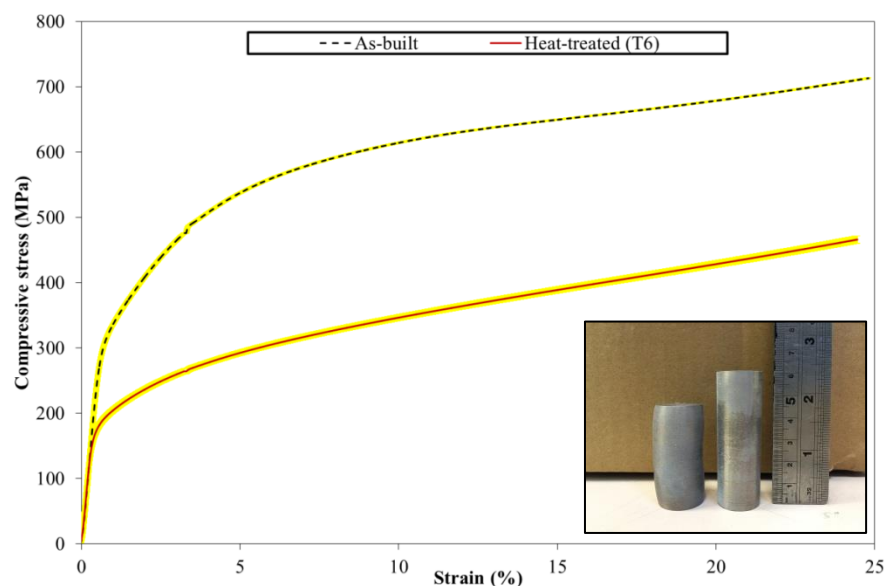


**Figure 120: The compressive behaviour of SLM AlSi10Mg with and without heat treatment (average of three results per condition). The standard error is highlighted in yellow. The inset shows samples before and after testing.**

As would be expected, the compressive modulus was not affected by the heat treatment, but the compressive yield strength was decreased by nearly 47 %. Most studies on SLM AlSi10Mg considering the compressive behaviour are concerned with lattice structures such as [37] without attention to the compressive behaviour of the solid SLM counterpart. So these results are helpful for the development of prediction and simulation models.

**Table 15: The compressive properties of SLM AlSi10Mg before and after heat treatment.**

Condition	Compressive yield strength (MPa)	Compressive modulus (GPa)	Compressive strength at 25% strain (MPa)
As-built	317± 2	51.6 ± 0.4	714 ± 1
Heat treated T6	169 ± 6	51 ± 1	466 ± 6

Although porosity is a key defect when it comes to SLM materials in general, it is not a key factor in the case of compressive loading. This is because the nature of loading tends to close the pores, consolidating the defected regions, as long as porosity is minimal. In contrast, under tensile loading, pores start to stretch, coalesce, and propagate in the form of cracks that lead to failure.

### **7.5. Macro scale properties: fatigue performance**

Fatigue behaviour of parts is one of the important properties to be considered when evaluating a material for applications in the industry. There are two concepts to adopt when designing for fatigue. The first concept is the safe-life concept where the service loading conditions are determined and the part is tested at the typical conditions for fatigue life. A factor of safety is then taken into account and it is therefore known as the safe life of the part after which it has to be changed even if it did not fail. But this concept is mainly theoretical

because it ignores fatigue cracking. Moreover, it is not desirable for economy and performance. The recommended concept is the fail-safe concept where the assembly is designed in a way that even if the part fails in service, the structure can still operate until the crack is detected [125]. The endurance limit is the loading limit below which the part is safe under cyclic loading for a defined duration [124],  $3 \times 10^7$  in the current study.

Fatigue tests can be either stress-controlled or strain-controlled. In a stress-controlled testing mode, the material under investigation experiences either cyclic softening or hardening [124, 125]. Annealed materials generally experience cyclic hardening under cyclic loading due to dislocation multiplication, whereas work-hardened materials experience cyclic softening due to rearrangement of dislocation networks [125]. The experiments conducted in this study were stress-controlled in axial loading mode. In the axial fatigue loading, the stress fluctuates between maximum and minimum stress values [124]. The stress ratio “R” is the ratio between these two values of stress ( $R = \sigma_{\min}/\sigma_{\max}$ ). Fatigue tests are either fully reversible in which case  $R = -1$ , otherwise the R value changes according to the stresses applied during the cyclic loading. In this study, R is fixed at 0.1.

#### **7.5.1. Surface quality of the test specimens**

The morphology of the fatigue samples in their as-built condition without post-processing machining can be seen in **Figure 121 (a)**. Surface irregularity features such as balling and satellites were observed. These surface defects are thought to contribute to depressing the fatigue life of SLM parts. According to Frazier [9], increasing the surface roughness by a factor of 1000 reduces the fatigue life of the part by an order of magnitude, i.e. from  $10^5$  to  $10^4$  cycles. On

the other hand, post-processing machining to improve the surface roughness eliminated all evidence for the SLM characteristic surface defects, as can be seen in **Figure 121 (b)**. The machined surface shows the machining marks from turning as well as some small pores that were revealed after machining.

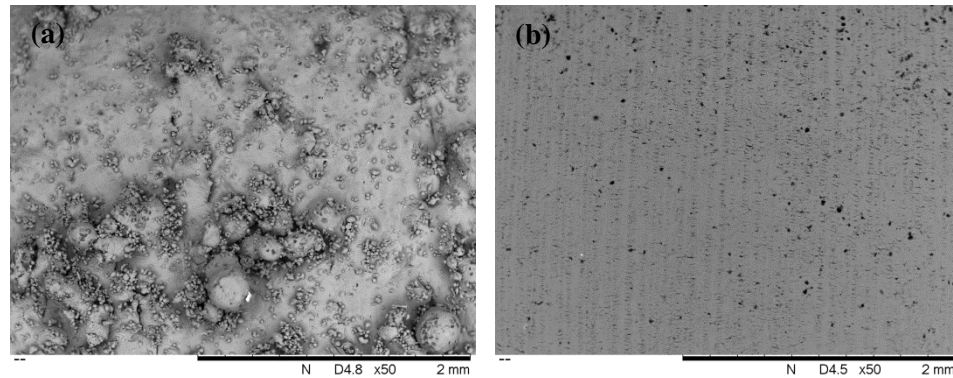


**Figure 121: Surface morphology of the sides of (a) an as-built fatigue sample and (b) a sample with machined surface (surface parallel to the building direction).**

Valleys and hills (also referred to as intrusions and extrusions) are formed on the surface of a sample under cyclic loading due to irreversibility of shear displacements. Valleys then act as micro-notches with stress concentrations. This results in slip-induced surface roughness. Fatigue cracks are nucleated at protrusions. Consequently, polishing the sample surface by electro-polishing to remove these intrusions and extrusions increases fatigue life of the part. In commercial alloys, fatigue life is depressed by the presence of pores or inclusions as they provide sites for fatigue crack nucleation, i.e. subsurface crack initiation [124, 125].

### **7.5.2. Stress-life (S-N) curves**

The S-N curve of the as-built samples can be seen in **Figure 122**. None of the tested samples in this condition ran out where the lowest maximum stress level examined in these experiments was 63 MPa. At the stress of 63 MPa, the

samples survived for an average of just over  $7.6 \times 10^6$  cycles. There are claims that the fatigue life of the SLM samples in their as-built condition is shorter than those with machined surfaces [9]. This is due to the poor surface roughness of the as-built samples since the surface is full of peaks and valleys, open pores, that act as points of weakness favouring crack initiation. From the results in **Figure 122**, showing the S-N curves for the samples with and without machining, it can be deduced that this cannot be generalised over the range of stress levels. For instance, the fatigue life of both as-built and machined samples was almost the same in the finite life region; higher stress levels ranging from 157 MPa to 220 MPa. At stress levels below 157 MPa, the machined samples started to show run outs defined in this study as samples surviving  $3 \times 10^7$  cycles without failure under the cyclic loading. This suggests that machining the samples improves the fatigue life at lower stress levels with no significant effect observed at the higher stress levels.

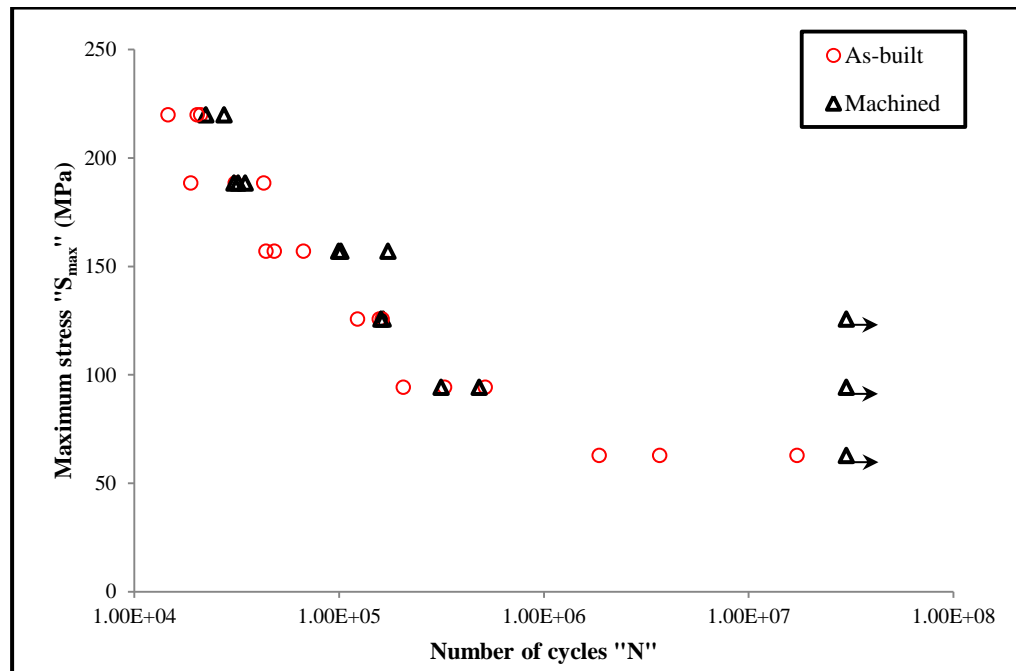


**Figure 122: Effect of machining on the fatigue performance of SLM AISi10Mg.**

Although machining improves the surface condition of the sample for the early stages of the test, the valleys and hills (extrusions and intrusions) formed on the surface of the sample during cyclic loading will result in protrusions where fatigue cracks originate [125].

The presence of Si in AlSi10Mg is beneficial because it increases the alloy's fluidity [152], which enhances process-ability by SLM. In addition, Si in Al-Si-Mg alloys acts as a strengthening element in the material to improve the mechanical properties, including performance under cyclic loading. However, as the Si content approaches the eutectic composition, its effect is inverted in case of cast materials because at this point Si forms platelets that are sites favoured for fatigue crack nucleation [152]. This scenario however is not valid in case of the SLM material because of its distinctive microstructure in the as-built condition (see chapter (6) for microstructure analysis).

Common defects in SLM parts (pores, non-molten spots, or surface roughness) suppress the fatigue life of parts [184]. Fatigue life of parts can be improved by shot peening, rolling, burnishing [124] and hot isostatic pressing (HIP) not only through stress relieving but also consolidating present porosity [23, 123]. Hot isostatic pressing (HIP) can be used to reduce pores' sizes or even close them totally leading to better fatigue life, as has been reported for Ti6Al4V [174].

Another approach that could be adopted to enhance the fatigue life of Al alloys is heat treatment via conventional T6 heat treatment, such as the work by Brandl *et al.* [18] where they referred to this heat treatment as peak hardening. This is confirmed by the S-N curves of the heat-treated samples (solution heat treated for 1 hr and aged for 6 hrs) compared to the as-built samples, which can

be found in **Figure 123**. These curves show that the applied heat treatment has significantly improved the fatigue performance of the samples at all stress levels tested, with the best improvement at the lower stress levels. The heat-treated samples started to run out at a stress of 94 MPa. The crystallographic texture of a material has an influence on its fatigue behaviour, where a random texture means a softer material [125], i.e. more ductile. According to the microstructure and earlier results (chapter (6) section 6.3.2), the SLM material is one of a strong texture [4]. The heat treatment has significantly altered the microstructure and randomized the microstructural texture because the evidence of directional solidification was wiped away. This explains the enhancement in fatigue life via heat treatment. Also, from evolution in the material's hardness by heat treatment in section 7.2, it was deduced that a conventional T6 heat treatment has softened the material, i.e. increased the material's ductility, which is an indication for improved fatigue strength. This was also evident in the enhancement in the ductility of the material under tensile and compressive loading (sections 7.2 and 7.3 in this chapter), as demonstrated by the higher strains achieved after heat treatment when compared to the as-built material.

The S-N curve of the samples that were heat-treated and then machined is shown in **Figure 124** along with that of the as-built samples for the sake of comparison. The combined effect of heat treatment and machining led to an overall enhancement in the fatigue behaviour of the samples at all stress levels tested. Samples started to run out at a stress of 126 MPa.

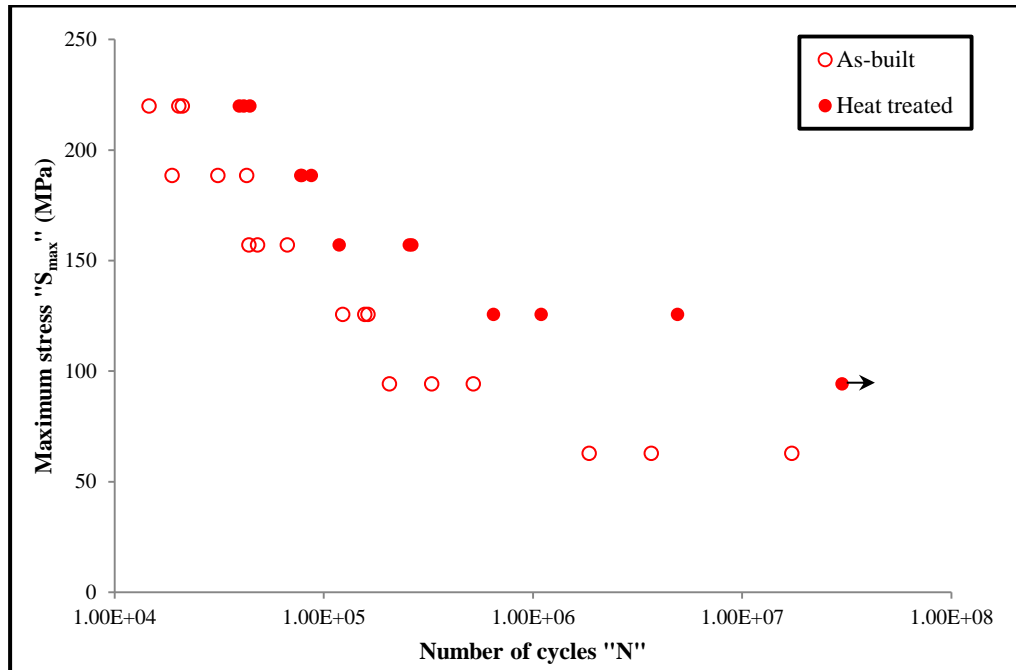


Figure 123: Effect of heat treatment on the fatigue behaviour of SLM AISi10Mg.

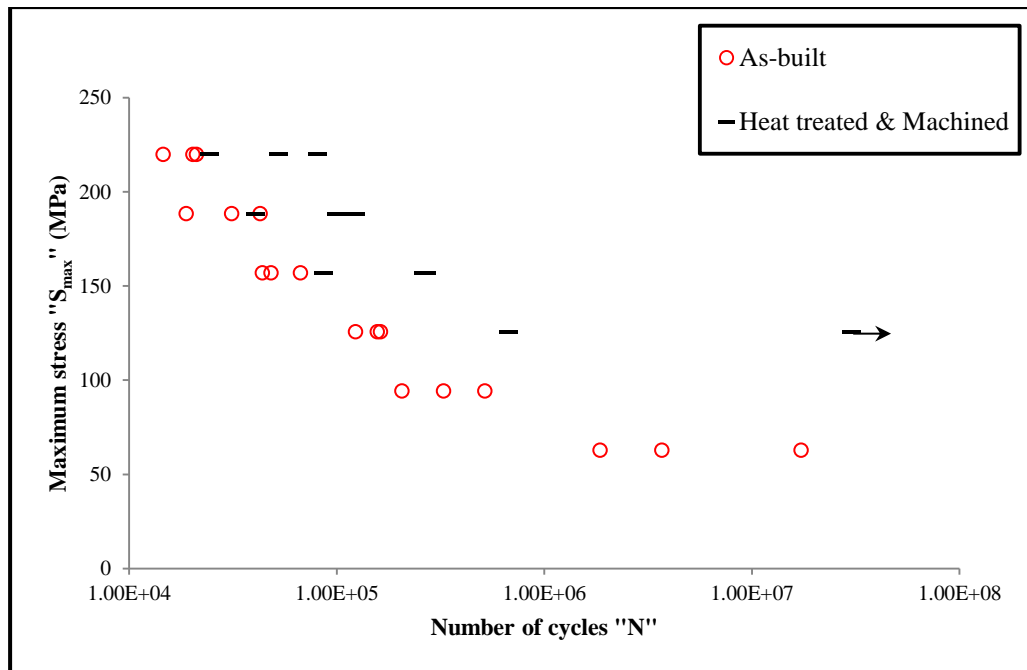


Figure 124: Effect of heat treatment followed by machining on the fatigue behaviour of SLM AISi10Mg.

For complete comparison, the S-N curves for all the samples tested in these experiments with their various conditions, namely, as-built, machined, heat-treated, and heat-treated and machined are all superimposed in the graph in **Figure 125**. Between improving the fatigue performance of the material using machining or heat treatment, it can now be stated that heat treatment has a stronger influence at the higher stress levels, whereas machining has a better effect at the lower levels. The use of both heat treatment and machining, simultaneously, developed improved fatigue performance at all stress levels tested ranging from 63 MPa up to 220 MPa.

There are not a lot of studies in the literature covering the fatigue behaviour of selectively laser melted Al alloys. However, the ones available normally overestimate the surface quality as a factor so they test the samples in a machined condition aiming at better fatigue performance [18], assuming the worst behaviour from the as-built samples. The results presented here in the current study, disagree with this assumption to an extent. Since machining the samples has improved the fatigue performance only at the lower stress levels, whereas the heat treatment was the significant contributor to enhancing the fatigue life at the higher levels (**Figure 125**). This result means that a well-designed or selected heat treatment procedure can significantly improve the fatigue performance of selectively laser melted parts without the need for post-processing machining for surface quality modification. This finding is in favour of SLM being a net shape manufacturing technology since the requirement for further machining is a setback especially for parts of complex structures such as lattice structures or topology optimised parts.

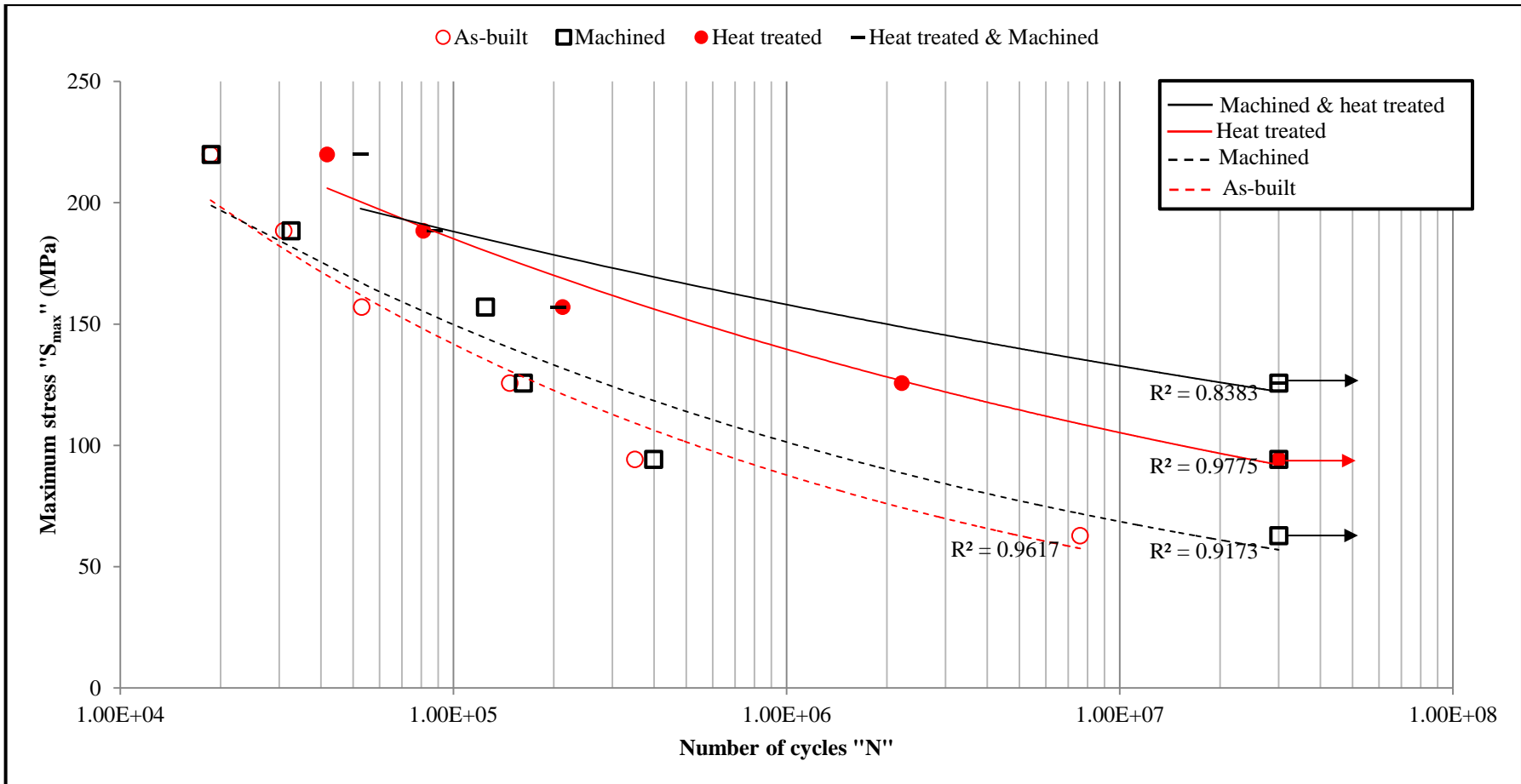


Figure 125: S-N curves superimposed for all the investigated conditions, namely, (1) as-built, (2) heat treated, (3) machined, and (4) heat-treated & machined.

One of the reasons the heat treatment has improved the fatigue performance of the material is its effect on the residual stresses. The SLM material is known to have high residual stresses [121] driven by the fast rate of solidification. Residual stresses yield a part susceptible to failure under cyclic loading. The use of a heated build plate during processing (200 °C) was reported to significantly reduce the amount of residual stresses produced in a part when using AlSi12 [121]. However, although the samples in the current study were processed on a heated build plate, the residual stresses in the as-built samples were quantified by means of X-ray diffraction, and found to be tensile residual stresses with a magnitude of 68.2 MPa. The heat-treated material, on the other hand, exhibited compressive residual stresses of 31.5 MPa. The nature of these residual stresses can be understood through tracing the processes the material was subjected to. For instance, the tensile residual stresses were driven by the directional solidification along the build direction, i.e. the layer-by-layer solidification. During heat treating the material, the solution heat treatment supposedly releases the residual stresses in the material. Although quenching after solution heat treatment can introduce compressive residual stresses in the heat-treated material, it is important to note that ageing should release these stresses. The compressive residual stresses observed in the heat-treated material might have been introduced due to the formation of Mg<sub>2</sub>Si precipitates; this can be confirmed using transmission electron microscopy and so this requires further investigation.

The results in this study were compared to data from the literature published by Brandl *et al.* [18] on the same alloy processed by SLM. The maximum stress at which the as-built samples in this study survived 10<sup>6</sup> cycles was 102 MPa,

whereas in [18] the maximum stress was around 120 MPa. After heat treatment, the samples in [18] survived the  $10^6$  cycles at a maximum stress of 170 MPa, whereas the samples in the current study were at a stress of 157.5 MPa. Bearing in mind that the heat treatment procedure Brandl *et al.* [18] used in their study was different from the one employed in this study (since they have solution heat treated their samples at 525°C for 6 hrs followed by ageing for 7 hrs at 165°C after water quenching), the results on hand then achieved a comparable behaviour while using shorter treatment durations. Results reported in [185] showed that cast samples from A356 treated using a T6 heat treatment survived  $10^6$  cycles at a maximum stress of ~139 MPa. This indicates superiority of the samples processed by SLM. This could be attributed to the finer microstructure, which means increased area of grain boundaries. Grain boundaries act as barriers to fatigue crack propagation, i.e. better fatigue crack propagation resistance can be achieved by refining the microstructure [186].

### **7.5.3. Fractography**

The fracture surface of a fatigue sample is generally flat from a macroscopic appearance viewpoint [187]. This is demonstrated by the topography micrograph in **Figure 126** for the fracture surface of an as-built fatigue sample loaded with a maximum stress of 94 MPa. It can be seen in this figure that failure originated at the surface of the sample.

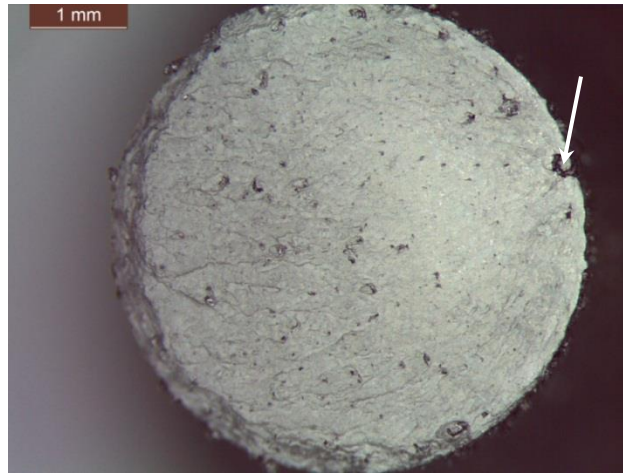


**Figure 126: Fracture surface of an as-built sample tested at a maximum stress of 94 MPa.**

A fatigue fracture surface is usually divided into four main regions: (1) the fatigue cracked region, (2) the stretched region, (3) the overload fracture region, and (4) the final fracture region [187, 188]. Some studies combine regions (1) and (2) and refer to them as the fatigue crack propagation region [175]. Hereafter, the fatigue fracture surface will be discussed in terms of three main zones that are (I) the cracked region, (II) the propagation region, and (III) the final overload/fracture region. These regions are shown in the fractographs in **Figure 127**, **Figure 128**, and **Figure 129**. These regions are developed through five stages the sample goes through under cyclic loading [125]:

1. Sub-structural and microstructural changes
2. The formation of microscopic cracks
3. Growth and coalescence of micro-cracks to create dominant cracks
4. Crack propagation to develop macro-cracks
5. Instability or complete failure

The fatigue cracked region represents the first stage of failure under cyclic loading. This is the region where a crack is first nucleated and it usually

occupies a small area fraction of the fracture surface compared to the further stages of failure [187]. The area of crack propagation is related to the nominal stress applied [44]. The fractographs at the various stress levels of loading show that the fatigue cracked region, or what is also known as the crack initiation region, is reduced by increasing the stress level. This is a common phenomenon in cyclic loading [175]. At a nominal stress of 52 MPa, the radius of zone (I) was  $2516 \pm 172 \mu\text{m}$ , whereas this radius decreased to  $1860 \pm 50 \mu\text{m}$  and  $1037 \pm 187 \mu\text{m}$  at nominal stresses of 86 MPa and 120 MPa, respectively. All the tested samples showed single crack origin no matter the stress applied.

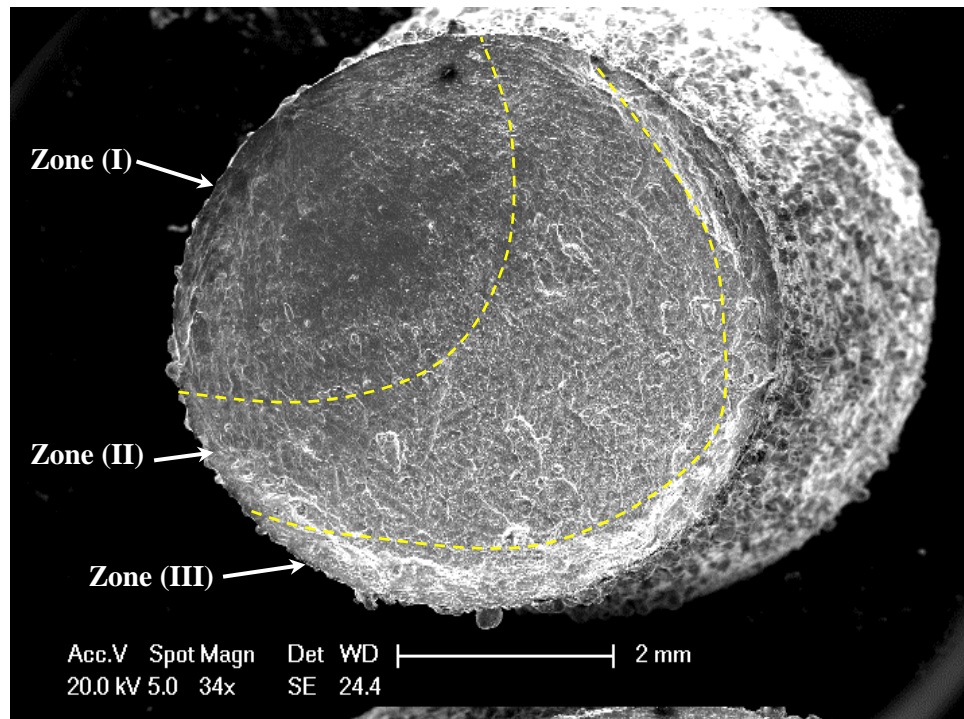


**Figure 127: Zones of fatigue fracture in an as-built sample loaded by a maximum stress of 94 MPa (a nominal stress of 52 MPa and an amplitude of 42 MPa).**

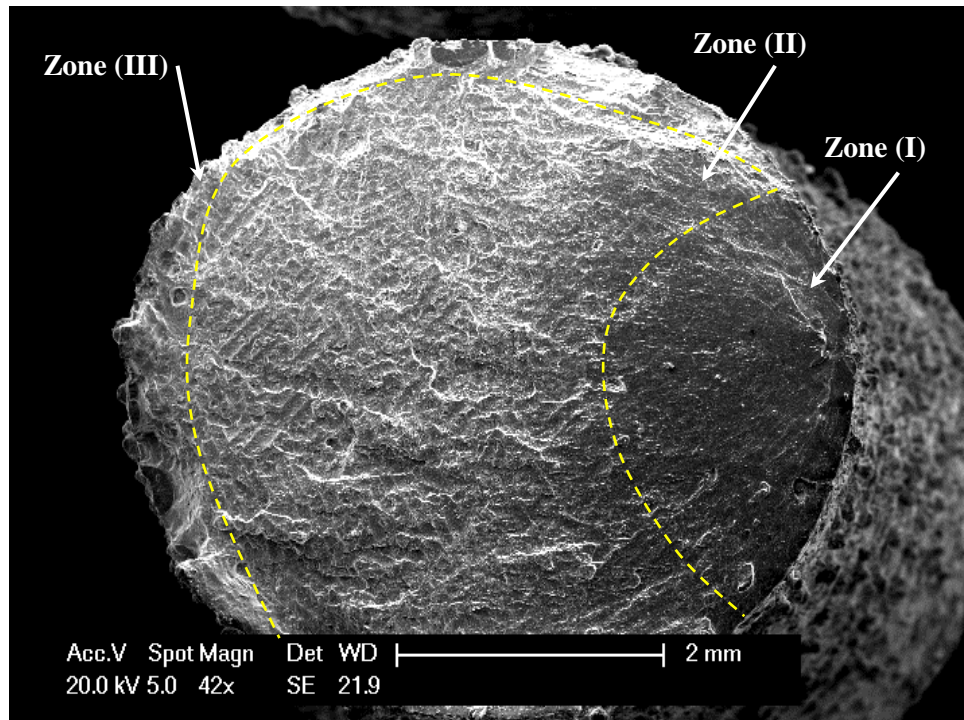


Figure 128: Zones of fatigue fracture in an as-built sample loaded by a maximum stress of 157 MPa (a nominal stress of 86 MPa and an amplitude of 71 MPa).

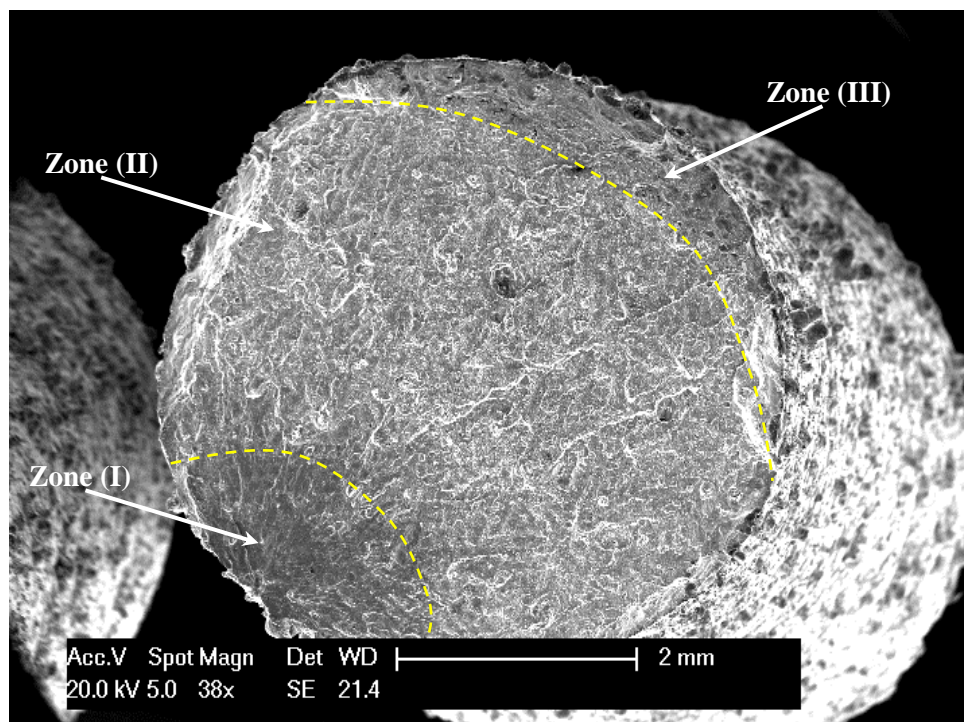
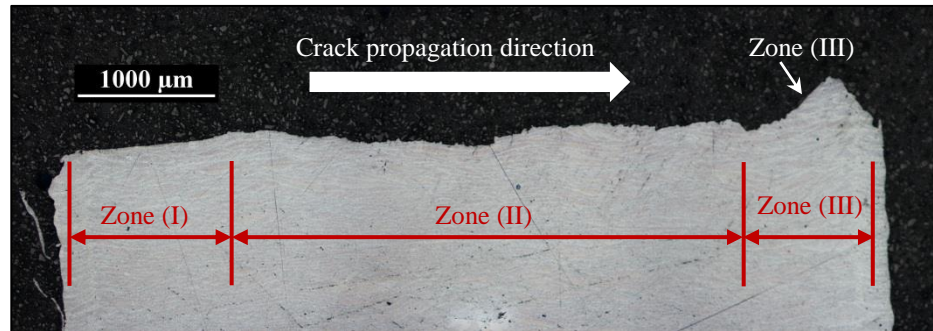


Figure 129: Zones of fatigue fracture in an as-built sample loaded by a maximum stress of 220 MPa (a nominal stress of 120 MPa and an amplitude of 99 MPa).

The final region (zone (III)), which is the fracture region, is when the area carrying the load becomes too small that it cannot handle the amount of load anymore leading to a fast propagation. The fracture surface in this region usually shifts to a plane that is inclined to the flat surface by an angle of  $45^\circ$ , as shown in **Figure 130**.



**Figure 130: Fatigue fracture surface cross-section.**

Fatigue micro-cracks were observed in zone (I) propagating from the origin of failure, as shown in **Figure 131**. Fatigue striations on the fracture surface of the as-built sample can be seen in **Figure 132**. These striations are brittle striations [187], which suggest the relative brittleness of the as-built samples. This brittleness could be attributed to the high residual stresses due to the rapid solidification during processing.

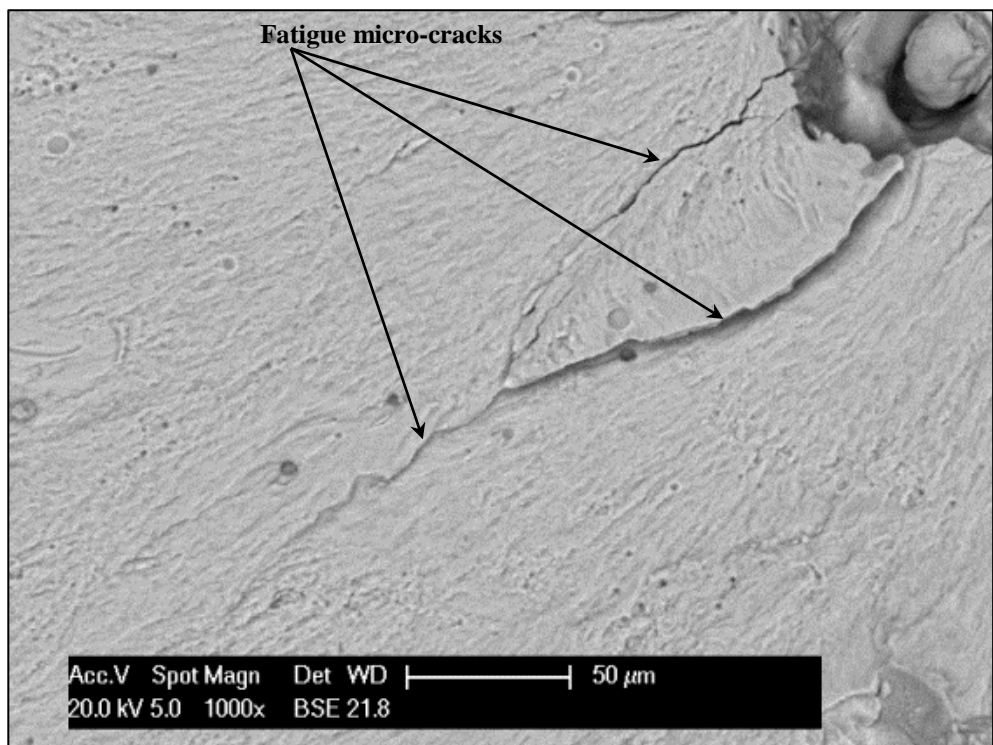
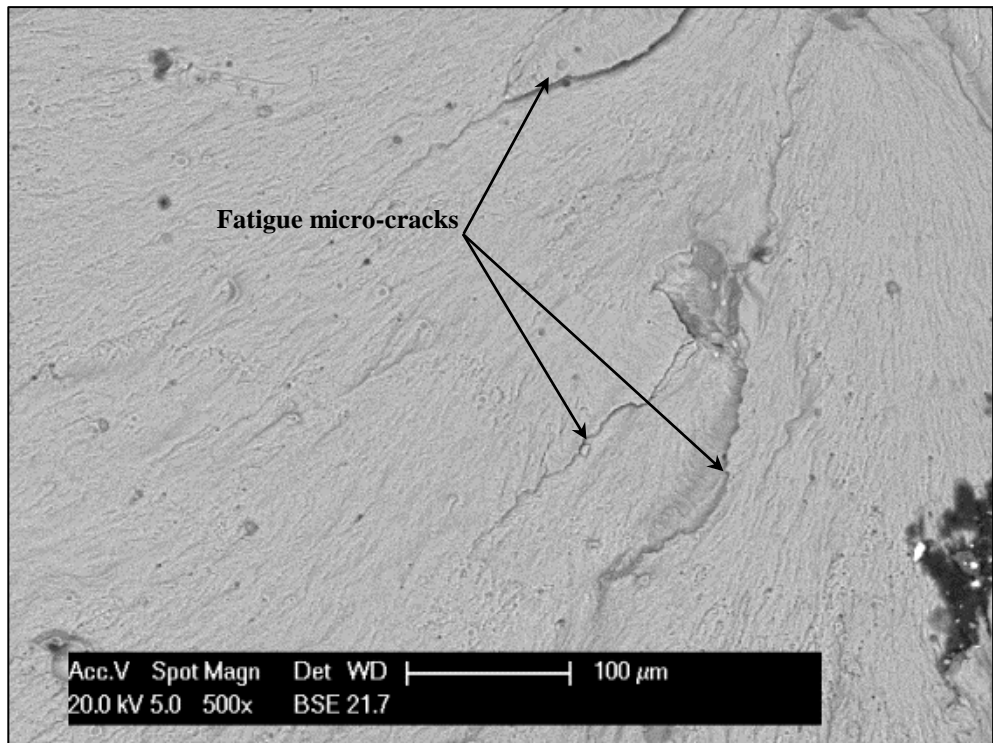
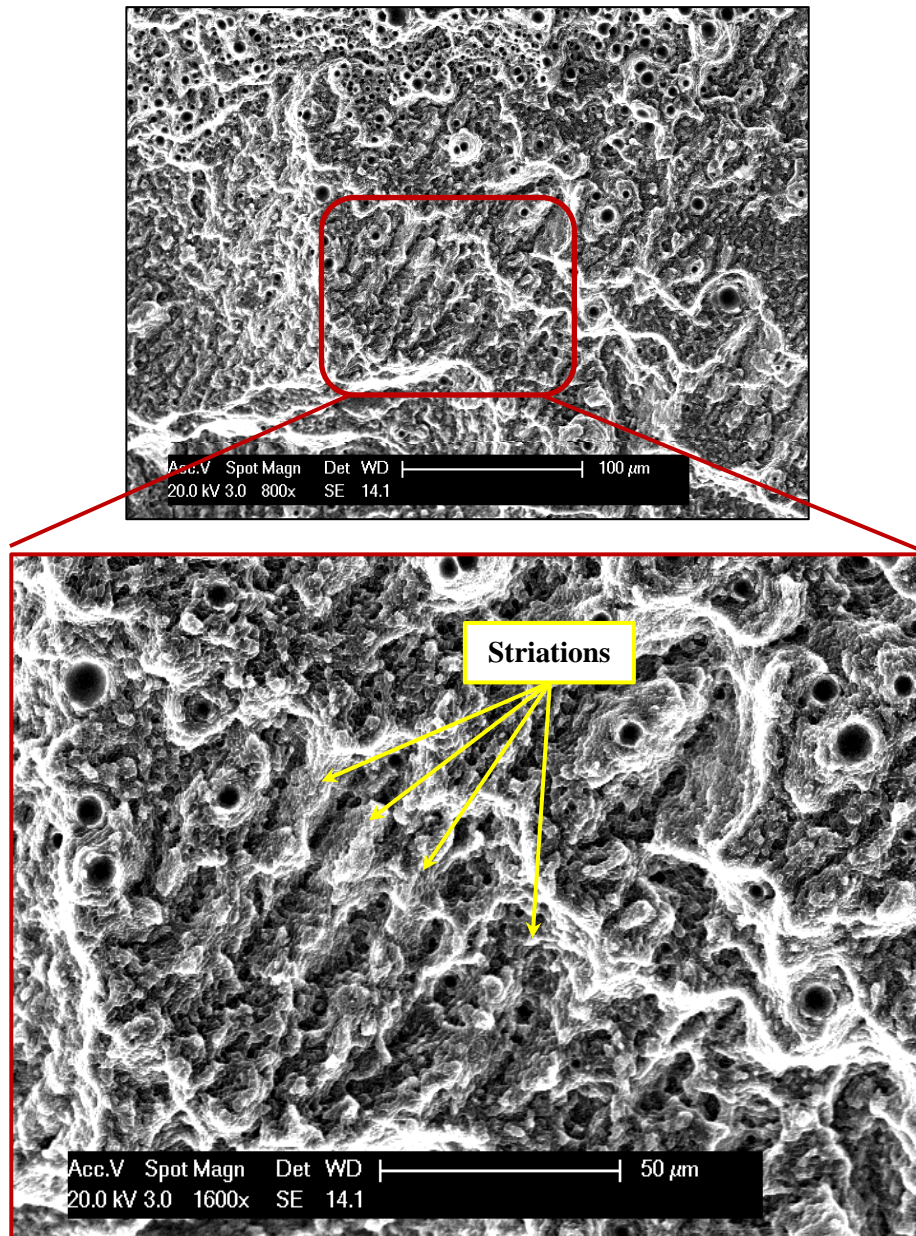
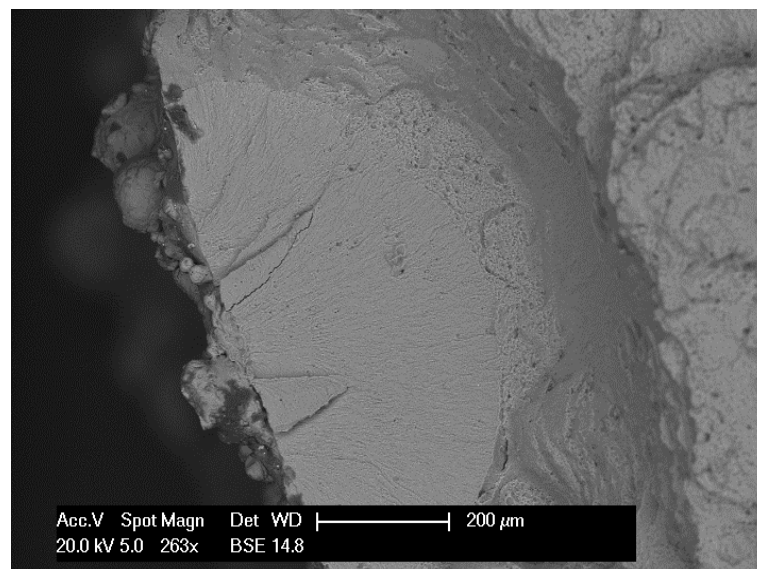
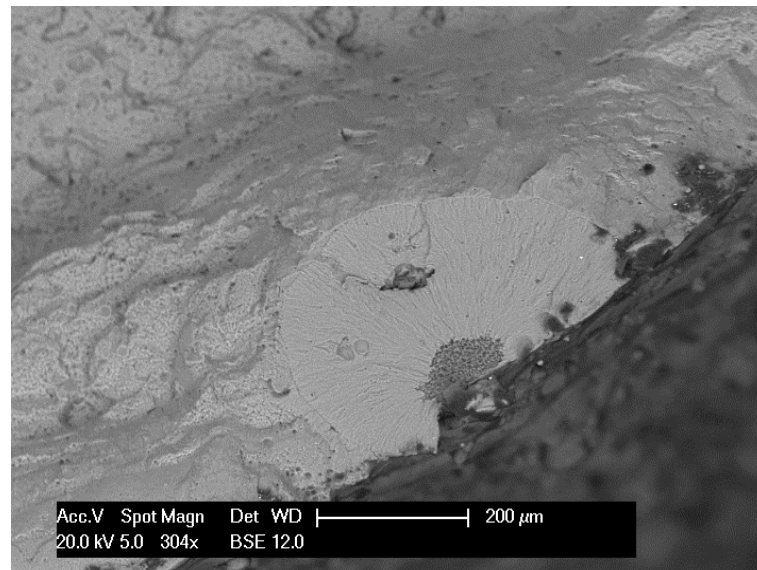


Figure 131: Fatigue cracks propagating through the fatigue cracked region.



**Figure 132:** Fatigue striations on the fracture surface of an as-built sample.

At the high stress levels, such as the samples loaded by a 120 MPa nominal stress, evidence of cleavage was observed in the final overload/fracture region. Failure in this region followed a fanlike fashion on planes at different levels [175]. Examples are shown in **Figure 133** for the cleavage fans and lines.



**Figure 133: Cleavage fans and lines on the fracture surface of as-built samples tested at high stress levels (120 MPa nominal stress).**

Wycisk *et al.* [15] categorised the types of crack initiation under fatigue loading of SLM parts into two categories; (1) failure due to lack of fusion between the layers, i.e. porosity in the polished samples, or (2) surface defect induced by the poor surface roughness in the as-built samples. The results in the current study support the second scenario, as was demonstrated in the fractographs that failure always originated at a surface or sub-surface defect. It

was also noticed that the scan tracks used to process the samples could be observed on the fracture surface, as shown in **Figure 134**, where the scan tracks formed using the checkerboard scan strategy can be seen. This observation supports the hypothesis that failure occurs through crack propagation along the melt pool boundaries of a certain layer at which the crack originated, similar to failure under tensile loading, presented in section 7.3.

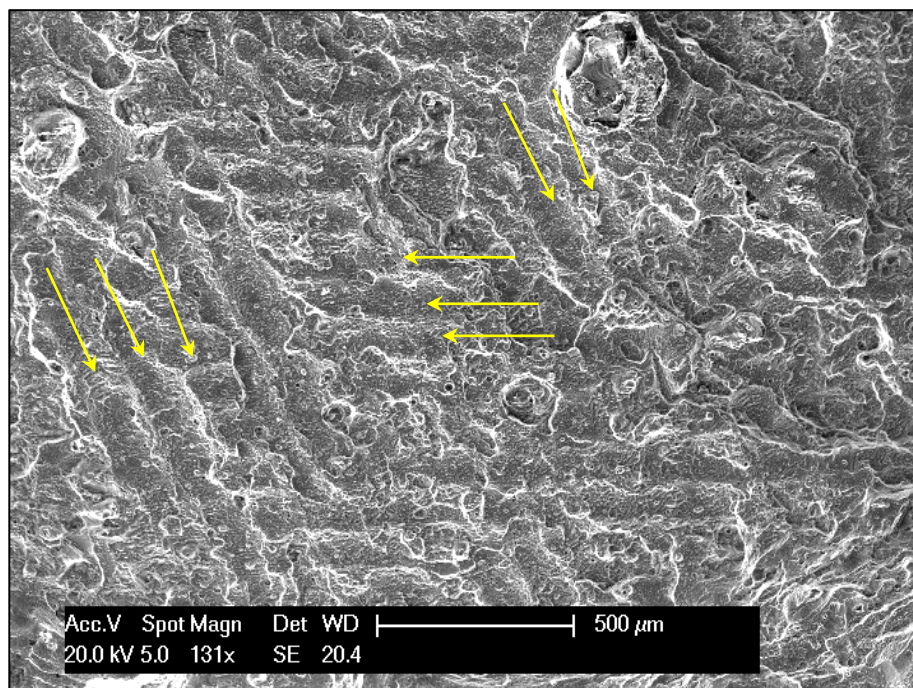


**Figure 134:** The scan tracks building up the sample using the checkerboard scan strategy clearly seen on the fracture surface of the as-built fatigue sample (pointed out by the arrows).

Some of the samples contained foreign particles of a spherical morphology on their surfaces, such as the one in **Figure 135**. Although fracture of these samples did not originate at the foreign particles, it is important to determine what these particles are and where they come from. Mapping the chemical composition distribution in this particle's region in **Figure 135** showed that this particle is rich in Si, Mg, and some O<sub>2</sub>, as demonstrated in **Figure 136**.

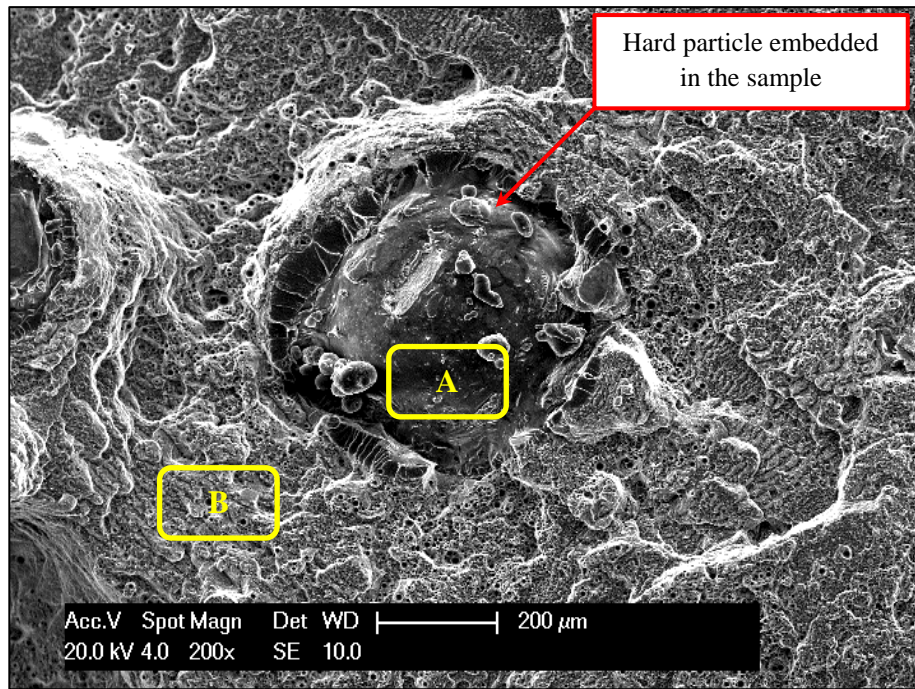


Figure 135: Foreign particle on the fracture surface of the as-built fatigue test sample.

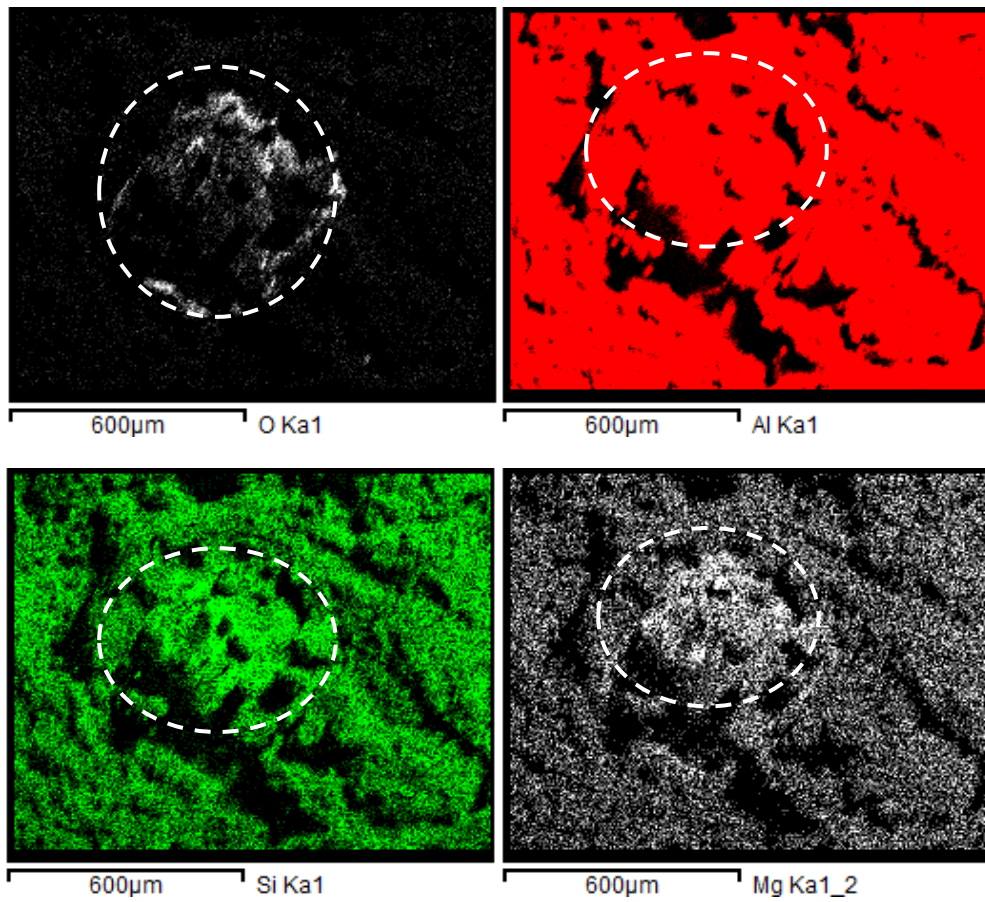
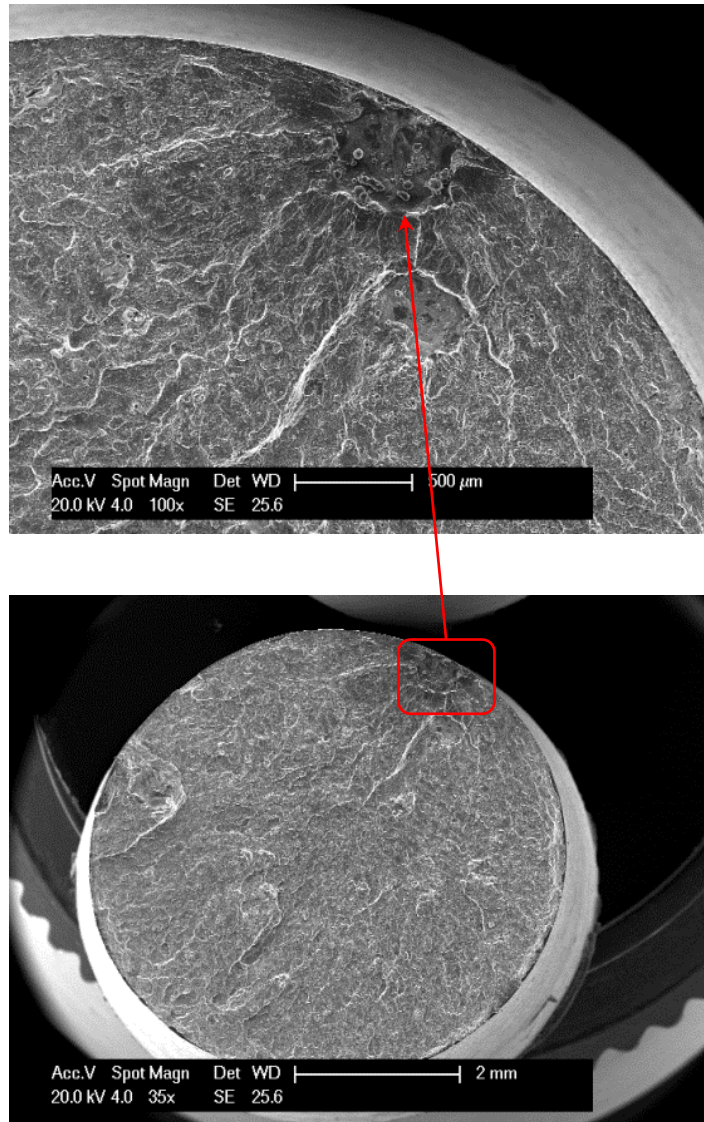


Figure 136: Mapping the chemical composition at the foreign particle on the fatigue fracture surface.

At point (A) in **Figure 135**, the relative chemical composition was 1.22 wt% Mg, 12.96 wt% Si, and 80.55 wt% Al. Whereas at point (B), the relative chemical composition was 0.37 wt% Mg, 8.55 wt% Si, and 91.08 wt% Al. This composition, as well as the spherical morphology, suggests that this particle could be laser spatter. The laser spatter was shown earlier in chapter (5) to be rich in Si and Mg [51]. Simonelli *et al.* [82] attributed the production of the laser spatter to selective oxidation. The presence of the laser spatter on the fracture surfaces of the fatigue samples indicates the importance of preventing their formation during processing as they get embedded in the final parts and so they become faulty.

It is now established that machining the fatigue test specimens prior to testing did not significantly improve the fatigue life at high stress levels. This contradicts results reported for other materials processed by SLM, such as Ti-6Al-4V [23] and 316L stainless steel [123]. Fractography also showed that even the machined samples still failed due to a sub-surface defect, as shown in **Figure 137**, which was a consistent behaviour across all the tested samples in the machined batch. Failure in machined samples due to sub-surface defects has been previously reported for AlSi12 processed using SLM by Siddique *et al.* [121]. Similarly, crack initiation at sub-surface defects has been reported for Al-Si alloys processed by casting [189]. Closer investigation of the surfaces of the samples after machining showed that some sub-surface pores were revealed, i.e. brought to the surface, through turning, as can be seen in **Figure 138**. This might explain that failure under cyclic loading for both as-built and machined samples always originated at the surface.



**Figure 137: Fracture surface of a fatigue test specimen with machined surface showing failure to originate at a sub-surface defect.**

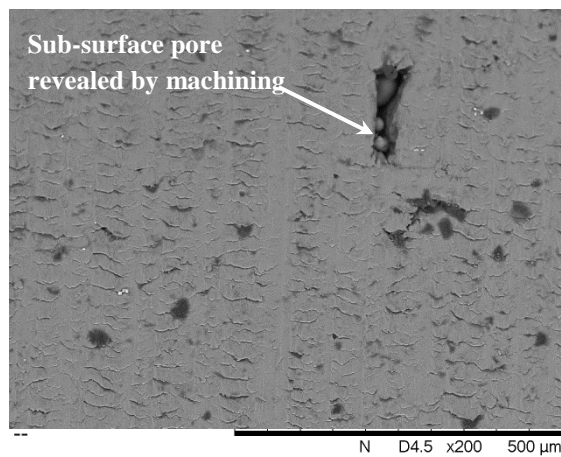


**Figure 138: Sub-surface pore that was revealed after machining the sample.**

The effect of heat treatment on the fracture of the samples under cyclic loading is demonstrated in **Figure 139**. It is clear that the heat treatment led to microstructural coarsening. Dimples appeared on the fracture surface of the heat-treated samples as well that were not apparent in the as-built specimens, indicating introduction of ductility. The ductile features on the surface of the heat-treated samples agree with the S-N curves presented earlier that showed heat treatment to improve the fatigue performance of the material.

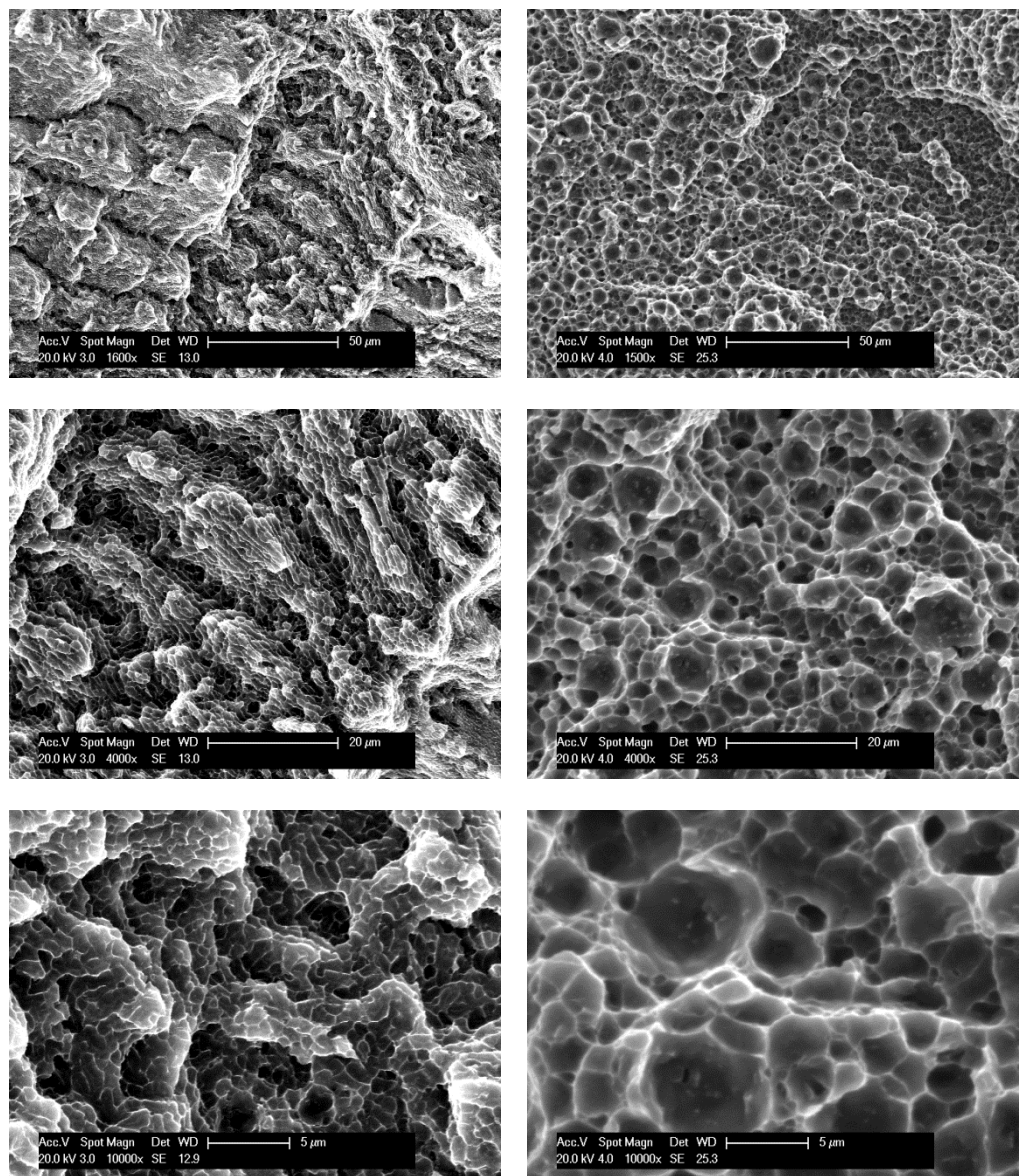


**Figure 139: High magnification images for the fracture surfaces of as-built (left) and heat-treated (right) fatigue samples.**

## 7.6. Summary

Near fully dense selectively laser melted AlSi10Mg parts were evaluated using a number of mechanical tests. The results reported in this study represent a comprehensive understanding of the mechanical properties at the nano, micro, and macro-scopic levels and their correlation to the material's microstructure.

- The nano-hardness profile across a melt pool was found to be considerably consistent without significant spatial variation. This was attributed to the fine microstructure and good dispersion of the alloying elements homogeneously.
- Re-melting the material whilst processing single layers or multi-layered parts led to a decrease in the nano-hardness, as summarised in **Table 16**.
- Using the pre-melt scan strategy returned higher nano-hardness when compared to the single scan. Areas in the vicinity of keyhole pores were softer than the rest of the samples.

**Table 16: The evolution of nano-hardness from a single track to a bulk sample.**

Sample	Average nano-hardness (GPa)
Laser irradiated material: Single track	$2.27 \pm 0.02$
Laser irradiated material: Single layer	$2.13 \pm 0.01$
Part 1: <i>single scan</i>	$1.70 \pm 0.03$
Part 2: <i>pre-melt scan</i>	$1.96 \pm 0.01$
Keyhole pore vicinity: <i>single scan</i>	$1.66 \pm 0.02$
Keyhole pore vicinity: <i>pre-melt scan</i>	$1.81 \pm 0.03$

- The ultimate and yield tensile strengths of the SLM material were significantly higher than the die cast counterpart, but the material also exhibited poor elongation to failure.
- The influence of a conventional T6 heat treatment on the mechanical properties was determined. A summary of the effect of heat treatment on the various mechanical properties can be found in **Table 17**.
- Both nano- and micro-hardness tests showed material softening upon heat treatment, a finding that opposes the behaviour of conventionally manufactured Al-Si-Mg alloys. This highlights the requirement to develop new heat treatment procedures if hardening the SLM material furthermore is needed.

**Table 17: Summary of the effect of a conventional T6 heat treatment on mechanical performance of SLM AlSi10Mg**

Mechanical property	Effect of heat treatment (%)
Nano-hardness	- (16 ± 1) ↓
Micro-hardness	- (28 ± 1) ↓
Ultimate tensile strength	- (12 ± 5) ↓
Yield tensile strength	- (11 ± 1) ↓
Tensile elongation at failure	+ (179 ± 57) ↑
Compressive strength at 25% strain	- (56 ± 0.003) ↓
Yield compressive strength	- (47 ± 2) ↓

- Variation in the nano-hardness across the material was observed after heat treatment due to the change in microstructure, i.e. the diffusion of the originally well-dispersed Si to form coarser particles (spheroids large enough to be detected by nano-indentation).

- The ductility was significantly enhanced by heat treatment, with only a small reduction in ultimate tensile strength and with a yield strength that is still higher than the die cast material.
- Both the as-built and heat-treated material demonstrated the ability to withstand high compressive strains as they buckled during compression with no evidence of fracture. Heat treatment resulted in reducing the compressive yield strength of the material.
- The SLM material showed tension-compression asymmetry that was attributed to the material being textured [4] as well as ultrafine-grained.
- The material had good fatigue performance that was improved significantly by the T6 heat treatment. Machining the samples to improve their surface roughness was found to play a minor role in enhancing the fatigue life since the behaviour of the as-built and machined samples was mostly similar.
- The work here demonstrates the need for a new set of heat treatment procedures to be designed and tailored specifically for SLM materials. The conventional treatments cannot be used with SLM materials with their characteristic microstructures, expecting to achieve the same effect. In combination with the design freedom of SLM, this work can be used to deliver parts with a range of previously unachievable mechanical properties.

## **CHAPTER (8): Conclusions and recommendations for future work**

This chapter is divided into two parts. The first part presents a summary of the conclusions drawn based on the results from this investigation. The second part proposes studies that are recommended for future work expanding from this research.

### **8.1. Conclusions**

This study has considered the various aspects of the process of selective laser melting of an Aluminium alloy, AlSi10Mg, from powders to producing near fully dense parts. Since one of the main challenges in selective laser melting of Al alloys is the formation of high degrees of porosity in the fabricated parts, this study has traced the development of defects that might contribute to porosity formation in single scan tracks, layers, and parts. Furthermore, near fully dense samples were characterised for microstructural and mechanical properties. The findings in this investigation conclude the following:

- Slower scan speeds are recommended when processing AlSi10Mg for a consolidated defect-free scan track.
- Keyhole mode melting dominates SLM of AlSi10Mg due to the high thermal conductivity and low absorptivity, producing melt pools of high aspect ratio.

- A well-consolidated layer can be processed by selecting a suitable hatch spacing bearing in mind the width of the scan track and its shape to provide a sufficient amount of overlap between adjacent tracks.
- For the range of speeds and hatch spacings examined in this study, no pores were observed in the single tracks or layers suggesting that their formation occurs with layers' accumulation.
- Similar to the conclusion drawn from the single tracks study, slower scan speeds were recommended to create defect-free individual layers.
- Increasing the hatch spacing led to the formation of gaps between the scan tracks building up the part, i.e. depressing the relative density.
- Two types of pores form during SLM of AlSi10Mg, namely metallurgical and keyhole pores. The type of pore formed was scan speed dependent.
- Increasing the scan speed promoted surface defects such as balling on the surface, hindering the deposition of a uniform layer of powder for the following layers, resulting in further porosity formation.
- Altering the scan strategy can be implemented to reduce porosity since the use of a pre-melt scan strategy significantly suppressed the volume of porosity.
- The successful fabrication of near fully dense parts ( $99.77 \pm 0.08$ ) % using an optimised process window was achieved.
- The use of the pre-melt scan strategy with powder that does not fully comply with the process requirements has significantly remedied powder-induced defects yielding parts with a relative density that is comparable to those processed from higher quality powders.

- Laser spatter is produced in SLM due to selective oxidation reactions [82] and its amount was proportional to the gas flow rate within the processing chamber. Controlling the gas flow rate can control the amount of spatter removed hence controlling porosity and the presence of inclusions in the final parts produced.
- Cellular-dendritic solidification resulted in fine equiaxed grains at the melt pool core and columnar grains at the boundary with inter-dendritic Si in the form of continuous segregations on the boundaries of  $\alpha$ -Al.
- Rapid solidification resulted in a fine homogeneous dispersion of the alloying elements.
- A strong crystallographic texture was developed in the material due to the directional solidification and layer-by-layer fabrication.
- Spherodisation took place when heat treating the material using T6 heat treatment and the melt pools and dendritic structure were dissolved.
- The SLM material exhibited uniform nano-hardness profiles due to the fine microstructure and good dispersion of alloying elements.
- Softening in the nano-hardness was observed with accumulating scan tracks and layers.
- Areas around pores had coarser microstructures that were softer than the rest of the material.
- After heat treatment, spatial variation in nano-hardness was observed due to the presence of Si particles that developed local sensitivity to the indented phases.
- The SLM material was anisotropic with a micro-hardness comparable to the die-cast equivalent. Anisotropy diminished after heat treatment.

- The T6 heat treatment resulted in softening the material. The micro-hardness of the SLM material was always higher than the heat-treated material at all examined treatment durations.
- The ultimate and yield tensile strengths of the as-built material were higher than the die-cast counterpart. The T6 heat treatment granted the material a compromise between the strength and ductility by significantly improving the poor ductility of the SLM material by 179%, with a minor loss in strength (12%).
- Failure always originated at a sub-surface defect and propagated along softer regions of the melt pool boundary.
- The as-built and heat-treated materials showed high compressive strains withstanding up to a stress of ~700 MPa without fracture. The material's ultimate and yield compressive strengths decreased after heat treatment.
- The SLM material was ultra-fine-grained with a crystallographic texture that led to tension-compression asymmetry.
- The as-built material showed good performance under cyclic loading. An improved fatigue performance was achieved when the samples with machined surfaces were heat-treated (T6).

## **8.2. Benefits of the study to academia**

The outcomes of this study are beneficial to the academic community as they contribute to filling the gaps in the literature in the various aspects of the SLM process for Al alloys. For instance, this study is the first to report the dominant mode of melting during Al SLM. The studies in the literature are mostly

considering stainless steels [24, 69], that shows conduction mode melting, resulting in spherical melt pools and demanding a different approach in selecting the process parameters. The spherical melt pool would allow the use of larger hatch spacings that in the case of Al results in a lack of overlap. The response of Al to laser irradiation in SLM was completely different from other materials, such as stainless steel [24], showing that the literature needed this data for better understanding of Al SLM.

The cumulative approach in defining the best combination of process parameters to produce near fully dense parts was not previously conducted with Al alloys and instead studies recommended the use of high laser powers to tackle the problem of porosity, such as the work done by Buchbinder *et al.* [25]. Whereas the current investigation managed to trace porosity formation from the formation of single tracks to multi-layered parts and propose a methodology to remedy defects and produce dense parts.

This study has presented the correlation between the microstructure developed during processing, mainly governed by the mode of melting and solidification behaviour, and the local and bulk mechanical behaviour of the material. Studying the effect of the T6 heat treatment on the microstructure is novel and the interrelation between the microstructural evolution and the mechanical performance required the clarification that this investigation has provided.

### **8.3. Benefits of the study to the industry**

This investigation achieved a number of findings that are of benefit to various industrial sectors interested in selective laser melting of Al alloys, such as the automotive and aerospace industries. For example, the successful fabrication of

near fully dense parts of Al using SLM paves the way for further use of the technology in new fields since the presence of porosity limits its utilisation in critical applications.

The compromise between the SLM material's strength and ductility that was achieved by applying the meticulously selected combination of T6 heat treatment parameters is new and appealing for numerous applications when considering the material's light-weight. The significant improvement in the fatigue performance of the SLM AlSi10Mg through heat treating the samples with machined surfaces also adds to the material and pushes it forward for use in a wide range of applications.

The availability of a complete set of the most common mechanical properties is also expected to help designers in the industry to decide on the feasibility of using SLM Al in various applications.

#### **8.4. Recommendations for future work**

Although this study has covered several aspects of the SLM process using AlSi10Mg starting from the powder to characterising the processed parts, there is still more to be done that cannot fit within the duration of the PhD. A few recommended studies are presented in this chapter that would complement our understanding and control of the process.

It was established that the variation in the properties of powder, from one supplier to another, affects SLM where powders that do not comply with the pre-requisites yield poor quality parts. Despite the success of resolving this issue by using double scan strategies in this study, standardizing the properties

of powders for SLM is urgent. A double scan strategy means longer processing times that would not be appreciated by the industry, especially when fabricating large parts. Finding the best powder properties to be able to predict its good processability can be done through processing with a wide range of powder with different properties until defining the basic requirements.

SLM attracts attention for the potential of producing zero waste because the leftover powder from one process is usually sieved and goes back into the system for re-use. This research has shown no significant difference between the fresh and leftover powder. Although this could be an indicator that using recycled powder would not negatively affect the process, practically determining the threshold after which powder cannot be recycled furthermore is quite important. Moreover, the laser spatter that was observed in the leftover powder needs to be studied thoroughly not just to know its properties but also to determine the mechanism of its production and formation during processing. Finding a means that would prohibit, or at the least minimize, the entrapment of the laser spatter in the fabricated part is crucial since this spatter was observed on the fracture surface of some of the test samples in this study. Their presence then contributes to defects in the final parts so elimination is a must.

It has been previewed that the literature is full of studies concerned with material qualification. However, material qualification on its own is not going to help AM in the industry. This is because aside from the material variability, it is important to understand the machine-to-machine variability [9]. In other words, optimising the parameters for a material on a machine does not mean that these parameters could be generalised for this material and the need to optimise the parameters for each material on each specific machine (make or

model) is a setback for AM. For instance, two machines were used in this study to produce near fully dense samples. It was shown in this study that the combination of process parameters used for each machine to achieve high relative density was considerably different from one another. Understanding the reasons behind the variability will help tackle this issue towards a more repeatable processing.

The current study presented a first step in understanding the response of the SLM material to heat treatments by adopting a conventional T6 procedure. Investigation of a larger range of solution heat treatment and ageing temperatures and durations should also be conducted. Although the focus of this study was on the T6 heat treatment, other heat treatment procedures require attention as well, given the characteristic microstructure of Al samples processed by SLM. This microstructure might require developing tailored heat treatment procedure to yield the mechanical behaviour needed in operation if further strengthening is required.

This research has shown that the surface quality was not found to be detrimental on the mechanical performance of SLM parts if focussing on fatigue behaviour, however, improving the surface quality cannot be overlooked. Optimising the process parameters to produce parts with a high quality surface finish is important, especially for parts that will be assembled together in function where relative motion might be required.

Developing new alloys that are tailored for the SLM process could be a turning point for research in this area. For example, adding alloying elements to pure Al or Al alloys to enhance their process-ability is a means that deserves

attention. Coating the powders or just mixing them with elements that would improve their laser absorptivity or surface tension could be an alternative way to process Al alloys with SLM more effectively.

## REFERENCES

- [1] Kruth JP, Levy G, Klocke F, Childs THC. Consolidation phenomena in laser and powder-bed based layered manufacturing. *CIRP Annuals - Manufacturing Technology*. 2007;56:730-59.
- [2] Gibson I, Rosen DW, Stucker B. *Additive Manufacturing Technologies*: Springer; 2010.
- [3] Osakada K, Shiomi M. Flexible manufacturing of metallic products by selective laser melting of powder. *International Journal of Machine Tools and Manufacture*. 2006;46:1188-93.
- [4] Thijs L, Kempen K, Kruth J-P, Van Humbeeck J. Fine-structured aluminium products with controllable texture by selective laser melting of pre-alloyed AlSi10Mg powder. *Acta Materialia*. 2013;61:1809-19.
- [5] Kempen K, Thijs L, Van Humbeeck J, Kruth JP. Mechanical Properties of AlSi10Mg Produced by Selective Laser Melting. *Physics Procedia*. 2012;39:439-46.
- [6] Bartkowiak K, Ullrich S, Frick T, Schmidt M. New Developments of Laser Processing Aluminium Alloys via Additive Manufacturing Technique. *Physics Procedia*. 2011;12, Part A:393-401.
- [7] Islam M, Purtonen T, Piili H, Salminen A, Nyrhilä O. Temperature Profile and Imaging Analysis of Laser Additive Manufacturing of Stainless Steel. *Physics Procedia*. 2013;41:835-42.
- [8] L. BD, W. RD, Ming L. The Roadmap for Additive Manufacturing and Its Impact. *3D Printing and Additive Manufacturing*. 2014;1:4.
- [9] Frazier WE. Metal Additive Manufacturing: A Review. *Journal of Materials Engineering and Performance*. 2014;23:12.

- [10] Matilainen V, Piili H, Salminen A, Syvänen T, Nyrhilä O. Characterization of Process Efficiency Improvement in Laser Additive Manufacturing. *Physics Procedia*. 2014;56:317-26.
- [11] Hofmann DC, Roberts S, Otis R, Kolodziejska J, Dillon RP, Suh JO, Shapiro A A, Liu Z K, Borgonia J P. Developing gradient metal alloys through radial deposition additive manufacturing. *Scientific reports*. 2014;4:5357.
- [12] McCue T. Additive manufacturing will change in the next 5-10 years. *Forbes*; 2012.
- [13] Schleifenbaum H, Meiners W, Wissenbach K, Hinke C. Individualized production by means of high power Selective Laser Melting. *CIRP Journal of Manufacturing Science and Technology*. 2010;2:161-9.
- [14] Conner BP, Manogharan GP, Martof AN, Rodomsky LM, Rodomsky CM, Jordan DC, Limperos J W. Making sense of 3-D printing: Creating a map of additive manufacturing products and services. *Additive Manufacturing*. 2014;1-4:64-76.
- [15] Wycisk E, Solbach A, Siddique S, Herzog D, Walther F, Emmelmann C. Effects of Defects in Laser Additive Manufactured Ti-6Al-4V on Fatigue Properties. *Physics Procedia*. 2014;56:371-8.
- [16] Ion JC. *Laser processing of engineering materials: Principles, Procedure and Industrial application*. United Kingdom: El Sevier; 2005.
- [17] Ferrar B, Mullen L, Jones E, Stamp R, Sutcliffe CJ. Gas flow effects on selective laser melting (SLM) manufacturing performance. *Journal of Materials Processing Technology*. 2012;212:355-64.
- [18] Brandl E, Heckenberger U, Holzinger V, Buchbinder D. Additive manufactured AlSi10Mg samples using Selective Laser Melting (SLM):

Microstructure, high cycle fatigue, and fracture behavior. *Materials & Design*. 2012;34:159-69.

[19] Zhang B, Liao H, Coddet C. Effects of processing parameters on properties of selective laser melting Mg–9%Al powder mixture. *Materials & Design*. 2012;34:753-8.

[20] Yadroitsev I, Bertrand P, Smurov I. Parametric analysis of the selective laser melting process. *Applied Surface Science*. 2007;253:8064-9.

[21] Li R, Shi Y, Wang Z, Wang L, Liu J, Jiang W. Densification behavior of gas and water atomized 316L stainless steel powder during selective laser melting. *Applied Surface Science*. 2010;256:4350-6.

[22] Maskery I, Aremu AO, Simonelli M, Tuck C, Wildman RD, Ashcroft IA, Hague R J M. Mechanical Properties of Ti-6Al-4V Selectively Laser Melted Parts with Body-Centred-Cubic Lattices of Varying cell size. *Exp Mech*. 2015:1-12.

[23] Edwards P, Ramulu M. Fatigue performance evaluation of selective laser melted Ti–6Al–4V. *Materials Science and Engineering: A*. 2014;598:327-37.

[24] Yadroitsev I, Smurov I. Selective laser melting technology: From the single laser melted track stability to 3D parts of complex shape. *Physics Procedia*. 2010;5, Part B:551-60.

[25] Buchbinder D, Schleifenbaum H, Heidrich S, Meiners W, Bültmann J. High Power Selective Laser Melting (HP SLM) of Aluminum Parts. *Physics Procedia*. 2011;12, Part A:271-8.

[26] Ardila LC, Garciandia F, González-Díaz JB, Álvarez P, Echeverría A, Petite MM, Deffley R, Ochoa J. Effect of IN718 Recycled Powder Reuse on

Properties of Parts Manufactured by Means of Selective Laser Melting. *Physics Procedia*. 2014;56:99-107.

[27] Aremu A, Ashcroft I, Wildman R, Hague R, Tuck C, Brackett D. The effects of bidirectional evolutionary structural optimization parameters on an industrial designed component for additive manufacture. *Proceedings of the Institution of Mechanical Engineers, Part B: Journal of Engineering Manufacture*. 2013.

[28] Brackett D, Ashcroft I, Hague R. Topology optimization for additive manufacturing. *Solid Freedom Fabrication Symposium*. Texas, USA2011.

[29] Gardan N. Knowledge Management for Topological Optimization Integration in Additive Manufacturing. *International Journal of Manufacturing Engineering*. 2014;2014:9.

[30] Brennan-Craddock J, Brackett D, Wildman R, Hague R. The design of impact absorbing structures for additive manufacture. *Journal of Physics: Conference series*; 2012.

[31] Brackett DJ, Ashcroft IA, Wildman RD, Hague RJM. An error diffusion based method to generate functionally graded cellular structures. *Computers & Structures*. 2014;138:102-11.

[32] Yan C, Hao L, Hussein A, Raymont D. Evaluations of cellular lattice structures manufactured using selective laser melting. *International Journal of Machine Tools and Manufacture*. 2012;62:32-8.

[33] Yan C, Hao L, Hussein A, Bubb SL, Young P, Raymont D. Evaluation of light-weight AlSi10Mg periodic cellular lattice structures fabricated via direct metal laser sintering. *Journal of Materials Processing Technology*. 2014;214:856-64.

- [34] Yan C, Hao L, Hussein A, Young P, Raymont D. Advanced lightweight 316L stainless steel cellular lattice structures fabricated via selective laser melting. *Materials & Design*. 2014;55:533-41.
- [35] Yan C, Hao L, Hussein A, Young P, Huang J, Zhu W. Microstructure and mechanical properties of aluminium alloy cellular lattice structures manufactured by direct metal laser sintering. *Materials Science and Engineering: A*. 2015;628:238-46.
- [36] Smith M, Guan Z, Cantwell WJ. Finite element modelling of the compressive response of lattice structures manufactured using the selective laser melting technique. *International Journal of Mechanical Sciences*. 2013;67:28-41.
- [37] Qiu C, Yue S, Adkins NJE, Ward M, Hassanin H, Lee PD, Withers P J, Attallah M M. Influence of processing conditions on strut structure and compressive properties of cellular lattice structures fabricated by selective laser melting. *Materials Science and Engineering: A*. 2015;628:188-97.
- [38] Tisza M. *Physical metallurgy for engineers*: ASM International and Freund Publishing House Ltd.; 2002.
- [39] Li Y, Gu D. Parametric analysis of thermal behavior during selective laser melting additive manufacturing of aluminum alloy powder. *Materials & Design*. 2014;63:856-67.
- [40] Totten GE, Mackenzie DS. *Handbook of Aluminum: Physical Metallurgy and Processes*. 1 ed. New York: CRC press; 2003.
- [41] Polmear IJ. *Light alloys: metallurgy of the light metals*. 3rd edition ed.
- [42] Hosford WH. *Physical Metallurgy*. Second ed. United States of America: CRC Press; 2010.

- [43] Zhao H, White DR, DebRoy T. Current issues and problems in laser welding of automotive aluminium alloys. *International Materials Reviews*. 1999;44:238-66.
- [44] González R, González A, Talamantes-Silva J, Valtierra S, Mercado-Solís RD, Garza-Montes-de-Oca NF, Colás R. Fatigue of an aluminium cast alloy used in the manufacture of automotive engine blocks. *International Journal of Fatigue*. 2013;54:118-26.
- [45] Aluminum: properties and physical metallurgy. Ohio: American society for metals; 1984.
- [46] Guo N, Leu MC. Additive manufacturing: technology, applications and research needs. *Frontiers of Mechanical Engineering*. 2013;8:215-43.
- [47] Simonelli M. Microstructure Evolution and Mechanical Properties of Selective Laser Melted Ti-6Al-4V [Doctoral Thesis]: Loughborough University; 2014.
- [48] Simonelli M, Tse YY, Tuck C. Microstructure of Ti-6Al-4V produced by selective laser melting. *Journal of Physics: Conference Series*. 2012;371.
- [49] Read N, Wang W, Essa K, Attallah MM. Selective laser melting of AlSi10Mg alloy: Process optimisation and mechanical properties development. *Materials & Design*. 2015;65:417-24.
- [50] Sharma CP. *Engineering Materials: properties and applications of metals and alloys*: Prentice Hall of India; 2004.
- [51] Aboulkhair NT, Everitt NM, Ashcroft I, Tuck C. Reducing porosity in AlSi10Mg parts processed by selective laser melting. *Additive Manufacturing*. 2014;1-4:77-86.

- [52] Standard Test Methods for Flow Rate of Metal Powders Using the Hall Flowmeter Funnel. West Conshohocken: ASTM International; 2013.
- [53] Louvis E, Fox P, Sutcliffe CJ. Selective laser melting of aluminium components. *Journal of Materials Processing Technology*. 2011;211:275-84.
- [54] Kempen K, Thijs L, Yasa E, Badrossamay M, Verheecke W, Kruth J-P. Process optimization and microstructural analysis for selective laser melting of AlSi10Mg. *Solid Freeform Fabrication Symposium*. Texas, Austin, USA2011. p. 484-95.
- [55] Boivineau M, Cagran C, Doytier D, Eyraud V, Nadal MH, Wilthan B, Pottlacher G. Thermophysical Properties of Solid and Liquid Ti-6Al-4V (TA6V) Alloy. *Int J Thermophys*. 2006;27:507-29.
- [56] ASM. *Material properties handbook: Titanium alloys*. United States of America: ASM International; 1994.
- [57] ASM. *ASM Metals Reference Book*. 3rd edition ed. United States of America: ASM International; 1993.
- [58] Schreuder D. *Outdoor Lighting: Physics, Vision and Perception: Physics, Vision and Perception*: Springer; 2008.
- [59] Macleod HA. *Thin Film Optical Filters*. 3rd edition ed. United Kingdom: CRC Press; 2001.
- [60] Dadbakhsh S, Hao L. Effect of Al alloys on selective laser melting behaviour and microstructure of in situ formed particle reinforced composites. *Journal of Alloys and Compounds*. 2012;541:328-34.
- [61] Brandt JL. *Aluminum (Properties, physical metallurgy, and phase diagrams)*. Ohio: American Society for Metals ASM; 1967.

- [62] Aboulkhair NT. Strength and ductility of bulk nanostructured aluminum processed by mechanical milling. AUC DAR Repository The American University in Cairo; 2012.
- [63] Aboulkhair NT, Esawi AMK. Effect of Milling Time and Annealing on the Mechanical Response of Mechanically Milled Aluminium. *Adv Mater Res-Switz*. 2012;445:815-20.
- [64] Choi HJ, Lee SW, Park JS, Bae DH. Tensile behavior of bulk nanocrystalline aluminum synthesized by hot extrusion of ball-milled powders. *Scripta Materialia*. 2008;59:1123-6.
- [65] Cooke A, Slotwinski J. Properties of Metal Powders for Additive Manufacturing: A Review of the State of the Art of Metal Powder Property Testing. *Materials Standards for Additive manufacturing* 2012.
- [66] Yang S, Evans JRG. Metering and dispensing of powder; the quest for new solid freeforming techniques. *Powder Technology*. 2007;178:56-72.
- [67] Prashanth KG, Shakur Shahabi H, Attar H, Srivastava VC, Ellendt N, Uhlenwinkel V, Eckert J, Scudino S. Production of high strength Al85Nd8Ni5Co2 alloy by selective laser melting. *Additive Manufacturing*. 2015;6:1-5.
- [68] Dai D, Gu D. Thermal behavior and densification mechanism during selective laser melting of copper matrix composites: Simulation and experiments. *Materials & Design*. 2014;55:482-91.
- [69] Yadroitsev I, Gusarov A, Yadroitsava I, Smurov I. Single track formation in selective laser melting of metal powders. *Journal of Materials Processing Technology*. 2010;210:1624-31.

- [70] Yadroitsev I, Krakhmalev P, Yadroitsava I, Johansson S, Smurov I. Energy input effect on morphology and microstructure of selective laser melting single track from metallic powder. *Journal of Materials Processing Technology*. 2013;213:606-13.
- [71] Weingarten C, Buchbinder D, Pirch N, Meiners W, Wissenbach K, Poprawe R. Formation and reduction of hydrogen porosity during selective laser melting of AlSi10Mg. *Journal of Materials Processing Technology*. 2015;221:112-20.
- [72] Airbus-Group. SCALMALLOY®RP Auminum-Magnesium-Scandium alloy powder. Available at: <http://www.technology-licensing.com/etl/int/en/What-we-offer/Technologies-for-licensing/Metallics-and-related-manufacturing-technologies/Scalmalloy-RP.html>
- [73] Sachs M, Hentschel O, Schmidt J, Karg M, Schmidt M, Wirth K-E. Production of Al/Cu-Particles and their Potential for Processing by Laser Beam Melting (LBM). *Physics Procedia*. 2014;56:125-34.
- [74] Olakanmi EO. Selective laser sintering/melting (SLS/SLM) of pure Al, Al–Mg, and Al–Si powders: Effect of processing conditions and powder properties. *Journal of Materials Processing Technology*. 2013;213:1387-405.
- [75] Chang F, Gu D, Dai D, Yuan P. Selective laser melting of in-situ Al<sub>4</sub>SiC<sub>4</sub>+SiC hybrid reinforced Al matrix composites: Influence of starting SiC particle size. *Surface and Coatings Technology*. 2015;272:15-24.
- [76] Dadbakhsh S, Hao L. Effect of layer thickness in selective laser melting on microstructure of Al/5 wt.%Fe<sub>2</sub>O<sub>3</sub> powder consolidated parts. *TheScientificWorldJournal*. 2014;2014:106129.

- [77] Gu D, Chang F, Dai D. Selective Laser Melting Additive Manufacturing of Novel Aluminum Based Composites with Multiple Reinforcements. *Journal of Manufacturing Science and Engineering*. 2014.
- [78] Gu D, Wang H, Chang F, Dai D, Yuan P, Hagedorn Y-C, Meiners W. Selective Laser Melting Additive Manufacturing of TiC/AlSi10Mg Bulk-form Nanocomposites with Tailored Microstructures and Properties. *Physics Procedia*. 2014;56:108-16.
- [79] Gu DD, Wang HQ, Dai DH, Yuan PP, Meiners W, Poprawe R. Rapid fabrication of Al-based bulk-form nanocomposites with novel reinforcement and enhanced performance by selective laser melting. *Scripta Materialia*. 2015;96:25-8.
- [80] Gu D, Wang Z, Shen Y, Li Q, Li Y. In-situ TiC particle reinforced Ti–Al matrix composites: Powder preparation by mechanical alloying and Selective Laser Melting behavior. *Applied Surface Science*. 2009;255:9230-40.
- [81] O'Neill CF. Method and apparatus for reconditioning oxidized powder. United States of America: United Technologies corporation; 2014.
- [82] Simonelli M, Tuck C, Aboulkhair NT, Maskery I, Ashcroft I, Wildman RD, Hague R. A Study on the Laser Spatter and the Oxidation Reactions During Selective Laser Melting of 316L Stainless Steel, Al-Si10-Mg, and Ti-6Al-4V. *Metall Mater Trans A*. 2015;46A:3842-51.
- [83] Handbook of Aluminum: Volume 2: Alloy Production and Materials Manufacturing 2003.
- [84] Wang XJ, Zhang LC, Fang MH, Sercombe TB. The effect of atmosphere on the structure and properties of a selective laser melted Al–12Si alloy. *Materials Science and Engineering: A*. 2014;597:370-5.

- [85] Prashanth KG, Scudino S, Klauss HJ, Surreddi KB, Löber L, Wang Z, Chaubey A K, Kühn U, Eckert J. Microstructure and mechanical properties of Al–12Si produced by selective laser melting: Effect of heat treatment. *Materials Science and Engineering: A*. 2014;590:153-60.
- [86] Zheng L, Liu Y, Sun S, Zhang H. Selective laser melting of Al–8.5Fe–1.3V–1.7Si alloy: Investigation on the resultant microstructure and hardness. *Chinese Journal of Aeronautics*. 2015;28:564-9.
- [87] Egry I, Brillo J, Holland-Moritz D, Plevachuk Y. The surface tension of liquid aluminium-based alloys. *Materials Science and Engineering: A*. 2008;495:14-8.
- [88] Egry I, Ricci E, Novakovic R, Ozawa S. Surface tension of liquid metals and alloys — Recent developments. *Advances in Colloid and Interface Science*. 2010;159:198-212.
- [89] Porter DA, Easterling KE. *Phase transformation in metals and alloys*. Great Britain: Chapman & Hall; 1992.
- [90] Brown MS, Arnold CB. Fundamentals of Laser-Material interaction and application to multiscale surface modification. In: Sugioka K, editor. *Laser Precision Microfabrication*. Germany: Springer; 2010. p. 91-120.
- [91] Ciurana J, Hernandez L, Delgado J. Energy density analysis on single tracks formed by selective laser melting with CoCrMo powder material. *International Journal of Additive Manufacturing Technologies*. 2013;68:1103-10.
- [92] Pupo Y, Delgado J, Serenó L, Ciurana J. Scanning Space Analysis in Selective Laser Melting for CoCrMo Powder. *Procedia Engineering*. 2013;63:370-8.

- [93] Kempen K, Thijs L, Van Humbeeck J, Kruth JP. Processing AlSi10Mg by selective laser melting: parameter optimisation and material characterisation. *Materials Science and Technology*. 2014;31:917-23.
- [94] Kamath C, El-dasher B, Gallegos GF, King WE, Sisto A. Density of Additively-Manufactured, 316L SS Parts Using Laser Powder-Bed Fusion at Powers Up to 400W. *International Journal of Additive Manufacturing Technologies*. 2013.
- [95] Ahuja B, Karg M, Nagulin KY, Schmidt M. Fabrication and Characterization of High Strength Al-Cu Alloys Processed Using Laser Beam Melting in Metal Powder Bed. *Physics Procedia*. 2014;56:135-46.
- [96] King WE, Barth HD, Castillo VM, Gallegos GF, Gibbs JW, Hahn DE, Kamath C, Rubenchik A M. Observation of keyhole-mode laser melting in laser powder-bed fusion additive manufacturing. *Journal of Materials Processing Technology*. 2014;214:2915-25.
- [97] Loh L-E, Chua C-K, Yeong W-Y, Song J, Mapar M, Sing S-L, Liu Z-H, Zhang D-Q. Numerical investigation and an effective modelling on the Selective Laser Melting (SLM) process with aluminium alloy 6061. *International Journal of Heat and Mass Transfer*. 2015;80:288-300.
- [98] Panwisawas C, Qiu CL, Sovani Y, Brooks JW, Attallah MM, Basoalto HC. On the role of thermal fluid dynamics into the evolution of porosity during selective laser melting. *Scripta Materialia*. 2015;105:14-7.
- [99] Su X, Yang Y. Research on track overlapping during Selective Laser Melting of powders. *Journal of Materials Processing Technology*. 2012;212:2074-9.

- [100] Yadroitsev I, Smurov I. Surface Morphology in Selective Laser Melting of Metal Powders. *Physics Procedia*. 2011;12, Part A:264-70.
- [101] Krauss H, Zaeh MF. Investigations on Manufacturability and Process Reliability of Selective Laser Melting. *Physics Procedia*. 2013;41:815-22.
- [102] Loeber L, Biamino S, Ackelid U, Sabbadini S, Epicoco P, Fino P, Eckert J. Comparison of selective laser and electron beam melted Titanium Aluminides. *Solid Freedom Fabrication Symposium 2011*.
- [103] Kempen K, Vrancken B, Thijs L, Bols S, Van Humbeeck J, Kruth J-P. Lowering thermal gradients in Selective Laser melting by pre-heating the baseplate. *Solid Freedom Fabrication Symposium 2013*.
- [104] Buchbinder D, Meiners W, Pirch N, Wissenbach K, Schrage J. Investigation on reducing distortion by preheating during manufacture of aluminum components using selective laser melting. *Journal of Laser Applications*. 2014;26.
- [105] Tuck C, Maskery I, Simonelli M, Aboulkhair N, Ashcroft I, Everitt N, Wildman R, Hague R. Aspects of the Process and Material Relationships in the Selective Laser Melting of Aluminium Alloys. *TMS Annual meeting and exhibition 2015*.
- [106] Song B, Dong S, Liao H, Coddet C. Process parameter selection for selective laser melting of Ti6Al4V based on temperature distribution simulation and experimental sintering. *Int J Adv Manuf Technol*. 2012;61:967-74.
- [107] Carter LN, Attallah MM, Reed RC. Laser Powder Bed Fabrication of Nickel-Base Superalloys: Influence of Parameters; Characterisation,

Quantification and Mitigation of Cracking. *Superalloys 2012*: John Wiley & Sons, Inc.; 2012. p. 577-86.

[108] Haboudou A, Peyre P, Vannes AB, Peix G. Reduction of porosity content generated during Nd:YAG laser welding of A356 and AA5083 aluminium alloys. *Materials Science and Engineering: A*. 2003;363:40-52.

[109] Li XP, Kang CW, Huang H, Sercombe TB. The role of a low-energy-density re-scan in fabricating crack-free Al<sub>85</sub>Ni<sub>5</sub>Y<sub>6</sub>Co<sub>2</sub>Fe<sub>2</sub> bulk metallic glass composites via selective laser melting. *Materials & Design*. 2014;63:407-11.

[110] Simonelli M, Tse YY, Tuck C. On the texture formation of selective laser melted Ti-6Al-4V. *Metallurgical and Materials Transactions A: Physical Metallurgy and Materials Science*. 2014;45:2863-72.

[111] Kanagarajah P, Brenne F, Niendorf T, Maier HJ. Inconel 939 processed by selective laser melting: Effect of microstructure and temperature on the mechanical properties under static and cyclic loading. *Materials Science and Engineering: A*. 2013;588:188-95.

[112] Ma P, Prashanth KG, Scudino S, Jia YD, Wang HW, Zou CM, Wei Z J, Eckert J. Influence of Annealing on Mechanical Properties of Al-20Si Processed by Selective Laser Melting. *Metals*. 2014;4:28-36.

[113] Dadbakhsh S, Hao L, Jerrard PGE, Zhang DZ. Experimental investigation on selective laser melting behaviour and processing windows of in situ reacted Al/Fe<sub>2</sub>O<sub>3</sub> powder mixture. *Powder Technology*. 2012;231:112-21.

[114] Song B, Dong S, Coddet P, Liao H, Coddet C. Fabrication of NiCr alloy parts by selective laser melting: Columnar microstructure and anisotropic mechanical behavior. *Materials & Design*. 2014;53:1-7.

- [115] Song B, Dong S, Deng S, Liao H, Coddet C. Microstructure and tensile properties of iron parts fabricated by selective laser melting. *Optics & Laser Technology*. 2014;56:451-60.
- [116] Takaichi A, Suyalatu, Nakamoto T, Joko N, Nomura N, Tsutsumi Y, Migita S, Doi H, Kurosu S, Chiba A, Wakabayashi N, Igarashi Y, Hanawa T. Microstructures and mechanical properties of Co–29Cr–6Mo alloy fabricated by selective laser melting process for dental applications. *Journal of the Mechanical Behavior of Biomedical Materials*. 2013;21:67-76.
- [117] Zhang B, Dembinski L, Coddet C. The study of the laser parameters and environment variables effect on mechanical properties of high compact parts elaborated by selective laser melting 316L powder. *Materials Science and Engineering: A*. 2013;584:21-31.
- [118] Attar H, Calin M, Zhang LC, Scudino S, Eckert J. Manufacture by selective laser melting and mechanical behavior of commercially pure titanium. *Materials Science and Engineering: A*. 2014;593:170-7.
- [119] Simonelli M, Tse YY, Tuck C. Effect of the build orientation on the mechanical properties and fracture modes of SLM Ti–6Al–4V. *Materials Science and Engineering: A*. 2014;616:1-11.
- [120] Hanzl P, Zetek M, Bakša T, Kroupa T. The Influence of Processing Parameters on the Mechanical Properties of SLM Parts. *Procedia Engineering*. 2015;100:1405-13.
- [121] Siddique S, Imran M, Wycisk E, Emmelmann C, Walther F. Influence of process-induced microstructure and imperfections on mechanical properties of AlSi12 processed by selective laser melting. *Journal of Materials Processing Technology*. 2015;221:205-13.

- [122] Prashanth KG, Damodaram R, Scudino S, Wang Z, Prasad Rao K, Eckert J. Friction welding of Al–12Si parts produced by selective laser melting. *Materials & Design*. 2014;57:632-7.
- [123] Riemer A, Leuders S, Thöne M, Richard HA, Tröster T, Niendorf T. On the fatigue crack growth behavior in 316L stainless steel manufactured by selective laser melting. *Engineering Fracture Mechanics*. 2014;120:15-25.
- [124] Eliahu Zahavi, Torbilo V. *Fatigue design - Life expectancy of machine parts*: CRC Press; 1996.
- [125] Suresh S. *Fatigue of materials*. 2nd ed: Cambridge University Press; 1998.
- [126] Kwai S. Chan, Marie Koike, Robert L. Mason, Okabe T. *Fatigue Life of Titanium Alloys Fabricated by Additive Layer Manufacturing Techniques for Dental Implants*. *Metallurgical and Materials Transactions A*. 2013;44.
- [127] Rajan; TV, Sharma; CP, Sharma A. *Heat Treatment: Principles and Techniques*. second edition ed. New Delhi: PHI Learning Private Limited; 2011.
- [128] Biedunkiewicz A, Figiel P, Biedunkiewicz W, Grzesiak D, Krawczyk M, Gabriel-Polrolniczak U. Mechanical Properties of Metal Matrix Nanocomposites Synthesized by Selective Laser Melting Measured by Depth Sensing Indentation Technique. *Key Eng Mater*. 2014;586:83-6.
- [129] Wits WW, Weitkamp SJ, van Es J. Metal Additive Manufacturing of a High-pressure Micro-pump. *Procedia CIRP*. 2013;7:252-7.
- [130] Abramoff MD, Magalhaes PJ, Ram SJ. *Image Processing with ImageJ*. *Biophotonics International*. 2004;11:7.

- [131] Voort GFV. Metallography: Principles & practice. United States of America: ASM International 1999.
- [132] Malvern. Mastersizer 3000. Available at this link: <http://www.malvern.com/en/products/product-range/mastersizer-range/mastersizer-3000/2014>.
- [133] Weidmann E, Guesnier A. Struers Application Notes: Metallographic preparation of aluminium and aluminium alloys. 2008.
- [134] ASTM. B212-13 Standard Test Method for Apparent Density of Free-Flowing Metal Powders Using the Hall Flowmeter Funnel. 2013.
- [135] Davies MI. High Temperature Nanoindentation Characterisation of P91 and P92 Steel. United Kingdom: University of Nottingham; 2013.
- [136] ASTM. E2546-07 Standard practice for instrumented indentation testing West Conshohocken: ASTM International; 2007.
- [137] ASTM. E8/E8M-13a Standard Test Method for Tension Testing of Metallic Materials. Book of standards volume 0301. West Conshohocken: American Society for Testing and Materials ASTM; 2013.
- [138] ASTM. E9-09 "Standard Test Method for Compression Testing of Metallic Materials at room temperature". Book of standards volume 0301. West Conshohocken: American Society for Testing and Materials ASTM; 2009.
- [139] ASTM. E466-07 Standard practice for conducting force controlled constant amplitude axial fatigue tests for metallic materials. West Conshohocken: ASTM International; 2007.
- [140] Frost NE, Marsh KJ, Pook LP. Metal Fatigue. United states of America: Dover Publications; 1999.

[141] Jeffus L. *Welding: Principles and Applications*. 7th edition ed. United States of America 2012.

[142] IMRA. *Materials Processing*. Available at this link: <http://www.imra.com/applications/application-areas/materials-processing/#transparent-materials>.

[143] Yadroitsev I, Krakhmalev P, Yadroitsava I. Hierarchical design principles of selective laser melting for high quality metallic objects. *Additive Manufacturing*.

[144] Shi D, Li D, Gao G. Relation between surface tension and microstructural modification in Al–Si alloys. *Materials Characterization*. 2008;59:1541-5.

[145] Molina JM, Voytovych R, Louis E, Eustathopoulos N. The surface tension of liquid aluminium in high vacuum: The role of surface condition. *International Journal of Adhesion and Adhesives*. 2007;27:394-401.

[146] Qiu C, Panwisawas C, Ward M, Basoalto HC, Brooks JW, Attallah MM. On the role of melt flow into the surface structure and porosity development during selective laser melting. *Acta Materialia*. 2015;96:72-9.

[147] Braun R. Nd:YAG laser butt welding of AA6013 using silicon and magnesium containing filler powders. *Materials Science and Engineering: A*. 2006;426:250-62.

[148]

[http://www.steelnumber.com/en/steel\\_alloy\\_composition\\_eu.php?name\\_id=12](http://www.steelnumber.com/en/steel_alloy_composition_eu.php?name_id=12)  
27: European steel and alloy grades.

[149] Dahotre NB, Harimkar S. *Laser Fabrication and Machining of Materials*: Springer; 2008.

- [150] Xiao R, Zhang X. Problems and issues in laser beam welding of aluminum–lithium alloys. *Journal of Manufacturing Processes*. 2014;16:166-75.
- [151] Murray JL, McAlister AJ. The Al-Si (Aluminum-Silicon) system. *Bulletin of Alloy Phase Diagrams*. 1984;5:74-84.
- [152] González R, Martínez DI, González JA, Talamantes J, Valtierra S, Colás R. Experimental investigation for fatigue strength of a cast aluminium alloy. *International Journal of Fatigue*. 2011;33:273-8.
- [153] Makhlouf MM, Guthy HV. The aluminum–silicon eutectic reaction: mechanisms and crystallography. *Journal of Light Metals*. 2001;1:199-218.
- [154] Sánchez-Amaya JM, Delgado T, González-Rovira L, Botana FJ. Laser welding of aluminium alloys 5083 and 6082 under conduction regime. *Applied Surface Science*. 2009;255:9512-21.
- [155] Buchbinder D, W.Meiners, Wissenbach K, Poprawe R. Selective laser melting of aluminum die-cast alloy -- Correlation between process parameters, solidification conditions, and resulting mechanical properties. *Journal of Laser Applications*. 2015;27.
- [156] Reza Abbashian, Lara Abbaschian, Reed-hill RE. *Physical metallurgy principles*. 4th Ed ed. USA: Cengage learning; 2010.
- [157] Altenpohl D. *Aluminum viewed from within*. Federal Republic of Germany 1982.
- [158] Suwas S, Ray RK. *Crystallographic Texture of Materials*: Springer; 2014.
- [159] Manfredi D, Calignano F, Krishnan M, Canali R, Ambrosio E, Atzeni E. *From Powders to Dense Metal Parts: Characterization of a Commercial*

AlSiMg Alloy Processed through Direct Metal Laser Sintering. *Materials*. 2013;6:856.

[160] Bose SK, Kumar R. Structure of rapidly solidified aluminium-silicon alloys. *J Mater Sci*. 1973;8:1795-9.

[161] Sabatino MD. Fluidity of Aluminium: Norwegian University of Science and Technology; 2005.

[162] Mohamed AMA, Samuel FH. A Review on the Heat Treatment of Al-Si-Cu/Mg Casting Alloys 2012. Heat Treatment - Conventional and Novel Applications, Dr. Frank Czerwinski (Ed.), ISBN: 978-953-51-0768-2, InTech, DOI: 10.5772/50282. Available from: <http://www.intechopen.com/books/heat-treatment-conventional-and-novel-applications/a-review-on-the-heat-treatment-of-al-si-cu-mg-casting-alloys>.

[163] Fischer-Cripps AC. Nanoindentation. United States of America: Springer; 2004.

[164] Harvey E, Ladani L, Weaver M. Complete mechanical characterization of nanocrystalline Al-Mg alloy using nanoindentation. *Mechanics of Materials*. 2012;52:1-11.

[165] Ma K, Wen H, Hu T, Topping TD, Isheim D, Seidman DN, Lavernia E J, Schoenung J M. Mechanical behavior and strengthening mechanisms in ultrafine grain precipitation-strengthened aluminum alloy. *Acta Materialia*. 2014;62:141-55.

[166] Zolotarevsky VS, Belov NA, Glazoff MV. Casting Aluminum Alloys. Great Britain: Elsevier; 2007.

- [167] Aboulkhair NT, Tuck C, Ashcroft I, Maskery I, Everitt NM. On the Precipitation Hardening of Selective Laser Melted AlSi10Mg. *Metall Mater Trans A*. 2015;46A:3337-41.
- [168] Aboulkhair NT, Maskery I, Tuck C, Ashcroft I, Everitt NM. Nano-hardness and microstructure of selective laser melted AlSi10Mg scan tracks. 4th UK Industrial Laser Applications Symposium. Kenilworth, UK: SPIE; 2015.
- [169] Nie JF, Muddle BC. On the form of the age-hardening response in high strength aluminium alloys. *Materials Science and Engineering: A*. 2001;319–321:448-51.
- [170] Sjölander E, Seifeddine S. The heat treatment of Al–Si–Cu–Mg casting alloys. *Journal of Materials Processing Technology*. 2010;210:1249-59.
- [171] Sjölander E, Seifeddine S. Artificial ageing of Al–Si–Cu–Mg casting alloys. *Materials Science and Engineering: A*. 2011;528:7402-9.
- [172] Sjölander E, Seifeddine S. Optimisation of solution treatment of cast Al–Si–Cu alloys. *Materials & Design*. 2010;31, Supplement 1:S44-S9.
- [173] Hu T, Ma K, Topping TD, Schoenung JM, Lavernia EJ. Precipitation phenomena in an ultrafine-grained Al alloy. *Acta Materialia*. 2013;61:2163-78.
- [174] Leuders S, Thöne M, Riemer A, Niendorf T, Tröster T, Richard HA, Maier H J. On the mechanical behaviour of titanium alloy TiAl6V4 manufactured by selective laser melting: Fatigue resistance and crack growth performance. *International Journal of Fatigue*. 2013;48:300-7.
- [175] Charlie R. Brooks, Choudhury A. Failure analysis of engineering materials. United states of America: McGraw-Hill; 2002.

- [176] Materials ASfTa. Electron Fractography. Rahway, N.J.: American Society for Testing and Materials; 1968.
- [177] Tinga T. Principles of Loads and Failure mechanisms: Applications in Maintenance, Reliability and Design: Springer; 2013.
- [178] Manfredi D, Calignano F, Krishnan M, Canali R, Ambrosio EP, Biamino S, Ugues D, Pavese M, Fino P. Additive Manufacturing of Al Alloys and Aluminium Matrix Composites (AMCs) 2014. Light Metal Alloys Applications, Dr. Waldemar A. Monteiro (Ed.), ISBN: 978-953-51-1588-5, InTech, DOI: 10.5772/58534. Available from: <http://www.intechopen.com/books/light-metal-alloys-applications/additive-manufacturing-of-al-alloys-and-aluminium-matrix-composites-amcs->
- [179] Properties of aluminum alloys tensile creep and fatigue data at high and low temperatures. Materials Park (Ohio): ASM International 1999.
- [180] Kiser M, He MY, Zok FW. The mechanical response of ceramic microballoon reinforced aluminum matrix composites under compressive loading. Acta Materialia. 1999;47:2685-94.
- [181] Frick C, Gali K, Ortega A, Tyber J, Maier H. Fatigue and asymmetric deformation of Nitinol shape memory alloys. In: Shrivastava S, editor. Materials and processes for medical devices conference: ASM International; 2004. p. 193-8.
- [182] Gürses E, El Sayed T. On tension–compression asymmetry in ultrafine-grained and nanocrystalline metals. Computational Materials Science. 2010;50:639-44.

- [183] Cheng S, Spencer JA, Milligan WW. Strength and tension/compression asymmetry in nanostructured and ultrafine-grain metals. *Acta Materialia*. 2003;51:4505-18.
- [184] Avalle M, Belingardi G, Cavatorta MP, Doglione R. Casting defects and fatigue strength of a die cast aluminium alloy: a comparison between standard specimens and production components. *International Journal of Fatigue*. 2002;24:1-9.
- [185] Wang QG, Apelian D, Lados DA. Fatigue behavior of A356-T6 aluminum cast alloys. Part I. Effect of casting defects. *Journal of Light Metals*. 2001;1:73-84.
- [186] Chen YQ, Pan SP, Zhou MZ, Yi DQ, Xu DZ, Xu YF. Effects of inclusions, grain boundaries and grain orientations on the fatigue crack initiation and propagation behavior of 2524-T3 Al alloy. *Materials Science and Engineering: A*. 2013;580:150-8.
- [187] McMillan JC, Hertzberg RW. Application of electron fractography to fatigue studies. *Electron Fractography ASTM STP 436* Rashway, N. J.: American Society for Testing and Materials; 1968.
- [188] Spitzig WA, Pellissier GE, Beachem CD, Brothers AJ, Hill M, Warke WR. A fractographic analysis of the relationships between fracture toughness and surface topography in ultrahigh-strength steels. *Electron Fractography ASTM STP 436* Rashway, N. J.: American Society for testing and and Materials; 1968.
- [189] Ammar HR, Samuel AM, Samuel FH. Effect of casting imperfections on the fatigue life of 319-F and A356-T6 Al-Si casting alloys. *Materials Science and Engineering: A*. 2008;473:65-75.